

**Predictive Expressions for Residual Stress and Distortion  
in Welding and Related Thermal Processes**

by

Mitchell R. Grams

A thesis submitted in partial fulfillment of the requirements for the degree of

Doctor of Philosophy

in

Materials Engineering

Department of Chemical and Materials Engineering  
University of Alberta

© Mitchell R. Grams, 2021

# Abstract

This work establishes the foundation for the estimation of forces and distortions induced by thermal processes, such as welding, as well as incorporates the effects of departure from idealizations. The Order of Magnitude Scaling (OMS) technique is applied to thermal-mechanical analysis of a moving point heat source. Under typical conditions, the thermal stress field is found to be best characterized by a uniaxial model. The region of plastic behaviour is set by the “first yield temperature”, a material property associated with thermal strain equivalent to the yield strain. The proposed scaling laws are applicable for any parameters that produce a sufficiently elongated first yield isotherm with  $\mathcal{R} \gtrsim 17$ . A survey of single pass welding procedures indicate that this criterion will be met in almost all cases. The resulting uniform residual stress distribution along the heat source trajectory may be separated into a local driving component and a global reaction component. The driving component is expressed as an equivalent concentrated load, termed the tendon force, which is proportional to the linear energy input. A universal estimate of the proportionality factor for any metal with temperature independent properties is obtained as  $\hat{H} \approx 0.23$ . The temperature dependent behaviour of materials is captured accurately using four independent dimensionless groups and the results are validated for common structural grades of steel, aluminum, and titanium with nonlinear finite element simulations. For some geometries, the section may not be sufficiently rigid to support uniaxial restraint. The concept of compliance is introduced as a simple, accurate, and general measure of the tendency for the geometry to distort at the location of a locally applied force. The effect of compliance is found to depend on a newly defined dimen-

sionless parameter, the Okerblom number ( $Ok$ ). For symmetric flat plate geometry, this parameter is physically interpreted as the normalized equilibrium temperature rise. The methodology of blended asymptotics is used to obtain explicit compliance correction factors for the yield temperatures and tendon force. The closed-form blended expressions are validated against literature data for flat plates, T-sections, and thin cylinders. The practical utility of the corrected asymptotic methodology is demonstrated with a case study on non-ideal fit-up of circumferential pipeline joints. Angular distortion at the pipe end produces bending across the weld root. The tendon force is used to derive a novel root susceptibility index which relates the welding procedure variables and material properties with the weld cross-section and pipe geometry. The stress concentration associated with non-ideal geometry is considered as a correction factor on the asymptotic case of ideal fit-up. The index presented is a contribution towards an objective criterion for acceptance of high-low offset. Although many of the illustrative examples presented this work relate to welding, the theory and equations presented here are broadly applicable to the fields of thermal cutting, laser processing (cladding and heat treatment), machining, grinding, and additive manufacturing. The simple, general, and accurate formulae presented in this work are well suited for use in procedure development and process design.

# Preface

The material presented in this thesis comprises the author’s research project under the supervision of Dr. Patricio Mendez. This work received funding from Enbridge Employee Services Inc. and the Natural Sciences and Engineering Research Council of Canada (NSERC) under a Collaborative Research and Development (CRD) grant No. 507483-2016.

Chapter 2 of this work is published as Grams, M. R. and Mendez, P. F., 2021 “Scaling analysis of the thermal stress field produced by a moving point heat source in a thin plate”, *ASME Journal of Applied Mechanics*. Dr. Patricio Mendez is the supervisory author.

Chapter 3 of this work has been accepted for publication as Grams, M. R. and Mendez, P. F., 2021 “A general expression for the welding tendon force”, *ASME Journal of Manufacturing Science and Engineering*. Dr. Patricio Mendez is the supervisory author.

Chapter 4 of this work has been prepared for submission as Grams, M. R. and Mendez, P. F., 2021 “Effect of compliance on residual stresses in manufacturing with moving heat sources”, *ASME Journal of Applied Mechanics*. Dr. Patricio Mendez is the supervisory author.

Chapter 5 of this work is published as Grams, M. R., Ludwig, L., and Mendez, P. F., 2021 “A quantitative index to assess the influence of joint fit-up on pipeline weld root discontinuities”, *Proceedings of the ASME 2020 13th International Pipeline Conference*. This submission was recognized with the distinguished “Best Paper Award” in the IPC 2020 student paper competition. Luke Ludwig is the industrial

advisor for this work. He provided valuable insight on the practical application of the proposed formula as well as advice throughout the writing process and is a co-author of the paper for his contributions. Dr. Patricio Mendez is the supervisory author.

As the supervisory author for all the papers presented in this thesis, Dr. Patricio Mendez provided advice regarding the analysis and revised all publications prior to submission. This thesis follows a paper-based format, and there may be some repetition, particularly in description of the research motivation and methods. Where appropriate, minor updates have been made to the mathematical notation used in the separate publications to achieve better consistency throughout this work.

*To Samantha and Luna, for your love and encouragement.*

# Acknowledgements

A friend once advised me that it is essential to choose your supervisor with care, as for better or worse, you will finish your degree having adopted at least a some of their style, character, and philosophy. I believe I chose wisely. Patricio, your enthusiasm drew me to this journey and encouraged me at each point along the way. Thank you for the inspiration that your love of welding provided; thank you for your patience as I often struggled to join my myriad of thoughts into a coherent whole; and thank you for the many lessons, opportunities, and memories that these last five years have provided. Above all else, thank you for teaching me that what you do matters some, why you do it matters more, but who you do it with matters most of all.

There are so many people who made the CCWJ an inviting and engaging environment. Thank you first and foremost to Goetz, for the innumerable discussions over coffee and sour cream glazed donuts. My time in the lab was made both more enjoyable and survivable through your advice and good company. Thank you to all CCWJ alumni, including (in no particular order) Steve, Ata, Jordan, Cory, Vivek, Gentry, Chris, Jason, Kurtis, Matt, and Nairn. The lab remains a unique and special place, in no small part because of your lasting efforts. I would be remiss if I did not also acknowledge Kyle, Syed, Daniel, Rishie, Julie, Jolene, Mackenzi, Carter, and Eddie whom I have had the great privilege to learn from, mentor, and labour alongside. Special thanks to Ying, Louie, Alejandro, and Dima for shouldering the conversational burden that came with occupying a desk next to my own, and for helping me take the first steps along the paths of mathematical and metallurgical enlightenment.

To the members of the welding industry, especially Luke Ludwig, thank you for

providing the knowledge and wisdom that guided my efforts. Thank you also to Dayton Block and all other welders and welding educators who gave me a practical appreciation of the welding art. My great thanks is likewise given to the UofA technical staff who endured with patience and good humour my numerous questions and inquiries. Thank you to Dan Tadic, Ken McKen, and all those who enable the CWB to support training the next generation of welding engineers. Special thanks to Dr. Thomas Lienert, Dr. Duane Miller, and the AWS leadership for inviting me to learn first-hand from true pillars of the industry. To all others in the Canadian and international welding communities who have provided me with mentorship, scholarships, and friendship, thank you for welcoming me into your midst.

To Mike, my friend and fellow MecE. My apologies for making grad school look so enjoyable that you came back to join me for more, but at least we got to produce one last ridiculous report together.

To all my family, I could not have done this without you. Mom, your love and support throughout this incredible experience has shaped me into the person I am today. Dad, thank you for inspiring me to pursue engineering, and opening my eyes to the incredible world of possibilities in this diverse and compelling profession. To my brothers, Alex and Ryan, your knowledge and insight was often sought and ever welcome. Thank you for all the time you gave to share in my pursuit of understanding.

Most importantly, my endless thanks and gratitude to my wife Samantha. This degree has truly been an adventure, and all the more enjoyable with you by my side. Likely you have now heard more of my contemplations of arcane welding theory and equations than all others mentioned here together. You have always believed in me and for that along with so much else, I love you.

Thank you to all who reviewed the many drafts and manuscripts that became this thesis. Looking back, I would not trade my time at the UofA for anything. I can only hope that those who read this see value in the product of my work, or failing that, may they at least find inspiration in my efforts.

# Table of Contents

<b>1</b>	<b>Introduction</b>	<b>1</b>
1.1	Methodology . . . . .	1
1.2	Background . . . . .	3
1.3	Objectives . . . . .	7
1.4	Thesis Outline . . . . .	8
	References . . . . .	9
<b>2</b>	<b>Scaling Analysis of the Thermal Stress Field Produced by a Moving Point Heat Source in a Thin Plate</b>	<b>11</b>
2.1	Introduction . . . . .	11
2.2	List of Symbols . . . . .	14
2.3	Asymptotic Analysis . . . . .	15
2.3.1	Order of Magnitude Scaling . . . . .	15
2.3.2	Construction of the Matrix of Coefficients . . . . .	17
2.3.3	Iterations Based on Matrix Operations . . . . .	20
2.3.4	Limit of Validity of Estimates . . . . .	23
2.4	Plasticity Considerations . . . . .	25
2.4.1	First Yield Temperature . . . . .	26
2.4.2	Plastic Zone Width . . . . .	28
2.5	Validation of Results . . . . .	30
2.5.1	Numerical Modelling . . . . .	30
2.6	Application to Industrial Practice . . . . .	34
2.6.1	Analytical Estimation of Aspect Ratio . . . . .	34
2.6.2	Survey of Typical Welding Procedures . . . . .	37
2.7	Discussion . . . . .	37
2.8	Conclusions . . . . .	41
2.9	Acknowledgements . . . . .	42
	References . . . . .	43

<b>3</b>	<b>A General Expression for the Welding Tendon Force</b>	<b>46</b>
3.1	Introduction . . . . .	46
3.2	List of Symbols . . . . .	48
3.3	Definition of Tendon Force . . . . .	50
3.3.1	Reaction Strain . . . . .	51
3.3.2	Inherent Strain . . . . .	52
3.3.3	Total Strain . . . . .	53
3.3.4	Relationship Between Tendon Force and Plasticity . . . . .	54
3.4	Constant Material Properties . . . . .	55
3.4.1	Strain Induced by the Thermal Cycle . . . . .	55
3.4.2	Thermal-Elastic Strain Relationship . . . . .	57
3.4.3	Distribution of Residual Plastic Strain . . . . .	60
3.4.4	Tendon Force with Constant Properties . . . . .	61
3.5	Computational Simulations . . . . .	63
3.5.1	Numerical Model . . . . .	63
3.5.2	Results from Computational Simulations . . . . .	65
3.6	Temperature Dependent Material Properties . . . . .	67
3.6.1	Temperature Dependent Yield Strain . . . . .	68
3.6.2	Temperature Dependent Thermal Expansion . . . . .	69
3.6.3	Temperature Dependent Heat Capacity . . . . .	70
3.6.4	Nonlinear Rate of Change for the Yield Strain . . . . .	71
3.6.5	Tendon Force with Variable Properties . . . . .	73
3.6.6	Correction Factors for Variable Properties . . . . .	73
3.6.7	Numerical Validation . . . . .	76
3.7	Example of Application . . . . .	77
3.8	Discussion . . . . .	81
3.9	Conclusions . . . . .	83
3.10	Acknowledgements . . . . .	84
3.11	Appendix: Effective Properties Calculation . . . . .	84
3.12	Appendix: High Temperature Effects . . . . .	86
	References . . . . .	88
<b>4</b>	<b>Effect of Compliance on Residual Stresses in Manufacturing with Moving Heat Sources</b>	<b>91</b>
4.1	Introduction . . . . .	91
4.2	List of Symbols . . . . .	93
4.3	Governing Equations . . . . .	95

4.3.1	Residual Strain Distribution . . . . .	95
4.3.2	Concept of Compliance . . . . .	95
4.3.3	Equivalent Load . . . . .	98
4.4	Thermal Strain . . . . .	99
4.4.1	Temperature Distribution . . . . .	99
4.4.2	Thermal Force . . . . .	100
4.5	Plastic Strain . . . . .	100
4.5.1	Plastic Strain During Heating . . . . .	101
4.5.2	First Yield Temperature . . . . .	103
4.5.3	Plastic Strain During Cooling . . . . .	103
4.5.4	Second Yield Temperature . . . . .	104
4.5.5	Plastic Force . . . . .	106
4.6	Total Strain . . . . .	107
4.6.1	Total Strain - Low Temperatures . . . . .	108
4.6.2	Total Strain - High Temperatures . . . . .	109
4.6.3	Total Strain - Equilibrium . . . . .	109
4.7	Compliance Effect on 1st Yield Temperature . . . . .	110
4.7.1	Implicit Expression . . . . .	110
4.7.2	Blended Asymptotics . . . . .	111
4.8	Compliance Effect on 2nd Yield Temperature . . . . .	112
4.8.1	Implicit Expression . . . . .	112
4.8.2	Blended Asymptotics . . . . .	113
4.9	Compliance Effect on Tendon Force . . . . .	114
4.9.1	Implicit Expression . . . . .	114
4.9.2	Blended Asymptotics . . . . .	115
4.10	Limits of Applicability . . . . .	116
4.10.1	Equilibrium Temperature Distribution . . . . .	116
4.10.2	Assumption of Concentrated Force . . . . .	118
4.11	Validation . . . . .	120
4.11.1	First Yield Temperature . . . . .	121
4.11.2	Tendon Force . . . . .	122
4.12	Discussion . . . . .	123
4.13	Conclusions . . . . .	125
4.14	Acknowledgements . . . . .	126
4.15	Appendix: Calculation of Compliance . . . . .	127
4.16	Appendix: Higher Order Correction . . . . .	129
	References . . . . .	132

<b>5</b>	<b>A Quantitative Index to Assess the Influence of Joint Fit-Up on Pipeline Weld Root Discontinuities</b>	<b>135</b>
5.1	Introduction . . . . .	135
5.2	List of Symbols . . . . .	138
5.3	Ideal Model . . . . .	139
5.3.1	Tendon Force . . . . .	139
5.3.2	Angular Distortion . . . . .	144
5.3.3	Correction Factor for Tendon Force Distribution . . . . .	145
5.3.4	Correction Factor for Resistance of Weld Bead . . . . .	146
5.3.5	Susceptibility Index . . . . .	149
5.3.6	Numerical Validation . . . . .	149
5.4	Non-Ideal Geometry . . . . .	154
5.4.1	Weld Profile . . . . .	154
5.4.2	Stress Concentration Factor . . . . .	154
5.4.3	Modified Susceptibility Index . . . . .	156
5.4.4	Numerical Validation . . . . .	157
5.5	Case Study . . . . .	159
5.6	Discussion . . . . .	161
5.7	Conclusions . . . . .	162
	References . . . . .	164
<b>6</b>	<b>Conclusions and Future Work</b>	<b>166</b>
6.1	Conclusions . . . . .	166
6.2	Future Work . . . . .	169
	<b>Bibliography</b>	<b>170</b>
	<b>Appendix A: Experimental Data</b>	<b>178</b>
A.1	Plastic Zone and Tendon Force in Flat Plates . . . . .	178
A.2	Plastic Zone and Tendon Force in T-Sections . . . . .	181
A.3	Plastic Zone in Circumferential Joints . . . . .	182
	<b>Appendix B: Simulation Data</b>	<b>183</b>
B.1	Effect of Aspect Ratio on Plastic Zone Size . . . . .	183
B.2	Tendon Force . . . . .	187
B.3	Pipe Root Strain . . . . .	188
B.4	Non-Ideal Stress Concentration . . . . .	192

<b>Appendix C: Material Properties</b>	<b>193</b>
C.1 ASTM A36 Structural Steel . . . . .	193
C.2 Aluminum Alloy 6082-T6 . . . . .	195
C.3 304 Stainless Steel . . . . .	197
C.4 316L Stainless Steel . . . . .	199
C.5 P91 Alloy Steel . . . . .	201
C.6 Titanium Alloy TiAl6V4 . . . . .	203

# List of Tables

2.1	Properties of selected materials at first yield temperature ( $T_{Y1}$ ) for a starting temperature of $T_0 = 20^\circ\text{C}$ . . . . .	28
2.2	Predicted width of the first yield isotherm for selected materials and welding heat input. . . . .	33
2.3	Summary data for Rosenthal number of typical welding processes with a starting temperature of $T_0 = 20^\circ\text{C}$ on ASTM A36 structural steel ( $T_{Y1} = 101^\circ\text{C}$ , $k = 53 \text{ W m}^{-1}\text{K}^{-1}$ ) and aluminum alloy 6082-T6 ( $T_{Y1} = 80^\circ\text{C}$ , $k = 213 \text{ W m}^{-1}\text{K}^{-1}$ ) using data from [45] (arc welding) and [52] (friction stir welding of low-carbon steel and 6xxx series aluminum). . . . .	38
3.1	Comparison of asymptotic expression for tendon force (Equation (3.17)) with computational simulation results (FEA). . . . .	67
3.2	Typical values for the correction factor associated with temperature dependent yield strain and CTE. . . . .	74
3.3	Typical values for the correction factor associated with the effective heat capacity. . . . .	75
3.4	Typical values of the yield temperatures, yield temperature ratio, and nonlinear yield strain correction factor assuming a starting/ambient temperature of $T_0 = 20^\circ\text{C}$ . . . . .	76
3.5	Maximum allowable heat input (resulting in 1 mm deflection of a 1 m member) for selected alloys. . . . .	79
4.1	Compliance of typical simple section geometries. . . . .	97
5.1	Calculated values of the first yield temperature change $\Delta T_{Y1}$ (Equation (5.2)) and non-dimensional coefficient $H$ (Equation (5.5)) for CSA Gr.483 (X70) pipe with a preheat of $T_0 = 25 - 150^\circ\text{C}$ . . . . .	142
5.2	Parameter ranges for root pass welding with SMAW on CSA Gr.483 (X70) pipe material. . . . .	153

5.3	Comparison of latent discontinuity susceptibility for two different SMAW root pass weld procedures on 36 in. (0.91 m) diameter, CSA Gr.483 (X70) pipe material with varying levels of high-low offset. . . . .	160
A.1	Correction factors for plastic zone and tendon force for centre weld on flat plate; data after Ref. [20], given $\alpha = 1.2 \times 10^{-5} \text{ K}^{-1}$ , $\epsilon_{Y,0} = 1.57 \times 10^{-3}$ , $\sigma_{Y,w} = 460 \text{ MPa}$ , $\sigma_{Y,b} = 330 \text{ MPa}$ , $\hat{y}_{pl} \approx 50 \text{ mm}$ , $\hat{F}_{Ten} \approx 158 \text{ kN}$ , $S^* = 1$ . . . . .	178
A.2	Correction factor for tendon force in aluminum for centre weld on flat plate ( $d = 10 \text{ mm}$ , $l = 1500 \text{ mm}$ , $w = 200 - 1500 \text{ mm}$ ); data after Ref. [50], given $\alpha = 2.4 \times 10^{-5} \text{ K}^{-1}$ , $\epsilon_{Y,0} = 2.0 \times 10^{-3}$ , $E \approx 75 \text{ GPa}$ , $\rho c = 0.0022 \text{ J mm}^{-3} \text{ K}^{-1}$ . . . . .	178
A.3	Correction factor for tendon force in lower strength structural steel for centre weld on flat plate ( $d = 10 \text{ mm}$ , $l = 1500 \text{ mm}$ , $w = 200 - 1500 \text{ mm}$ ); data after Ref. [50], given $\alpha = 1.2 \times 10^{-5} \text{ K}^{-1}$ , $\epsilon_{Y,0} = 2.0 \times 10^{-3}$ , $E \approx 200 \text{ GPa}$ , $\rho c = 0.0040 \text{ J mm}^{-3} \text{ K}^{-1}$ . . . . .	179
A.4	Correction factor for tendon force in higher strength structural steel for centre weld on flat plate ( $d = 10 \text{ mm}$ , $l = 1500 \text{ mm}$ , width $w = 200 - 1500 \text{ mm}$ ); data after Ref. [50], given $\alpha = 1.2 \times 10^{-5} \text{ K}^{-1}$ , $\epsilon_{Y,0} = 4.0 \times 10^{-3}$ , $E \approx 200 \text{ GPa}$ , $\rho c = 0.0040 \text{ J mm}^{-3} \text{ K}^{-1}$ . . . . .	179
A.5	Correction factor for tendon force in austenitic stainless steel for centre weld on flat plate ( $d = 10 \text{ mm}$ , $l = 1500 \text{ mm}$ , width $w = 200 - 1500 \text{ mm}$ ); data after Ref. [50], given $\alpha = 1.8 \times 10^{-5} \text{ K}^{-1}$ , $\epsilon_{Y,0} = 1.4 \times 10^{-3}$ , $E \approx 200 \text{ GPa}$ , $\rho c = 0.0040 \text{ J mm}^{-3} \text{ K}^{-1}$ . . . . .	180
A.6	Geometry of T-sections fabricated from two plates with thickness ( $d$ ), vertical plate height ( $h$ ), horizontal plate width ( $w$ ), and distance ( $z$ ) between mid-thickness of horizontal plate and section centre of gravity; data after Ref. [21]. . . . .	181
A.7	Correction factors for plastic zone size and tendon force; data after Ref. [21], given $\alpha = 1.2 \times 10^{-5} \text{ K}^{-1}$ , $E = 210 \text{ GPa}$ , $\sigma_{Y,w} = 520 \text{ MPa}$ , $\sigma_{Y,b} = 330 \text{ MPa}$ , $\hat{y}_{pl} = 50 \text{ mm}$ , $\hat{F}_{Ten} = 499 \text{ kN}$ . . . . .	181
A.8	Geometry and compliance for circumferential joint between two thin cylinders; data after Ref. [87], given $\nu = 0.3$ . . . . .	182
A.9	Correction factor for plastic zone size; data after Ref. [87], given $\alpha = 1.2 \times 10^{-5}$ , $\epsilon_Y \approx 1.81 \times 10^{-3}$ ( $\sigma_Y = 380 \text{ MPa}$ , $E = 210 \text{ GPa}$ ), $\Delta T_{Y1} \approx \epsilon_Y/\alpha = 151 \text{ }^\circ\text{C}$ . . . . .	182

B.1	Welding parameters used for numerical studies of plastic zone size for centre weld on flat plate ( $d = 3$ mm, $l = 2400$ mm, $w = 2000$ mm).	183
B.2	Numerical results for first yield aspect ratio, plastic zone size, and correction factor for ASTM A36 structural steel ( $\rho c = 0.0037$ J mm <sup>-3</sup> K <sup>-1</sup> , $\Delta T_{Y1} = 80$ °C, $\hat{y}_{pl} \approx 33$ mm), and $Q' = 0.12$ kJ/mm.	184
B.3	Numerical results for first yield aspect ratio, plastic zone size, and correction factor for ASTM A36 structural steel ( $\rho c = 0.0037$ J mm <sup>-3</sup> K <sup>-1</sup> , $\Delta T_{Y1} = 80$ °C, $\hat{y}_{pl} \approx 65$ mm), and $Q' = 0.24$ kJ/mm.	184
B.4	Numerical results for first yield aspect ratio, plastic zone size, and correction factor for ASTM A36 structural steel ( $\rho c = 0.0037$ J mm <sup>-3</sup> K <sup>-1</sup> , $\Delta T_{Y1} = 80$ °C, $\hat{y}_{pl} \approx 130$ mm), and $Q' = 0.48$ kJ/mm.	185
B.5	Numerical results for first yield aspect ratio, plastic zone size, and correction factor for aluminum alloy 6082-T6 ( $\rho c = 0.0025$ J mm <sup>-3</sup> K <sup>-1</sup> , $\Delta T_{Y1} = 59$ °C, $\hat{y}_{pl} \approx 133$ mm), and $Q' = 0.24$ kJ/mm.	185
B.6	Numerical results for first yield aspect ratio, plastic zone size, and correction factor for 316L stainless steel ( $\rho c = 0.0040$ J mm <sup>-3</sup> K <sup>-1</sup> , $\Delta T_{Y1} = 66$ °C, $\hat{y}_{pl} \approx 73$ mm), and $Q' = 0.24$ kJ/mm.	186
B.7	Numerical results for first yield aspect ratio, plastic zone size, and correction factor for P91 alloy steel ( $\rho c = 0.0039$ J mm <sup>-3</sup> K <sup>-1</sup> , $\Delta T_{Y1} = 191$ °C, $\hat{y}_{pl} \approx 26$ mm), and $Q' = 0.24$ kJ/mm.	186
B.8	Summary of results from Simufact numerical studies of tendon force for centre weld on flat plate ( $d = 3$ mm, $l = 2400$ mm, $w = 1200$ mm).	187
B.9	Input geometry and plastic zone size used for numerical simulations of circumferential pipe joint, given $\eta = 0.8$ , $1/\rho c = 250$ J <sup>-1</sup> mm <sup>3</sup> K and $\Delta T_{Y1} = 180$ °C.	188
B.10	Comparison of model predictions with numerical results of pipe root strain, for tests with $Q' = 0.6$ kJ/mm, given $H\eta = 0.18$ and $E = 200$ GPa. Values for $f_D$ (Sim.) are estimated using the theoretical moment correction factor $f_M(\Pi_2)$ ; values for $f_M$ (Sim.) assume the theoretical distribution correction factor $f_D(\Pi_1)$ .	189
B.11	Comparison of model predictions with numerical results of pipe root strain, for tests with $Q' = 1.2$ kJ/mm, given $H\eta = 0.18$ and $E = 200$ GPa. Values for $f_D$ (Sim.) are estimated using the theoretical moment correction factor $f_M(\Pi_2)$ ; values for $f_M$ (Sim.) assume the theoretical distribution correction factor $f_D(\Pi_1)$ .	190

B.12 Comparison of model predictions with numerical results of pipe root strain, for tests with  $Q' = 1.8$  kJ/mm, given  $H\eta = 0.18$  and  $E = 200$  GPa. Values for  $f_D$  (Sim.) are estimated using the theoretical moment correction factor  $f_M(\Pi_2)$ ; values for  $f_M$  (Sim.) assume the theoretical distribution correction factor  $f_D(\Pi_1)$ . . . . . 191

B.13 Numerical results for non-ideal susceptibility index and geometry stress concentration factor, given  $a = 0.914$  m,  $d = 12.7$  mm, and  $\theta = 0.01$  rad.192

# List of Figures

1.1	Various possible types of distortion induced by thermal processes such as welding; after Papazoglou & Masubuchi [7]. . . . .	4
2.1	Schematic of 2-D temperature field in a thin plate for a single pass, full penetration weld [33]. . . . .	17
2.2	Schematic of characteristic isotherm geometry. . . . .	18
2.3	Definition of first yield temperature. . . . .	27
2.4	Width of the weld fusion zone and plastic zone for a GMAW butt weld between two 150 mm × 150 mm × 3 mm plates with a current of 98 A, a voltage of 16 V, and a travel speed of 5 mm/s. . . . .	30
2.5	Top view of mesh used in numerical simulations. . . . .	32
2.6	Numerical validation of the plastic zone width as a function of the first yield isotherm aspect ratio for selected materials and welding heat inputs. . . . .	35
2.7	Aspect ratio as a function of the dimensionless Rosenthal number. . . . .	36
2.8	Typical range and median value for the dimensionless Rosenthal number based on first yield temperature and the estimated corresponding aspect ratio for selected welding processes [53] using data from [45] (arc welding) and [52] (friction stir welding of low-carbon steel and 6xxx series aluminum). . . . .	39
3.1	Superposition of tendon force (i.e., inherent strain) local to the heat source trajectory with reaction strain throughout the entire geometry. . . . .	53
3.2	Characteristic thermal cycle. . . . .	56
3.3	Relationship between elastic and thermal strain for thermal cycles with three different maximum temperatures; after [13]. . . . .	58
3.4	Distribution of residual plastic strain. . . . .	60
3.5	Top view of mesh used in numerical simulations. . . . .	65
3.6	Method for estimating tendon force from simulation results for 6082-T6 aluminum alloy with heat input of 0.36 kJ/mm. . . . .	66

3.7	Elastic and plastic strain development in material with temperature dependent yield strain for thermal cycle with $T_{\max} = T_{Y2}$ . . . . .	69
3.8	Validation of the tendon force for constant material properties (Equation (3.17), open markers) and for temperature dependent properties (Equation (3.42), filled markers). . . . .	77
3.9	Cross-sectional properties of hollow structural section. . . . .	78
4.1	Residual strain distribution for selected common section geometries. . . . .	96
4.2	Temperature and elastic strain evolution over time. . . . .	102
4.3	Plastic and thermal strain at the instant $t_{Y1}$ . . . . .	107
4.4	Total strain evolution over time. . . . .	108
4.5	Illustration of flat plastic zone criterion. . . . .	119
4.6	Validation of correction factor for first yield temperature with literature data for plastic zone size [20, 21, 87]. . . . .	121
4.7	Validation of correction factor for tendon force with literature data [20, 21, 50]. . . . .	122
5.1	High-low offset at weld root ( $\delta$ ) due to local pipe radius mismatch or ovality ( $\Delta a$ ) combined with local wall thickness mismatch ( $\Delta d$ ). . . . .	136
5.2	Calculated properties for CSA Gr.483 (X70) pipe material from JMatPro. . . . .	141
5.3	Deflection profile due to distributed radial load ( $P$ ) over a distance ( $y_c$ ) from the pipe end. . . . .	144
5.4	Geometry and bending stress distribution resulting from 1-D beam approximation of weld root pass. . . . .	147
5.5	Numerical validation of the correction factor on the susceptibility index to account for distribution of the tendon force over a length ( $y_c$ ) from the pipe end. . . . .	151
5.6	Numerical validation of the correction factor on the susceptibility index to account for the effect of a reactionary moment in the weld bead. . . . .	152
5.7	Key parameters for determining weld geometry in joint fit-up with high-low offset. . . . .	154
5.8	Stress concentration factor for a curved beam in bending. Source: Pilkey 1997, chart 5.14, p.425 [103]. Reproduced with permission of John Wiley & Sons Inc. . . . .	155
5.9	Numerical validation of the proposed correction factor on the susceptibility index to account for the effect of high-low offset. . . . .	158

5.10	Welding variables and geometry for (a) a procedure with a higher heat input and a thinner, wider weld bead; and (b) a procedure with a lower heat input and a thicker, narrower weld bead. . . . .	159
C.1	Thermal property data for ASTM A36 structural steel. . . . .	193
C.2	Mechanical property data for ASTM A36 structural steel. . . . .	194
C.3	Thermal property data for aluminum alloy 6082-T6. . . . .	195
C.4	Mechanical property data for aluminum alloy 6082-T6. . . . .	196
C.5	Thermal property data for 304 stainless steel. . . . .	197
C.6	Mechanical property data for 304 stainless steel. . . . .	198
C.7	Thermal property data for 316L stainless steel. . . . .	199
C.8	Mechanical property data for 316L stainless steel. . . . .	200
C.9	Thermal property data for P91 alloy steel. . . . .	201
C.10	Mechanical property data for P91 alloy steel. . . . .	202
C.11	Thermal property data for titanium alloy TiAl6V4. . . . .	203
C.12	Mechanical property data for titanium alloy TiAl6V4. . . . .	204

*“Either do things worth the writing, or write things worth the reading.”*  
*-Thomas Fuller*

# Chapter 1

## Introduction

### 1.1 Methodology

Welding, and more broadly all fabrication processes which utilize moving heat sources, plays an essential and ever expanding role in modern advanced manufacturing. The current state of the art in prediction of thermal-mechanical phenomena in welding are computational algorithms that incorporate coupled numerical heat transfer, fluid mechanics, and solid mechanics; these models are capable of simulating transient stress development with temperature dependent elastic-plastic material models [1–3]. Although it is possible to achieve high accuracy for a specific application, there is limited or unknown applicability outside the specific parameters used. These numerical solutions are thus not well suited to general issues of procedure design.

Welding codes and standards in North America provide minimum acceptable results for tests of metallurgical and mechanical properties (e.g., minimum notch toughness for joints in low-temperature service) [4–6]. Allowable deviations from the tested parameters are also outlined for specified essential process variables, but limited guidance is provided on what parameters should be used to achieve these results for a given situation. Industrial operators must therefore rely on the experience of skilled tradespeople and equipment operators to achieve the desired outcomes through a process of trial-and-error.

Although adequate for minor deviations from existing practice, this approach is

costly, inefficient, and may not be suitable for all cases. This is a particular concern for new or improved material systems, where existing intuition is often insufficient to identify even a good starting point of proposed parameters and operating conditions. Numerical techniques are often marketed as a solution to such problems. Unfortunately, even with modern computational power, the complexity of multicoupled, multiphysics numerical models requires a significant investment of time and money to explore even limited ranges of parameters or materials. The shortcomings of empirical approaches, whether experimental or numerical, are further emphasized in applications to automated processes and equipment. It is not enough to only know the optimal parameters for a specific case; adaptive programming techniques necessitate a comprehensive understanding of the underlying phenomena that can be translated into a set of rules or heuristics and implemented in control algorithms.

Calibrated analytical engineering formulae offer an alternative to purely empirical methods and are widely employed in other areas of engineering practice. For applications ranging from design of heat exchangers to gear trains, engineering equations based on fundamental analytical solutions are employed to solve complex real-world problems. The key to these approaches is the development and provision of appropriate limits of validity and correction factors. Correction factors allow for a simple base solution to be flexibly adjusted, only when necessary, to account for more complex secondary phenomena.

Welding engineers are required to extract insights from idealized conditions during procedure development and integrate this knowledge into the non-ideal realities of industrial fabrication environments. Calibrated engineering expressions are well suited to help bridge the gap between theory and application, providing much needed understanding without sacrificing practical relevance. This work employs the mathematical techniques of dimensional analysis, asymptotic approximation, and scaling to derive engineering formulae that are capable of meeting the needs of industrial operators dealing with issues of residual stress and distortion.

## 1.2 Background

Common fabrication methods such as welding, cutting, cladding, surface heat treatment, and additive manufacturing all rely on concentrated heat sources to achieve localized addition, removal, or transformation of material. Non-uniform heating of the underlying geometry results in differential levels of thermal strain which produce internal stresses as well as changes of the component shape. In some cases, the stresses and distortion are reversible upon cooling, but in other cases, residual effects will persist even after the component returns to the starting temperature.

Residual stress and distortion share a common driving force and are often produced together, but these terms should not be considered interchangeable. The trends in behaviour for stress and distortion do not always move together and in some cases may even be entirely opposite. For example, highly restrained components may be expected to experience reduced distortion during welding. However, as is shown in this work, a greater degree of restraint will also tend to increase the plastic strain and thus increase the volume of material with yield magnitude residual tensile stresses.

In general, stresses and distortion due to thermal processing can be broadly divided into two categories, based on whether they are primarily associated with: transverse effects in the direction perpendicular to the heat source movement; or longitudinal effects in the direction parallel to the heat source movement. Transverse shrinkage, angular change, and rotational distortion are predominantly associated with the development of transverse residual stresses. Longitudinal shrinkage, longitudinal distortion (i.e., out-of-plane bending), and buckling distortion are associated with longitudinal residual stresses. The various forms of distortion are illustrated for the case of welding in Figure 1.1.

This work is primarily focused on longitudinal stresses and distortion, and their relation to the transient temperature gradients that surround a moving point heat source in a thin (i.e., 2-D) geometry. Modern power supplies and advanced processing

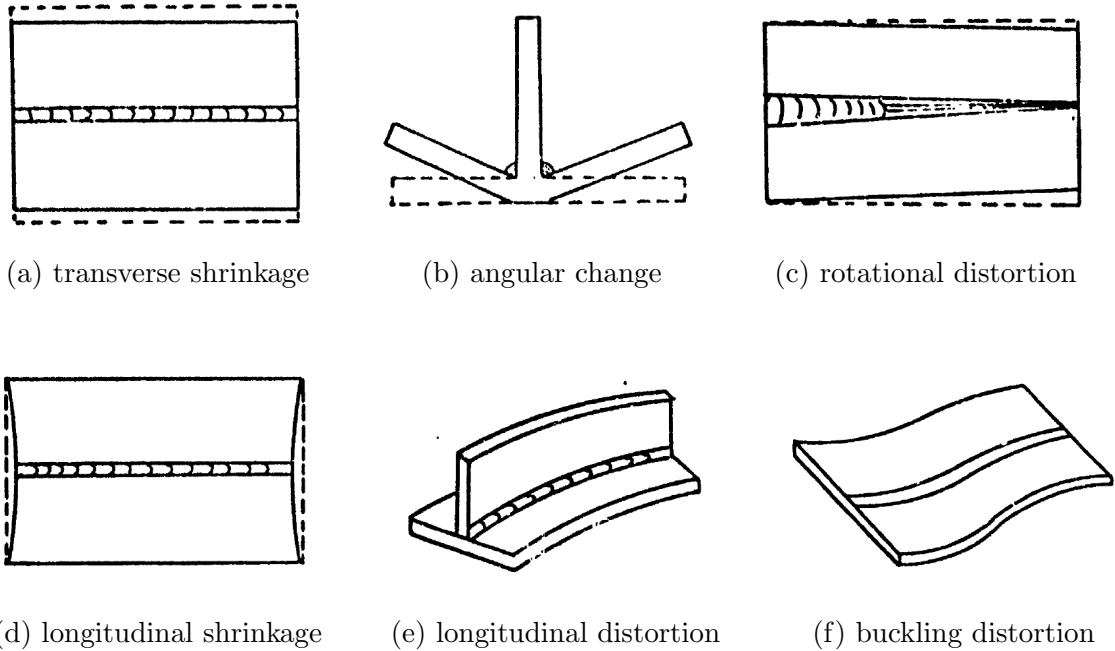


Figure 1.1: Various possible types of distortion induced by thermal processes such as welding; after Papazoglou & Masubuchi [7].

equipment, such as lasers, enable the use of fast moving, high power heat sources that result in relatively low thermal gradients in the direction of heat source movement. The temperature distribution along the heat source trajectory is thus approximately uniform and thermal stresses due to internal restraint in the transverse direction are expected to be small compared to the longitudinal direction. An exact criterion for when the thermal gradients may be considered sufficiently small to employ this approximation has not previously been presented, but is derived for the first time in this work.

Transverse effects may not be expected to be entirely negligible in all cases. In welded construction, transverse stresses have been widely studied and are known to be a contributing factor in formation of solidification cracks [8]; when combined with stress concentrations at the weld toe or root, residual stresses can also lead to a reduction in fatigue life of welded components [9]. Satoh [10] has shown that these stresses are associated with external restraint of thermal shrinkage during cooling, rather than

the transient temperature distribution. The distinct mechanism that governs formation of transverse residual stresses, supports an independent and decoupled treatment of longitudinal stresses and distortions.

The mechanisms for development of longitudinal residual stress and distortion have been under investigation since the mid 1930s. Boulton & Lance-Martin [11] first proposed a theoretical model to relate the thermal strains due to heating with development of plastic strain; the region of plastic strain was measured experimentally and found to significantly exceed the region of melting. Rodgers & Fetcher [12] performed a similar study and identified that for a symmetric flat plate geometry, the residual stress distribution consists of yield magnitude tensile stresses near the line of heating with balancing compressive stresses in the surrounding material.

The “three-bar model” was established by Wells [13] to explain the development of these counterbalancing tensile and compressive zones. During heating, material expansion near the heat source is restrained by the cooler surrounding material resulting in the development of compressive plastic strain. During cooling to a uniform temperature, there is a mismatch between the material with and without this plastic strain. Assuming that the cross-section of material remains planar, the strain must be uniform, so elastic strains are produced to compensate for this strain mismatch. The elastic strains and associated residual stresses are thus positive (tensile) in the region with plastic strain and negative (compressive) in the surrounding material to maintain an overall uniform strain across the section.

Consistent through the early analytical work on welding residual stresses is the simplifying assumption that, for typical conditions, the weld may be treated as uniaxially restrained and the distributions of longitudinal stress and strain may be assumed uniform along the weld length. This simplification also enabled the early numerical algorithms created by Tall [14] and Masubuchi *et al.* [15].

These early simplified approaches evolved into the concept of inherent strain, a term coined by Ueda *et al.* [16] in reference to the mismatch produced by plastic

behaviour as described in the three-bar model. The inherent strain concept addresses the complex transient thermal-mechanical phenomena separate from the reaction of the larger geometry. Subsets of this approach include both those methods which use a separate computational model to obtain values for inherent strain [17–19] as well as those which rely on estimates of inherent strain from analytical formulae or a database of experimental measurements [20, 21]. Implementations in numerical software apply the inherent strain as a static load distribution to a simple linear model yielding significantly improved computational efficiency compared to full transient elastic-plastic models [22–24].

Analytical estimates of inherent strain and associated stresses and distortions are the focus of this work since they provide necessary generality to address problems of procedure development and process design. Blodgett [25] pioneered the “weld-as-a-line” concept to calculate the necessary weld size for a given load capacity. This methodology provides the basis for guidelines used to size welds in modern structural welding codes and standards. The goal of this work is to enable a similarly convenient and powerful tool to estimate longitudinal stresses and distortions.

The primary challenge in adapting this efficient methodology are the limitations of existing analytical models for the inherent strain distribution. Traditional implementations of inherent strain are focused on applications to structural construction [14, 26] and thus existing models are primarily validated for low-carbon steels. General applicability to modern materials and new processing techniques, such as additive manufacturing, necessitates that these models be validated with consideration of more complex material property behaviour.

A secondary challenge is that the limits of applicability for the model must be rigorously defined and easily evaluated for a given situation. This is essential both for model validation as well as for practical application of the results. Specific considerations include the impact of the overall geometry size and shape on estimates of the inherent strain, and most importantly the criterion for application of the assumptions

that enable a simplified uniaxial model of thermal and residual stress.

This work brings fresh insights to a 100 year-old problem. The new contribution to knowledge includes both an improved theoretical understanding, and also a practical consideration of how to apply this understanding to real-world non-ideal problems of immediate and significant industrial relevance.

### **1.3 Objectives**

The main purpose of this research project is to generate simple, general, and accurate formulae to describe the longitudinal residual stresses, strains, and distortions produced during thermal processes such as welding. In order to achieve this goal, the following objectives were established:

- Formulate a fundamental mathematical framework to link the mechanical response to thermal processing with material properties and procedural variables.
- Identify key characteristic values of the residual stress field and obtain descriptive normalized asymptotic expressions with associated limits of applicability.
- Develop and validate correction factors to account for secondary phenomena that may produce deviations from the asymptotic model in specific cases.
- Demonstrate the utility of the proposed expressions to problems of practical industrial relevance.

## 1.4 Thesis Outline

The remaining 5 chapters of this thesis focus on achieving the above objectives. A brief outline of each chapter is included below.

- Chapter (2) presents an order of magnitude scaling analysis which establishes the foundation for the uniaxial thermal stress field applied throughout this work. Novel limits of validity for the uniaxial model are obtained and the applicability to typical welding procedures is verified for a wide range of common processes and materials.
- Chapter (3) outlines a methodology for reducing the residual stress field produced during thermal processing of materials to an equivalent load concentrated at the application of heating. This approach enables prediction of the overall stress and distortion based on information from only a small area of interest near the heat source.
- Chapter (4) characterizes the influence of the component geometry on the residual stress distribution using the concept of compliance. Closed-form blended expressions are derived that extend the asymptotic tendon force model to any general thin section geometry.
- Chapter (5) provides a practical application of the tendon force approach to assess the influence of non-ideal fit-up on the integrity of circumferential pipeline joints. An analytical solution is presented for the local angular distortion associated with the welding tendon force, and used to derive a numerical index for the susceptibility to formation of latent root discontinuities.
- Chapter (6) summarizes the major findings and conclusions of this body of work. Recommendations for potential future work are also provided.

## References

- [1] M. Asadi, J. A. Goldak, J. Nielsen, J. Zhou, S. Tchernov, and D. Downey, “Analysis of predicted residual stress in a weld and comparison with experimental data using regression model,” *Int. J. Mech. Mater. Des.*, vol. 5, no. 4, pp. 353–364, Nov. 2009. DOI: 10.1007/s10999-009-9107-5.
- [2] D. Deng, C. Zhang, X. Pu, and W. Liang, “Influence of material model on prediction accuracy of welding residual stress in an austenitic stainless steel multi-pass butt-welded joint,” *J. Mater. Eng. Perform.*, vol. 26, pp. 1494–1505, Mar. 2017. DOI: 10.1007/s11665-017-2626-6.
- [3] T. Mukherjee, W. Zhang, and T. DebRoy, “An improved prediction of residual stresses and distortion in additive manufacturing,” *Comput. Mater. Sci.*, vol. 126, pp. 360–372, Jan. 2017. DOI: 10.1016/j.commatsci.2016.10.003.
- [4] CSA Group, *Certification of companies for fusion welding of steel*. CSA W47.1, 2019.
- [5] ASME, *Welding, brazing, and fusing qualifications*. BPVC-IX, 2019.
- [6] CSA Group, *Oil and Gas Pipeline Systems*. CAN/CSA-Z662, 2019.
- [7] V. Papazoglou and K. Masubuchi, “Integration of M.I.T. studies on prediction and control of distortion in welded aluminum structures,” *M.I.T. Tech. Rep.* (submitted to Office Nav. Res.), Contract No. N00014-75-C-0469, NR 031-773, Sept. 1976.
- [8] S. Kou, “Weld metal solidification cracking,” in *Welding Metallurgy*, 2nd, Hoboken, NJ: John Wiley & Sons, Inc., 2003, ch. 11, pp. 263–300.
- [9] Z. Barsoum and I. Barsoum, “Residual stress effects on fatigue life of welded structures using LEFM,” *Eng. Fail. Anal.*, vol. 16, no. 1, pp. 449–467, Jan. 2009. DOI: 10.1016/j.engfailanal.2008.06.017.
- [10] K. Satoh, “Preheat and restraint versus weld cracking in steel constructions,” *Trans. JWS*, vol. 1, no. 1, pp. 43–50, Apr. 1970.
- [11] N. S. Boulton and H. E. Lance Martin, “Residual stresses in arc-welded plates,” *Proc. Inst. Mech. Eng.*, vol. 133, no. 1, pp. 295–347, June 1936. DOI: 10.1243/pime\_proc\_1936\_133\_017\_02.
- [12] O. E. Rodgers and J. R. Fetcher, “Determination of internal stress from the temperature history to a butt-welded plate,” *Welding J.*, vol. 17, no. 11, pp. 4s–7s, Nov. 1938.
- [13] A. A. Wells, “The mechanics of notch brittle fracture,” *Weld. Res.*, vol. 7, no. 2, pp. 34r–56r, Feb. 1953.
- [14] L. Tall, “Residual stresses in welded plates - a theoretical study,” *Welding J.*, vol. 43, no. 1, pp. 10s–23s, Jan. 1964.

- [15] K. Masubuchi, F. B. Simmons, and R. E. Monroe, "Analysis of thermal stresses and metal movement during welding," in *Batelle Memorial Institute Tech. Rep.* Restone Arsenal, AL: Redstone Scientific Information Centre, Jul. 1968, RSIC–820.
- [16] Y. Ueda, K. Fukuda, K. Nakacho, and S. Endo, "A new measuring method of residual stresses with the aid of finite element method and reliability of estimated values," *Trans. JWRI*, vol. 4, no. 2, pp. 123–131, Oct. 1975. DOI: 11094/11113.
- [17] P. Michaleris and A. Debicari, "Prediction of welding distortion," *Welding J.*, vol. 76, no. 4, pp. 172s–181s, Apr. 1997.
- [18] G. H. Jung and C. L. Tsai, "Plasticity-based distortion analysis for fillet welded thin-plate T-joints," *Welding J.*, vol. 83, no. 6, pp. 177s–187s, June 2004.
- [19] L. Zhang, P. Michaleris, and P. Marugabandhu, "Evaluation of applied plastic strain methods for welding distortion prediction," *ASME J. Manuf. Sci. Eng.*, vol. 129, no. 6, pp. 1000–1010, Dec. 2007. DOI: 10.1115/1.2716740.
- [20] Y. Ueda and M. G. Yuan, "Prediction of residual stresses in butt welded plates using inherent strains," *ASME J. Eng. Mater. Technol.*, vol. 115, no. 4, pp. 417–423, Oct. 1993. DOI: 10.1115/1.2904240.
- [21] M. G. Yuan and Y. Ueda, "Prediction of residual stresses in welded T- and I-joints using inherent strains," *ASME J. Eng. Mater. Technol.*, vol. 118, no. 2, pp. 229–234, Apr. 1996. DOI: 10.1115/1.2804892.
- [22] D. Deng and H. Murakawa, "Prediction of welding distortion and residual stress in a thin plate butt-welded joint," *Comput. Mater. Sci.*, vol. 43, no. 2, pp. 353–365, Aug. 2008. DOI: 10.1016/j.commatsci.2007.12.006.
- [23] D. Deng and H. Murakawa, "FEM prediction of buckling distortion induced by welding in thin plate panel structures," *Comput. Mater. Sci.*, vol. 43, no. 4, pp. 591–607, Oct. 2008. DOI: 10.1016/j.commatsci.2008.01.003.
- [24] H. Murakawa, D. Deng, N. Ma, and J. Wang, "Applications of inherent strain and interface element to simulation of welding deformation in thin plate structures," *Comput. Mater. Sci.*, vol. 51, pp. 43–52, Jan. 2012. DOI: 10.1016/j.commatsci.2011.06.040.
- [25] O. W. Blodgett, "Joint design and production: Determining weld size," in *Design of Welded Structures*, Cleveland, OH: The James F. Lincoln Arc Welding Foundation, 1966, ch. 7.4.
- [26] J. B. Dwight and K. E. Moxham, "Welded steel plates in compression," *Struct. Eng.*, vol. 47, no. 2, pp. 49–66, Feb. 1969.

## Chapter 2

# Scaling Analysis of the Thermal Stress Field Produced by a Moving Point Heat Source in a Thin Plate

### 2.1 Introduction

Residual stresses produced during welding and additive manufacturing of materials can lead to undesirable distortion of initial geometry [27] and may also have significant implications on the stress carrying capacity of the welded structure [26, 28]. For industrial practitioners, combating these issues requires knowledge of the magnitude and distribution of the residual stresses. The development of residual stresses is a complex process dependent on interactions between the physics governing heat flow and mechanical deformation, as well as the potential for these processes to produce changes in material properties. Estimation of the residual stresses resulting from a given welding process is generally attempted through one of three methods: experiments (i.e., trial and error), numerical techniques, or analytical expressions, with the bulk of existing work focused on the first two methodologies.

All of these methods contain a balance of advantages and disadvantages in terms of capital cost, time, accuracy, and generality. Experimentally derived empirical models have historically been widely applied to problems in welding. The low capital and time investment for individual experiments makes this method appealing to industrial

practitioners. Direct in-situ measurement of residual stresses poses a significant challenge, while indirect measurement techniques such as strain-gauge hole-drilling have limited accuracy, and may not be suitable for complex geometries or sub-surface stress measurement. Volumetric strain measurement with neutron-diffraction has been utilized in many recent studies to overcome some of the limitations of traditional residual stress measurement techniques [29, 30], but the time and cost to perform these measurements is prohibitive for day-to-day industrial practice.

Numerical models have emerged in recent decades as a potential solution to the limitations of experimental measurement techniques, and have been used to successfully analyze welds on a range of complex weld geometries [1, 31, 32]. Numerical techniques have the potential to provide high accuracy at the expense of significant investment of time and capital, particularly if considerations of complex phenomena such as phase transformations are necessary.

The utility of simple analytical formulae for estimation of key properties of the temperature field surrounding a moving point heat source has been recently demonstrated by [33, 34]. Central to the practical application of these formulae are well established limits of applicability. This study applies a similar methodology to obtain an analytical formula for the characteristic size of the welding residual stress field.

A simple uniaxial analytical model for thermal stresses in welding or additive manufacturing was first considered for edge welded plates in [11] and butt welded plates in [12]. This model idealizes the material behaviour as analogous to a cylindrical specimen with a rigidly fixed length, such as is used in a Satoh Test [35]. Variations on this analysis have been used to provide analytical predictions of welding residual stress [13, 36, 37], to simplify early computational algorithms [14, 15] as well as in combined analytical-computational approaches [20, 21]. Despite excellent correlation with experimental results, due to the unknown limits of applicability, this simple and powerful model remains inaccessible to industry, denying welding engineers a much needed tool for estimation of residual stress.

This study utilizes a novel analytical technique presented in [38] to derive the range of validity of the uniaxial model of residual stresses. The proposed criterion for application of the uniaxial model is validated against numerical simulations and applied to a survey of typical procedures for a variety of different welding processes. For the first time, a simple and general formula is provided which enables industrial practitioners to evaluate and apply the uniaxial model to a wide range of different materials and procedural variables.

## 2.2 List of Symbols

Symbol	SI Unit	Description
<b>Roman Letters</b>		
$\mathcal{R}$	1	Aspect ratio of isotherm
$d$	m	Plate thickness
$E$	$\text{N m}^{-2}$	Elastic modulus
$f_{\mathcal{R}}$	1	Correction factor
$G$	$\text{N m}^{-2}$	Shear modulus
$k$	$\text{W m}^{-1} \text{K}^{-1}$	Thermal conductivity
$Q'$	$\text{J m}^{-1}$	Linear energy input (i.e., welding heat input)
$q$	W	Power absorbed by the substrate
$\text{Ro}$	1	Dimensionless Rosenthal number
$T_{Y1}$	K	First yield temperature
$T_s$	K	Solidus temperature
$T_0$	K	Starting temperature
$U$	$\text{m s}^{-1}$	Heat source travel speed
$x_b$	m	Distance between heat source and back of isotherm
$x_{\max}$	m	Distance between heat source and max. width of isotherm
$x_f$	m	Distance between heat source and front of isotherm
$y_{fz}$	m	Fusion zone size (i.e., half-width)
$y_{\max}$	m	Maximum isotherm half-width
$y_{pl}$	m	Plastic zone size (i.e., half-width)
<b>Greek Letters</b>		
$\bar{\alpha}$	$\text{K}^{-1}$	Mean linear coefficient of thermal expansion
$\epsilon_x$	1	Normal strain parallel to heat source movement
$\epsilon_y$	1	Normal strain perpendicular to heat source movement
$\gamma_{xy}$	1	In-plane shear strain
$\eta$	1	Thermal efficiency
$\nu$	1	Poisson's ratio
$\rho c$	$\text{J m}^{-3} \text{K}^{-1}$	Volumetric specific heat capacity
$\sigma_Y$	$\text{N m}^{-2}$	Material yield strength
$\sigma_x$	$\text{N m}^{-2}$	Normal stress parallel to heat source movement
$\sigma_y$	$\text{N m}^{-2}$	Normal stress perpendicular to heat source movement
$\tau_{xy}$	$\text{N m}^{-2}$	In-plane shear stress

## 2.3 Asymptotic Analysis

### 2.3.1 Order of Magnitude Scaling

The OMS (Order of Magnitude Scaling) algorithm is used to perform an automated scaling analysis to simplify a multi-coupled, multi-physics problem. The OMS approach is described in detail in [39] and consists of three stages. Stage 1: identify the governing equations for the system, normalize each term in the equations by characteristic values and create a matrix of coefficients by substituting normalized expressions into the governing equations. Stage 2: select a subset of the governing terms and use them to create and solve a system of linear equations, check that the solution is self-consistent and non-singular and, if this is not the case, repeat the process with a different subset of terms. Stage 3: assess the output from the automated algorithm, select the appropriate self-consistent balance and verify the reasonableness of the associated estimations.

The asymptotic analysis considers the heat source to be represented by a moving point as proposed by Rosenthal [40]. The substrate is assumed to be infinite in the  $y$  (width) and  $x$  (length) dimensions and sufficiently small in  $z$  (thickness) such that the temperature, stress, and strain fields have negligible variation through the thickness. In the absence of an external traction on the surface of the substrate, this geometry will be in a state of plane stress.

Calculation of the stress and strain components for a 2-D plane stress state in a linear elastic material requires the simultaneous solution of a set of six partial differential equations: 3 constitutive laws, 2 equations of motion/equilibrium, and 1 compatibility condition [41]

$$\epsilon_x = \frac{1}{E}\sigma_x - \frac{\nu}{E}\sigma_y + \bar{\alpha}\Delta T \quad (2.1a)$$

$$\epsilon_y = \frac{1}{E}\sigma_y - \frac{\nu}{E}\sigma_x + \bar{\alpha}\Delta T \quad (2.1b)$$

$$\gamma_{xy} = \frac{1}{G}\tau_{xy} \quad (2.1c)$$

$$\frac{\partial\sigma_x}{\partial x} + \frac{\partial\tau_{xy}}{\partial y} = 0 \quad (2.1d)$$

$$\frac{\partial\tau_{xy}}{\partial x} + \frac{\partial\sigma_y}{\partial y} = 0 \quad (2.1e)$$

$$\frac{\partial^2\epsilon_y}{\partial x^2} + \frac{\partial^2\epsilon_x}{\partial y^2} = \frac{\partial^2\gamma_{xy}}{\partial x\partial y} \quad (2.1f)$$

where  $\epsilon_x, \epsilon_y, \gamma_{xy}$  are the in-plane strains,  $\sigma_x, \sigma_y, \tau_{xy}$  are the in-plane stress components,  $E$  is the modulus of elasticity,  $G$  is the shear modulus,  $\nu$  is Poisson's ratio,  $\bar{\alpha}$  is the mean coefficient of thermal expansion, and  $\Delta T = T(x, y) - T_0$  is the temperature change relative to a reference state of zero strain at the starting temperature  $T_0$ .

This analysis considers boundary conditions of zero normal and shear forces acting on the lateral and longitudinal plate edges at infinity and zero traction on the plate surfaces. Distortions of the plate in the out of plane direction will be negligible for a plane stress state and are not considered.

For the temperature field to be compatible with the plane stress assumption it must be uniform in the thickness direction. Figure 2.1 illustrates the typical 2-D

temperature field for a plate where the thickness is small relative to the width of the isotherm. A 2-D temperature distribution is appropriate for a single pass, full penetration weld if the width of the isotherms in the temperature range of interest are significantly greater than the thickness ( $d$ ) of the substrate. This condition has been expressed graphically in the work of Myhr and Grong [42].

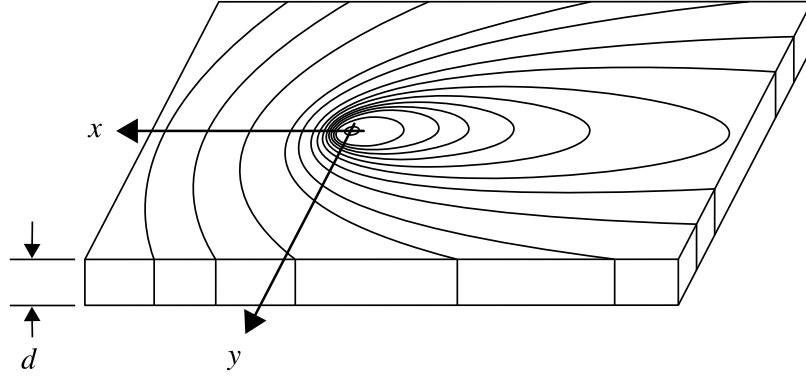


Figure 2.1: Schematic of 2-D temperature field in a thin plate for a single pass, full penetration weld [33].

### 2.3.2 Construction of the Matrix of Coefficients

As shown in Equation (2.1), the mathematical formulation for the thermal stress field in a 2-D plane composed of a homogeneous, isotropic, linear elastic material involves a total of six equations, with six (unknown) dependent variables, three independent variables and seven fixed parameters. The dependent variables are  $\{U\} = \{\epsilon_x, \epsilon_y, \gamma_{xy}, \sigma_x, \sigma_y, \tau_{xy}\}$ ; the independent variables are  $\{X\} = \{\Delta T, x, y\}$ ; and the parameters are  $\{P\} = \{\Delta T_c, x_c, y_c, \nu, G, E, \bar{\alpha}\}$ , where  $x_c = x_b - x_f$  and  $y_c = 2y_{\max}$  are the characteristic length and width of the characteristic isotherm  $T(x, y) = T_c$  as shown in Figure 2.2. This notation follows the convention used in [34], where  $x_f$  is the distance from the heat source to the leading point on the front of the isotherm,  $x_b$  is the distance from the heat source to the trailing point on the back of the isotherm, and  $y_{\max}$  is the maximum width of the isotherm.

The OMS analysis requires input of a set of parameters which fall within the desired

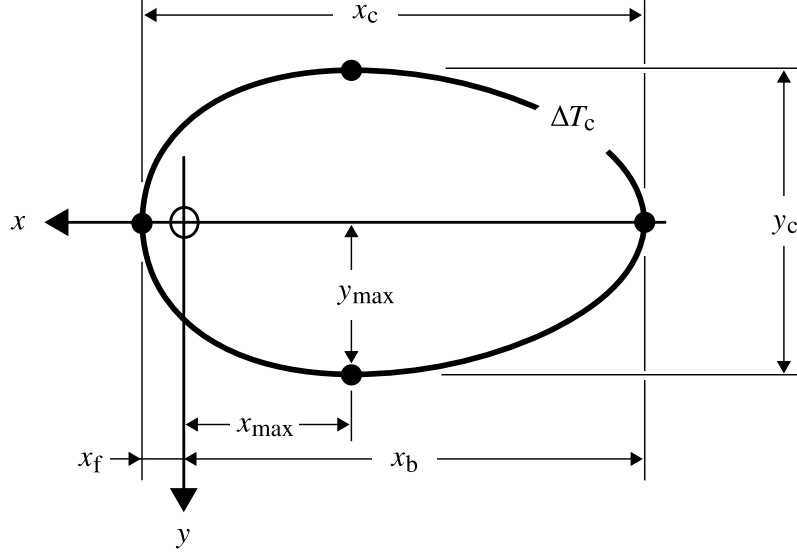


Figure 2.2: Schematic of characteristic isotherm geometry.

asymptotic regime. Empirical validation of the uniaxial stress model has predominantly focused on arc welding of low-carbon structural steels [26, 43, 44]. Recommended parameters for a single pass GMAW butt weld on a 3 mm carbon steel plate are provided in [45] (absorbed power  $q = 1920$  W, travel speed  $U = 8$  mm/s). The mechanical properties of a nominally composed ASTM A36 structural steel were obtained using the computational materials software JMatPro [46] ( $\nu = 0.3$ ,  $G = 76$  GPa,  $E = 197$  GPa,  $\bar{\alpha} = 12.6 \times 10^{-6}$  1/K). A characteristic temperature for residual stress development in low-carbon structural steel of approximately  $T_c = \sigma_Y/E\bar{\alpha} + T_0 \approx 120^\circ\text{C}$  is proposed in [26] for a starting temperature of  $T_0 = 20^\circ\text{C}$ . This approximation assumes the yield strength  $\sigma_Y$  is constant for temperatures  $< 200^\circ\text{C}$ . A decrease in yield strength of approximately  $0.625$  MPa/ $^\circ\text{C}$  to  $100^\circ\text{C}$  and  $0.275$  MPa/ $^\circ\text{C}$  from  $100$ – $200^\circ\text{C}$  is predicted by JMatPro. Accounting for the decreased yield strength at elevated temperatures, an improved estimate of the characteristic temperature is  $T_c \approx 100^\circ\text{C}$ . Using the equations provided by [34] and thermal properties at the characteristic temperature (thermal conductivity  $k = 53$  W m $^{-1}$ K $^{-1}$ , volumetric specific heat capacity  $\rho c = 3.8 \times 10^6$  J m $^{-3}$ K $^{-1}$ ) the characteristic width and length are

$x_c = 3.2$  m and  $y_c = 0.13$  m.

The normalization approach presented in [47] is used to calculate characteristic values of the differential expressions given in Equation (2.1). The independent variables are normalized as  $x^* = x/x_c$ , and  $y^* = y/y_c$ . The characteristic temperature for normalization is  $\Delta T_c = T_c - T_0$ , yielding a normalized temperature  $T^*(x^*, y^*) = \Delta T(x, y)/\Delta T_c$ . The normalized equivalent of Equations (2.1a) to (2.1f) is then:

$$\epsilon_{x,c}\epsilon_x^* = \frac{1}{E}\sigma_{x,c}\sigma_x^* - \frac{\nu}{E}\sigma_{y,c}\sigma_y^* + \bar{\alpha}\Delta T_c T^* \quad (2.2a)$$

$$\epsilon_{y,c}\epsilon_y^* = \frac{1}{E}\sigma_{y,c}\sigma_y^* - \frac{\nu}{E}\sigma_{x,c}\sigma_x^* + \bar{\alpha}\Delta T_c T^* \quad (2.2b)$$

$$\gamma_{xy,c}\gamma_{xy}^* = \frac{1}{G}\tau_{xy,c}\tau_{xy}^* \quad (2.2c)$$

$$\left(\frac{\partial\sigma_x}{\partial x}\right)_c \left(\frac{\partial\sigma_x}{\partial x}\right)^* + \left(\frac{\partial\tau_{xy}}{\partial y}\right)_c \left(\frac{\partial\tau_{xy}}{\partial y}\right)^* = 0 \quad (2.2d)$$

$$\left(\frac{\partial\tau_{xy}}{\partial x}\right)_c \left(\frac{\partial\tau_{xy}}{\partial x}\right)^* + \left(\frac{\partial\sigma_y}{\partial y}\right)_c \left(\frac{\partial\sigma_y}{\partial y}\right)^* = 0 \quad (2.2e)$$

$$\left(\frac{\partial^2\epsilon_y}{\partial x^2}\right)_c \left(\frac{\partial^2\epsilon_y}{\partial x^2}\right)^* + \left(\frac{\partial^2\epsilon_x}{\partial y^2}\right)_c \left(\frac{\partial^2\epsilon_x}{\partial y^2}\right)^* = \left(\frac{\partial^2\gamma_{xy}}{\partial x\partial y}\right)_c \left(\frac{\partial^2\gamma_{xy}}{\partial x\partial y}\right)^* \quad (2.2f)$$



term 1 and term 4 in Equation (2.2b), and term 2 and term 3 in Equation (2.2f). Equations (2.2c) to (2.2e) have only two terms and the dominant balance is trivial. This balance yields the following estimates for the characteristic values of the dependent variables:

$$\widehat{\sigma}_{x,c} = \bar{\alpha}\Delta T_c E \quad (2.4a)$$

$$\widehat{\sigma}_{y,c} = \bar{\alpha}\Delta T_c \frac{y_c^2}{x_c^2} E \quad (2.4b)$$

$$\widehat{\tau}_{xy,c} = \bar{\alpha}\Delta T_c \frac{y_c}{x_c} E \quad (2.4c)$$

$$\widehat{\epsilon}_{x,c} = \bar{\alpha}\Delta T_c \frac{y_c^2}{x_c^2} \frac{E}{G} \quad (2.4d)$$

$$\widehat{\epsilon}_{y,c} = \bar{\alpha}\Delta T_c \quad (2.4e)$$

$$\widehat{\gamma}_{xy,c} = \bar{\alpha}\Delta T_c \frac{y_c}{x_c} \frac{E}{G} \quad (2.4f)$$

Numerical values for the characteristic stresses and strains can be obtained for a given welding procedure by substituting in values for the parameters  $\{P\} = \{\Delta T_c, x_c, y_c, \nu, G, E, \bar{\alpha}\}$ . For the GMAW weld on ASTM A36 structural steel, the characteristic values for the thermal stresses and strains are  $\widehat{\sigma}_{x,c} = 198.6$  MPa,  $\widehat{\sigma}_{y,c} = 0.3$  MPa,  $\widehat{\tau}_{xy,c} = 8.1$  MPa,  $\widehat{\epsilon}_{x,c} = 4$   $\mu\text{m}/\text{m}$ ,  $\widehat{\epsilon}_{y,c} = 1008$   $\mu\text{m}/\text{m}$ , and  $\widehat{\gamma}_{xy,c} = 106$   $\mu\text{m}/\text{m}$ .

Using the expressions given in Equations (2.4a) to (2.4f) the original Equations (2.1a) to (2.1f) can be rewritten in dimensionless form:

$$\left(\frac{y_c^2 E}{x_c^2 G}\right) \epsilon_x^* = \sigma_x^* - \left(\frac{y_c^2 \nu}{x_c^2}\right) \sigma_y^* + T^* \quad (2.5a)$$

$$\epsilon_y^* = \left(\frac{y_c^2}{x_c^2}\right) \sigma_y^* - (\nu) \sigma_x^* + T^* \quad (2.5b)$$

$$\gamma_{xy}^* = \tau_{xy}^* \quad (2.5c)$$

$$\frac{\partial \sigma_x^*}{\partial x^*} + \frac{\partial \tau_{xy}^*}{\partial y^*} = 0 \quad (2.5d)$$

$$\frac{\partial \tau_{xy}^*}{\partial x^*} + \frac{\partial \sigma_y^*}{\partial y^*} = 0 \quad (2.5e)$$

$$\left(\frac{G}{E}\right) \frac{\partial^2 \epsilon_y^*}{\partial x^{*2}} + \frac{\partial^2 \epsilon_x^*}{\partial y^{*2}} = \frac{\partial^2 \gamma_{xy}^*}{\partial x^* \partial y^*} \quad (2.5f)$$

Considering only the dominant terms, Equation (2.5a) can be reduced to:

$$\sigma_x^*(x^*, y^*) = -T^*(x^*, y^*) \quad (2.6)$$

with the dimensional counterpart:

$$\sigma_x(x, y) = -E\bar{\alpha}\Delta T(x, y) \quad (2.7)$$

For the self-consistent dominant balance, the total strain in the direction parallel to the heat source movement ( $\epsilon_x$ ) and the stress in the perpendicular direction ( $\sigma_y$ ) are both found to be non-dominant. The stress in the parallel direction ( $\sigma_x$ ) may therefore be approximated as the product of the elastic modulus ( $E$ ) and the thermal strain ( $\bar{\alpha}\Delta T$ ). This is identical to the result obtained if the plate is idealized as

having been formed of a number of independent parallel fibres of a fixed length. The dominant balance obtained for the GMAW welding procedure is therefore equivalent to the uniaxial stress model.

### 2.3.4 Limit of Validity of Estimates

Although the scaling expressions in Equations (2.5a) to (2.5f) were derived by considering only a single welding procedure, the advantage of this scaling approach is that these expressions, and therefore the uniaxial stress model, will remain valid for any set of parameters which generates the same force balance. The scaling estimates for  $\sigma_{x,c}$ ,  $\sigma_{y,c}$ ,  $\tau_{xy,c}$ ,  $\epsilon_{x,c}$ ,  $\epsilon_{y,c}$ , and  $\gamma_{xy,c}$  are produced by considering only the dominant forces (i.e., assuming the secondary forces are zero). The relative magnitude of the secondary forces may be estimated from the corresponding coefficients on the non-dominant terms in Equations (2.5a) to (2.5f).

The normalized coefficients can be written in matrix form as:

$$[\hat{N}] = \begin{array}{c} \begin{array}{ccccccc} \Delta T_c & x_c & y_c & \nu & G & E & \bar{\alpha} \\ \hline & -2 & 2 & & -1 & 1 & \\ & -2 & 2 & 1 & & & \\ \hline & -2 & 2 & & & & \\ & & & 1 & & & \\ \hline & & & & 1 & -1 & \end{array} \end{array} \quad (2.8)$$

where the zeros have been omitted for clarity. The dominant terms have a normalized coefficient of 1 (i.e., all exponents are zero) and the corresponding rows are empty.

Equations (2.1c), (2.1d), and (2.1e) are omitted since they have only two terms each and would appear as completely empty rows in Equation (2.8).

For the force balance to be self consistent, the coefficients on the non-dominant terms should be less than the coefficients on the dominant terms (i.e.,  $\leq 1$ ). Based on this consideration, the limits of validity of Equations (2.4a) to (2.4f) can be written as:

$$\left\{ \nu, \frac{G}{E}, \left( \frac{y_c^2}{x_c^2} \right), \left( \frac{y_c^2 \nu}{x_c^2} \right), \left( \frac{y_c^2 E}{x_c^2 G} \right) \right\} \leq 1 \quad (2.9)$$

The conditions given by Equation (2.9) can be simplified using dimensional analysis. The number of independent rows in  $[\hat{N}]$  determines the number of independent dimensionless groups ( $m$ ) in Equation (2.9). For this analysis,  $m = 3$  which indicates there can only be exactly three independent dimensionless groups. Any three dimensionless groups that form an independent set may be selected. In this analysis,  $\nu$ ,  $G/E$ , and  $x_c/y_c$  are selected. The dimensionless group  $x_c/y_c$  is physically interpreted as the aspect ratio ( $\mathcal{R}$ ) for the isotherm of interest ( $T(x, y) = T_c$ ) as shown in Figure 2.2. There are in fact only two truly independent dimensionless groups, since for an isotropic elastic material the ratio of the shear and elastic modulus ( $G/E$ ) can be expressed in terms of Poisson's ratio ( $\nu$ ) [41]:

$$G/E = \frac{1}{2(1 + \nu)} \quad (2.10)$$

The range of validity given by Equation (2.9) can therefore be equivalently expressed in terms of only  $\mathcal{R}$  and  $\nu$  as:

$$-0.5 \leq \nu \leq 1 \quad (2.11a)$$

$$\mathcal{R}^2 \geq 2(1 + \nu) \quad (2.11b)$$

The upper bound of Equation (2.11a) is satisfied for all isotropic materials, which must have a Poisson’s ratio between -1 and 0.5 [48]; this includes elastic behaviour of most metals ( $\nu = 0.25 - 0.35$ ), and even the Poisson’s ratio of incompressible deformation (such as in plasticity), with  $\nu = 0.5$ . The lower bound of Equation (2.11a) poses no additional restrictions on the range of validity of the OMS solution since one of the underlying assumptions of this approach is that all parameters do not change sign (i.e.,  $\nu \geq 0$ ). Consideration of both an upper and lower bound on  $\nu$  means that there will not exist an asymptotic case in which the corresponding coefficients on non-dominant terms both approach zero, since  $\nu$  cannot simultaneously be  $\ll 1$  and  $\gg -0.5$ . The mean value for metals of  $\nu = 0.3$ , is in the middle of the range of validity and the model should therefore be expected to provide reasonable approximations.

For isotropic materials, the highest possible Poisson’s ratio is  $\nu = 0.5$  and therefore Equation (2.11b) will always be satisfied if the moving heat source develops isotherms with an aspect ratio  $\mathcal{R} \geq \sqrt{3} \approx 1.732$ . This criteria is not a strict limit, but an approximate indication of the centre of the transition from the asymptotics of fast to slow heat sources. Typically, asymptotic solutions in welding yield small errors when the corresponding dimensionless groups are an order of magnitude away from the centre of the transition, yielding the following criterion:

$$\mathcal{R} \gtrsim 17 \tag{2.12}$$

For the previously considered GMAW welding procedure on ASTM A36 structural steel, the estimated aspect ratio is  $\mathcal{R} = 25$ .

## 2.4 Plasticity Considerations

The asymptotic analysis corroborates the common practice of using a uniaxial model to describe the transient thermal stress field produced during welding and additive manufacturing of 2-D geometries. In welding applications, the transient thermal stress

field is often of secondary importance, while the residual stress field that remains following welding is of primary concern. Although the linear elastic asymptotic analysis alone is not sufficient to derive the complete residual stress field, it can be used to estimate one of the most important properties of the stress field, the plastic zone width.

The width of the plastic zone corresponds to the boundary between regions of elastic and plastic material behaviour. The proposed model is self-consistent for prediction of material behaviour up to and including this boundary. The existence of a uniaxial stress state implies that the plate will behave in an equivalent manner to a series of independent parallel strips. The behavior of the material outside the plastic zone and up to this boundary may therefore be treated as independent of the material within the plastic zone. The location of this boundary and therefore the width of the plastic zone may be estimated as the perpendicular distance from the heat source trajectory at which the elastic thermal stresses equal the material yield strength.

### **2.4.1 First Yield Temperature**

As the heat source moves, points of the substrate ahead of it experience heating, and a consequent thermal expansion. In a large plate, the cold region far from the heat source does not expand, and acts as a rigid constraint to the hot material. Under the condition of uniaxial constraint, the thermal expansion results in compressive thermal stresses, which in the elastic regime are proportional to the temperature increase. The maximum temperature at each point depends on the proximity to the line on which the heat source moves. The closer a point is to the line, the higher maximum temperature it experiences and the larger the magnitude of the compressive thermal stresses. At some distance from the weld line, the maximum temperature will be sufficient to cause thermal stresses which exceed the elastic capacity of the material and result in plasticity. The temperature increase necessary to produce plastic behaviour is termed

the “yield temperature” in the welding literature [49, 50] and will be referred to as “first yield temperature” in this line of work to distinguish it from the temperature associated with additional plasticity which may be produced during cooling, to be discussed in a separate publication.

The first yield temperature is defined by the intersection between the elastic and plastic behaviour. The mathematical expression of the first yield temperature is:

$$T_{Y1} = \Delta T_{Y1} + T_0 = \frac{\sigma_Y}{E\bar{\alpha}} \Big|_{T_{Y1}} + T_0 \quad (2.13)$$

where the yield stress ( $\sigma_Y$ ), the elastic modulus ( $E$ ), and the mean coefficient of thermal expansion ( $\bar{\alpha}$ ) are all evaluated at the yield temperature ( $T_{Y1}$ ). Figure 2.3 illustrates the definition of the first yield temperature.

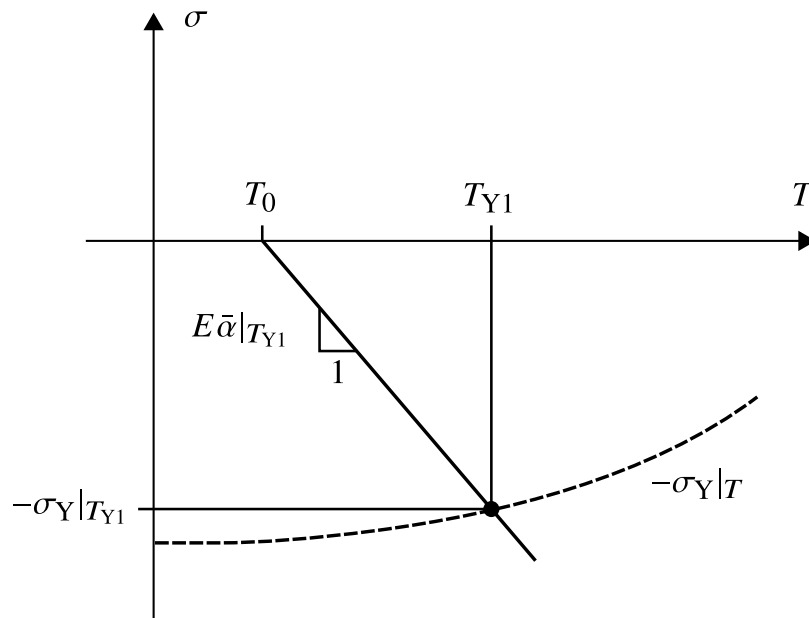


Figure 2.3: Definition of first yield temperature.

Table 2.1 lists the first yield temperature for a number of alloys commonly welded or used in additive manufacturing assuming a starting temperature of 20°C. For moderate variations in starting temperatures, the first yield temperature varies by approximately the same amount (e.g., the first yield temperature for ASTM A36 structural

steel with a starting temperature of 50°C is approximately 130°C). Table 2.1 shows that high strength alloys such as TiAl6V4 and high temperature service alloys such as P91 alloy steel and Inconel 718 exhibit high first yield temperatures. Lower strength materials, such as aluminum alloys, show comparatively low first yield temperatures.

Table 2.1: Properties of selected materials at first yield temperature ( $T_{Y1}$ ) for a starting temperature of  $T_0 = 20^\circ\text{C}$ .

Material	$\sigma_Y$ [MPa]	$E$ [GPa]	$\bar{\alpha}$ [1/K]	$T_{Y1}$ [°C]	$T_s$ [°C]
ASTM A36	201	197	$12.6 \times 10^{-6}$	101	1467
SS 304	208	196	$16.7 \times 10^{-6}$	84	1280
SS 316	230	191	$15.2 \times 10^{-6}$	99	1280
SS 316L	195	192	$15.1 \times 10^{-6}$	87	1280
Al 1050	89	69	$24.0 \times 10^{-6}$	73	585
Al 6082-T6	99	70	$23.3 \times 10^{-6}$	80	645
P91	454	207	$11.1 \times 10^{-6}$	217	1420
In 718	729	185	$13.9 \times 10^{-6}$	305	1260
TiAl6V4	507	81	$9.8 \times 10^{-6}$	663	1550

## 2.4.2 Plastic Zone Width

The size of the plastic zone ( $y_{pl}$ ) corresponds to the maximum width of the first yield isotherm ( $T(x, y) = T_{Y1}$ ) and can therefore be approximated using the asymptotic expression for the isotherm half-width provided by [33]:

$$y_{pl} = y_{\max}|_{T_{Y1}} = \sqrt{\frac{2\pi}{e}} \frac{Q'}{2\pi\rho cd(T_{Y1} - T_0)} \quad (2.14)$$

where  $y_{pl}$  is the half-width of the plastic zone and  $Q' = q/U$  is heat input given by the intensity of heat absorbed by the substrate ( $q$ ) and the travel velocity ( $U$ ).

This equation is valid for plates much thinner than the half-width of the isotherm ( $d \ll y_{max}$ ), and for high values of the dimensionless Rosenthal number ( $Ro \gg 1$ ), which is defined as:

$$Ro = \frac{q}{2\pi kd(T_{Y1} - T_0)} \quad (2.15)$$

where  $k$  is the thermal conductivity of the substrate. Equation (2.14) is based on fixed values (i.e., temperature independent) for material properties. If temperature dependent properties are available, effective values can be calculated as indicated in [33].

Combining Equation (2.14) and Equation (2.13) provides an expression for the estimated plastic zone width:

$$y_{pl} = y_{max}|_{T_{Y1}} = \sqrt{\frac{1}{2\pi e} \frac{E\bar{\alpha}}{\rho c} \frac{Q'}{d\sigma_Y}} \quad (2.16)$$

The solidus temperature  $T_s$  for each of the various materials is also shown in Table 2.1. For ambient starting temperature (i.e.,  $T_0 \approx 20^\circ\text{C}$ ), the first yield temperature change is typically an order of magnitude less than the solidus temperature change.

The half-width of the fusion ( $y_{fz} = 3.6$  mm) is estimated by substituting  $T_s$  into Equation (2.14). The best estimate of the fusion zone size is obtained using material properties at elevated temperatures, but for the purposes of this rough comparison, a reasonable estimate is obtained using the material properties at  $T_{Y1}$ . The ratio of the half-width of the fusion zone to the half-width of the plastic zone ( $y_{fz}/y_{pl}$ ) is approximately equal to the inverse of the ratio of the corresponding temperature changes (i.e.,  $\Delta T_{Y1}/\Delta T_s$ ). Under typical thin plate conditions the fusion zone therefore comprises a small fraction of the region of material subject to residual stress. Figure 2.4 illustrates the relative size of the fusion zone and the plastic zone for an

experimental GMAW weld between two 3 mm plates of ASTM A36 structural steel with an effective heat input of  $Q' = \eta VI/U \approx 240$  J/mm ( $I = 98$  A,  $V = 16$  V,  $U = 5$  mm/s and an assumed thermal efficiency of  $\eta \approx 0.77$ ).

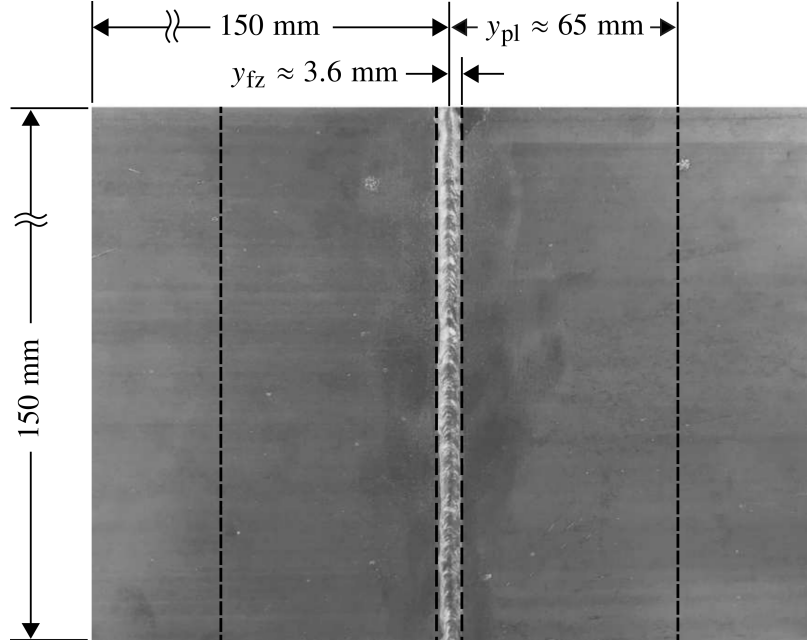


Figure 2.4: Width of the weld fusion zone and plastic zone for a GMAW butt weld between two 150 mm × 150 mm × 3 mm plates with a current of 98 A, a voltage of 16 V, and a travel speed of 5 mm/s.

## 2.5 Validation of Results

### 2.5.1 Numerical Modelling

The validation in this study was performed using numerical methods due to the lack of literature data related to plastic zone measurement in sufficiently large plates. The welding simulation software utilizes the proprietary nonlinear finite element analysis tool sfMarc to perform a thermal-mechanically coupled analysis. The matrix solution is obtained by a direct sparse solver implementing the full Newton-Raphson technique. The transient thermal solution considers a heat source with constant thermal load (i.e., energy flux) that moves along a specified weld trajectory at a prescribed

travel speed. The resultant temperature field for each time increment is used to calculate thermal strains. These thermal strains are treated as mechanical loads for the subsequent computation of stress and distortion. The mechanical solution is obtained from the force-displacement relations where the stiffness matrix is determined from the combination of the strain-displacement relation and the stress-strain relation. The nonlinear stress-strain relation for each material is based on tabulated values for the temperature and strain dependent flow stress.

The geometry considered for all procedures was a centre weld on a large plate  $2000 \text{ mm} \times 2400 \text{ mm} \times 3 \text{ mm}$  (width  $\times$  length  $\times$  thickness). The mesh used in the numerical validation is shown in Figure 2.5. The plate was meshed using 8-node isoparametric brick elements with a size of 2.5 mm at the weld line, increasing to 10 mm at the boundary of the plastic zone, and 40 mm at the plate edge. A single layer of elements was used for the thickness dimension of the plate since through thickness temperature and stress gradients are beyond the scope of the 2-D analytical model explored in this work. The boundary conditions consist of: (1) a  $y$  symmetry plane coincident with the weld trajectory, (2) fixed  $x$  displacement for a single node on both the top and bottom surface of the plate in one corner and (3) a  $z$  bearing surface supporting the plate from beneath. A cooling time of 2700 s (45 min) after the completion of the simulated weld allowed for the entire plate to cool below the first yield temperature and therefore ensure the plastic zone achieved its maximum size.

Since the area of interest (i.e., the plastic zone) is significantly larger than the fusion zone, computational efficiencies were possible by using a simple cylindrical heat source rather than the more computational intensive double-ellipsoid heat source model. The cylindrical heat source used a radius of 5 mm (i.e., twice the mesh size near the heat source), which was adequately large to prevent instability due to jumping of the heat source between subsequent nodes. The depth of the heat source was set equal to the thickness of the plate to mimic a full penetration single pass weld.

The numerical studies consisted of two groups of tests. The first group of tests

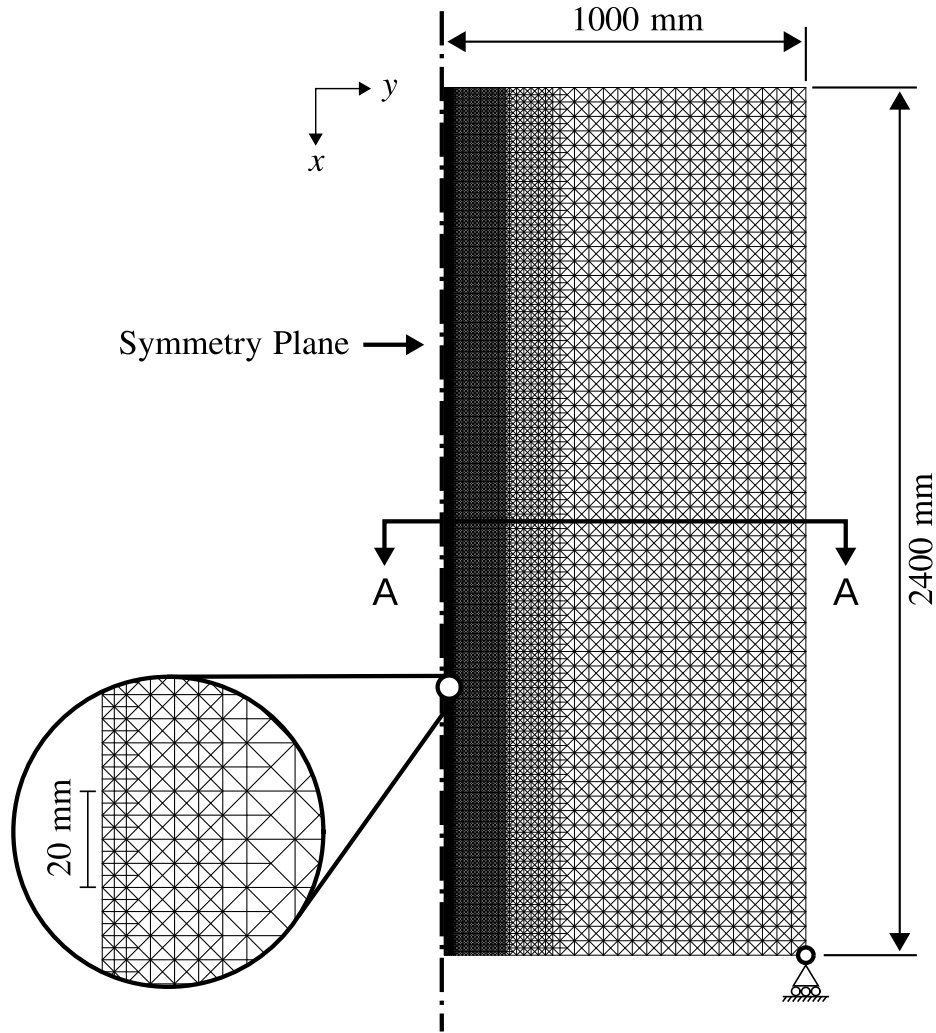


Figure 2.5: Top view of mesh used in numerical simulations.

considered four different commonly welded materials for the substrate: ASTM A36 structural steel, 316L stainless steel, P91 alloy steel, and aluminum alloy 6082-T6. For each material, the same set of welding parameters were simulated with a fixed heat input of 240 J/mm and variable travel speed ranging from 0.25 mm/s to 128 mm/s. The wide range of travel speeds correspond to aspect ratios for the first yield isotherm which span three orders of magnitude from  $10^0$ – $10^2$ . The intermediate travel speed (log-scale) of  $U = 8$  mm/s results in an equivalent procedure to the GMAW process considered in the OMS analysis. The second group of tests considered only ASTM A36 structural steel, with varying heat input from 120–480 J/mm and the same set

of travel speeds considered in the first group of tests.

The suitability of the uniaxial model was assessed for each procedure by comparing the width of the plastic zone measured from the simulation to the estimate based on the maximum width of the first yield isotherm (Equation (2.16)). The estimated and measured widths of the plastic zone are shown in Table 2.2. For the simulations, the reported value is the mean width of the plastic zone for all tests with a yield isotherm aspect ratio in the fast asymptotic regime ( $\mathcal{R} > 17$ ). Measurements for the width of the plastic zone are based on the nodes on the top surface of the plate adjacent to the cross-section A-A shown in Figure 2.5. The width of the plastic zone was estimated as the midpoint between the furthest node from the weld trajectory with a plastic strain  $\geq 1 \mu\text{m}/\text{m}$  and the closest node with a plastic strain  $< 1 \mu\text{m}/\text{m}$ . The predicted and the mean measured size of the plastic zones, for  $\mathcal{R} > 17$ , were in relatively close agreement with a maximum error of 17%. The greatest differences were associated with the larger plastic zones obtained on aluminum alloy 6082-T6 and ASTM A36 structural steel with  $Q' = 480 \text{ J}/\text{mm}$ .

Table 2.2: Predicted width of the first yield isotherm for selected materials and welding heat input.

Material	$Q'$ [J/mm]	$y_{\text{pl}}$ [mm] Equation (2.16)	$\overline{y}_{\text{pl}}$ [mm] Sim. Results for $\mathcal{R} > 17$	$\overline{y}_{\text{max}} _{T_{Y1}}$ [mm]
A36	120	32.5	33 (+2%)	33 (+2%)
	240	65.0	63 (-3%)	67 (+3%)
	480	130	114 (-12%)	135 (+4%)
316L	240	73.5	71 (-3%)	75 (+2%)
P91	240	25.7	27 (+5%)	28 (+9%)
6082	240	134	111 (-17%)	134 ( $\pm 0\%$ )

The width of the yield isotherm was measured by linearly interpolating between

the maximum temperature value on the nodes adjacent to cross-section A-A. As shown in Table 2.2, these values were in close agreement with the values predicted by Equation (2.16) with a maximum error of 9%. For 316L stainless steel, P91 alloy steel, and ASTM A36 structural steel with low to moderate heat input (i.e.,  $Q' = 120$  J/mm and  $Q' = 240$  J/mm), the error in the prediction of the isotherm width was of similar magnitude to the error in prediction of the plastic zone width. For aluminum alloy 6082-T6 and ASTM A36 structural steel with high heat input (i.e.,  $Q' = 480$  J/mm), the error in the prediction of the isotherm width was significantly less than the error in the prediction of the plastic zone width.

Figure 2.6 plots the simulation data for the plastic zone size and yield isotherm width as a function of the aspect ratio ( $\mathcal{R}$ ). This data is plotted in the form of a correction factor  $f_{\mathcal{R}} = y_{\text{pl}}/y_{\text{max}}|_{T_{Y1}}$ . Results for small aspect ratios are beyond the scope of this paper, but the deviation shows a narrow scatter, that can be captured with the empirical asymptote  $\ln(\mathcal{R})$  and blending as described in [33, 51], resulting in:

$$f_{\mathcal{R}} = [\ln^n(\mathcal{R}) + 1]^{1/n} \quad (2.17)$$

where an optimized blending exponent of  $n = -2$  provides a balance between simplicity and a reasonable fit with the data.

## 2.6 Application to Industrial Practice

### 2.6.1 Analytical Estimation of Aspect Ratio

The asymptotic scaling analysis presented in this work reveals that the aspect ratio of the first yield isotherm is a critical parameter for residual stress analysis. The aspect ratio may be readily obtained from computational weld modelling or experimental trials with the use of a thermographic imaging camera, but may also be estimated with simple analytical expressions.

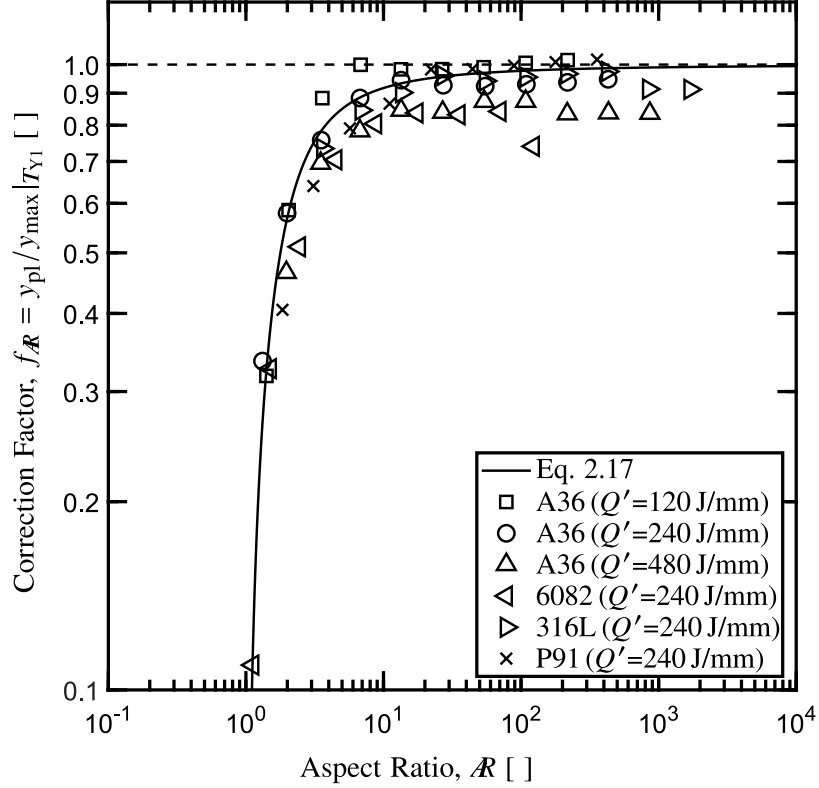


Figure 2.6: Numerical validation of the plastic zone width as a function of the first yield isotherm aspect ratio for selected materials and welding heat inputs.

It has been previously shown in Refs. [33, 34] that the characteristic values of the 2-D temperature field surrounding a moving point heat source can be related to the dimensionless Rosenthal number. This understanding is used to establish limits of applicability for the asymptotic expressions of key characteristic values (such as Equation (2.14)). All characteristic values of the temperature field, including the aspect ratio of a given isotherm, have a unique one-to-one relationship with the Rosenthal number. Figure 2.7 illustrates this relationship for the aspect ratio.

The term “fast” is used in reference to moving heat sources to describe the condition in which advection (i.e., transfer of heat due to motion of the solid) is dominant over conduction in the temperature range of interest [34]. Faster heat sources are associated with larger values of the Rosenthal number (Equation (2.15)) which is proportional to the heat source power. Metallurgical considerations during welding

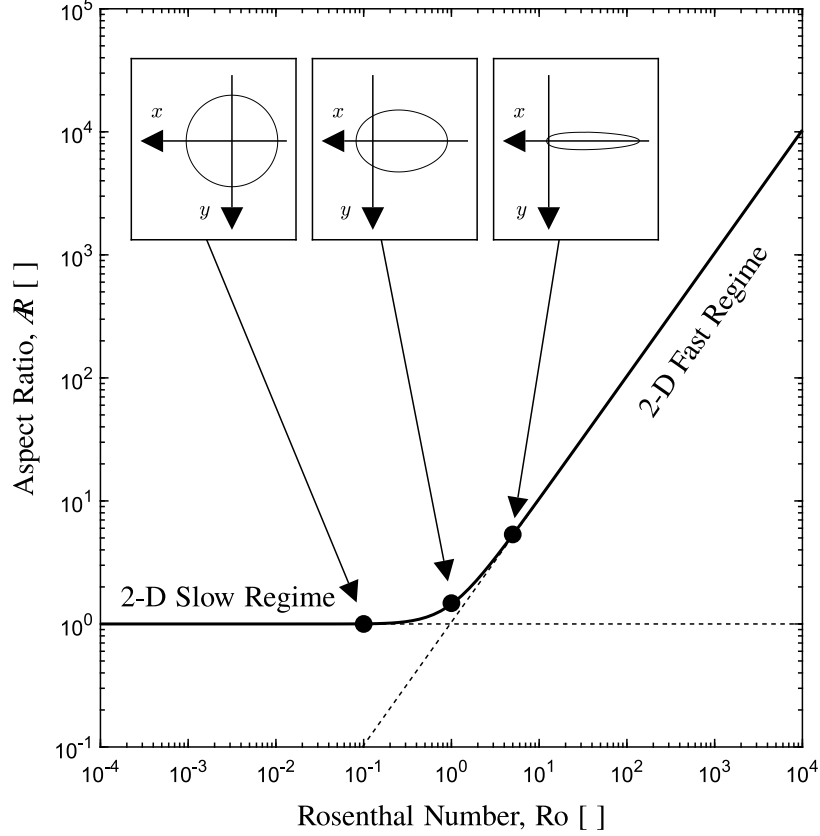


Figure 2.7: Aspect ratio as a function of the dimensionless Rosenthal number.

and additive manufacturing of materials result in a limited range for heat input ( $Q' = q/U$ ), and it is generally true that higher power ( $q$ ) processes (e.g., submerged-arc welding) also have relatively fast travel speed ( $U$ ) compared to lower power processes (e.g., gas tungsten arc welding or friction stir welding).

A blended analytical expression is presented in [34] to compute the aspect ratio of both fast and slow heat sources:

$$\mathcal{R} = \left[ 1 + \left( \sqrt{\frac{\pi e}{8}} \text{Ro} \right)^n \right]^{1/n} \quad (2.18)$$

where the blending exponent has an optimized value of  $n = 1.972$ .

When  $\text{Ro} > 2.1$ , the simplified fast asymptotic expression  $\mathcal{R} = \sqrt{\pi e/8} \text{Ro} \approx \text{Ro}$  may be used with minimal (i.e.,  $< 10\%$ ) error. The uniaxial stress field criterion

$\mathcal{R} \gtrsim 17$ , is therefore equivalently expressed in terms of the Rosenthal number as:

$$\text{Ro} \gtrsim 17 \tag{2.19}$$

This expression is particularly useful for procedure design, since the Rosenthal number depends solely on material properties and welding parameters which may all be determined a priori.

### 2.6.2 Survey of Typical Welding Procedures

A survey of the typical Rosenthal number for 645 different welding procedures was conducted using data for arc welding processes from [45] and solid-state friction stir welding from [52]. The Rosenthal number was computed for each set of steel welding parameters considering a base material of ASTM A36 structural steel, and for each set of aluminum welding parameters considering a base material of aluminum alloy 6082-T6. In total, 369 (57%) of the procedures had a Rosenthal number which satisfied the criterion of  $\text{Ro} \gtrsim 17$  (Table 2.3).

The range and median value for the Rosenthal number and corresponding aspect ratio (Equation (2.18)) for each process are shown in Figure 2.8. The median value satisfies the criterion  $\text{Ro} \gtrsim 17$  for 5 out of the 7 processes on steel, but neither of the two processes on aluminum. There are some procedures at the lower bound of each process range which result in a value  $\text{Ro} < 17$ . The uniaxial model is still applicable to these cases but Equation (2.16) is expected to overestimate the plastic zone size. More precise estimates of the plastic zone size are obtainable with the use of a correction factor such as is provided in Equation (2.17).

## 2.7 Discussion

The results of the numerical validation show a clear trend that is independent of the material and heat input. As the aspect ratio increases above  $\mathcal{R} = 17$ , the correc-

Table 2.3: Summary data for Rosenthal number of typical welding processes with a starting temperature of  $T_0 = 20^\circ\text{C}$  on ASTM A36 structural steel ( $T_{Y1} = 101^\circ\text{C}$ ,  $k = 53 \text{ W m}^{-1}\text{K}^{-1}$ ) and aluminum alloy 6082-T6 ( $T_{Y1} = 80^\circ\text{C}$ ,  $k = 213 \text{ W m}^{-1}\text{K}^{-1}$ ) using data from [45] (arc welding) and [52] (friction stir welding of low-carbon steel and 6xxx series aluminum).

Material	Process [53]	# Procedures		Median
		Total	Ro > 17	Ro
ASTM A36	SAW	87	82 (94%)	60.2
	GMAW	68	60 (88%)	34.2
	FCAW-S	59	49 (83%)	41.4
	FCAW-G	60	40 (67%)	22.3
	SMAW	248	138 (56%)	18.7
	GTAW	41	–	7.1
	FSW	9	–	8.9
Al 6082-T6	GMAW	40	–	6.4
	FSW	33	–	3.5
All Materials/Processes		645	369 (57%)	–

tion factor achieves a constant value of approximately  $f_{\mathcal{R}} = 1$ . As the aspect ratio decreases, approaching the lower asymptotic limit of  $\mathcal{R} = 1$ , the correction factor decreases sharply. Development of an analytical model for the behaviour in the low aspect ratio regime is beyond the scope of this work, but it should be noted that the proposed model for the high aspect ratio will represent a conservative estimate of the plastic zone size for low values of the aspect ratio.

The numerical validation studies confirmed that the error in using a uniaxial model to estimate the width of the plastic zone is relatively constant for aspect ratios larger than a critical value of  $\mathcal{R} = 17$ . There were also observed some relatively small

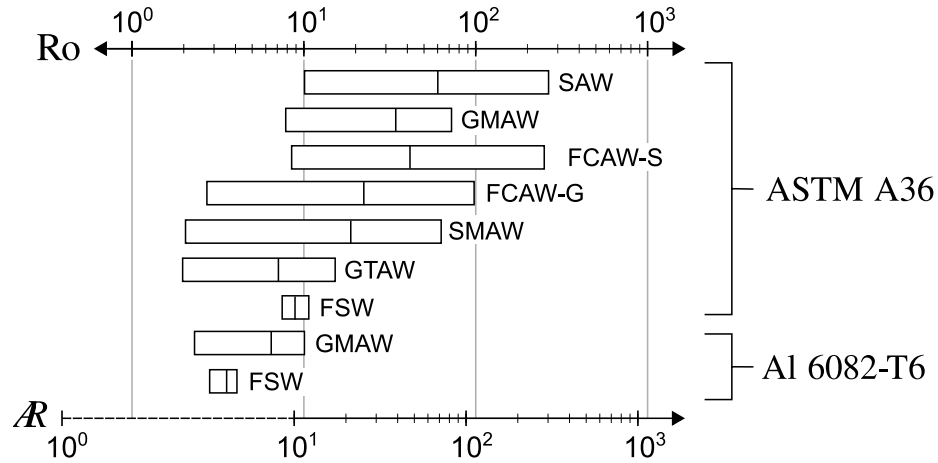


Figure 2.8: Typical range and median value for the dimensionless Rosenthal number based on first yield temperature and the estimated corresponding aspect ratio for selected welding processes [53] using data from [45] (arc welding) and [52] (friction stir welding of low-carbon steel and 6xxx series aluminum).

(< 20%) systematic errors in the asymptotic regime. These errors were observed to be larger for the tests which resulted in larger plastic zone widths indicating that they could be attributed to the effect of finite plate size. Large dimensions were used in the numerical validation to minimize the influence of plate size, but small errors are expected to persist unless the plate dimensions are several orders of magnitude larger than the plastic zone size, which would require significantly more computational power and time with diminishing returns. An additional correction factor to account for finite plate size has been previously proposed by [20] with numerical validation for butt welds on mild steel plates. A more general formulae for the effect of plate compliance on the first yield temperature and corresponding plastic zone width is the subject of a separate ongoing study. A slight decrease in the correction factor for the highest value of the aspect ratio was observed for aluminum alloy 6082-T6 and to a lesser extent 316L stainless steel and A36 structural steel at the highest heat input level. The high aspect ratio in these tests result in a characteristic isotherm length which exceeds the plate length used for the numerical studies. The observed deviation may therefore be attributed to the compliance effects of in-plane bending, which are

expected to be most significant for aluminum due to the lower elastic modulus.

In practice the process window for GMAW (or arc welding in general) would not permit the use of the extreme values of power and travel speed that were tested in the simulations. Although all of the parameters could be reproduced using advanced welding processes (e.g., laser welding), for the extreme low end of the heat source power (i.e., 60 W) an extremely high density heat source (on the order of  $\sigma = 150 \mu\text{m}$ ) would be necessary to achieve melting of the steel substrate [54]. Although this is within the capabilities of modern laser optics, operating at such a low travel speed would be far from optimal. A more likely application of this combination of low power and travel speed would be in brazing, heat treatment, or friction stir welding where the heat source is significantly less dense, but melting of the substrate is not desired.

For three processes (P91 alloy steel, aluminum alloy 6082-T6, and ASTM A36 structural steel with  $Q' = 120 \text{ J/mm}$ ), at the lowest travel speed, the simulated heat source was not sufficiently dense to produce any measurable plastic strain. The low aspect ratios for these welds correspond to an estimated correction factor (Equation (2.17)) of  $f_R \approx 0.1$ , indicating that the temperature change that corresponds to the onset of plastic strain is approximately  $10\times$  larger than the first yield temperature. For the heat source size used in the numerical simulations, the maximum temperature is greater than the yield temperature, but in these cases not  $10\times$  greater and therefore no yielding or plastic strain occurs.

The analysis presented in this work considers a linear elastic model of material behaviour and thus is unable to provide predictions of behaviour within the plastic zone itself. It is reasonable to assume that if the aspect ratio is sufficient to achieve conditions of uniaxial restraint outside the plastic zone, similar constraint may exist within the plastic zone. A uniaxial model, such as was presented in [43], might therefore be expected to provide reasonable estimates of the residual stress distribution, although additional validation with numerical or experimental results should be performed to verify.

This study establishes the foundation for further work to be published separately on the estimation of forces and distortions induced by welding or other moving heat sources, and also the analysis of effects of departure from idealizations, such as finite plate size.

## 2.8 Conclusions

The thermal stress and strain fields caused by a moving point heat source on large thin plates were studied using the OMS (Order of Magnitude Scaling) technique.

- An asymptotic analysis of a linear elastic formulation indicates that when isotherms are elongated the stress and strain fields tend towards a uniaxial stress state.
- A novel criterion for the threshold of aspect ratio is presented for the first time ( $\mathcal{R} \gtrsim 17$ , Equation (2.12)). This criterion determines the applicability of the uniaxial model, which was previously used in residual stress calculations without a check of validity.
- The aspect ratio is a function of only the Rosenthal number (Equation (2.18)) and the criterion for elongated isotherms can be expressed as  $\text{Ro} \gtrsim 17$ . A survey of 645 typical welding procedures indicates that the majority of welds (57%) fulfill the conditions of the asymptotic analysis presented here.
- A critical temperature is identified: the first yield temperature ( $T_{Y1}$ , Equation (2.13)), corresponding to the lowest temperature in the plate at which thermal stresses induce plasticity. This temperature is a fundamental material property, tabulated in Table 2.1 for a wide variety of structural alloys.
- The size of the plastic zone surrounding the heat source trajectory corresponds to the maximum width of the first yield isotherm ( $y_{\text{pl}} = y_{\text{max}}|_{T_{Y1}}$ , Equation (2.16)).

Application of typical materials and process parameters to this equation indicates that the width of the plastic zone is typically much larger than the width of the weld bead (Figure 2.4).

- The asymptotic model was validated against nonlinear numerical simulations with a temperature dependent elastic-plastic material model for commonly welded grades of carbon steel, stainless steel, and aluminum. The results confirmed that the maximum width of the first yield isotherm provides appropriate estimates for the width of the plastic strain region when the proposed criterion on aspect ratio is met (Figure 2.6).
- Analytical treatment of cases in which the aspect ratio criterion is not met are outside the scope of this work; however, predictions of plastic width show a consistent trend of overestimation at small aspect ratios. This trend is captured accurately by the empirical relationship of Equation (2.17), enabling useful predictions of plastic width even for aspect ratios close to 1.

## 2.9 Acknowledgements

The authors would like to acknowledge Simufact Engineering, a subsidiary of MSC Software for providing a license of Simufact Welding simulation software for use in this study. Valuable discussions and feedback from J. Goldak, Y. Wang, and Y. Lu were gratefully received.

## References

- [1] M. Asadi, J. A. Goldak, J. Nielsen, J. Zhou, S. Tchernov, and D. Downey, “Analysis of predicted residual stress in a weld and comparison with experimental data using regression model,” *Int. J. Mech. Mater. Des.*, vol. 5, no. 4, pp. 353–364, Nov. 2009. DOI: 10.1007/s10999-009-9107-5.
- [11] N. S. Boulton and H. E. Lance Martin, “Residual stresses in arc-welded plates,” *Proc. Inst. Mech. Eng.*, vol. 133, no. 1, pp. 295–347, June 1936. DOI: 10.1243/pime\_proc\_1936\_133\_017\_02.
- [12] O. E. Rodgers and J. R. Fetcher, “Determination of internal stress from the temperature history to a butt-welded plate,” *Welding J.*, vol. 17, no. 11, pp. 4s–7s, Nov. 1938.
- [13] A. A. Wells, “The mechanics of notch brittle fracture,” *Weld. Res.*, vol. 7, no. 2, pp. 34r–56r, Feb. 1953.
- [14] L. Tall, “Residual stresses in welded plates - a theoretical study,” *Welding J.*, vol. 43, no. 1, pp. 10s–23s, Jan. 1964.
- [15] K. Masubuchi, F. B. Simmons, and R. E. Monroe, “Analysis of thermal stresses and metal movement during welding,” in *Batelle Memorial Institute Tech. Rep.* Restone Arsenal, AL: Redstone Scientific Information Centre, Jul. 1968, RSIC–820.
- [20] Y. Ueda and M. G. Yuan, “Prediction of residual stresses in butt welded plates using inherent strains,” *ASME J. Eng. Mater. Technol.*, vol. 115, no. 4, pp. 417–423, Oct. 1993. DOI: 10.1115/1.2904240.
- [21] M. G. Yuan and Y. Ueda, “Prediction of residual stresses in welded T- and I-joints using inherent strains,” *ASME J. Eng. Mater. Technol.*, vol. 118, no. 2, pp. 229–234, Apr. 1996. DOI: 10.1115/1.2804892.
- [26] J. B. Dwight and K. E. Moxham, “Welded steel plates in compression,” *Struct. Eng.*, vol. 47, no. 2, pp. 49–66, Feb. 1969.
- [27] K. Masubuchi, “Distortion in weldments,” in *Analysis of Welded Structures*, 1st, Oxford, UK: Pergamon Press Ltd., 1980, pp. 235–327.
- [28] O. W. Blodgett and D. K. Miller, “Welded connections,” in *Structural Engineering Handbook*, Boca Raton, FL: CRC Press LLC, 1999, ch. 22.
- [29] N. Hempel, J. R. Bunn, T. Nitschke-Pagel, E. A. Payzant, and K. Dilger, “Study on the residual stress relaxation in girth-welded steel pipes under bending load using diffraction methods,” *Mater. Sci. Eng., A*, vol. 688, pp. 289–300, Mar. 2017. DOI: 10.1016/j.msea.2017.02.005.
- [30] H. Suzuki, J. Katsuyama, and Y. Morii, “Comparison of residual stress distributions of similar and dissimilar thick butt-weld plates,” *J. Solid Mech. Mater. Eng.*, vol. 6, no. 6, pp. 574–583, June 2012. DOI: 10.1299/jmmp.6.574.

- [31] D. Qiao, Z. Feng, W. Zhang, Y. Wang, and P. Crooker, “Modeling of weld residual plastic strain and stress in dissimilar metal butt weld in nuclear reactors,” in *Proc. ASME 2013 Pressure Vessels Pip. Conf.*, Paris, July 14-18, 2013, (PVP2013-9801), pp. V06BT06A091. DOI: 10.1115/pvp2013-98081.
- [32] H. Eisazadeh, A. Achuthan, J. A. Goldak, and D. K. Aidun, “Effect of material properties and mechanical tensioning load on residual stress formation in GTA 304-A36 dissimilar weld,” *J. Mater. Process. Technol.*, vol. 222, pp. 344–355, Aug. 2015. DOI: 10.1016/j.jmatprotec.2015.03.021.
- [33] Y. Lu, Y. Wang, and P. F. Mendez, “Width of thermal features induced by a 2-D moving heat source,” *Int. J. Heat Mass Transfer*, vol. 156, pp. 119793, Aug. 2020. DOI: 10.1016/j.ijheatmasstransfer.2020.119793.
- [34] Y. Lu and P. F. Mendez, “Characteristic values of the temperature field induced by a moving line heat source,” *Int. J. Heat Mass Transfer*, vol. 166, pp. 120671, Feb. 2021. DOI: 10.1016/j.ijheatmasstransfer.2020.120671.
- [35] K. Satoh, “Transient thermal stresses of weld heat-affected zone by both-ends-fixed bar analogy,” *Trans. JWS*, vol. 3, no. 1, pp. 125–134, Apr. 1972.
- [36] M. Watanabe, “Thermal stress and its residual stress of rectangular plate under one-dimensionally distributed temperature,” *J. Zosen Kiokai* [in Japanese], vol. 86, pp. 173–184, 1954. DOI: 10.2534/jjasnaoe1952.1954.86\_173.
- [37] S. Vaidyanathan, A. F. Todaro, and I. Finnie, “Residual stresses due to circumferential welds,” *ASME J. Eng. Mater. Technol.*, vol. 95, no. 4, pp. 233–237, Oct. 1973. DOI: 10.1115/1.3443159.
- [38] P. F. Mendez and N. Stier, “OMS: a computer algorithm to develop closed-form solutions to multicoupled multiphysics problems,” Graz-Seggau, Austria: TU Graz, 2012, pp. 219–254.
- [39] P. F. Mendez and T. W. Eagar, “Order of Magnitude Scaling: a systematic approach to approximation and asymptotic scaling of equations in engineering,” *ASME J. Appl. Mech.*, vol. 80, no. 1, pp. 011009, Oct. 2013. DOI: 10.1115/1.4006839.
- [40] D. Rosenthal, “The theory of moving sources of heat and its application to metal treatments,” *Trans. ASME*, vol. 68, no. 11, pp. 849–866, Nov. 1946.
- [41] S. Timoshenko and J. Goodier, *Theory of Elasticity*, 2nd. McGraw-Hill, 1951.
- [42] O. R. Myhr and Ø. Grong, “Dimensionless maps for heat flow analyses in fusion welding,” *Acta Metall. Mater.*, vol. 38, no. 3, pp. 449–460, Mar. 1990. DOI: 10.1016/0956-7151(90)90151-6.
- [43] N. O. Okerblom, *Raschet Deformatsii Metallokonstruktsii pri Svarke* [The Calculations of Deformations of Welded Metal Structures]. Moscow: Mashgiz, 1955 (Transl. by London: HMSO, 1958).
- [44] J. White, “Longitudinal shrinkage of a single pass weld,” *Univ. Cambridge Tech. Rep.*, CUED/C-Struct/TR.57, 1977.

- [45] *The Procedural Handbook of Arc Welding*, 14th. Cleveland, OH: The James F. Lincoln Arc Welding Foundation, 2000.
- [46] Sente Software Ltd., *JMatPro* (ver. 11.0), Computer Software, Guildford, UK, 2019. [Online]. Available: [www.sentesoftware.co.uk/jmatpro](http://www.sentesoftware.co.uk/jmatpro).
- [47] P. F. Mendez, “Characteristic values in the scaling of differential equations in engineering,” *ASME J. Appl. Mech.*, vol. 77, no. 6, pp. 061017, Sept. 2010. DOI: 10.1115/1.4001357.
- [48] G. N. Greaves, A. L. Greer, R. S. Lakes, and T. Rouxel, “Poisson’s ratio and modern materials,” *Nat. Mater.*, vol. 10, no. 11, pp. 823–837, Oct. 2011. DOI: 10.1038/nmat3134.
- [49] S. Li, S. Ren, Y. Zhang, D. Deng, and H. Murakawa, “Numerical investigation of formation mechanism of welding residual stress in P92 steel multi-pass joints,” *J. Mater. Process. Technol.*, vol. 244, pp. 240–252, June 2017. DOI: 10.1016/j.jmatprotec.2017.01.033.
- [50] S. Okano and M. Mochizuki, “Dominant factors and quantification of tendon force in welded structural materials,” *Trans. JSME* [in Japanese], vol. 81, no. 830, pp. 15–00277, Sept. 2015. DOI: 10.1299/transjsme.15-00277.
- [51] P. F. Mendez, “Reduced order models for welding and solidification processes,” *IOP Conf. Ser.: Mater. Sci. Eng.*, vol. 861, pp. 012003, June 2020. DOI: 10.1088/1757-899X/861/1/012003.
- [52] P. F. Mendez, K. E. Tello, and T. J. Lienert, “Scaling of coupled heat transfer and plastic deformation around the pin in friction stir welding,” *Acta Mater.*, vol. 58, no. 18, pp. 6012–6026, Oct. 2010. DOI: 10.1016/j.actamat.2010.07.019.
- [53] American Welding Society, *Standard Welding Terms and Definitions*. AWS A3.0M/A3.0:2020, 2020.
- [54] Y. Lu and P. F. Mendez, “Analytical modelling of moving heat source based on a 3-D conduction model,” in *Proc. CanWeld Conf.*, Montreal, Canada, Sept. 12-13, 2018.

# Chapter 3

## A General Expression for the Welding Tendon Force

### 3.1 Introduction

Residual stress is a significant concern in metal fabrication by thermal processes. Development of residual stresses is associated with permanent residual plastic strain which is produced local to the weld seam. In many applications, geometric distortion and reaction stresses that occur in the overall geometry may be of even more significant concern than the residual stresses and strains local to the weld. This has been shown to be the case in circumferential pipeline welding [37, 55, 56], ship-building [57, 58], welding of built-up members [14, 26], and additive manufacturing [59].

During the initial design process, it is desirable to know what impact the stresses and strains local to the heat source trajectory have on the overall geometry; however, prediction of the exact nature of the complete residual stress distribution requires relatively advanced multi-physics computation modelling packages to achieve sufficient granularity. To simplify such an analysis, it is useful to initially obtain an equivalent load to describe the local effects of thermal processing followed by a subsequent analysis applying this equivalent load to the overall geometry to compute the resulting stresses, strains, and distortions.

Equivalent load models have been shown to provide reasonable estimates of bending distortion [60] and residual stresses [20, 21] produced during fabrication of longitu-

dinally welded structural steel members. A similar approach has also been used for efficient optimization of the weld and assembly sequence for manufacturing of thin plate structures [57, 61]. Due to the lack of a general analytical formula, these applications typically require that the effective load be obtained through empirical methods increasing the cost and complexity, while limiting the generality of the results.

The tendon force model proposed in Ref. [44] establishes an equivalent load which depends on a limited number of material properties and procedural parameters which may be obtained a priori. To utilize this approach in modern engineering design practice, it is necessary that a general expression be obtained that allows for application to a range of materials with varying properties and behaviour. In addition, the limits of application of the model must be clearly expressed.

This work utilizes the minimal representation and correction factor (MRCF) approach, that has been previously applied to address similar issues of generality in modelling of the moving heat source temperature field [33, 62, 63] as well as solid-state friction stir welding [52]. The effect of temperature dependence is accounted for by correction factors on the simplest case of constant material properties. A general equation is proposed for the tendon force which captures temperature dependent material behaviour, thereby expanding the applicability of the tendon force model to a broad set of real world scenarios.

## 3.2 List of Symbols

Symbol	SI Unit	Description
<b>Roman Letters</b>		
$A_c$	$m^2$	Cross-sectional area
$A_w$	$m^2$	Weld fusion zone area
$d$	m	Section thickness
$E$	$N m^{-2}$	Elastic modulus
$F_{Ten}$	N	Tendon force
$f_1$	1	Correction factor for CTE and yield strain
$f_2$	1	Correction factor for heat capacity
$f_3$	1	Correction factor for yield temperature ratio
$H$	1	Normalized tendon force parameter
$I_{yy}$	$m^4$	Second moment of inertia with respect to $y$ axis
$K$	$N m^{-2}$	Bulk modulus
$L$	m	HSS member length
$N_T$	1	Dimensionless yield temperature ratio
$N_\alpha$	1	Normalized rate of change of CTE
$N_\epsilon$	1	Normalized rate of change of yield strain
$N_{\rho c}$	1	Normalized rate of change of heat capacity
$Q'$	$J m^{-1}$	Linear energy input (i.e., heat input)
$T_{lm}$	K	Log-mean yield temperature
$T_{max}$	K	Maximum temperature
$T_{Y1}$	K	First yield temperature
$T_{Y2}$	K	Second yield temperature
$T_0$	K	Starting/ambient temperature
$t_{max}$	s	Time at which maximum temperature is achieved
$y_{max}$	m	Maximum isotherm width
$y_{pl}$	m	Plastic zone size (i.e., half-width)
$z_c$	m	Eccentricity of weld relative to neutral axis

Symbol	SI Unit	Description
<b>Greek Letters</b>		
$\alpha$	$\text{K}^{-1}$	Linear coefficient of thermal expansion
$\bar{\alpha}$	$\text{K}^{-1}$	Mean linear coefficient of thermal expansion
$\beta$	$\text{K}^{-1}$	Volumetric coefficient of thermal expansion
$\delta$	m	Maximum deflection of longitudinally welded section
$\eta$	1	Heat transfer efficiency
$\epsilon_{\text{el}}$	1	Elastic strain
$\epsilon_{\text{inh}}$	1	Inherent strain
$\epsilon_{\text{pl}}$	1	Plastic strain
$\epsilon_{\text{res}}$	1	Residual elastic strain
$\epsilon_{\text{rxn}}$	1	Reaction strain
$\epsilon_{\text{T}}$	1	Total strain
$\epsilon_{\text{th}}$	1	Thermal strain
$\epsilon_{\text{Y}}$	1	Yield strain
$\gamma$	1	Dimensionless Grüneisen ratio
$\nu$	1	Poisson's ratio
$\rho c$	$\text{J m}^{-3} \text{K}^{-1}$	Volumetric specific heat capacity
$\sigma_{\text{res}}$	$\text{N m}^{-2}$	Residual stress parallel to weld axis
$\sigma_{\text{rxn}}$	$\text{N m}^{-2}$	Reaction stress parallel to weld axis
$\sigma_{\text{Y}}$	$\text{N m}^{-2}$	Material yield strength

Symbol	Description
<b>Superscripts</b>	
$\wedge$	Asymptotic behaviour
$+$	Correction for secondary phenomena
<b>Subscripts</b>	
eff	Effective property value
I	Region I ( $T_{\text{max}} < T_{\text{Y1}}$ )
II	Region II ( $T_{\text{Y1}} < T_{\text{max}} < T_{\text{Y2}}$ )
III	Region III ( $T_{\text{max}} > T_{\text{Y2}}$ )

### 3.3 Definition of Tendon Force

Residual stresses develop during non-uniform heating of materials when thermal strains exceed the material elastic strain limit and produce plasticity [11]. Early analyses of the global response to local plastic behaviour at the weld use an equivalent shrinkage force computed from the cooling of the deposited metal and surrounding material [26, 64, 65]. This interpretation has its roots in empirical studies in which a weld was cast in place using the thermit process [12].

In many practical cases of welding and additive manufacturing, the effects of plasticity are confined to a region near the heat source trajectory which is small compared to the overall size of the geometry. It is desirable to separate this small region of complex nonlinear material behaviour from the linear response throughout the rest of the structure.

An idealized analysis of residual stresses was proposed in Ref. [13] as the “three-bar model”. In this model, a butt joint between two plates is simplified to a system of three cylindrical bars which are rigidly fixed together at either end. The centre bar, representing the fusion zone and adjacent material, is assumed to have an unstressed length which is shorter than the bars on either side due to shrinkage during cooling. The resulting tensile force in the centre bar is proportional to the area of the shrinkage zone as well as the magnitude of the shrinkage strain. The balancing compressive stresses in the remaining plate area, represented by the left and right bars, are obtained from equilibrium. The key limitation of the three-bar model is that it requires separation of the plate area depending on whether the residual stress is compressive or tensile.

An improved model is proposed in Ref. [44] in which an equivalent “tendon force” is defined as “the force which is resisted by the whole cross section of the plate.” A mathematical definition for this force was first presented in Ref. [43], which can be

rewritten as:

$$F_{\text{Ten}} \equiv \int_{A_c} E(\epsilon_{\text{res}} - \epsilon_{\text{rxn}}) dA \quad (3.1)$$

where  $A_c$  is the cross-section of the whole plate,  $E$  is the elastic modulus of the material,  $\epsilon_{\text{res}}$  is the residual elastic strain distribution in the material (strains that could be measured), and  $\epsilon_{\text{rxn}}$  is a “reaction strain” discussed below.

### 3.3.1 Reaction Strain

The reaction strain is a fictitious strain distribution with important properties. This distribution corresponds to the strain caused by a concentrated force of magnitude  $F_{\text{Ten}}$  applied along the heat source trajectory in an unstressed geometry.

Saint-Venant’s principle indicates that in the region far away from the heat source trajectory, the effect of the tendon force is equivalent to that of the external load. The reaction strain is therefore associated with the elastic response of the geometry to the plastic residual strains developed during heating and cooling.

In practice, the equivalence between thermally-induced elastic residual stress and reaction stress is reached near the boundary of areas affected by plastic deformation, such that  $\epsilon_{\text{res}}$  tends to equal  $\epsilon_{\text{rxn}}$  outside the area that experienced thermally-induced plasticity. Equation (3.1) can then be approximated closely using only the fraction of cross-sectional area affected by plasticity.

The tendon force model thus enables prediction of the stress and strain distribution in the overall geometry based on information from only a relatively small area of interest near the heat source trajectory.

### 3.3.2 Inherent Strain

The difference between the the residual elastic strain distribution ( $\epsilon_{\text{res}}$ ) and the elastic reaction strain ( $\epsilon_{\text{rxn}}$ ) is termed the inherent strain [16]:

$$\epsilon_{\text{inh}} \equiv \epsilon_{\text{res}} - \epsilon_{\text{rxn}} \quad (3.2)$$

Based on the definition of inherent strain, it is possible to interpret the residual elastic strain distribution ( $\epsilon_{\text{res}} = \epsilon_{\text{inh}} + \epsilon_{\text{rxn}}$ ) as the superposition of two components: (a) an inherent strain ( $\epsilon_{\text{inh}}$ ), and (b) a reaction strain ( $\epsilon_{\text{rxn}}$ ).

The reaction strain is present throughout the entire cross-section. Outside the approximate boundary where heating caused plasticity, the reaction strains and the residual strains are equivalent; thus, the inherent strain is zero everywhere except within the plastic zone. The inherent strain may then be considered to capture the effect of plasticity.

Since it occurs only in a finite area near the heat source trajectory, a powerful property of the inherent strain is that it can be can be calculated from heat source parameters, independent from the reaction of the base material, to obtain a tendon force. After calculating the tendon force, the reaction strain is calculated and superimposed on the inherent strain distribution to obtain the residual elastic strain distribution throughout the geometry. This process is illustrated schematically for a flat plate in Figure 3.1.

Although a uniform reaction strain will result in some geometries, such as the flat plate shown in Figure 3.1, in general this is not a requirement to apply the tendon force model. The equations presented in this study may be used for any geometry with a “thin” cross-section (e.g., hollow structural sections).

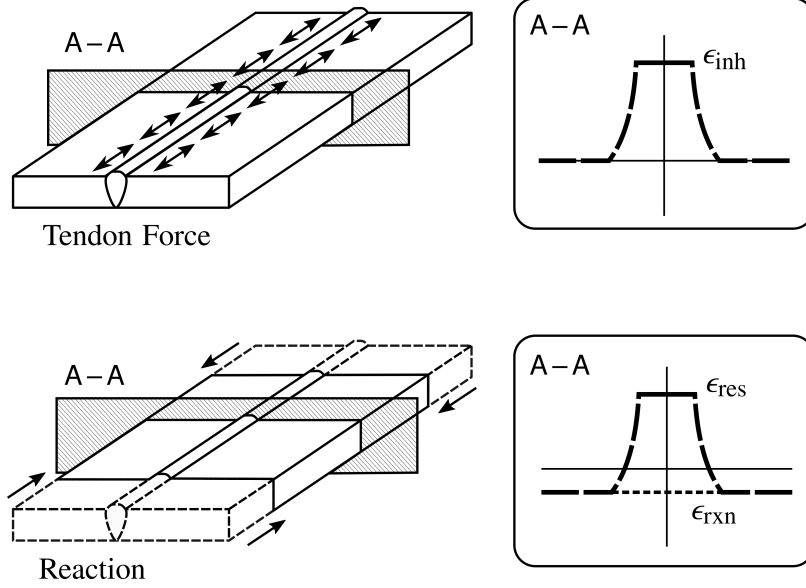


Figure 3.1: Superposition of tendon force (i.e., inherent strain) local to the heat source trajectory with reaction strain throughout the entire geometry.

### 3.3.3 Total Strain

To evaluate the inherent strain it is necessary to consider the various contributions to the total strain in a material. In general, the total strain in a material is given by:

$$\epsilon_T = \epsilon_{el} + \epsilon_{pl} + \epsilon_{th} \quad (3.3)$$

where  $\epsilon_{el}$  is the elastic strain,  $\epsilon_{pl}$  is the plastic strain,  $\epsilon_{th}$  is the thermal strain, and  $\epsilon_T$  is the total strain distribution parallel to the heat source trajectory. In this work, the plastic strain is considered as a signed scalar value which is positive for strain associated with tensile loading and negative for strain under compressive loading.

The goal of this study is to predict the final residual stress distribution at a sufficiently long time after thermal processing is completed for the temperature distribution to achieve equilibrium. For large enough geometries, or by cooling to the environment, the final temperature resembles the starting temperature (even when preheat is used), and therefore  $\epsilon_{th} \approx 0$  in Equation (3.3).

Also, the elastic strains in the final state correspond to the residual strains, and therefore  $\epsilon_{el} = \epsilon_{res}$  in Equation (3.3). The final total strain can then be expressed as:

$$\epsilon_T = \epsilon_{res} + \epsilon_{pl} \quad (3.4)$$

Ref. [66] has previously shown that the total strain ( $\epsilon_T$ ) corresponds to uniaxial tension in the vast majority of welding applications, and is uniform throughout the length of a long weld on a substrate of constant cross-section. A similar condition is proposed in Ref. [43] for the case of edge welded plates, which relates closely to additive manufacturing of thin-walled structures.

### 3.3.4 Relationship Between Tendon Force and Plasticity

Outside the plastic zone there is no inherent strain and the residual elastic strain is equal to the reaction strain ( $\epsilon_{rxn} = \epsilon_{res}$ ). The plastic strain in this region is also zero, which gives:

$$\epsilon_T = \epsilon_{res} = \epsilon_{rxn} \quad (3.5)$$

Inside the plastic zone, the residual plastic strain is obtained by combining Equation (3.4) and Equation (3.5) to give:

$$\epsilon_{pl} = \epsilon_{rxn} - \epsilon_{res} = -\epsilon_{inh} \quad (3.6)$$

Replacing Equation (3.6) into Equation (3.1), and keeping in mind that  $\epsilon_{inh} = 0$  outside the plastic zone, the tendon force can then be expressed as the integral of the residual plastic strain produced during thermal processing:

$$F_{Ten} = E \int_{A_c} \epsilon_{inh} dA = -Ed \int_{y_{pl}} \epsilon_{pl} dy \quad (3.7)$$

where  $d$  is the uniform section thickness and  $y_{pl}$  is the plastic zone size.

## 3.4 Constant Material Properties

The strain equality in Equation (3.3) will be satisfied at all times during the thermal cycle. In general, computation of the plastic strain is complicated by the presence of a non-zero total strain in the material ( $\epsilon_T$ ).

From Equation (3.5) the residual total strain is equivalent to the reaction strain produced by the tendon force. For very large or very rigid geometries, the magnitude of the reaction strain will be sufficiently small compared to the elastic, plastic, and thermal strains that it may be neglected during the thermal processing. The strain equality of Equation (3.3) may then be rearranged to give:

$$-\epsilon_{th} = \epsilon_{el} + \epsilon_{pl} \quad (3.8)$$

Equation (3.8) is exact for an infinitely rigid geometry, and may also be used as a first estimate for the general case of a geometry which is not sufficiently rigid to neglect the total strain. An iterative approach can then be applied using the resulting values of tendon force and reaction strain to correct the previous estimates for the plastic strain. This study focuses on the case of large rigid geometries such as are common in welding for structural construction, or large scale wire arc additive manufacturing. A closed-form expression to correct for the “compliance” effects in smaller or less rigid geometries is the subject of an ongoing work to be published separately.

### 3.4.1 Strain Induced by the Thermal Cycle

Figure 3.2 illustrates a typical thermal cycle experienced by a material during thermal processing, consisting of a period of monotonic heating followed by a period of monotonic cooling. The thermal cycle can be described using two characteristic temperatures: the starting temperature ( $T_0$ ) and the maximum temperature ( $T_{max}$ ). There also exists a characteristic time ( $t_{max}$ ) which corresponds with the occurrence of the maximum temperature. In welding, it is generally assumed that all relevant

regions in the cross-section share the same starting temperature, but the maximum temperature and characteristic time will depend on the distance from the weld centreline. This assumption remains valid for additive manufacturing of thin-walled sections, although the starting temperature may vary between subsequent passes.

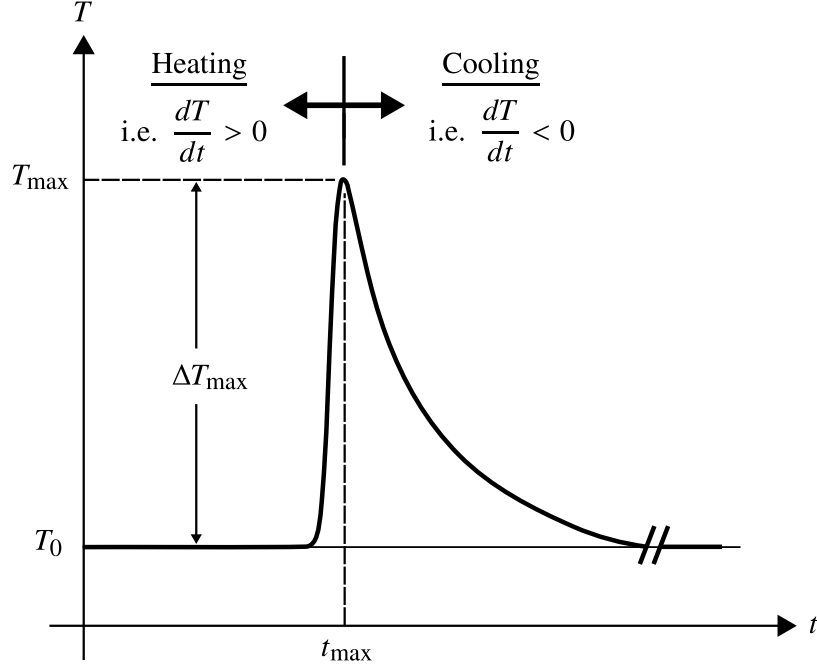


Figure 3.2: Characteristic thermal cycle.

The thermal strain relative to the starting temperature ( $T_0$ ) is expressed as:

$$\epsilon_{\text{th}}|_T = \bar{\alpha}|_T (T - T_{\text{ref}}) - \bar{\alpha}|_{T_0} (T_0 - T_{\text{ref}}) \quad (3.9)$$

where  $\bar{\alpha}|_T$  is the mean linear coefficient of thermal expansion (CTE) between the temperatures  $T_{\text{ref}}$  and  $T$ , and  $\bar{\alpha}|_{T_0}$  is the mean CTE between the temperatures  $T_{\text{ref}}$  and  $T_0$ . If the reference temperature is chosen to be equal to the starting temperature, then the second term in Equation (3.9) will be equal to zero. For a material with a constant CTE,  $\bar{\alpha}|_T$  may be substituted for a constant value  $\alpha$ .

In general, the temperature and thermal strain distributions are a function of two variables: the time ( $t$ ) and the distance ( $y$ ). To evaluate the tendon force, it is only

necessary to obtain the value of the plastic strain in the final or residual state. The residual plastic strain may be readily obtained by consideration of the material's uniaxial thermal yield behaviour.

### 3.4.2 Thermal-Elastic Strain Relationship

For a rigidly constrained specimen ( $\epsilon_T = 0$ ), the thermal, elastic, and plastic strains will always balance. The plastic strain throughout a thermal cycle may be obtained directly from the difference of the elastic and thermal strain.

In practical applications to material characterization, the elastic strain and thermal strain are typically inferred from direct measurement of force and temperature. Although force-temperature plots were used by various authors [13, 67] in earlier theoretical work, Satoh [35] first presented a suitable experimental apparatus and thus the force-temperature diagram is commonly associated with the ‘‘Satoh Test’’.

A typical diagram of elastic strain (force) vs. temperature for a material in which the onset of plasticity is independent of temperature is shown in Figure 3.3. Three different thermal cycles are displayed with maximum temperatures corresponding to points  $a'$ ,  $b$  and  $b'$ .

The cycle with the lowest maximum temperature is  $o-a-a'-c$ . From point  $o$  to point  $a$ , the thermal strain steadily increases and a corresponding elastic compressive stress is produced in the material. At point  $a$ , the compressive stress in the material reaches yield magnitude.

The corresponding critical temperature is defined as the ‘‘first yield temperature,’’ [66] and for the case of constant material properties may be written as:

$$T_{Y1} - T_0 = \Delta T_{Y1} = \frac{\epsilon_Y}{\alpha} \quad (3.10)$$

where  $\epsilon_Y = \sigma_Y/E$  is the material ‘‘yield strain’’ corresponding to the onset of plasticity. The thermal strain at point  $a$  is equal to the yield strain ( $\epsilon_Y$ ).

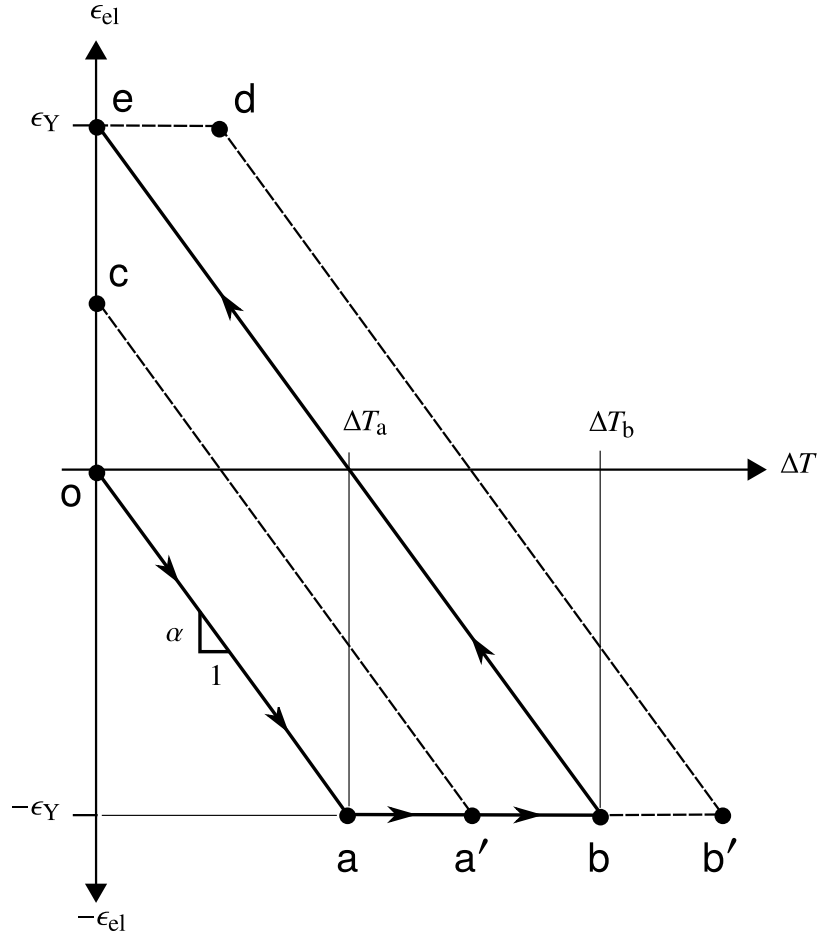


Figure 3.3: Relationship between elastic and thermal strain for thermal cycles with three different maximum temperatures; after [13].

From point  $a$  to point  $a'$ , the thermal strain is further increased resulting in the development of a compressive (negative) plastic strain  $\epsilon_{pl} = \epsilon_{th}|_{\Delta T_a} - \epsilon_{th}|_{\Delta T_{a'}}$ . At point  $a'$ , the temperature and thermal strain reach their maximum value. From point  $a'$  to point  $c$ , the thermal strain decreases, the elastic strain increases proportionally and the plastic strain remains unchanged. The residual plastic strain at point  $c$  is therefore equal to the plastic strain at point  $a'$ . The residual elastic strain at point  $c$  is positive (tensile) with a magnitude less than the yield strain ( $\epsilon_Y$ ).

The cycle with the intermediate maximum temperature is  $o$ - $a$ - $b$ - $e$ . From point  $o$  to point  $a'$ , the material behaviour is identical to the previous cycle. From point  $a'$  to point  $b$ , additional compressive (negative) plastic strain develops to a maximum

value of  $\epsilon_{pl} = \epsilon_{th}|_{\Delta T_a} - \epsilon_{th}|_{\Delta T_b}$  at point **b**. From point **b** to point **e**, the thermal strain decreases and the elastic strain increases proportionally while the plastic strain remains constant. The plastic strain at point **e** is therefore equal to the plastic strain at point **b**.

This cycle is unique in that the residual elastic strain at point **e** is equal to the yield strain ( $\epsilon_Y$ ). Since in the final state the thermal strain is also equal to zero, it follows that the residual plastic strain is equal and opposite to the residual elastic strain. The maximum temperature for this cycle at point **b** marks the minimum temperature change necessary to produce yield magnitude residual plastic strain during cooling.

This critical temperature is defined as the “second yield temperature,” and for constant material properties is given by:

$$T_{Y2} - T_0 = \Delta T_{Y2} = \frac{2\epsilon_Y}{\alpha} \quad (3.11)$$

The cycle with the highest maximum temperature is **o-a-b'-d-e**. From point **o** to point **b**, the material behaviour is identical to the previous cycle. From point **b** to point **b'**, additional compressive (negative) plastic strain develops to a maximum value of  $\epsilon_{pl} = \epsilon_{th}|_{\Delta T_a} - \epsilon_{th}|_{\Delta T_{b'}}$  at point **b'**. From point **b'** to point **d** the temperature and thermal strain decrease, the elastic strain increases proportionally and the plastic strain remains constant. At point **d**, the material begins to yield in tension and develop tensile (positive) plastic strain. From point **d** to point **e**, the thermal strain decreases back to zero as the temperature returns to ambient. At point **e** the thermal strain is zero and the residual elastic strain is equal to the yield strain ( $\epsilon_Y$ ). The residual plastic strain will therefore also have a magnitude equal to the yield strain. This result is verified by observing that the tensile plastic strain developed between point **d** and point **e** is equal and opposite to the compressive (negative) plastic strain developed between point **b** and point **b'**.

### 3.4.3 Distribution of Residual Plastic Strain

The tendon force depends on the residual plastic strain distribution. The first and second yield temperatures divide the distribution of residual plastic strain into three distinct regions as shown in Figure 3.4.

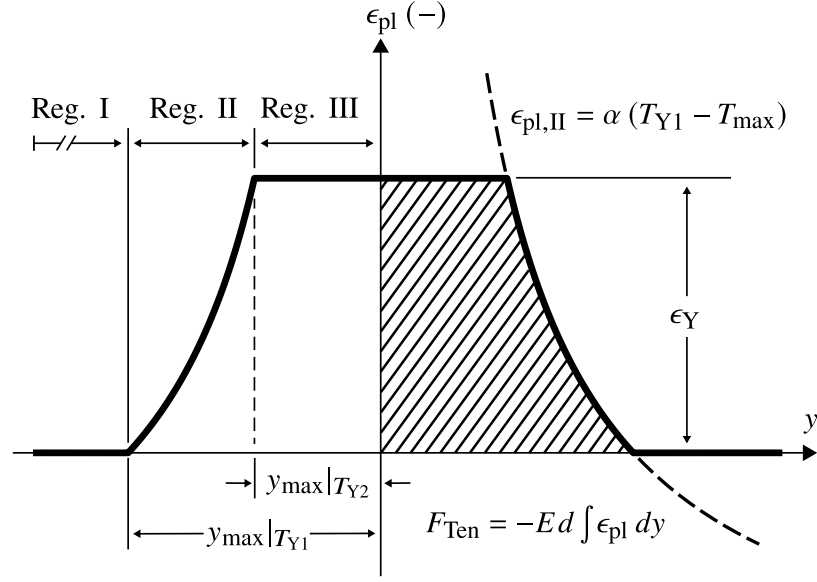


Figure 3.4: Distribution of residual plastic strain.

#### Region I

If the maximum temperature is less than the first yield temperature ( $T_{\max} < T_{Y1}$ ) plastic strain will not be produced in the material. The plastic strain in Region I is therefore simply:

$$\epsilon_{pl,I} = 0 \quad (3.12)$$

#### Region II

For maximum temperatures between the first and second yield temperatures ( $T_{Y1} < T_{\max} < T_{Y2}$ ), plastic strain will be produced during heating only. The residual plastic strain when the thermal cycle is complete will be proportional to the difference be-

tween the thermal strain associated with the maximum temperature and the thermal strain associated with the first yield temperature. The plastic strain in Region II may be expressed as:

$$\epsilon_{\text{pl,II}} = \epsilon_{\text{th}}|_{T_{Y1}} - \epsilon_{\text{th}}|_{T_{\text{max}}} = \alpha (T_{Y1} - T_{\text{max}}) \quad (3.13)$$

### Region III

In the region where the maximum temperature is greater than the second yield temperature ( $T_{\text{max}} > T_{Y2}$ ), plastic strain will be produced during both heating and cooling. The compressive (negative) plastic strain developed during heating, in excess of the second yield temperature, is balanced by a tensile (positive) plastic strain produced during cooling. The net residual plastic strain is therefore the same as the residual plastic strain for a thermal cycle with a maximum temperature equal to the second yield temperature, which is by definition equal to the yield strain. The plastic strain in Region III is therefore uniformly equal to the yield strain:

$$\epsilon_{\text{pl,III}} = \epsilon_{\text{th}}|_{T_{Y1}} - \epsilon_{\text{th}}|_{T_{Y2}} = \alpha (T_{Y1} - T_{Y2}) = -\epsilon_Y \quad (3.14)$$

#### 3.4.4 Tendon Force with Constant Properties

The integral of the plastic strain distribution gives the tendon force according to Equation (3.7). To evaluate this integral, it is necessary to relate the maximum temperature to the distance from the heat source trajectory. The isotherm half-width ( $y_{\text{max}}$ ) of a given temperature ( $T_{\text{max}}$ ) for a fast moving heat source in a thin plate, with negligible heat losses, is given by [33]:

$$y_{\text{max}}|_T = \frac{1}{\sqrt{2\pi e}} \frac{Q'}{d \rho c} \frac{1}{\Delta T_{\text{max}}} \quad (3.15)$$

where  $Q'$  is the linear energy input (typically referred to as the heat input) and  $\rho c$  is the volumetric specific heat capacity.

Equation (3.15) assumes a symmetric temperature field. For the case of edge heating (such as in additive manufacturing) an effective heat input of  $Q'_{\text{eff}} = 2Q'$  should be used [34]. The integral covers only one side of the distribution shown in Figure 3.4 so the tendon force value is unchanged.

For constant material properties, the yield temperature ratio  $\Delta T_{Y2}/\Delta T_{Y1} = 2$  and the tendon force is given by:

$$\widehat{F}_{\text{Ten}} = \sqrt{\frac{2}{\pi e}} \ln(2) \frac{E\alpha}{\rho c} Q' \approx 0.335 \frac{E\alpha}{\rho c} Q' \quad (3.16)$$

where the  $\widehat{\phantom{x}}$  indicates this is an asymptotic expression for the case in which the variation of material properties with temperature is negligible. Equation (3.16) is equivalent to the tendon force proposed in Ref. [43]. This fundamental, but simple, expression captures the key dependencies between material properties, heat source parameters, and the tendon force.

As a result of the proportionality between the tendon force and the heat input, in welding literature the tendon force is often expressed as a dimensionless parameter:

$$H = \frac{\widehat{F}_{\text{Ten}}}{Q'} = \sqrt{\frac{2}{\pi e}} \ln(2) \frac{E\alpha}{\rho c} \quad (3.17)$$

where the group  $E\alpha/(\rho c)$  is a combination of thermal and elastic material properties. Relating these properties is a common issue in geophysics [68]; researchers in this field use a very similar dimensionless group, the Grüneisen ratio [69]:

$$\gamma = \frac{K\beta}{\rho c} \quad (3.18)$$

where  $K = E/[3(1 - 2\nu)]$  is the material bulk modulus and  $\beta \approx 3\alpha$  is the volumetric coefficient of thermal expansion.

In metals, the Grüneisen ratio can be expressed in terms of Poisson’s ratio: [70]

$$\gamma = \frac{3}{2} \frac{1 + \nu}{2 - 3\nu} \quad (3.19)$$

Combining Equation (3.18) and Equation (3.19) gives:

$$\frac{E\alpha}{\rho c} = \frac{3(1 + \nu)(1 - 2\nu)}{2(2 - 3\nu)} \quad (3.20)$$

Poisson’s ratio ( $\nu$ ) for metals is provided in Ref. [48], and ranges between 0.25 and 0.35; thus, the corresponding range for  $E\alpha/(\rho c)$  is 0.64–0.75 and for  $H$  is 0.21–0.25. In practice, material property variation with temperature and other secondary phenomena may be expected to result in a slightly larger range for  $H$  than this prediction; however, this relation provides insight into the relatively narrower scatter in experimental values for  $H$  across materials, despite the large variation in the values of individual properties.

## 3.5 Computational Simulations

To validate the proposed expression for tendon force, a series of numerical simulations were performed using the computational weld mechanics software package Simufact Welding [71]. The validation in this study was performed using numerical methods due to the lack of literature data related to tendon force measurement in sufficiently large plates to neglect secondary compliance effects.

### 3.5.1 Numerical Model

The numerical simulation software implements the proprietary finite element analysis (FEA) tool sfMarc. Transient, thermal-mechanically coupled studies were performed with the nonlinear, temperature dependent material models available in the Simufact Materials database.

The thermal solutions consider a heat source with constant power moving along the weld axis at a constant travel speed. Thermal strains corresponding to the instantaneous temperature field from the thermal solution are treated as loads in the subsequent mechanical solutions.

The resultant stresses and distortion at each time increment are computed from the force-displacement relations. The stiffness matrix is obtained from the combination of the strain-displacement relations and nonlinear stress-strain relations based on tabulated values for the material flow stress. A direct sparse solver implementing the full Newton-Raphson technique is used to obtain the matrix solution.

All studies utilized the component geometry and mesh shown in Figure 3.5. The mesh consists of 8-node isoparametric brick elements with a minimum size of 2.5 mm at the weld axis, increasing to a maximum size of 40 mm at the plate edge. A single layer of elements in the thickness dimension is sufficient to capture the 2-D behaviour of the thin plate geometry.

The boundary conditions used for all studies include: (1) a  $y$  symmetry plane coincident with the heat source trajectory, (2) fixed  $x$  displacement for a single node on the bottom surface of the plate in one corner, and (3) fixed  $z$  displacement for all nodes on the bottom surface of the plate. The symmetry plane fixes displacement of the adjacent nodes in the normal ( $y$ ) direction but allows free movement of the nodes in the ( $xz$ ) plane. The cooling time for each study was selected such that the temperature deviation across section A-A in the final state was  $<1$  °C.

The depth of the heat source was set equal to the thickness of the plate to produce a 2-D temperature field representative of a full penetration, single pass butt weld. Under typical conditions, the fusion zone composes only a subset of the plastic zone and computational efficiencies are possible by using a simple cylindrical heat source. To prevent instabilities associated with the heat source jumping between subsequent node, the radius was chosen to be twice the minimum mesh size (i.e., 5 mm).

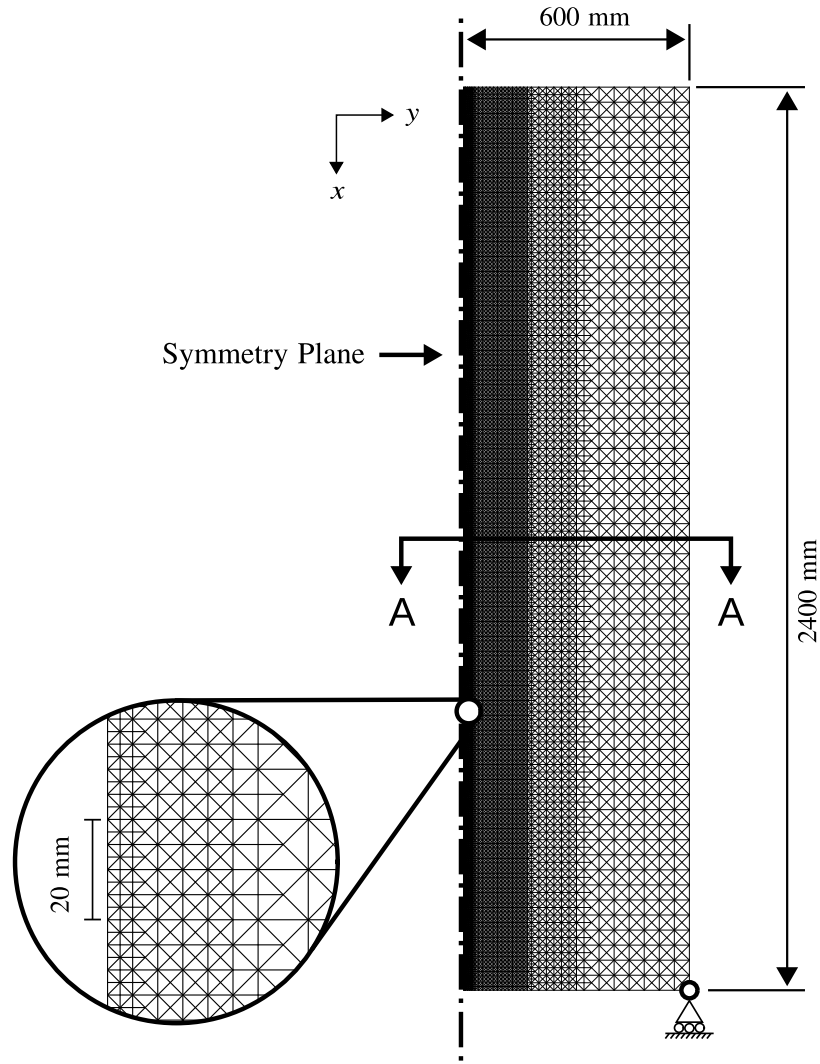


Figure 3.5: Top view of mesh used in numerical simulations.

### 3.5.2 Results from Computational Simulations

Figure 3.6 illustrates the procedure used to compute the tendon force from the residual stress distribution for an example case of 6082-T6 aluminum alloy ( $Q' = 0.36$  kJ/mm). The integral of  $\sigma_{\text{res}} - \sigma_{\text{rxn}}$  was evaluated in MATLAB using trapezoidal numerical integration with the `trapz` function [72] within the plastic region ( $|\epsilon_{\text{pl}}| > 1 \times 10^{-6}$ ).

The residual stress distribution parallel to the weld axis ( $\sigma_{\text{res}} = E\epsilon_{\text{res}}$ ) was measured at the nodes on the top surface of the plate adjacent to the mid section A-A. The tendon force is equal to the integral of the difference between the residual stress and

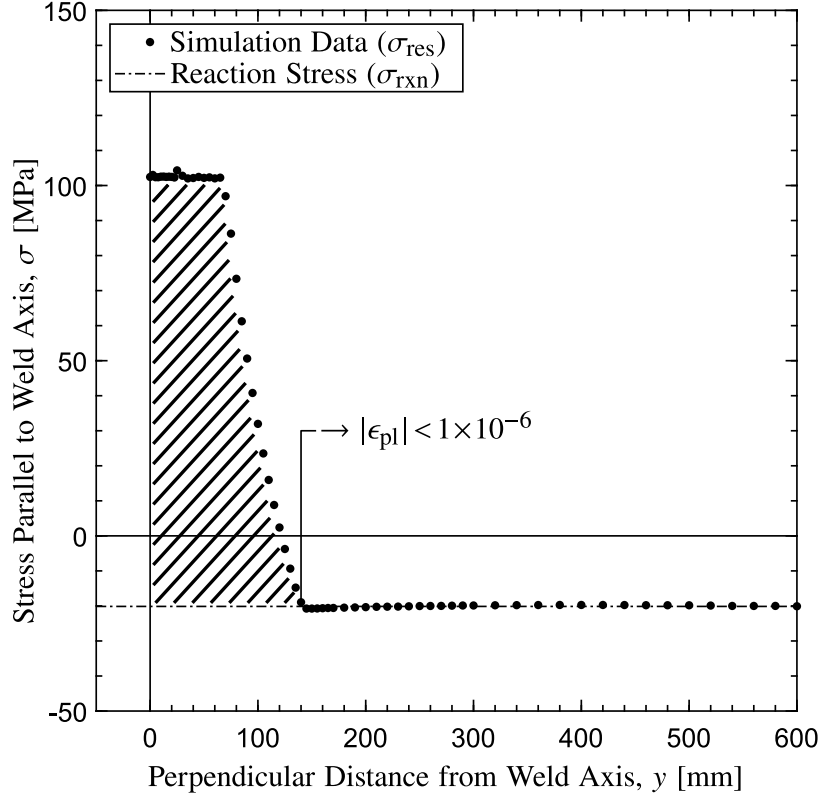


Figure 3.6: Method for estimating tendon force from simulation results for 6082-T6 aluminum alloy with heat input of 0.36 kJ/mm.

the compressive reaction stress ( $\sigma_{rxn} = E\epsilon_{rxn}$ ). The reaction stress was obtained with a linear fit to the residual stress in the region of the plate with negligible plastic strain ( $|\epsilon_{pl}| < 1 \times 10^{-6}$ ). The integral assumes a uniform distribution of reaction stress in the plastic zone, equal to the value at the middle of each half plate ( $y = 300$  mm).

The validation uses five commonly welded structural alloys: ASTM A36 structural steel, aluminum alloy 6082-T6, 304 stainless steel, P91 alloy steel, and titanium alloy TiAl6V4. Simulations were performed for each material with a low ( $Q' = 0.12$  kJ/mm), moderate ( $Q' = 0.24$  kJ/mm), and high ( $Q' = 0.36$  kJ/mm) heat input. Values of the parameter  $H$  were obtained as the linear best-fit to the results at the three heat input levels. Table 3.1 compares the FEA results to Equation (3.17) evaluated at ambient temperature ( $T_0 = 20$  °C).

Although overall the analytical expression provides a good estimate of the com-

Table 3.1: Comparison of asymptotic expression for tendon force (Equation (3.17)) with computational simulation results (FEA).

Material	$H$ (FEA)	$\hat{H}$ Equation (3.17)	$(\hat{H}/H - 1)$
ASTM A36 Structural Steel	0.25	0.24	-5%
P91 Alloy Steel	0.20	0.23	+15%
304 Stainless Steel	0.30	0.27	-11%
Aluminum Alloy 6082-T6	0.21	0.24	+17%
Titanium Alloy TiAl6V4	0.22	0.14	-38%

putational results, the error for most cases exceeds 10% which might be considered a reasonable threshold for incorporating higher order effects. For large geometries, such as the plates used in the computational simulations, material property variation with temperature is expected to be the greatest source of error in Equation (3.17). In the following section, a correction for the effects of temperature dependent material properties is derived.

### 3.6 Temperature Dependent Material Properties

For temperature dependent variation of properties, it is necessary to address both thermal properties which influence the temperature distribution, and mechanical properties which influence the relationship between the temperature distribution and the resulting stress distribution.

The relevant thermal property for determining the relationship between temperature and isotherm width (Equation (3.15)) is the volumetric specific heat capacity ( $\rho c$ ). The relevant mechanical properties for the calculation of tendon force are the yield strain ( $\epsilon_Y$ ) and the CTE ( $\alpha$ ). The elastic modulus ( $E$ ) is present in the tendon force expression but it appears outside the integral of plastic strain so the tendon

force depends only on the value at the final (i.e., ambient) temperature.

### 3.6.1 Temperature Dependent Yield Strain

The plastic strain in Region II ( $T_{Y1} < T_{\max} < T_{Y2}$ ) is determined assuming that the total strain will remain constant between  $T_{Y1}$  and  $T_{\max}$ . For the case of constant properties, the plastic strain difference is proportional to the difference in thermal strain  $\epsilon_{\text{th}}|_{T_{\max}} - \epsilon_{\text{th}}|_{T_{Y1}}$ . For a material in which the yield strain decreases as the temperature increases, it is necessary to also consider the elastic strain difference given by the reduced yield strain capacity  $\epsilon_Y|_{T_{\max}} - \epsilon_Y|_{T_{Y1}}$ . From the definition of the first yield strain (Equation (3.10)),  $\epsilon_Y|_{T_{Y1}} = \epsilon_{\text{th}}|_{T_{Y1}}$ . The residual plastic strain in Region II may thus be written as:

$$\epsilon_{\text{pl,II}} = \epsilon_Y|_{T_{\max}} - \epsilon_{\text{th}}|_{T_{\max}} \quad (3.21)$$

If the yield strain is assumed to be a linear function of temperature, as illustrated in Figure 3.7, the rate of plastic strain development will differ from the rate of thermal strain development by an amount  $d\epsilon_Y/dT$  to account for development of additional plastic strain due to the decreased elastic strain capacity at elevated temperatures. Differentiating Equation (3.21) gives a general expression for the rate of plastic strain development:

$$\frac{d\epsilon_{\text{pl}}}{dT} = \frac{d\epsilon_Y}{dT} - \frac{d\epsilon_{\text{th}}}{dT} = \frac{d\epsilon_Y}{dT} - \alpha|_T \quad (3.22)$$

where  $d\epsilon_Y/dT$  is the rate of change of the yield strain with respect to temperature.

For real materials, this rate of change will not be constant for all temperatures; however, within the limited range of interest ( $T_{Y1} < T_{\max} < T_{Y2}$ ) it is reasonable to

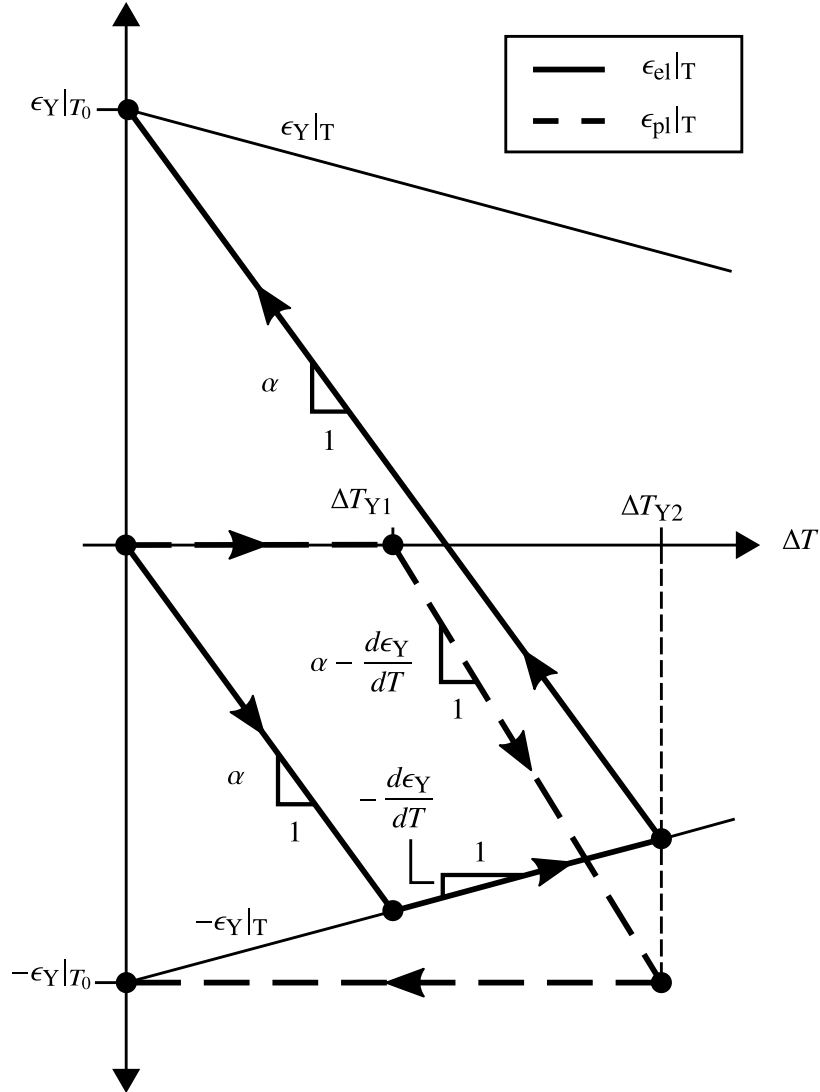


Figure 3.7: Elastic and plastic strain development in material with temperature dependent yield strain for thermal cycle with  $T_{\max} = T_{Y2}$ .

use an average value given by:

$$\frac{d\epsilon_Y}{dT} = \frac{\epsilon_Y|_{T_{Y2}} - \epsilon_Y|_{T_{Y1}}}{T_{Y2} - T_{Y1}} \quad (3.23)$$

### 3.6.2 Temperature Dependent Thermal Expansion

A temperature dependent CTE results in a rate of plastic strain development which varies as a function temperature. For many materials, the property values at the first

and second yield temperatures are sufficiently close that the rate of change between  $T_{Y1}$  and  $T_{Y2}$  may be approximated as linear.

Effective values for temperature dependent properties can be estimated at an intermediate temperature calculated as follows:

$$T_{\text{lm}} - T_0 = \Delta T_{\text{lm}} = \frac{T_{Y2} - T_{Y1}}{\ln(\Delta T_{Y2}/\Delta T_{Y1})} \quad (3.24)$$

where  $\Delta T_{\text{lm}}$  is the log-mean temperature change of the first and second yield temperatures.

A complete derivation of the effective CTE and justification for the selection of the log-mean temperature change is provided in Section 3.11.

To match the form of the constant properties expression for tendon force, the combined effect of variation in the yield strain and CTE is captured by the effective CTE defined as:

$$\alpha_{\text{eff}} = - \left. \frac{d\epsilon_{\text{pl}}}{dT} \right|_{T_{\text{lm}}} = \alpha|_{T_{\text{lm}}} - \frac{d\epsilon_Y}{dT} \quad (3.25)$$

### 3.6.3 Temperature Dependent Heat Capacity

The estimation of maximum temperature (Equation (3.15)) is based on the 2-D Rosenthal model [40] which assumes constant thermal properties ( $\rho c$ ). In this work, a representative constant value of  $\rho c$  is chosen at the log-mean yield temperature:

$$(\rho c)_{\text{eff}} = (\rho c)|_{T_{\text{lm}}} \quad (3.26)$$

For most materials, the temperature range of interest for the yield temperatures is sufficiently low that the latent heat associated with phase transformations does not influence the values obtained.

For high strength materials, the yield temperatures can be high enough such that

phase transformations might play a role. In such cases, an improved estimate of  $(\rho c)_{\text{eff}}$  may be obtained from the mean rate of change in enthalpy as is presented in Ref. [33]. The effective volumetric specific heat for a critical temperature change of  $\Delta T = \Delta T_{\text{lm}}$  is therefore given by:

$$(\rho c)_{\text{eff}} = \frac{1}{\Delta T_{\text{lm}}} \int_{T_{\text{lm}}} (\rho c) dT \quad (3.27)$$

### 3.6.4 Nonlinear Rate of Change for the Yield Strain

In addition to the individual effects of each property, there will also be a combined effect on the yield temperatures. The tendon force equation depends on the yield temperature ratio, and therefore these changes must also be considered.

The first yield temperature change is implicitly defined by the point where the thermal strain is equal to the instantaneous yield strain ( $\epsilon_Y|_{T_{Y1}}$ ):

$$\bar{\alpha}|_{T_{Y1}}(T_{Y1} - T_{\text{ref}}) - \bar{\alpha}|_{T_0}(T_0 - T_{\text{ref}}) = \epsilon_Y|_{T_{Y1}} \quad (3.28)$$

The first yield temperature is therefore written in general as:

$$T_{Y1} - T_0 = \Delta T_{Y1} = \frac{\epsilon_Y|_{T_{Y1}}}{\bar{\alpha}|_{T_{Y1}} + (d\bar{\alpha}/dT)(T_0 - T_{\text{ref}})} \quad (3.29)$$

The second yield temperature change is implicitly defined by the point where the thermal strain is equal to the sum of the instantaneous yield strain ( $\epsilon_Y|_{T_{Y2}}$ ) and the nominal yield strain ( $\epsilon_Y|_{T_0}$ )

$$\bar{\alpha}|_{T_{Y2}}(T_{Y2} - T_{\text{ref}}) - \bar{\alpha}|_{T_0}(T_0 - T_{\text{ref}}) = \epsilon_Y|_{T_{Y2}} + \epsilon_Y|_{T_0} \quad (3.30)$$

A general expression for the second yield temperature is thus:

$$T_{Y2} - T_0 = \Delta T_{Y2} = \frac{\epsilon_Y|_{T_{Y2}} + \epsilon_Y|_{T_0}}{\bar{\alpha}|_{T_{Y2}} + (d\bar{\alpha}/dT)(T_0 - T_{\text{ref}})} \quad (3.31)$$

If the reference temperature ( $T_{\text{ref}}$ ) and the starting/ambient temperature ( $T_0$ ) are equivalent, the second term in the denominators of Equation (3.29) and Equation (3.31) may be neglected.

The yield temperature ratio is given by the ratio of Equation (3.29) and Equation (3.31) as:

$$\frac{\Delta T_{Y2}}{\Delta T_{Y1}} = \frac{\epsilon_Y|_{T_{Y2}} + \epsilon_Y|_{T_0}}{\epsilon_Y|_{T_{Y1}}} \frac{\bar{\alpha}|_{T_{Y1}}}{\bar{\alpha}|_{T_{Y2}}} \quad (3.32)$$

For most materials, the rate of change for CTE is small and the ratio  $\bar{\alpha}|_{T_{Y1}}/\bar{\alpha}|_{T_{Y2}}$  will be close to 1. The deviation of the temperature ratio from the ideal value of 2 can then be approximated as:

$$\frac{\Delta T_{Y2}}{\Delta T_{Y1}} - 2 = \frac{\epsilon_Y|_{T_{Y2}} - \epsilon_Y|_{T_{Y1}}}{\epsilon_Y|_{T_{Y1}}} + \frac{\epsilon_Y|_{T_0} - \epsilon_Y|_{T_{Y1}}}{\epsilon_Y|_{T_{Y1}}} \quad (3.33)$$

If the yield strain has a linear temperature dependence, the terms on the right hand side of this expression will cancel and the yield temperature ratio will equal the constant property value of 2. For real materials, the linear temperature dependence of yield strain is only an approximation, and the mean value obtained from Equation (3.23) should not be applied at  $T < T_{Y1}$ .

Consideration of a distinct rate of change of yield strain for temperatures below  $T_{Y1}$  results in an overall nonlinear temperature dependence between  $T_0$  and  $T_{Y2}$  and adds an additional degree of freedom. The yield temperature ratio obtained from Equation (3.32) may be considered as an independent dimensionless group associated with the nonlinear rate of change for the yield strain.

### 3.6.5 Tendon Force with Variable Properties

A general form of the normalized tendon force in terms of the effective properties and yield temperature ratio is obtained as:

$$H \approx \widehat{H}^+ = \sqrt{\frac{2}{\pi e}} \ln \left( \frac{\Delta T_{Y2}}{\Delta T_{Y1}} \right) \frac{E \alpha_{\text{eff}}}{(\rho c)_{\text{eff}}} \quad (3.34)$$

where  $\Delta T_{Y1}$  and  $\Delta T_{Y2}$  are the yield temperature changes given in Equation (3.29) and Equation (3.31),  $\alpha_{\text{eff}}$  is the effective CTE from Equation (3.25) and  $(\rho c)_{\text{eff}}$  is the effective volumetric specific heat given by Equation (3.26) or Equation (3.27).

The  $^+$  symbol indicates that the asymptotic expression involves correction factors for additional phenomena. These correction factors are defined explicitly in the following section.

### 3.6.6 Correction Factors for Variable Properties

The effective CTE may also be expressed in the form of a correction factor ( $f_1 = \alpha_{\text{eff}}/\alpha$ ) given by:

$$f_1(N_\alpha, N_\epsilon) = 1 - N_\alpha - N_\epsilon \quad (3.35)$$

$$N_\alpha = \frac{\alpha|_{T_0} - \alpha|_{T_{\text{im}}}}{\alpha|_{T_0}} \quad (3.36)$$

$$N_\epsilon = \frac{d\epsilon_Y}{dT} \frac{1}{\alpha|_{T_0}} \quad (3.37)$$

where  $N_\alpha$  and  $N_\epsilon$  are dimensionless variables which capture the temperature dependence of CTE and yield strain. These two additional degrees of freedom in the problem correspond to the two new physical phenomena considered: variation of yield strain and variation of CTE with temperature.

This factor multiplies the asymptotic tendon force expressions with constant CTE

and yield strain (Equation (3.17)) to account for the temperature dependence. For small values of  $N_\alpha$  and  $N_\epsilon$ , the factor approaches 1 and the asymptotic expression may be used without correction.

Temperature dependent material properties for a selection of common structural alloys were obtained from the MSC Simufact Material database, and corresponding values of the correction factor are shown in Table 3.2.

Table 3.2: Typical values for the correction factor associated with temperature dependent yield strain and CTE.

Material	$\alpha _{T_0}$	$\alpha _{T_{lm}}$	$d\epsilon_Y/dT$	$f_1$
	[ $10^{-6}$ K $^{-1}$ ]			
ASTM A36	12.5	12.9	-1.2	1.13
P91	10.7	11.8	0.2	1.08
SS 304	16.3	17.4	-1.6	1.17
Al 6082-T6	22.7	24.4	0.0	1.07
TiAl6V4	8.8	11.8	-14.2	2.95

The effective thermal properties can similarly be expressed in the form of a correction factor ( $f_2 = \rho c / (\rho c)_{\text{eff}}$ ) given by:

$$f_2(N_{\rho c}) = \frac{1}{1 - N_{\rho c}} \quad (3.38)$$

$$N_{\rho c} = \frac{(\rho c)|_{T_0} - (\rho c)|_{T_{lm}}}{(\rho c)|_{T_0}} \quad (3.39)$$

where  $N_{\rho c}$  is a dimensionless variables which captures the temperature dependence of the heat capacity.

Typical values of the effective heat capacity and correction factor for various structural alloys are shown in Table 3.3. For titanium alloy TiAl6V4 the alternative

definition of the effective property (Equation (3.27)) is substituted for  $(\rho c)|_{T_{\text{im}}}$  in Equation (3.39).

Table 3.3: Typical values for the correction factor associated with the effective heat capacity.

Material	$(\rho c) _{T_0}$	$(\rho c)_{\text{eff}}$	$f_2$
	[ $10^6 \text{ J m}^{-3} \text{ K}^{-1}$ ]		
ASTM A36	3.50	3.85	0.91
P91	3.45	4.14	0.83
SS 304	4.10	4.23	0.97
Al 6082-T6	2.40	2.49	0.96
TiAl6V4	2.42	2.90	0.83

The effect of correction factors  $f_1$  and  $f_2$  are in all cases opposite, and in most cases, of similar magnitude. Recall that the dimensionless group  $E\alpha/(\rho c)$  can be related to Poisson's ratio ( $\nu$ ). If the temperature dependence of the elastic parameters  $E$  and  $\nu$  are relatively small, then the effect of temperature on  $\alpha$  and  $\rho c$  should be expected to mostly cancel.

The effect of nonlinearity in the dependence of the yield strain with temperature is expressed in the form of a correction factor ( $f_3$ ) given by:

$$f_3(N_T) = \frac{\ln(N_T)}{\ln(2)} \quad (3.40)$$

$$N_T = \frac{\Delta T_{Y2}}{\Delta T_{Y1}} \quad (3.41)$$

where the dimensionless temperature ratio  $N_T$  captures the additional degree of freedom provided by consideration of a nonlinear rate of change for the yield strain.

Calculated values for the yield temperatures, yield temperature ratio, and corre-

sponding correction factor for selected materials are shown in Table 3.4.

Table 3.4: Typical values of the yield temperatures, yield temperature ratio, and nonlinear yield strain correction factor assuming a starting/ambient temperature of  $T_0 = 20^\circ\text{C}$ .

Material	$T_{Y1}$ [ $^\circ\text{C}$ ]	$T_{Y2}$ [ $^\circ\text{C}$ ]	$\Delta T_{Y2}/\Delta T_{Y1}$	$f_3$
ASTM A36	101	190	2.10	1.07
P91	217	417	2.01	1.01
SS 304	84	151	2.05	1.04
Al-6082	80	139	1.97	0.98
TiAl6V4	663	1060	1.62	0.70

The normalized tendon force given in Equation (3.34) can thus be expressed in the form of correction factors on the asymptotic expression of Equation (3.17)

$$\hat{H}^+ = \sqrt{\frac{2}{\pi e}} \ln(2) \left. \frac{E\alpha}{(\rho c)} \right|_{T_0} f_1(N_\alpha, N_\epsilon) f_2(N_{\rho c}) f_3(N_T) \quad (3.42)$$

where  $f_1$ ,  $f_2$ , and  $f_3$  are the correction factors given by Equation (3.35), Equation (3.38), and Equation (3.40).

### 3.6.7 Numerical Validation

Figure 3.8 compares the computational simulation data to the constant properties tendon force expression (Equation (3.17)) and the corrected expression (Equation (3.42)). The constant properties expression produces a maximum difference of 38% (TiAl6V4) and a mean difference of 17% compared to the FEA results for the normalized tendon force parameter. The corrected expression reduces this difference to a maximum value of 17% (Al 6082-T6) and a mean value of only 7%.

The correction factors for temperature dependence are observed to produce a consistent trend of a slight overestimate of the tendon force compared to the simulation

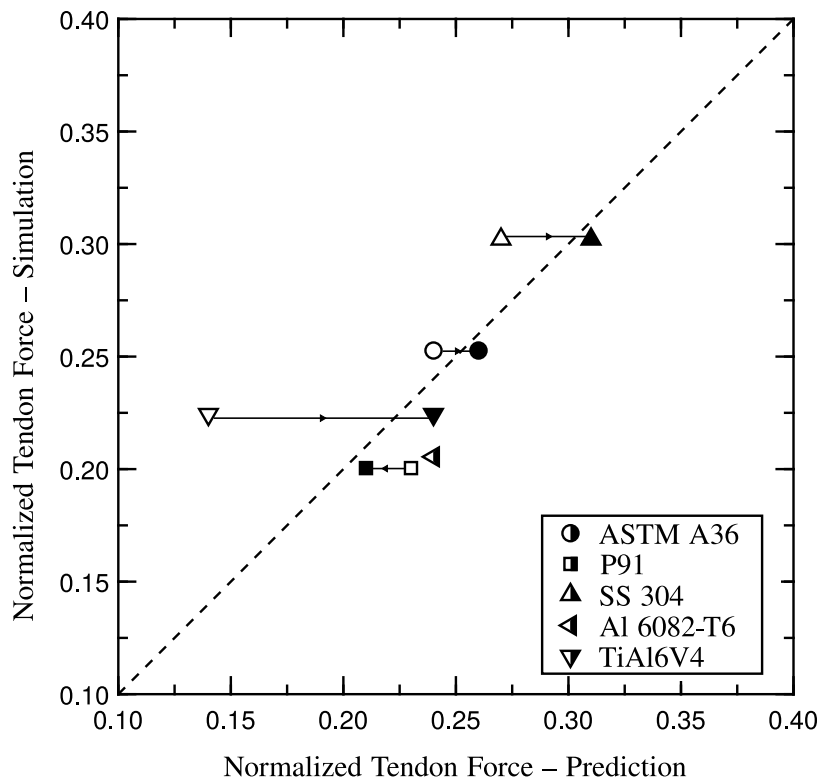


Figure 3.8: Validation of the tendon force for constant material properties (Equation (3.17), open markers) and for temperature dependent properties (Equation (3.42), filled markers).

results. The error is most significant for aluminum alloy 6082-T6, where the cumulative effect of all temperature dependent correction factors is found to be negligible.

The systematic error may be attributed to compliance of the large but still finite plates used in the computational simulations. Aluminum alloy 6082-T6 has the lowest yield strength of the materials considered in the validation and would be expected to be most affected by compliance. Additional corrections for the influence of compliance on the yield temperatures and tendon force will be discussed in a separate publication.

### 3.7 Example of Application

The tendon force model provides a simple and powerful tool for estimating the effects of thermal processing of materials in problems of structural design. By decoupling the transient and temperature dependent phenomena of heating and cooling from

the reaction in the larger geometry, the tendon force model enables the use of simple static mechanics equations to estimate distortion.

An example of a hollow structural member with a uniform cross-section is shown in Figure 3.9. The cross-sectional area is  $A_c = 1.44 \times 10^3 \text{ mm}^2$ . The second moment of inertia about the neutral axis is  $I_{yy} = 3.55 \times 10^6 \text{ mm}^4$ . One common method to fabricate this shape is by bending a flat piece of material into the desired form and welding the resulting seam. This procedure will result in a bowing distortion of the final member. The tendon force concept can be utilized to develop a design equation that relates this bowing distortion to the material properties and welding procedure.

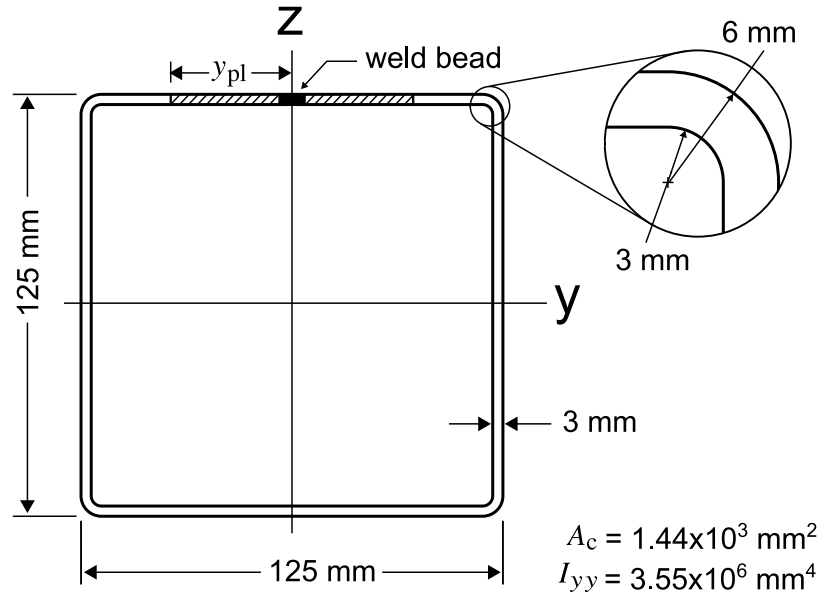


Figure 3.9: Cross-sectional properties of hollow structural section.

The tendon force acts as an eccentric load at the mid-thickness of the top plate. The maximum deflection ( $\delta$ ) at mid-span of an eccentrically loaded member with a uniform cross-section is given from classic beam theory [73]:

$$\delta = \frac{F_{\text{Ten}} L^2 z_c}{8EI_{yy}} \quad (3.43)$$

where  $L$  is the length of the member and  $z_c$  is the weld eccentricity given by the

distance between the neutral ( $y$ ) axis and the mid-thickness of the top plate. The geometry shown in Figure 3.9 gives  $z_c = (125 \text{ mm} - 3 \text{ mm})/2 = 61 \text{ mm}$ .

Consider the design of a welding procedure with the goal to produce a vertical distortion of  $\delta \leq 1 \text{ mm}$  in a member with a length of 1000 mm. Substituting into Equation (3.43), this condition is found to be equivalent to a requirement that  $F_{\text{Ten}}/E \leq 0.466 \text{ mm}^2$ . Using the general expression for the tendon force, with correction factors for temperature dependent material properties, the maximum allowable heat inputs to achieve this tolerance for various structural materials are shown in Table 3.5.

Table 3.5: Maximum allowable heat input (resulting in 1 mm deflection of a 1 m member) for selected alloys.

Material	$\hat{H}^+ \approx F_{\text{Ten}}/Q'$ Equation (3.42)	$E _{20^\circ\text{C}}$ [GPa]	Max. $Q'$ [kJ/mm]
ASTM A36	0.26	200	0.36
P91	0.21	218	0.48
SS 304	0.31	200	0.30
Al 6082-T6	0.24	75	0.15
TiAl6V4	0.24	116	0.23

In addition to reaction stress associated with the bending distortion, the tensile tendon force will also produce an axial reaction compressive stress with associated longitudinal shrinkage of the member. The uniform shrinkage will not produce any additional lateral deflection of the beam but will influence the compressive load carrying capacity of the member, as shown in Ref. [26].

The tendon force model reduces an otherwise complex design problem to a simple calculation in which the behaviour of various materials may be easily compared. The suitable welding heat input will not be the same for each of the materials considered

above but is confined to a relatively narrow operating regime for a given material and process. For example, assuming a heat transfer efficiency of approximately  $\eta = 0.8$  the recommended heat input for gas metal arc welding (GMAW) on 1/8 in. (3.2 mm) A36 structural steel is  $\approx 0.3$  kJ/mm [45]. The suggested heat input for the GMAW process on TiAl6V4 titanium alloy of similar thickness is  $\approx 0.5$  kJ/mm [74]. The specified maximum distortion of 1 mm is therefore likely achievable with GMAW on A36 structural steel, but a lower heat input process than GMAW will be necessary to achieve the desired results for TiAl6V4 titanium alloy.

The results given in Table 3.5 may be validated by comparison to existing guidance for structural steel welding. Ref. [60] provides the following general expression for distortion of a welded longitudinal member:

$$\delta = 0.005 \frac{A_w L^2 z_c}{I_{yy}} \quad (3.44)$$

where  $A_w$  is the total cross-sectional area within the weld fusion line. Equation (3.44) has the same form as Equation (3.43); however, the fusion area is used as a measure of the tendon force rather than the heat input. Comparing these two equations gives a reasonable equivalence of  $Q'/A_w \approx 30$  J/mm<sup>3</sup>.

Although this example considers a relatively simple geometry compared to what might be encountered in industrial practice, the approach presented here may be readily applied to more complex geometries. For larger structures, analytical solutions to the static behaviour may not be available and the tendon force may be applied as an external load in a static structural analysis with finite element software. The tendon force model enables the use of fast and computationally efficient linear FEA to predict the results of highly nonlinear thermal processing.

## 3.8 Discussion

The utility of the expressions for the tendon force presented in Equation (3.17) and Equation (3.42) are not strictly limited to applications which satisfy all of the assumptions utilized in this work. Many additional phenomena may be accounted for simply by incorporation of additional correction factors. Unpacking the tendon force into this modular approach with clear dependencies and limits of validity provides a powerful basis for estimation of the effect of phase transformations, compliance, external stresses, surface heat losses, and other secondary considerations.

The MRCF approach is used to provide a simple model of the problem with the flexibility to address complex phenomena, but only when necessary. For a large flat plate geometry, it is expected that the largest source of deviation from the simplest constant properties model will be captured through consideration of the correction factors related to temperature dependent material properties. For ASTM A36 structural steel, 304 stainless steel, P91 alloy steel, and TiAl6V4 titanium alloy, these correction factors produce agreement between the analytical estimate and the computational simulation results within the limits of industrial measurement capabilities ( $\pm 10\%$ ).

For 6082-T6 aluminum, the constant properties model overestimates the tendon force compared to the simulation results, and correction for temperature dependent properties does not reduce the error. Due to the lower yield strength, the tendon force in aluminum alloys is expected to show the greatest sensitivity to compliance effects of plate size. Aluminum's relatively high thermal conductivity will also produce a lesser first yield isotherm aspect ratio at a given power level which might also be expected to reduce the plastic zone size and consequently the tendon force [66].

Metallurgical phenomena, such as phase transformations, may result in complex material behaviour at high temperatures. For most materials, the temperature relevant for these phenomena is sufficiently high that it exceeds the second yield tem-

perature and therefore influences only a subset of Region III within the plastic zone. The analysis in this work results in a constant stress distribution in Region III with a residual stress value equal to the yield stress of the material. Consideration of phase transformations is beyond the scope of this work but could be readily addressed through the inclusion of an additional correction factor.

A similar approach could also be used to address the influence of secondary mechanical phenomena such as strain hardening and stress-strain hysteresis (i.e., Bauschinger effect). Strain hardening will tend to increase the yield strain, and therefore the inherent strain of material within Region III. This will typically be opposite to the influence of the structural changes associated with phase transformations (e.g., austenite decomposition in steels) which affects a similar subset of the plastic zone. The exact effect of phase transformations and strain hardening will depend on the specific material composition and microstructure, but it is reasonable to expect that the combination of these two secondary effects will be even less significant than either one alone.

The assumption that the tendon force is concentrated at the heat source trajectory may not be suitable for all geometries. As a general rule, it is a good idea to check the size of the plastic zone before applying this model and correct for distribution effects if necessary. For the application considered above, distribution effects would be relevant if the plastic zone exceeds the width of the section. Another example of a correction for distribution effects is provided for calculation of the local distortion due to circumferential pipeline welds in Ref. [56].

In general, the yield temperature ratio may be used to account for not just temperature dependent properties, but also other nonlinear phenomena. For example, consideration of pre-existing stress states in a material can be used to extend the theory in this work to multiple welds or sequential passes in additive manufacturing. The presence of pre-existing compressive stress/strain may be considered as a nonlinear effect which reduces the apparent yield strain in compression but increases the

apparent yield strain in tension. Although these subtleties are beyond the scope of this work, the fundamental framework derived for the tendon force model provides a critical basis which may be built upon in future work to account for these and other practical considerations.

### 3.9 Conclusions

This work presents a new, practical, and rigorous expression for calculating the tendon force parameter ( $\hat{H}^+$ , Equation (3.42)) with consideration of temperature dependent thermal and mechanical material properties. The proposed expression has the form of an ideal expression multiplied by three correction factors.

- A preliminary treatment considering constant material properties relates the tendon force to the heat input ( $Q'$ ) through a single dimensionless property grouping  $E\alpha/(\rho c)$ . This property grouping is relatively constant for all metals, and determines a universal normalized tendon force parameter for constant material properties of  $\hat{H} \approx 0.23$  for all metals.
- Novel closed-form analytical expressions are presented which provide correction factors derived from analysis of the governing equations, without the need for empirical correlations. The first correction factor ( $f_1$ , Equation (3.35)) captures the temperature dependence of the yield strain and the coefficient of thermal expansion. The second correction factor ( $f_2$ , Equation (3.38)) accounts for variation in the thermal properties, and the third correction factor ( $f_3$ , Equation (3.40)) captures the nonlinear rate of change for the yield strain.
- General expressions are presented for the first yield temperature ( $T_{Y1}$ , Equation (3.29)) and the second yield temperature ( $T_{Y2}$ , Equation (3.31)). The yield temperature ratio ( $N_T$ , Equation (3.41)) has an ideal value of 2 for yield strain that is temperature independent or linearly varying. Pre-existing stress/strain

fields relevant to additive manufacturing may be considered as additional non-linear effects through the yield temperature ratio.

- Computational simulations were performed to validate the proposed expressions for a range of common structural alloys. The normalized values for the tendon force parameter are in close agreement, with a mean difference of 7%. The small remaining systematic error is attributed to compliance effects of the finite substrate geometry. Further correction factors to account for both the mechanical and thermal effects of component geometry are the subject of ongoing work.

### 3.10 Acknowledgements

The authors would like to acknowledge Simufact Engineering, a subsidiary of MSC Software for providing a license of Simufact Welding simulation software for use in this study. Valuable discussions and feedback from Y. Wang and Y. Lu were gratefully received.

### 3.11 Appendix: Effective Properties Calculation

The tendon force is proportional to the integral of the total residual plastic strain over the complete thermal cycle with initial/final temperature ( $T_0$ ) and maximum temperature ( $T_{\max}$ ):

$$F_{\text{TEN}} = -E \int_{A_c} \epsilon_{\text{pl}} dA = -E \int_{A_c} \left[ \int_{T_0}^{T_{\max}} \left( \frac{d\epsilon_{\text{pl}}}{dT} \right) dT \right] dy \quad (3.45)$$

Switching the integration order and recognizing that  $d\epsilon_{\text{pl}}/dT = 0$  for temperatures below  $T_{Y1}$  this can be written equivalently as:

$$F_{\text{TEN}} = -2Ed \int_{T_{Y1}}^{\infty} \left[ \int_0^{y_{\max}} \left( \frac{d\epsilon_{\text{pl}}}{dT} \right) dy \right] dT \quad (3.46)$$

Evaluating the inner integral this expression is reduced to:

$$F_{\text{Ten}} = -Q' E \sqrt{\frac{2}{\pi e}} \int_{T_{Y1}}^{\infty} \left( \frac{d\epsilon_{\text{pl}}}{dT} \frac{1}{\rho c} \frac{1}{\Delta T} \right) dT \quad (3.47)$$

Plastic strain during heating above  $T_{Y2}$  is cancelled during cooling. The infinite integral can therefore be reduced to:

$$F_{\text{Ten}} = -Q' E \sqrt{\frac{2}{\pi e}} \int_{T_{Y1}}^{T_{Y2}} \left( \frac{d\epsilon_{\text{pl}}}{dT} \frac{1}{\rho c} \frac{1}{\Delta T} \right) dT \quad (3.48)$$

It is desirable to define effective properties such that:

$$\frac{\alpha_{\text{eff}}}{(\rho c)_{\text{eff}}} \int_{T_{Y1}}^{T_{Y2}} \left( \frac{1}{\Delta T} \right) dT = - \int_{T_{Y1}}^{T_{Y2}} \left( \frac{d\epsilon_{\text{pl}}}{dT} \frac{1}{\rho c} \frac{1}{\Delta T} \right) dT \quad (3.49)$$

Within the temperature range of interest, the combination of the rate of plastic strain development and heat capacity is approximated as a linear function with parameters  $x_1$  and  $x_0$  such that:

$$- \frac{d\epsilon_{\text{pl}}}{dT} \frac{1}{\rho c} = x_1 \Delta T + x_0 \quad (3.50)$$

Evaluating the these two integrals yields an expression for the effective properties:

$$\frac{\alpha_{\text{eff}}}{(\rho c)_{\text{eff}}} = \frac{x_1(\Delta T_{Y2} - \Delta T_{Y1}) + x_0 \ln(\Delta T_{Y2}/\Delta T_{Y1})}{\ln(\Delta T_{Y2}/\Delta T_{Y1})} \quad (3.51)$$

The above expression results in values for the effective properties which are equivalent to the value at the logarithmic mean temperature ( $T_{\text{lm}}$ ):

$$\frac{\alpha_{\text{eff}}}{(\rho c)_{\text{eff}}} = - \left( \frac{d\epsilon_{\text{pl}}}{dT} \frac{1}{\rho c} \right) \Big|_{T_{\text{lm}}} \quad (3.52)$$

The effective CTE may therefore be written as:

$$\alpha_{\text{eff}} = - \left. \frac{d\epsilon_{\text{pl}}}{dT} \right|_{T_{\text{lm}}} = \alpha|_{T_{\text{lm}}} - \frac{d\epsilon_Y}{dT} \quad (3.53)$$

For materials with a CTE that has only a weak temperature dependence, the difference in the value of the CTE at the arithmetic mean temperature compared to the logarithmic mean temperature will be small. The effective CTE may therefore be approximated as:

$$\alpha_{\text{eff}} \approx \frac{\alpha|_{T_{Y1}} + \alpha|_{T_{Y2}}}{2} - \frac{d\epsilon_Y}{dT} = \frac{\epsilon_Y|_{T_0}}{T_{Y2} - T_{Y1}} \quad (3.54)$$

This approximation may be expected to produce greater error than the expression based on the logarithmic mean temperature; however, in some situations it may be preferable since it depends on only the nominal yield strain and yield temperatures, which may be obtained directly from a Satoh Test.

### 3.12 Appendix: High Temperature Effects

This chapter includes additional numerical simulation results for P91 alloy steel which were not previously incorporated into the paper version of this work. Materials with greater strength at high temperatures, such as P91 alloy steel, tend to display a smaller plastic zone relative to the weld bead and heat affected zone (HAZ) leading to the potential for more significant effects of phase transformations on the overall residual stress distribution. A residual stress level below yield magnitude is expected in the HAZ of P91 steel due to martensitic phase transformations during cooling.

This reduction, although not entirely negligible, is still of only secondary importance for the parameters considered in this study. The region with sufficiently high peak temperatures to produce phase transformations comprises <20% of the total plastic zone, and is therefore expected to contribute <30% of the total tendon force.

Assuming a reduction in the residual stress in this region of up to half of yield magnitude, the total change in the estimate of the tendon force value would not exceed 15%. This difference approaches the limit of what is detectable in industrial practice. The equations presented here might therefore be expected to provide a small, and conservative, overestimate of the true tendon force for P91 and other similar alloys.

## References

- [11] N. S. Boulton and H. E. Lance Martin, “Residual stresses in arc-welded plates,” *Proc. Inst. Mech. Eng.*, vol. 133, no. 1, pp. 295–347, June 1936. DOI: 10.1243/pime\_proc\_1936\_133\_017\_02.
- [12] O. E. Rodgers and J. R. Fetcher, “Determination of internal stress from the temperature history to a butt-welded plate,” *Welding J.*, vol. 17, no. 11, pp. 4s–7s, Nov. 1938.
- [13] A. A. Wells, “The mechanics of notch brittle fracture,” *Weld. Res.*, vol. 7, no. 2, pp. 34r–56r, Feb. 1953.
- [14] L. Tall, “Residual stresses in welded plates - a theoretical study,” *Welding J.*, vol. 43, no. 1, pp. 10s–23s, Jan. 1964.
- [16] Y. Ueda, K. Fukuda, K. Nakacho, and S. Endo, “A new measuring method of residual stresses with the aid of finite element method and reliability of estimated values,” *Trans. JWRI*, vol. 4, no. 2, pp. 123–131, Oct. 1975. DOI: 11094/11113.
- [20] Y. Ueda and M. G. Yuan, “Prediction of residual stresses in butt welded plates using inherent strains,” *ASME J. Eng. Mater. Technol.*, vol. 115, no. 4, pp. 417–423, Oct. 1993. DOI: 10.1115/1.2904240.
- [21] M. G. Yuan and Y. Ueda, “Prediction of residual stresses in welded T- and I-joints using inherent strains,” *ASME J. Eng. Mater. Technol.*, vol. 118, no. 2, pp. 229–234, Apr. 1996. DOI: 10.1115/1.2804892.
- [26] J. B. Dwight and K. E. Moxham, “Welded steel plates in compression,” *Struct. Eng.*, vol. 47, no. 2, pp. 49–66, Feb. 1969.
- [33] Y. Lu, Y. Wang, and P. F. Mendez, “Width of thermal features induced by a 2-D moving heat source,” *Int. J. Heat Mass Transfer*, vol. 156, pp. 119793, Aug. 2020. DOI: 10.1016/j.ijheatmasstransfer.2020.119793.
- [34] Y. Lu and P. F. Mendez, “Characteristic values of the temperature field induced by a moving line heat source,” *Int. J. Heat Mass Transfer*, vol. 166, pp. 120671, Feb. 2021. DOI: 10.1016/j.ijheatmasstransfer.2020.120671.
- [35] K. Satoh, “Transient thermal stresses of weld heat-affected zone by both-ends-fixed bar analogy,” *Trans. JWS*, vol. 3, no. 1, pp. 125–134, Apr. 1972.
- [37] S. Vaidyanathan, A. F. Todaro, and I. Finnie, “Residual stresses due to circumferential welds,” *ASME J. Eng. Mater. Technol.*, vol. 95, no. 4, pp. 233–237, Oct. 1973. DOI: 10.1115/1.3443159.
- [40] D. Rosenthal, “The theory of moving sources of heat and its application to metal treatments,” *Trans. ASME*, vol. 68, no. 11, pp. 849–866, Nov. 1946.
- [43] N. O. Okerblom, *Raschet Deformatsii Metallokonstruktsii pri Svarke [The Calculations of Deformations of Welded Metal Structures]*. Moscow: Mashgiz, 1955 (Transl. by London: HMSO, 1958).

- [44] J. White, “Longitudinal shrinkage of a single pass weld,” *Univ. Cambridge Tech. Rep.*, CUED/C-Struct/TR.57, 1977.
- [45] *The Procedural Handbook of Arc Welding*, 14th. Cleveland, OH: The James F. Lincoln Arc Welding Foundation, 2000.
- [48] G. N. Greaves, A. L. Greer, R. S. Lakes, and T. Rouxel, “Poisson’s ratio and modern materials,” *Nat. Mater.*, vol. 10, no. 11, pp. 823–837, Oct. 2011. DOI: 10.1038/nmat3134.
- [52] P. F. Mendez, K. E. Tello, and T. J. Lienert, “Scaling of coupled heat transfer and plastic deformation around the pin in friction stir welding,” *Acta Mater.*, vol. 58, no. 18, pp. 6012–6026, Oct. 2010. DOI: 10.1016/j.actamat.2010.07.019.
- [55] R. H. Legatt, “Residual stresses at girth welds in pipes,” in *Welding in Energy-Related Projects*, 1984, pp. 429–440.
- [56] M. R. Grams, L. Ludwig, and P. F. Mendez, “A quantitative index to assess the influence of joint fit-up on pipeline weld root discontinuities,” in *Proc. ASME 13th Int. Pipeline Conf.*, Calgary, Canada, Sep. 28-30, 2020, (IPC2020-9706), pp. V003T05A032. DOI: 10.1115/IPC2020-9706.
- [57] D. Camilleri, T. Comlekci, and T. G. F. Gray, “Design support tool for prediction of welding distortion in multiply-stiffened plate structures experimental and computational investigation,” *J. Ship. Prod.*, vol. 21, no. 4, pp. 219–234, Nov. 2005. DOI: 10.5957/jsp.2005.21.4.219.
- [58] C. R. Fisher, L. L. Denault, S. Rhodes, J. Finley, and Y. Gooroochurn, “Computational tool development for weld sequence planning in major assemblies,” *J. Ship. Prod.*, vol. 35, no. 3, pp. 281–288, Aug. 2019. DOI: 10.5957/JSPD.11170054.
- [59] E. R. Denlinger, J. Irwin, and P. Michaleris, “Thermomechanical modeling of additive manufacturing large parts,” *ASME J. of Manuf. Sci. Eng.*, vol. 136, no. 6, pp. 061007, Dec. 2014. DOI: 10.1115/1.4028669.
- [60] O. W. Blodgett, “Joint design and production: Control of shrinkage and distortion,” in *Design of Welded Structures*, Cleveland, OH: The James F. Lincoln Arc Welding Foundation, 1966, ch. 7.7.
- [61] H. Murakawa, D. Deng, N. Ma, and J. Wang, “Applications of inherent strain and interface element to simulation of welding deformation in thin plate structures,” *Comput. Mater. Sci.*, vol. 51, no. 1, pp. 43–52, Jan. 2012. DOI: 10.1016/j.commatsci.2011.06.040.
- [62] P. F. Mendez, Y. Lu, and Y. Wang, “Scaling analysis of a moving point heat source in steady-state on a semi-infinite solid,” *ASME J. Heat Transfer*, vol. 140, no. 8, pp. 081301, Apr. 2018. DOI: 10.1115/1.4039353.
- [63] Y. Wang, Y. Lu, and P. F. Mendez, “Scaling expressions of characteristic values for a moving point heat source in steady state on a semi-infinite solid,” *Int. J. Heat Mass Transfer*, vol. 135, pp. 1118–1129, June 2019. DOI: 10.1016/j.ijheatmasstransfer.2019.02.042.

- [64] A. G. Kamtekar, K. D. White, and J. B. Dwight, “Shrinkage stresses in a thin plate with a central weld,” *J. Strain Anal. Eng. Des.*, vol. 12, no. 2, pp. 140–147, Apr. 1977. DOI: 10.1243/03093247V122140.
- [65] T. Sasayama, K. Masubuchi, and S. Moriguchi, “Longitudinal deformation of long beam due to fillet welding,” *Welding J.*, vol. 34, no. 12, pp. 581s–582s, Dec. 1955.
- [66] M. R. Grams and P. F. Mendez, “Scaling analysis of the thermal stress field produced by a moving point heat source in a thin plate,” *ASME J. Appl. Mech.*, vol. 88, no. 1, pp. 011001, Jan. 2021. DOI: 10.1115/1.4048318.
- [67] A. M. Freudenthal, “Effect of rheological behavior on thermal stresses,” *J. Appl. Phys.*, vol. 25, no. 9, pp. 1110–1117, Sept. 1954. DOI: 10.1063/1.1721824.
- [68] F. D. Stacey and J. H. Hodgkinson, “Thermodynamics with the Grüneisen parameter: Fundamentals and applications to high pressure physics and geophysics,” *Phys. Earth Planet. Inter.*, vol. 286, no. 1, pp. 42–68, Jan. 2019. DOI: 10.1016/j.pepi.2018.10.006.
- [69] E. Grüneisen, “Zustand des festen körpers [the state of a solid body],” in *Handbuch der Physik, Bd. 10*, Berlin: Julius Springer, 1926 (Transl. by NASA, 1959), pp. 1–52.
- [70] V. N. Belomestnykh and E. P. Tesleva, “Interrelation between anharmonicity and lateral strain in quasi-isotropic polycrystalline solids,” *Tech. Phys.*, vol. 49, no. 8, pp. 1098–1100, Aug. 2004. DOI: 10.1134/1.1787679.
- [71] Simufact Engineering GmbH, *Simufact Welding* (ver. 8.0, 2019), Computer Software, Hamburg, Germany. [Online]. Available: [www.simufact.com](http://www.simufact.com).
- [72] The Mathworks, Inc., “Trapezoidal numerical integration (trapz),” in *MATLAB Function Reference(R2020b)*, Natick, MA, 2020, 1–13245–13250. [Online]. Available: [www.mathworks.com/help/pdf\\_doc/matlab/matlab\\_ref.pdf](http://www.mathworks.com/help/pdf_doc/matlab/matlab_ref.pdf).
- [73] S. Timoshenko, “Combined bending and tension,” in *Strength of Materials, Part I: Elementary Theory and Problems*, 2nd, New York: D. Van Nostrand Company, Inc., 1940, ch. 8, pp. 226–260.
- [74] J. J. Vagi, R. E. Monroe, R. M. Evans, and D. C. Martin, “Welding processes: MIG welding,” in *Welding Procedures for Titanium and Titanium Alloys*, NASA, 1965, TM X-53432, pp. 84–102.

# Chapter 4

## Effect of Compliance on Residual Stresses in Manufacturing with Moving Heat Sources

### 4.1 Introduction

The mechanical effects of thermal fabrication processes such as welding, cutting, heat treatment, and additive manufacturing are a fundamental consideration for design with modern engineering materials. An improved understanding of the interaction between residual stresses and geometry is essential to developing mitigation techniques and determining the fitness-for-service of the overall structure.

The effect of residual stresses and strains on a structure depends on the geometry. The uneven distribution of residual stresses produced during fabrication of built-up members has been shown to reduce the compressive load capacity of welded columns [26]; the significance of this behaviour depends on the ratio of the section width and thickness. Similarly, during manufacturing of structural T-/I-sections, eccentric thermal strain and associated residual plastic strain will lead to longitudinal bending distortion of the member [65]. Ref. [60] provides empirical expressions which relate distortion to beam length, weld eccentricity, and section moment of inertia. Even for relatively simple applications, such as welding of flat plates, the threshold for buckling is related to the geometric aspect ratio of the plate [36].

Although the influence of residual stresses on geometry is well addressed in lit-

erature, the influence of geometry on development of residual stresses is more often neglected. This simplification is central to traditional implementation of models based on the concept of inherent strain [16] which rely on measurements or computations of thermal-mechanical behaviour in a reduced geometry.

Despite its convenience, this assumption severely limits the potential for understanding of modern processes, such as additive manufacturing, where it is not reasonable to separate the local development of strain from the overall geometry. In such processes, residual plastic strains will drive deviation in the overall part geometry which must be accounted for to achieve desired final shape and tolerances [75, 76].

Analytical corrections for the influence of geometry on the tendon force and residual plastic strain have been previously studied for edge-welded plates [43, 77], flat plates [20, 44, 50, 78, 79] as well as T-/I-sections [21, 80]. Although similarities exist within these works, there is a lack of a general model applicable to the practical range of geometries and materials, nor are there clear limits of validity for the proposed corrections. Further, the existing work is primarily limited to welding applications on steel, and there is an immediate need for a universal understanding suitable for the wide range of modern materials and processes involving moving heat sources.

A simple and general methodology for application of blending techniques is presented in Refs. [51, 81] based on the theory of blended asymptotics developed by Ref. [82, 83]. This methodology has been previously applied to successfully predict characteristic values of the 3-D temperature field [62, 63] relevant for high temperature isotherms and cladding applications, as well as the 2-D temperature field [33, 34] relevant for lower temperature isotherms and thin sections.

This work, for the first time, applies the techniques of asymptotic blending to the thermal-mechanical theory of residual stress. Novel closed-form correction factors are derived to capture the effect of substrate size and shape on the critical aspects of the residual plastic strain distribution. These simple, accurate, and general expressions provide a powerful and much needed tool for use by engineering practitioners.

## 4.2 List of Symbols

Symbol	SI Unit	Description
<b>Roman Letters</b>		
$A_c$	$\text{m}^2$	Cross-sectional area
$a$	$\text{m}^2 \text{s}^{-1}$	Thermal diffusivity
$d$	$\text{m}$	Section thickness
$E$	$\text{N m}^{-2}$	Elastic modulus
$F$	$\text{N}$	Equivalent load
$F_{\text{th}}$	$\text{N}$	Thermal force
$F_{\text{pl}}$	$\text{N}$	Plastic force
$F_{\text{Ten}}$	$\text{N}$	Tendon force
$f_{Y1}$	1	Correction factor for first yield temperature
$f_{Y2}$	1	Correction factor for second yield temperature
$f_S$	1	Correction factor for higher order compliance effects
$f_{\text{Ten}}$	1	Correction factor for tendon force
$I_{yy}$	$\text{m}^4$	Second moment of inertia with respect to $y$ axis through c. g.
$L$	$\text{m}$	Cylinder axial length
$N_T$	1	Dimensionless yield temperature ratio
$Ok$	1	Dimensionless Okerblom number
$Q'$	$\text{J m}^{-1}$	Linear energy input (i.e., heat input)
$r$	$\text{m}$	Cylinder radius
$S$	$\text{N}^{-1}$	Geometric compliance
$T_{\text{eq}}$	$\text{K}$	Equilibrium temperature
$T_{\text{max}}$	$\text{K}$	Maximum temperature in thermal cycle
$T_Y$	$\text{K}$	Critical temperature associated with plastic zone size
$T_{Y1}$	$\text{K}$	First yield temperature
$T_{Y2}$	$\text{K}$	Second yield temperature
$T_0$	$\text{K}$	Initial/starting temperature
$t_{\text{eq}}$	$\text{s}$	Time for section temperature to reach equilibrium
$t_i$	$\text{s}$	Time for maximum width of isotherm $T(y, t) = T_i$
$w$	$\text{m}$	Plate half-width
$y_{\text{max}}$	$\text{m}$	Maximum isotherm half-width
$y_{\text{pl}}$	$\text{m}$	Residual plastic zone size (i.e., half-width)
$z$	$\text{m}$	Eccentricity of equivalent load with respect to c. g.

Symbol	SI Unit	Description
<b>Greek Letters</b>		
$\alpha$	$K^{-1}$	Linear coefficient of thermal expansion
$\beta$	$m^{-1}$	Cylinder stiffness parameter
$\epsilon_0$	1	Initial/pre-existing strain
$\epsilon_{el}$	1	Elastic strain
$\epsilon_{inh}$	1	Inherent strain
$\epsilon_{pl}$	1	Plastic strain
$\epsilon_{rxn}$	1	Reaction strain
$\epsilon_T$	1	Total strain
$\epsilon_{th}$	1	Thermal strain
$\epsilon_{th,eq}$	1	Thermal strain in final/equilibrium state
$\epsilon_Y$	1	Yield strain
$\rho c$	$J m^{-3} K^{-1}$	Volumetric specific heat capacity
$\sigma_x$	$N m^{-2}$	Normal stress parallel to heat source movement
$\sigma_Y$	$N m^{-2}$	Material yield strength

Symbol	Description
<b>Superscripts</b>	
$\uparrow$	Associated with heating process
$\downarrow$	Associated with cooling process
*	Dimensionless/normalized variable
$\wedge$	Asymptotic behaviour
+	Correction for intermediate values
<b>Subscripts</b>	
b	Property of base material
w	Property of filler material
res	Residual value
I	Asymptotic regime for negligible compliance
II	Asymptotic regime for infinite compliance

## 4.3 Governing Equations

### 4.3.1 Residual Strain Distribution

Ref. [84] derives a general model for the tendon force that separates the elastic residual strain distribution ( $\epsilon_{el}$ ) into a driving/inherent strain component ( $\epsilon_{inh}$ ) and a reaction component ( $\epsilon_{rxn}$ ). The residual strain distributions and corresponding tendon force area for several common geometry are shown in Figure 4.1.

The inherent strain is zero except in the plastic zone near the line of heating ( $y = 0$ ). In the region away from the line of heating, the elastic strain is equal to the reaction strain. In the final state, the thermal strain is assumed to be zero so the elastic strain in the far region is also equal to the total strain ( $\epsilon_T$ ).

In the asymptotic tendon force model for an infinite geometry, the total strain is neglected for the purposes of computing the inherent strain. Correcting the tendon force model for compliance involves consideration of the simultaneous development of total strain and inherent strain. This is accomplished by defining equivalent loads, not just for the residual state, but also at intermediate states during the development of the total and inherent strain.

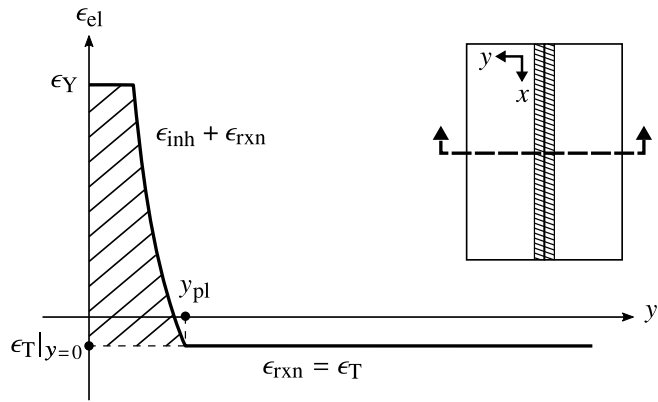
### 4.3.2 Concept of Compliance

The concept of compliance is used to relate the total strain with a load concentrated at the line of heating. The geometric compliance of a structure is defined as:

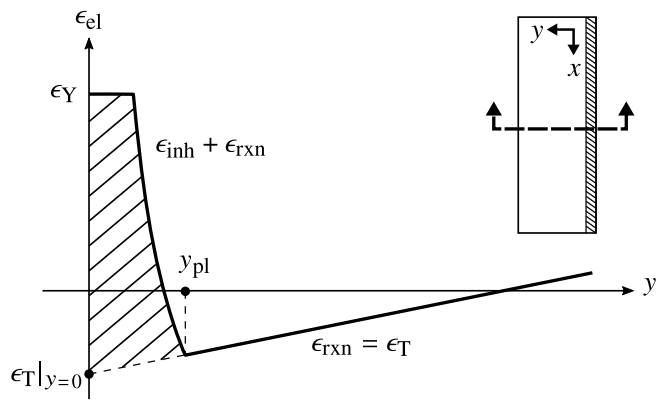
$$S = -\frac{\epsilon_T|_{y=0}}{F} \quad (4.1)$$

where  $F$  is a concentrated load at the line of heating and  $\epsilon_T|_{y=0}$  is the resulting total strain at the location of the load ( $y = 0$ ).

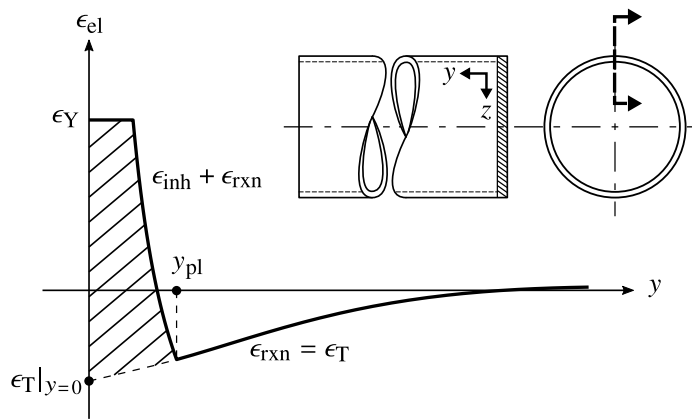
As shown in Figure 4.1, for some geometries the total strain may vary within the plastic zone ( $0 \leq y \leq y_{pl}$ ). In many practical cases, the width of the plastic zone is sufficiently small compared to the overall component geometry, that this variation



(a) centre heating on thin flat plate



(b) edge heating on thin flat plate



(c) edge heating of thin cylinder

Figure 4.1: Residual strain distribution for selected common section geometries.

is negligible and the total strain throughout the plastic zone may be approximated with the total strain at the line of heating ( $\epsilon_T|_{y=0}$ ). The following analysis remains applicable even when this criteria is not satisfied; treatment of these special cases is discussed in Section 4.10.

The normalized compliance ( $S^*$ ) is obtained as the ratio of the compliance of a given section to the compliance of centre heating on a flat plate with equivalent area:

$$S^* = S E A_c \quad (4.2)$$

The compliance of any cross-section may be computed with simple linear FEA. Analytical closed-form solutions may also be obtained for simple geometries. The compliance of a selection of common geometric shapes applicable to additive manufacturing, welding, and for the general case are computed in Section 4.15 and the results are shown in Table 4.1.

Table 4.1: Compliance of typical simple section geometries.

Section Geometry	$S$	$S^* = S E A_c$
Centre Heating of Thin Flat Section	$\frac{1}{E} \frac{1}{wd}$	1
Edge Heating of Thin Flat Section	$\frac{1}{E} \frac{4}{wd}$	4
Edge Heating of Thin Cylinder	$\frac{1}{E} \frac{2\beta}{d}$	$2\beta L$
Longitudinal Heating of General Thin Section	$\frac{1}{E} \left( \frac{1}{A_c} + \frac{z^2}{I_{yy}} \right)$	$1 + \frac{A_c z^2}{I_{yy}}$

### 4.3.3 Equivalent Load

A concentrated “equivalent load” can be thought of as a time-dependent tendon force [84], and is defined as the equivalent load necessary to reproduce, at any time, the effect of thermal and plastic strains in an otherwise unloaded plate for a given point along the path of a moving heat source:

$$F(t) = \int_{A_c} E [\epsilon_{el}(t) - \epsilon_T(t)] dA \quad (4.3)$$

where  $\epsilon_{el}$  is the elastic strain and  $\epsilon_T$  is the total strain distribution. At long times after the application of heating, the equivalent load becomes the tendon force.

The total strain is equal to the sum of its thermal ( $\epsilon_{th}$ ), elastic, and plastic ( $\epsilon_{pl}$ ) strain components:

$$\epsilon_T = \epsilon_{th} + \epsilon_{el} + \epsilon_{pl} \quad (4.4)$$

Combining Equation (4.3) and Equation (4.4) gives:

$$F(t) = F_{th}(t) + F_{pl}(t) \quad (4.5)$$

$$F_{th}(t) = -E \int_{A_c} \epsilon_{th}(t) dA \quad (4.6)$$

$$F_{pl}(t) = -E \int_{A_c} \epsilon_{pl}(t) dA \quad (4.7)$$

where  $F_{th}$  and  $F_{pl}$  are the equivalent thermal and plastic forces.

## 4.4 Thermal Strain

Thermal strain is proportional to the temperature increase from the initial condition:

$$\epsilon_{\text{th}} = \alpha \Delta T = \alpha (T - T_0) \quad (4.8)$$

where  $\alpha$  is the coefficient of thermal expansion and  $T_0$  is the temperature of the component in the broad area before the moving heat source arrives. A constant value is assumed for the coefficient of thermal expansion, but variable properties may be readily considered through the use of effective values as outlined in Ref. [84].

### 4.4.1 Temperature Distribution

The approximation of manufacturing processes as fast moving point heat sources on a 2-D substrate has been previously shown to provide reasonably accurate predictions in the temperature range relevant for thermal stresses and the power typically considered for welding and similar processes ( $10^3 - 10^4$  W) [33, 34, 66]. The temperature distribution at a given time after the application of heating ( $t$ ), across the width ( $y$ ) of a thin section is therefore [40]:

$$T(y, t) - T_0 = \Delta T(y, t) = \Delta T(0, t) \exp\left(\frac{-y^2}{4at}\right) \quad (4.9)$$

$$\Delta T(0, t) = \frac{Q'}{d\rho c} \frac{1}{\sqrt{4\pi at}} \quad (4.10)$$

where  $T_0$  is the initial temperature,  $\Delta T(0, t)$  is the temperature at the line of heating,  $a = k/(\rho c)$  is the thermal diffusivity of the material,  $Q'$  is the energy input to the cross-section per unit length (typically referred to as the heat input),  $d$  is the section thickness, and  $\rho c$  is the volumetric heat capacity of the material.

Each point in a section, normal to the travel direction of the heat source, will experience a distinct thermal cycle with a unique maximum temperature. For the

fast moving heat sources typical of manufacturing, this maximum temperature is given by [34]:

$$\Delta T_{\max}(y) = \frac{1}{\sqrt{2\pi e}} \frac{Q'}{d\rho c} \frac{1}{y} \quad (4.11)$$

#### 4.4.2 Thermal Force

The thermal force  $F_{\text{th}}$  is defined as an equivalent load balancing the elastic effect of the thermal strains induced by the moving heat source:

$$F_{\text{th}} = -E \int_{A_c} \epsilon_{\text{th}} dA \quad (4.12)$$

Equation (4.9) has the form of a normal distribution with constant area which flattens over time and the net thermal strain thus has a constant value of:

$$\int \epsilon_{\text{th}} dA = \alpha \int_{A_c} \Delta T dA = \frac{\alpha Q'}{\rho c} \quad (4.13)$$

which yields the following thermal force that is independent of time:

$$F_{\text{th}} = -\frac{E\alpha}{\rho c} Q' \quad (4.14)$$

### 4.5 Plastic Strain

For the conditions typical of manufacturing with moving heat sources on 2-D substrates (such as additive manufacturing of walls or welding of relatively thin plates), it has been shown that the thermal stress field is equivalent to that of a uniaxial stress test [66], and the conditions of validity of this approximation are established and validated. It is assumed here that the uniaxial state of stress is also applicable during plasticity; this approximation is standard in the analytical treatment of residual stresses and tendon force in welding [43, 44].

In this work, the material will be considered elastic-plastic with no strain hardening and no phase transformations. The theoretical foundation presented here can be extended with small effort to account for those effects, and it is the subject of current ongoing research.

### 4.5.1 Plastic Strain During Heating

Figure 4.2 illustrates the development of strain as temperature changes due to the moving heat source. The thermal cycle starts with zero elastic strain, developing compressive elastic strain as temperature increases. This elastic strain will increase until it reaches the yield strain ( $\epsilon_{el} = -\epsilon_Y$ ), and plasticity starts. In the elastic regime  $\epsilon_{pl} = 0$ , and considering Equation (4.4), the onset of plasticity during heating can be determined when:

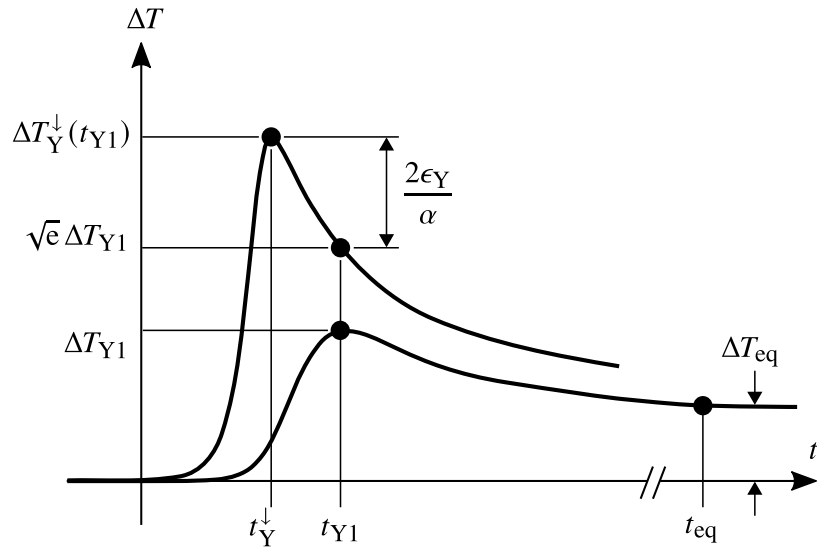
$$\epsilon_{th} = \epsilon_Y + \epsilon_T \quad (4.15)$$

Thermal strain during heating in excess of that in Equation (4.15) results in the development of a heating (indicated as  $\uparrow$ ) plastic strain, which can be expressed in general form as:

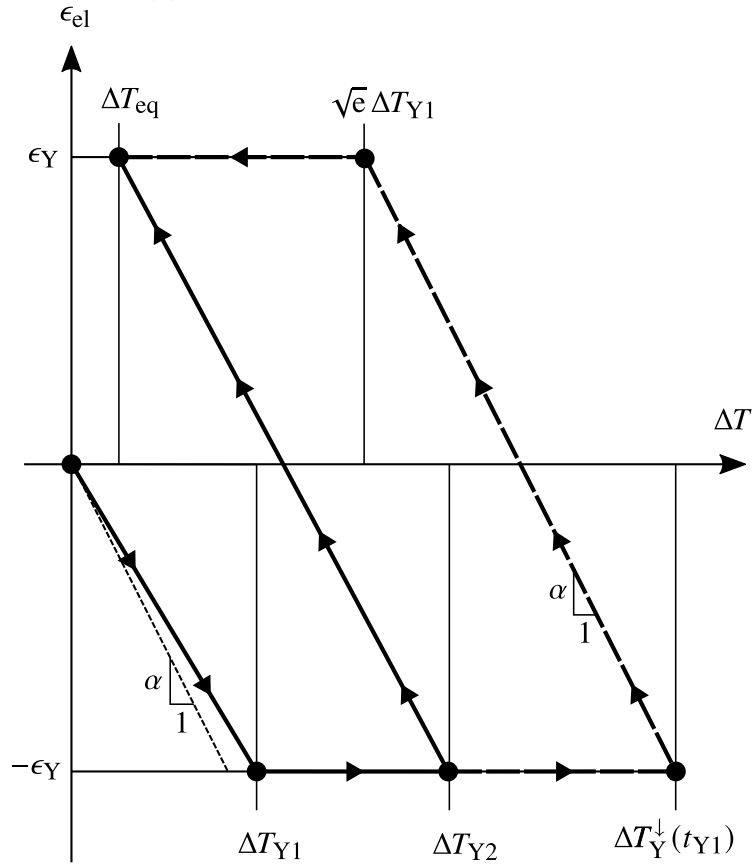
$$\epsilon_{pl}^{\uparrow}(y, t) = -\max\{0, \epsilon_{th}(y, t) - \epsilon_T(t) - \epsilon_Y\} \quad (4.16)$$

The residual plastic strain during heating corresponds to the maximum plastic strain occurring at each point. For a point at a given distance ( $y$ ) from the line of heating, the maximum thermal strain occurs at time ( $t_{\max}(y)$ ), thus:

$$\begin{aligned} \epsilon_{pl, res}^{\uparrow}(y) &= \epsilon_{pl}^{\uparrow}[y, t_{\max}(y)] \\ &= \epsilon_T[t_{\max}(y)] - \epsilon_{th}[y, t_{\max}(y)] + \epsilon_Y \end{aligned} \quad (4.17)$$



(a) temperature change vs. time



(b) elastic strain vs. temperature change

Figure 4.2: Temperature and elastic strain evolution over time.

### 4.5.2 First Yield Temperature

The onset of plasticity during heating is associated with a particular temperature termed the “first yield temperature” ( $T_{Y1}$ ) illustrated in Figure 4.2, and defined as:

$$\Delta T_{Y1} = T_{Y1} - T_0 = \frac{\epsilon_{th,Y1}^\uparrow}{\alpha} \quad (4.18)$$

where  $\epsilon_{th,Y1}^\uparrow$  is the thermal strain when yield is first obtained during heating.

Considering the threshold for heating plastic strain development given in Equation (4.16), the first yield temperature can be expressed as:

$$\Delta T_{Y1} = \frac{\epsilon_Y + \epsilon_{T,Y1}^\uparrow}{\alpha} \quad (4.19)$$

where  $\epsilon_{T,Y1}^\uparrow$  is the total strain when yield is first obtained during heating. Equation (4.19) accounts for the effect of compliance. When compliance is negligible, this equation reduces to the definition used in Ref. [84] and can be determined experimentally with a Satoh Test [35].

### 4.5.3 Plastic Strain During Cooling

Figure 4.2 also illustrates the mechanism for development of plastic strain during cooling ( $t > t_{max}$ ). For thermal cycles with a maximum temperature that exceeds the first yield temperature, elastic unloading starts from an initial state of compression at the level of yield strain. As the temperature decreases, the elastic unloading becomes elastic loading in tension. When the temperature decrease is sufficient to produce an elastic tensile strain equal to the yield strain, plasticity will begin again, but this time in tension. The total amount of elastic strain to reach plasticity during cooling is thus  $2\epsilon_Y$ , and the onset of plasticity during cooling is given by:

$$\epsilon_{el}(y, t) - \epsilon_{el}[y, t_{max}(y)] = 2\epsilon_Y \quad (4.20)$$

Representing the criterion for plasticity development as a change in elastic strain relative to the maximum temperature state is convenient since it eliminates the need to consider the magnitude of the heating plastic strain in development of equations for the cooling plastic strain. An identical result is obtained by using a criterion for plasticity of  $\epsilon_{el} = \epsilon_Y$  (similar to the case of heating).

For any given state, the elastic strain can be expressed as an equivalent sum of the thermal, plastic, and total strain components according to Equation (4.4). Recognizing that additional plastic strain will not develop during cooling until the onset of yielding (and therefore the associated terms will cancel), Equation (4.20) is equivalently expressed as:

$$\{\epsilon_{th}[y, t_{max}(y)] - \epsilon_{th}(y, t)\} - \{\epsilon_T[t_{max}(y)] - \epsilon_T(t)\} = 2\epsilon_Y \quad (4.21)$$

The cooling plastic strain produced when the thermal strain exceeds the elastic capacity of the material is thus:

$$\epsilon_{pl}^\downarrow(y, t) = \max \{0, \epsilon_{th}[y, t_{max}(y)] - \epsilon_{th}(y, t) - \epsilon_T[t_{max}(y)] + \epsilon_T(t) - 2\epsilon_Y\} \quad (4.22)$$

#### 4.5.4 Second Yield Temperature

The onset of plasticity during cooling to equilibrium is associated with a particular temperature termed the “second yield temperature” ( $T_{Y2}$ ) illustrated in Figure 4.2, and defined as:

$$\Delta T_{Y2} = T_{Y2} - T_0 = \frac{\epsilon_{th, Y2}^\downarrow}{\alpha} \quad (4.23)$$

where  $\epsilon_{th, Y2}^\downarrow$  is the maximum thermal strain required to produce yielding during cooling to the equilibrium state at  $t_{eq}$ .

Unlike the heating plastic zone, the cooling plastic zone size will vary throughout

the duration of the thermal cycle as the substrate continually cools. It is therefore also necessary to develop an expression for the temperature which governs the size at an arbitrary non-residual state.

This general plasticity temperature is denoted here as  $\Delta T_Y^\downarrow$ , defined by:

$$\Delta T_Y^\downarrow(t) = T_Y^\downarrow(t) - T_0 = \frac{\epsilon_{\text{th},Y}^\downarrow(t)}{\alpha} \quad (4.24)$$

where  $\epsilon_{\text{th},Y}^\downarrow(t)$  is the maximum thermal strain required to produce yielding during cooling to any arbitrary state.

In the residual state ( $t \geq t_{\text{eq}}$ ) the cooling plasticity temperature reduces to the second yield temperature such that:

$$\lim_{t \rightarrow t_{\text{eq}}} \Delta T_Y^\downarrow(t) = \Delta T_{Y2} \quad (4.25)$$

Considering the threshold for cooling plastic strain development given in Equation (4.22), the general plasticity temperature can be expressed as:

$$\Delta T_Y^\downarrow(y, t) = \Delta T(y, t) + \frac{2\epsilon_Y + \epsilon_T(t_Y^\downarrow) - \epsilon_T(t)}{\alpha} \quad (4.26)$$

where  $t_Y^\downarrow$  is the time at which the isotherm  $T(y, t) = \Delta T_Y^\downarrow(y, t) + T_0$  achieves its maximum width and  $\Delta T(y, t)$  is the instantaneous temperature distribution for any time  $t \geq t_{Y1}$ .

The dependence of  $\Delta T_Y^\downarrow$  on the spatial variable ( $y$ ) complicates further analysis since it implies plasticity temperature will vary across the section width. To address this, it is observed that cooling plastic strain will only occur in a region which is relatively close to the line of heating ( $y = 0$ ). It is therefore reasonable to approximate  $\Delta T(y, t) \approx \Delta T(0, t) = \sqrt{e} \Delta T_{\text{max}}(t)$  which gives:

$$\Delta T_Y^\downarrow(t) = \sqrt{e} \Delta T_{\text{max}}(t) + \frac{2\epsilon_Y + \epsilon_T(t_Y^\downarrow) - \epsilon_T(t)}{\alpha} \quad (4.27)$$

### 4.5.5 Plastic Force

For any time  $t \geq t_{Y1}$ , the heating plastic strain is equal to the residual value. Substituting Equation (4.19) into Equation (4.17), the distribution of residual heating plastic strain is written in terms of the maximum temperature as:

$$\epsilon_{\text{pl, res}}^{\uparrow}(y) = \begin{cases} 0 & \Delta T_{\text{max}}(y) \leq \Delta T_{Y1} \\ \alpha [\Delta T_{Y1} - \Delta T_{\text{max}}(y)] & \Delta T_{\text{max}}(y) > \Delta T_{Y1} \end{cases} \quad (4.28)$$

Similarly, substituting Equation (4.27) into Equation (4.22), the distribution of cooling plastic strain distribution is written in terms of the maximum temperature as:

$$\epsilon_{\text{pl}}^{\downarrow}(y, t) = \begin{cases} 0 & \Delta T_{\text{max}}(y) < \Delta T_{Y}^{\downarrow}(t) \\ \alpha [\Delta T_{\text{max}}(y) - \Delta T_{Y}^{\downarrow}(t)] & \Delta T_{\text{max}}(y) \geq \Delta T_{Y}^{\downarrow}(t) \end{cases} \quad (4.29)$$

Combining Equation (4.28) and Equation (4.29) gives a net plastic strain of:

$$\epsilon_{\text{pl}}(y, t) = \begin{cases} 0 & \Delta T_{\text{max}}(y) \leq \Delta T_{Y1} \\ \alpha [\Delta T_{Y1} - \Delta T_{\text{max}}(y)] & \Delta T_{Y1} < \Delta T_{\text{max}}(y) < \Delta T_{Y}^{\downarrow}(t) \\ \alpha [\Delta T_{Y1} - \Delta T_{Y}^{\downarrow}(t)] & \Delta T_{\text{max}}(y) \geq \Delta T_{Y}^{\downarrow}(t) \end{cases} \quad (4.30)$$

The integral of the net plastic strain results in a plastic force which is given by:

$$F_{\text{pl}}(t) = -E \int \epsilon_{\text{pl}} dA = \sqrt{\frac{2}{\pi e}} \ln \left( \frac{\Delta T_{Y}^{\downarrow}(t)}{\Delta T_{Y1}} \right) \frac{E\alpha}{\rho c} Q' \quad (4.31)$$

The plastic force is a function of time through the temperature ratio  $\Delta T_{Y}^{\downarrow}(t)/\Delta T_{Y1}$ . In residual ( $t \geq t_{\text{eq}}$ ) state, the cooling plasticity temperature is replaced by the second yield temperature and the plastic force is equal to the tendon force [44, 84]:

$$F_{\text{Ten}} = \lim_{t \rightarrow t_{\text{eq}}} F_{\text{pl}}(t) = \sqrt{\frac{2}{\pi e}} \ln \left( \frac{\Delta T_{Y2}}{\Delta T_{Y1}} \right) \frac{E\alpha}{\rho c} Q' \quad (4.32)$$

The relationship between the thermal force, plastic force, tendon force, and critical temperatures is illustrated in Figure 4.3.

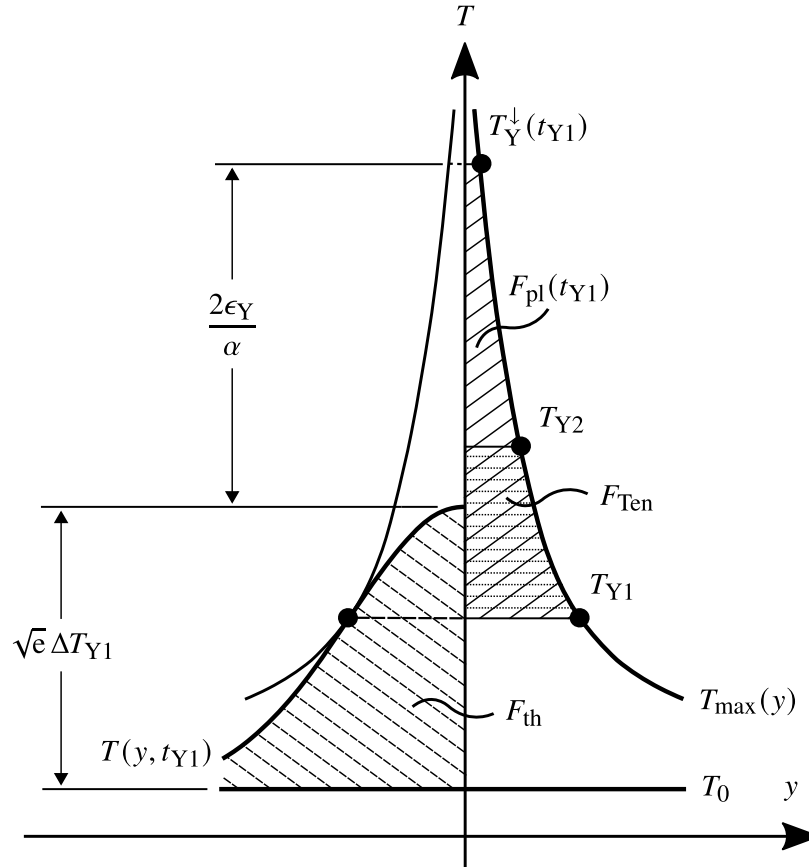


Figure 4.3: Plastic and thermal strain at the instant  $t_{Y1}$ .

## 4.6 Total Strain

Using the concept of compliance, at any given time the total strain can be obtained from the thermal force and plastic force. As shown in Figure 4.4, the two critical times  $t_{Y1}$  and  $t_{eq}$  can be used to divide the total strain into three regions of behaviour.

When the temperatures in the cross-section are relatively low ( $t > t_{Y1}$ ,  $t \ll t_{eq}$ ), the plastic zone size is constant and thermal strain is concentrated near the line of heating and can be treated as a point load. When the temperatures in the cross-section are relatively high ( $t < t_{Y1}$ ), the plastic zone size has not yet reached its

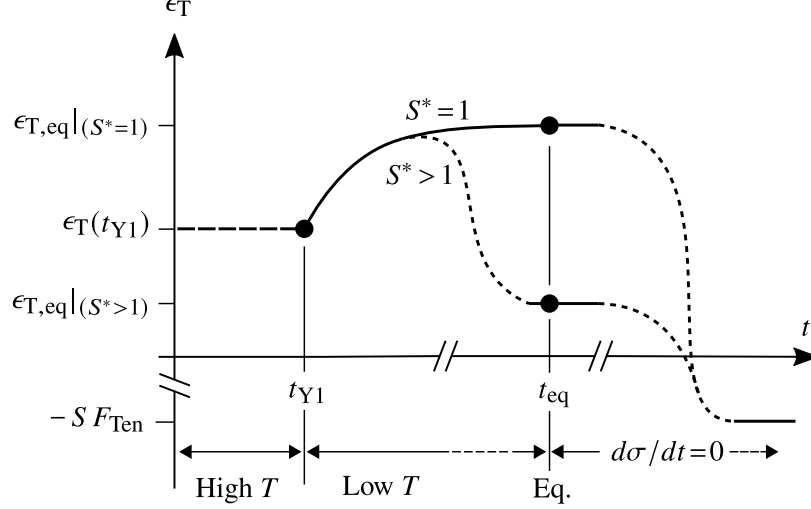


Figure 4.4: Total strain evolution over time.

final size. At equilibrium ( $t = t_{eq}$ ), the temperature and thermal strain is distributed evenly over the section.

This analysis assumes that for  $t < t_{eq}$  the total energy in the substrate remains approximately constant (i.e., negligible surface losses). For any real geometry, at times  $t \gg t_{eq}$  even small surface losses by convection and radiation to the surrounding environment will eventually lead to uniform cooling of the substrate to the ambient temperature. However, in the absence of external restraint, uniform cooling will not impact the residual stress state of the substrate and need not be considered here.

#### 4.6.1 Total Strain - Low Temperatures

Using the concept of compliance, the total strain at any time  $t_{Y1} \leq t \ll t_{eq}$  is:

$$\epsilon_T(t) = -S(F_{th} + F_{pl}) \quad (4.33)$$

Substituting Equation (4.14) and Equation (4.31) into the above expression gives:

$$\epsilon_T(t) = \left( \frac{E\alpha}{\rho c} \right) Q'S \left[ 1 - \sqrt{\frac{2}{\pi e}} \ln \left( \frac{\Delta T_Y^\dagger(t)}{\Delta T_{Y1}} \right) \right] \quad (4.34)$$

Equation (4.34) is not a closed-form expression since  $\Delta T_Y^\downarrow(t)$  is itself a function of  $\epsilon_T(t)$  as given by Equation (4.27).

### 4.6.2 Total Strain - High Temperatures

For  $t < t_{Y1}$ , the plastic heating strain zone will not have achieved its maximum width and therefore both the plastic heating strain and plastic cooling strain will change with time. Although the relative magnitude of these changes are not identical, they will tend to partially cancel and thus it may be assumed that:

$$\epsilon_T(t_{Y1} - \delta t) \approx \epsilon_T(t_{Y1}) \quad (4.35)$$

when  $\delta t$  is positive and relatively small.

Substituting Equation (4.35) into Equation (4.27), the plastic zone width at the instant  $t_{Y1}$  is associated with the critical temperature:

$$\Delta T_Y^\downarrow(t_{Y1}) = \sqrt{e} \Delta T_{Y1} + \frac{2\epsilon_Y}{\alpha} \quad (4.36)$$

Substituting Equation (4.36) into Equation (4.34), the total strain for any time  $t \leq t_{Y1}$  is then equal to the constant value:

$$\epsilon_T(t_{Y1}) = \left( \frac{E\alpha}{\rho c} \right) Q'S \left[ 1 - \sqrt{\frac{2}{\pi e}} \ln \left( \sqrt{e} + \frac{2\epsilon_Y}{\alpha \Delta T_{Y1}} \right) \right] \quad (4.37)$$

### 4.6.3 Total Strain - Equilibrium

Equation (4.34) assumes that  $F_{th}(t)$  and  $F_{pl}(t)$  are both sufficiently concentrated near the heat source trajectory that the resulting strains may be estimated using the compliance concept. The validity of this assumption does not change with time for the plastic force, however the same cannot be said of the thermal force. As the temperature distribution tends to an equilibrium state (i.e.,  $t \rightarrow t_{eq}$ ), the thermal

force becomes evenly distributed over the cross-sectional area ( $A_c$ ) with an associated uniform thermal strain of:

$$\lim_{t \rightarrow t_{\text{eq}}} \epsilon_{\text{th}}(y, t) = \alpha \Delta T_{\text{eq}} \quad (4.38)$$

where  $\Delta T_{\text{eq}}$  is the uniform equilibrium temperature change.

The total strain in the equilibrium state is therefore:

$$\epsilon_{\text{T,eq}} = \lim_{t \rightarrow t_{\text{eq}}} \epsilon_{\text{T}}(t) = \alpha \Delta T_{\text{eq}} - S F_{\text{Ten}} \quad (4.39)$$

Substituting Equation (4.32) into Equation (4.39) results in an expression for the equilibrium total strain in terms of the yield temperature ratio:

$$\epsilon_{\text{T,eq}} = \alpha \Delta T_{\text{eq}} - \left( \frac{E\alpha}{\rho c} \right) Q'S \sqrt{\frac{2}{\pi e}} \ln \left( \frac{\Delta T_{\text{Y2}}}{\Delta T_{\text{Y1}}} \right) \quad (4.40)$$

## 4.7 Compliance Effect on 1st Yield Temperature

### 4.7.1 Implicit Expression

The first yield temperature depends on the total strain at the instant  $t_{\text{Y1}}$  when the heating plastic zone achieves its maximum width. Substituting Equation (4.37) into Equation (4.19) results in the implicit expression for the first yield temperature with compliance:

$$\alpha \Delta T_{\text{Y1}} = \epsilon_{\text{Y}} + \left( \frac{E\alpha}{\rho c} \right) Q'S \left[ 1 - \sqrt{\frac{2}{\pi e}} \ln \left( \sqrt{e} + \frac{2\epsilon_{\text{Y}}}{\alpha \Delta T_{\text{Y1}}} \right) \right] \quad (4.41)$$

This can also be expressed in dimensionless form as:

$$T_{\text{Y1}}^* = \frac{\alpha \Delta T_{\text{Y1}}}{\epsilon_{\text{Y}}} = 1 + \text{Ok} \left[ 1 - \sqrt{\frac{2}{\pi e}} \ln \left( \sqrt{e} + \frac{2}{T_{\text{Y1}}^*} \right) \right] \quad (4.42)$$

where the dimensionless Okerblom number (Ok) is defined as:

$$\text{Ok} = \frac{E\alpha Q'S}{\rho c \epsilon_Y} \quad (4.43)$$

For the case of a centre weld on a flat substrate, the dimensionless parameter Ok is equivalent to the normalized average temperature rise. The average temperature was first identified by Okerblom [43] as significant in determining the effect of finite plate size on the curvature distortion produced in edge heated plates.

### 4.7.2 Blended Asymptotics

Asymptotic analysis of Equation (4.42) results in power laws for each of the two asymptotic regimes:

$$\widehat{T}_{Y1,I}^* = 1 \quad \text{Regime I (Ok} \ll 1) \quad (4.44)$$

$$\widehat{T}_{Y1,II}^* = \text{Ok} \left( 1 - \frac{1}{\sqrt{2\pi e}} \right) \quad \text{Regime II (Ok} \gg 1) \quad (4.45)$$

where the asymptotic Regime I (Ok  $\ll$  1) is associated with negligible compliance and Regime II (Ok  $\gg$  1) corresponds to infinite compliance.

An explicit analytical solution for the first yield temperature is obtained using the traditional method of blended asymptotics as described in Ref. [34]. The resulting correction factors are:

$$f_{Y1,I/II}(\text{Ok}) = \left\{ 1 + \left[ \text{Ok} \left( 1 - \frac{1}{\sqrt{2\pi e}} \right) \right]^{\pm n} \right\}^{1/n} \quad \begin{array}{l} + n \text{ for Ok} \ll 1 \\ - n \text{ for Ok} \gg 1 \end{array} \quad (4.46)$$

where an optimized value for the blending parameter of  $n = 1.3581$  results in a maximum error of 2.18% compared to the exact numerical solution obtained using MATLAB. The crossover point for the correction factors is Ok=1.3192. Asymptotic expressions without correction factors result in an error less than 10% for Ok < 0.31904

or  $Ok > 5.4548$ .

The corresponding engineering expressions with units for the first yield temperature are obtained by substituting Equation (4.43) into Equation (4.44) and Equation (4.45) and combining with Equation (4.46):

$$\begin{aligned}\Delta\widehat{T}_{Y1}^+ &= \Delta\widehat{T}_{Y1,I} f_{Y1,I}(Ok) \\ &= \frac{\epsilon_Y}{\alpha} f_{Y1,I}(Ok)\end{aligned}\quad \text{Regime I } (Ok \ll 1) \quad (4.47)$$

$$\begin{aligned}\Delta\widehat{T}_{Y1}^+ &= \Delta\widehat{T}_{Y1,II} f_{Y1,II}(Ok) \\ &= \frac{Q'SE}{\rho c} \left(1 - \frac{1}{\sqrt{2\pi e}}\right) f_{Y1,II}(Ok)\end{aligned}\quad \text{Regime II } (Ok \gg 1) \quad (4.48)$$

## 4.8 Compliance Effect on 2nd Yield Temperature

### 4.8.1 Implicit Expression

The second yield temperature corresponds to the residual ( $t \geq t_{eq}$ ) width of the cooling plastic strain zone. The second yield temperature is given from the limit of Equation (4.27) as:

$$\Delta T_{Y2} = \lim_{t \rightarrow t_{eq}} \Delta T_Y^\downarrow(t) = \Delta T_{eq} + \frac{2\epsilon_Y + \epsilon_T(t_{Y2}) - \epsilon_{T,eq}}{\alpha} \quad (4.49)$$

where  $t_{Y2}$  is the time at which the isotherm  $T(y, t) = \Delta T_{Y2} + T_0$  achieves its maximum width.

From Equation (4.35) the total strain at the instant  $t_{Y2}$  is approximately equal to the total strain at the instant  $t_{Y1}$ . Substituting Equation (4.19) into Equation (4.49) therefore gives:

$$\alpha \Delta T_{Y2} = \epsilon_Y + \alpha \Delta T_{Y1} + [\alpha \Delta T_{eq} - \epsilon_{T,eq}] \quad (4.50)$$

The second yield temperature depends on the total strain in the equilibrium state. Substituting Equation (4.40) into Equation (4.50) produces an implicit expression for the second yield temperature:

$$\alpha\Delta T_{Y2} = \epsilon_Y + \alpha\Delta T_{Y1} + \left(\frac{E\alpha}{\rho c}\right) Q'S\sqrt{\frac{2}{\pi e}} \ln\left(\frac{\Delta T_{Y2}}{\Delta T_{Y1}}\right) \quad (4.51)$$

This can also be expressed in dimensionless form as:

$$T_{Y2}^* = \frac{\alpha\Delta T_{Y2}}{\epsilon_Y} = 1 + T_{Y1}^* + \text{Ok}\sqrt{\frac{2}{\pi e}} \ln\left(\frac{T_{Y2}^*}{T_{Y1}^*}\right) \quad (4.52)$$

## 4.8.2 Blended Asymptotics

The two normalized asymptotic equations for the second yield temperature are given by the following power laws:

$$\widehat{T}_{Y2,I}^* = 2 \quad \text{Regime I (Ok} \ll 1) \quad (4.53)$$

$$\widehat{T}_{Y2,II}^* = \text{Ok} \left(1 - \frac{1}{\sqrt{2\pi e}}\right) \quad \text{Regime II (Ok} \gg 1) \quad (4.54)$$

An explicit analytical solution for the second yield temperature is obtained using the same traditional blending techniques as the first yield temperature. The resulting correction factors are:

$$f_{Y2,I/II}(\text{Ok}) = \left\{ 1 + \left[ \frac{\text{Ok}}{2} \left(1 - \frac{1}{\sqrt{2\pi e}}\right) \right]^{\pm n} \right\}^{1/n} \quad \begin{array}{l} + n \text{ for Ok} \ll 1 \\ - n \text{ for Ok} \gg 1 \end{array} \quad (4.55)$$

where an optimized value for the blending parameter of  $n = 0.95378$  results in a maximum error of 2.47% compared to the exact numerical solution obtained using MATLAB. The crossover point for the correction factors is  $\text{Ok} = 2.6384$ . Asymptotic expressions without correction factors result in an error less than 10% for  $\text{Ok} < 0.23617$

or  $Ok > 29.476$ .

The corresponding engineering expressions with units for the second yield temperature are obtained by substituting Equation (4.43) into Equation (4.53) and Equation (4.54) and combining with Equation (4.55):

$$\begin{aligned}\Delta\widehat{T}_{Y2}^+ &= \Delta\widehat{T}_{Y2,I} f_{Y2,I}(Ok) \\ &= \frac{2\epsilon_Y}{\alpha} f_{Y2,I}(Ok)\end{aligned}\quad \text{Regime I } (Ok \ll 1) \quad (4.56)$$

$$\begin{aligned}\Delta\widehat{T}_{Y2}^+ &= \Delta\widehat{T}_{Y2,II} f_{Y2,II}(Ok) \\ &= \frac{Q'SE}{\rho c} \left(1 - \frac{1}{\sqrt{2\pi e}}\right) f_{Y2,II}(Ok)\end{aligned}\quad \text{Regime II } (Ok \gg 1) \quad (4.57)$$

## 4.9 Compliance Effect on Tendon Force

### 4.9.1 Implicit Expression

The tendon force is equal to the residual value of the plastic force as shown in Equation (4.32).

Equation (4.32) can also be expressed in dimensionless form as:

$$F_{\text{Ten}}^* = \frac{F_{\text{Ten}}}{Q'} \frac{\rho c}{E\alpha} = \sqrt{\frac{2}{\pi e}} \ln(N_T) \quad (4.58)$$

$$N_T = \frac{\Delta T_{Y2}}{\Delta T_{Y1}} = \frac{\Delta T_{Y2}^*}{\Delta T_{Y1}^*} \quad (4.59)$$

where  $N_T$  is the dimensionless yield temperature ratio. The value of this ratio, with consideration of compliance, is obtained by solution of the system of equations formed from Equation (4.42) and Equation (4.52).

## 4.9.2 Blended Asymptotics

Asymptotic analysis of Equation (4.58) produces the following power laws for the tendon force:

$$\widehat{F}_{\text{Ten,I}}^* = \sqrt{\frac{2}{\pi e}} \ln(2) \quad \text{Regime I (Ok} \ll 1) \quad (4.60)$$

$$\widehat{F}_{\text{Ten,II}}^* = \frac{1}{\text{Ok}} \frac{2}{\sqrt{2\pi e} - 3} \quad \text{Regime II (Ok} \gg 1) \quad (4.61)$$

An explicit analytical solution for the tendon force is obtained using the same traditional blending techniques as the yield temperatures. The resulting correction factors are given by:

$$f_{\text{Ten,I/II}}(\text{Ok}) = \left\{ 1 + \left[ \text{Ok} \left( 1 - \frac{3}{\sqrt{2\pi e}} \right) \ln(2) \right]^{\pm n} \right\}^{-1/n} \quad \begin{array}{l} + n \text{ for Ok} \ll 1 \\ - n \text{ for Ok} \gg 1 \end{array} \quad (4.62)$$

where an optimized value for the blending parameter of  $n=1.1125$  results in a maximum error of 5.01% compared to the exact numerical solution obtained using MATLAB. The crossover point for the correction factors is  $\text{Ok}=5.2636$ . Asymptotic expressions without correction factors result in an error less than 10% for  $\text{Ok}<0.76908$  or  $\text{Ok}>36.025$ .

The corresponding engineering expressions with units for the tendon force are obtained by substituting Equation (4.43) into Equation (4.60) and Equation (4.61) and

combining with Equation (4.62):

$$\begin{aligned}\widehat{F}_{\text{Ten}}^+ &= \widehat{F}_{\text{Ten,I}} f_{\text{Ten,I}}(\text{Ok}) \\ &= \sqrt{\frac{2}{\pi e}} \ln(2) \frac{E\alpha}{\rho c} Q' f_{\text{Ten,I}}(\text{Ok})\end{aligned}\quad \begin{array}{l} \text{Regime I (Ok} \ll 1) \\ \end{array} \quad (4.63)$$

$$\begin{aligned}\widehat{F}_{\text{Ten}}^+ &= \widehat{F}_{\text{Ten,II}} f_{\text{Ten,II}}(\text{Ok}) \\ &= \frac{\epsilon_Y}{S} \frac{2}{\sqrt{2\pi e} - 3} f_{\text{Ten,II}}(\text{Ok})\end{aligned}\quad \begin{array}{l} \text{Regime II (Ok} \gg 1) \\ \end{array} \quad (4.64)$$

## 4.10 Limits of Applicability

### 4.10.1 Equilibrium Temperature Distribution

The 2-D Rosenthal temperature distribution assumes an infinite substrate resulting in a thermal cycle with a final (i.e., equilibrium) temperature equal to the starting temperature ( $T_0$ ) [40]. Consideration of a finite geometry will result in an equilibrium temperature change of  $\Delta T_{\text{eq}}$ . For the case of a material with a constant cross-sectional area and negligible thermal losses, the equilibrium temperature is equal to the average temperature rise given by:

$$T_{\text{eq}} - T_0 = \Delta T_{\text{eq}} = \frac{Q'}{\rho c A_c} \quad (4.65)$$

Refs. [43, 44, 78, 85] have previously correlated the average temperature rise with deviations from asymptotic models for inherent strain and tendon force (Equation (4.60)). A normalized average temperature is also presented by Ref. [50] as one of several thermal elastic-plastic parameters relevant to understanding the influence of the plate geometry on the tendon force in centre heating of flat plates:

$$T_{\text{eq}}^* = \frac{\alpha \Delta T_{\text{eq}}}{\epsilon_Y} = \frac{E\alpha}{\rho c} \frac{Q'}{A_c} \frac{1}{\sigma_Y} \quad (4.66)$$

For centre heating of a flat plate, the dimensionless parameters  $T_{\text{eq}}^*$  and  $\text{Ok}$  are equivalent. For any other geometry, the dimensionless parameter  $\text{Ok}$  may be calculated as:

$$\text{Ok} = T_{\text{eq}}^* S^* \quad (4.67)$$

Refs. [11, 14, 86] propose that the true temperature distribution in a finite plate of half-width ( $w/2$ ) may be obtained by superposition of the temperature field from a second imaginary heat source, moving on a parallel trajectory at a distance of  $\pm w$  from the actual heating line. This so-called mirror-method is equivalent to considering the temperature distribution to be reflected by the plate edge with negligible loss.

For sufficiently small plates, it may be necessary to consider additional reflections by superimposing heat sources at distances  $\pm n w$  for  $n = 2, 3, \dots$  until the value of the remaining temperature distribution is negligible. Numerical approximation of the infinite series solution indicates that the finite size influence on isotherm width is relatively minor for characteristic temperatures which do not exceed the equilibrium temperature rise. A necessary criterion for application of the infinite plate solution is thus:

$$\frac{\Delta T_{\text{eq}}}{\Delta T_{\text{max}}} \lesssim 1 \quad (4.68)$$

The lowest temperature relevant for tendon force is the first yield temperature ( $\Delta T_{Y1}$ ). Substituting in the corrected asymptotic expression for first yield temperature gives:

$$\frac{\Delta T_{\text{eq}}}{\Delta T_{Y1}} = \frac{T_{\text{eq}}^*}{f_{Y1,I}(\text{Ok})} \lesssim 1 \quad (4.69)$$

For centre heating of a flat plate ( $T_{\text{eq}}^* = \text{Ok}$ ) this gives  $T_{\text{eq}}^* \lesssim f_{Y1,I}(T_{\text{eq}}^*)$  which is equivalent to:

$$T_{\text{eq}}^* \lesssim 2.3 \tag{4.70}$$

For a general thin section geometry,  $S^* \geq 1$  which gives  $\text{Ok} \geq T_{\text{eq}}^*$ . The correction factor  $f_{Y1,I}(T_{\text{eq}}^*)$  will therefore be less than  $f_{Y1,I}(\text{Ok})$  (see Figure 4.6). The condition given by Equation (4.70) is thus sufficient, but not necessary, to ensure applicability of the proposed equations to any general thin section.

#### 4.10.2 Assumption of Concentrated Force

The theory presented here assumes that the total strain is approximately uniform throughout the plastic zone. For a general closed thin section it is thus required that the plastic zone be sufficiently flat and located at an approximately constant perpendicular distance from the section centre of gravity. This criterion is expressed as:

$$\Delta z \ll z \tag{4.71}$$

where  $z$  is the eccentric distance between the centre of gravity (c.g.) and the midsection at the line of heating and  $\Delta z$  is the deviation in  $z$  from the line of heating to the edge of the plastic zone width. This condition is illustrated in Figure 4.5.

The eccentric distance ( $z$ ) and relevant section moment of inertia ( $I_{yy}$ ) are defined relative to the body coordinates, which are denoted  $z'$  and  $y'$  here to distinguish from the local quasi-static coordinate system employed to describe the temperature field. The  $z'$  axis is given by the line intersecting both the centre of gravity and the application of heating. The  $y'$  axis is oriented perpendicular to the  $z'$  axis and intersects the centre of gravity.

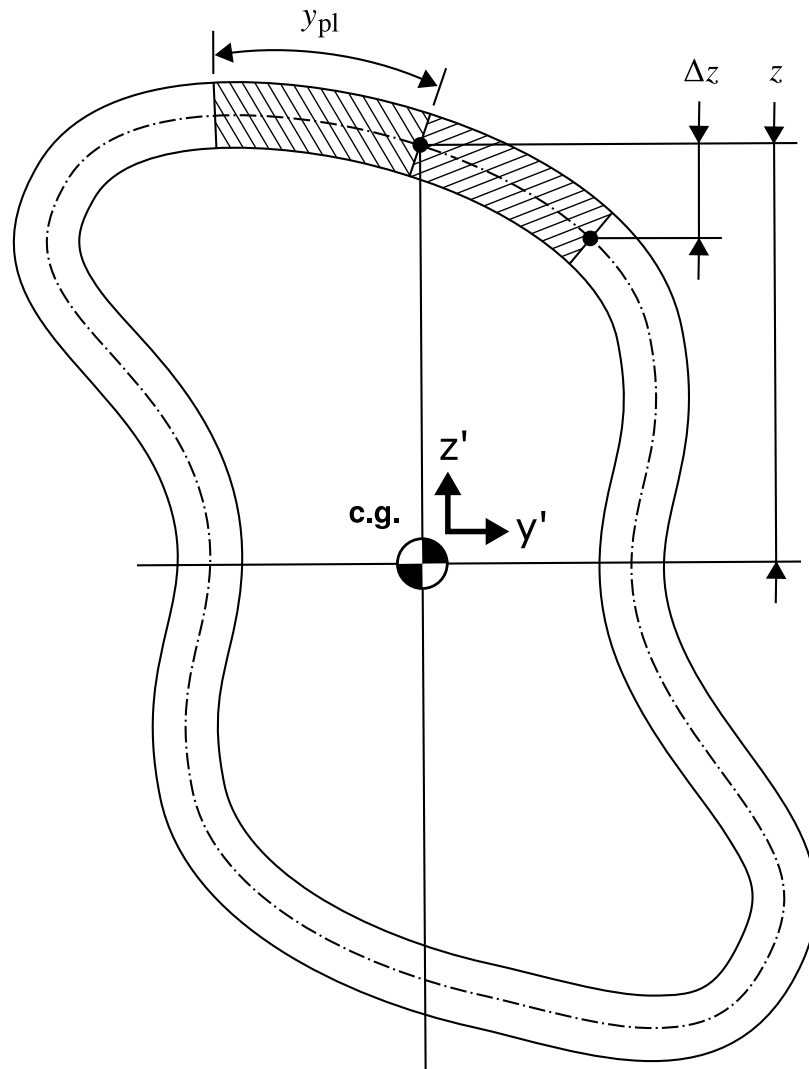


Figure 4.5: Illustration of flat plastic zone criterion.

Although in general, the criterion given in Equation (4.71) is more likely to be satisfied for larger sections with less local curvature, the size of the plastic zone also exerts a strong influence. This is particularly true when the plastic zone and the  $z'$  axis are not oriented perpendicular. The limiting case is edge heating of a flat plate where the  $z'$  axis is parallel to the plastic zone. The criterion for an approximately uniform strain thus becomes analogous to a condition that  $y_{pl} \ll w$ .

Considering the asymptotic case of negligible compliance,  $y_{pl}/w \propto T_{eq}^*$ . As a result, the condition for uniform strain is the same as the criterion for negligible compliance  $Ok \approx T_{eq}^* \ll 1$ . A similar condition exists for edge heating of a thin cylinder due to its mathematical equivalence with a flat plate on an elastic foundation [56].

For these practical geometries, a higher order correction for compliance can be applied to improve the accuracy of the predictions. This higher order correction takes the form of a correction factor on the compliance ( $S$ ).

Development of this correction considers both the distribution of the load over the plastic width ( $y_{pl}$ ) as well as the variation of the total strain within the plastic width. Examples for the development of this higher order correction are given for several typical geometric sections in Section 4.16. The expressions are not implicit as they depend on the normalized plastic width ( $y_{pl}^*$ ), and thus necessitate iterative approaches or computational techniques.

## 4.11 Validation

The proposed compliance correction factors are validated against available published data of residual stresses in weldments. Literature data includes a combination of both experimental data and numerical simulations.

Validation is limited to the first yield temperature and tendon force which are both the most critical in practice and the most readily measured attributes of the residual stress distribution. The second yield temperature is associated with the cooling plastic strain region. This point may not be accurately measured from the residual stress

distribution due to more limited data points nearer to the melted region, as well as the potential for interaction with secondary phenomena such as strain hardening, phase transformations, and mixing between the filler and base material.

#### 4.11.1 First Yield Temperature

Figure 4.6 plots literature data against the proposed blended formula as well as the exact numerical solution.

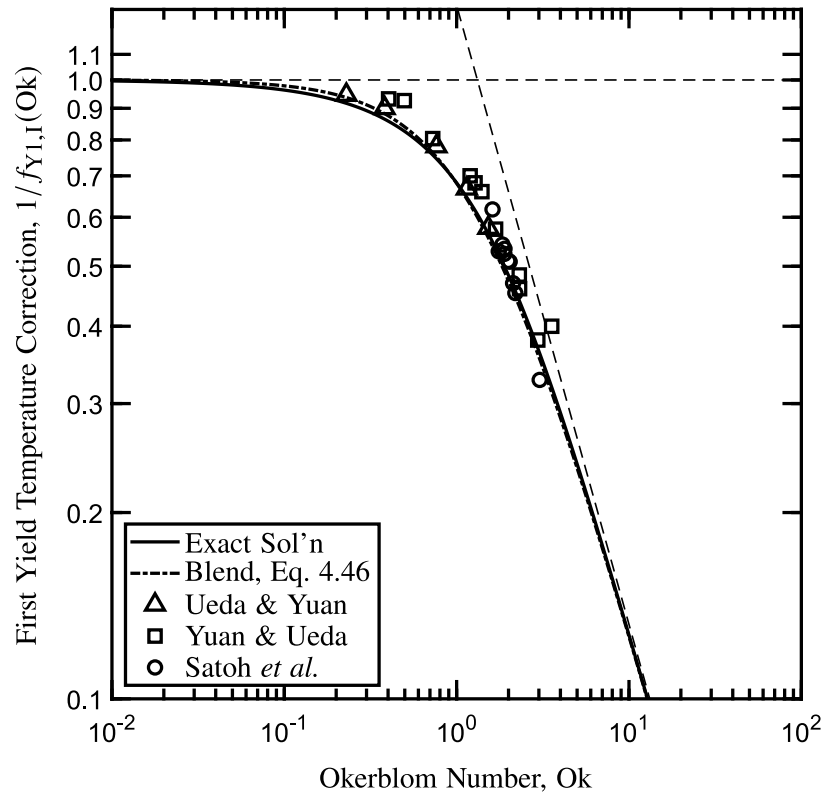


Figure 4.6: Validation of correction factor for first yield temperature with literature data for plastic zone size [20, 21, 87].

Although the first yield temperature cannot be obtained directly from the residual stress distribution, the proposed correction factor for first yield temperature can be validated using the plastic zone size. As shown in Equation (4.11), the temperature of a given isotherm is inversely proportional to the maximum width. The plastic zone size corresponds to the half-width of the first yield temperature isotherm. The

correction factor for the first yield temperature is therefore equivalent to the inverse ratio of the measured plastic zone size to the predicted plastic zone size from the asymptotic formula. The higher order correction derived in Section 4.16 was used to calculate compliance of the circumferential pipe joints considered in Ref. [87].

### 4.11.2 Tendon Force

The proposed blended expression for the tendon force compliance correction factor is compared to literature data and the exact numerical solution in Figure 4.7.

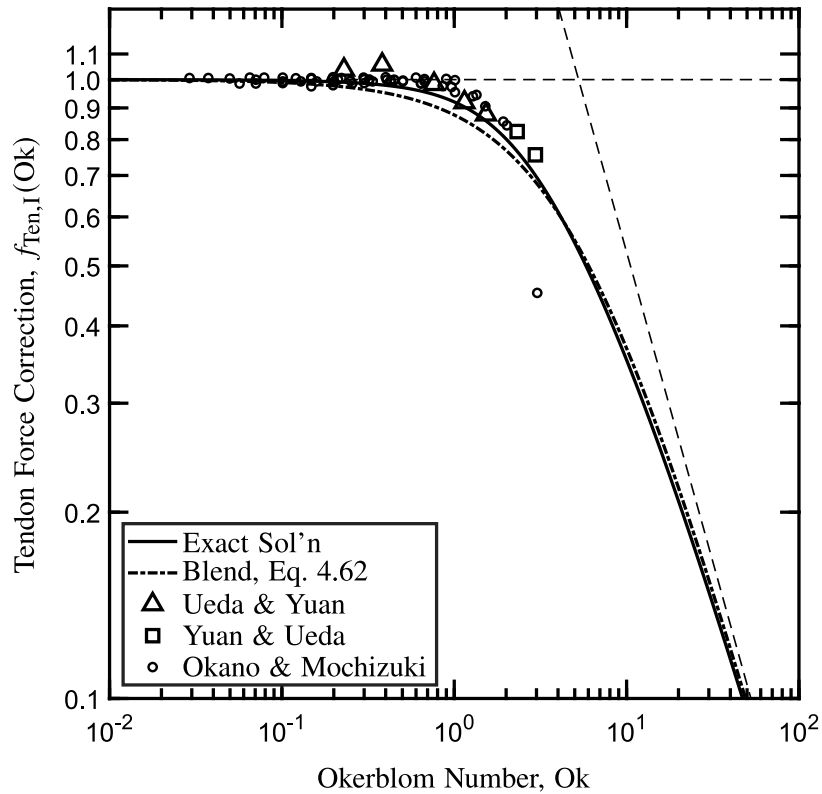


Figure 4.7: Validation of correction factor for tendon force with literature data [20, 21, 50].

In some literature sources, the tendon force value is reported with the residual stress distribution. For sources in which the tendon force is not provided, the data was digitized and the area between the residual stress and the reaction stress was integrated numerically. The reaction stress curve was obtained by a linear fit to the

stress distribution outside the plastic zone. The experimental correction factors were obtained by dividing the integrated value by the asymptotic estimate from Equation (4.32).

Some studies utilized a higher strength filler material which requires an additional correction to the asymptotic formula. This behaviour can be approximated as a special case of the general analysis for variable material properties described in Ref. [84]. This is only an approximation since the higher strength filler material represents a property variation with position rather than temperature. In general, this approximation should still give a reasonable estimate for the tendon force, although not exact given that the region of filler material is typically smaller than the residual cooling plastic zone size.

The higher strength of the filler material compared to the base material is a non-linear change, but only represents a single additional degree of freedom, with an associated single independent parameter. The nonlinear and linear components of the property variation are thus coupled. The single independent parameter is chosen as the asymptotic yield temperature ratio ( $N_T$ ) with adjustment for the variable properties. The corresponding correction factor is [84]:

$$f(N_T) = \frac{\ln(N_T)}{2(1 - 1/N_T)\ln(2)} \quad (4.72)$$

$$N_T \approx \frac{2\sigma_{Y,w}}{\sigma_{Y,b}} \quad (4.73)$$

where  $\sigma_{Y,w}$  is the nominal yield strength of the filler material and  $\sigma_{Y,b}$  is the nominal yield strength of the base plate.

## 4.12 Discussion

In general, the proposed blended asymptotic expressions agree closely with the existing literature data. The single outlier data point for the tendon force in the flat plate

studies from Ref. [50] may be attributed to the relatively high value of the dimensionless parameter  $Ok = T_{eq}^* > 2.3$ . In this case, the plate dimensions are not sufficiently large to use the maximum temperature distribution proposed by Rosenthal and an over prediction of the tendon force (i.e., under prediction of the plate size effect) is expected and observed.

The traditional (i.e., single parameter) blending technique is used to obtain correction factors for the first yield temperature ( $T_{Y1}$ , Equation (4.46)), the second yield temperature ( $T_{Y2}$ , Equation (4.55)) and the tendon force ( $F_{Ten}$ , Equation (4.62)). The maximum error in the blended correction factor for yield temperatures ( $\approx 3\%$ ) and tendon force ( $\approx 5\%$ ) is less than the repeatability of measurements and properties associated with thermo-physical phenomena, which is on the order of 10%. However, consideration of higher order effects in compliance could lead to amplification of these errors as the correction factor for first yield temperature is used as an input for subsequent computations. Ref. [34] presents a modified technique which uses up to two additional blending parameters to improve the fit for intermediate values. Three parameter blending results in an order of magnitude reduction of error for a maximum error in the correction factor for first yield temperature of only 0.2%. In computational algorithms, the additional complexity associated with encoding three parameter correction factors is negligible, but for practical representation in design guidelines the simplified single parameter formulae are preferred.

This analysis assumes an initial state of zero stress/strain in the substrate. The potential exists for pre-existing stresses due to both external forces as well as prior heating. Provided that the line of heating does not intersect with any prior plastic region, both of these situations can be readily treated with only a minor modification to the theory presented here. The formula for the total strain is adjusted to give  $\epsilon_T = \epsilon_0 - S F$ , where  $\epsilon_0$  is the initial or pre-existing strain parallel to the heat source trajectory.

The implicit formula for the first yield temperature (Equation (4.42)) is thus mod-

ified by adding an additional term of  $\epsilon_0^* = \epsilon_0/\epsilon_Y$ . A initial tensile strain field ( $\epsilon_0 > 0$ ) will increase the first yield temperature while an initial compressive stress field will decrease it. A similar correction is not necessary for the second yield temperature since the total strain terms cancel. Closed-form corrections for the first yield temperature and tendon force as a function of  $Ok$ , at a given value of the parameter  $\epsilon_0^*$ , may be obtained using the same techniques of blended asymptotics as shown in this work. A general blended solution for an arbitrary value of both  $Ok$  and  $\epsilon_0^*$  necessitates a multi-dimensional blending technique which is still under development.

The methodology and engineering expressions presented here are applicable to a wide range of thermal processes and geometries. The cases of edge heating of a thin, flat section and cylinder are particularly relevant for processes such as wire arc additive manufacturing, and it should be acknowledged that comprehensive treatment of these applications may give rise to some minor additional complexity. In addition to the potential for transient starting temperature and initial elastic strain as mentioned above, it may also be necessary to account for the influence of initial plastic strain in the previously deposited material. Consideration of such cases in efficient computational implementations is possible with minimal adjustment to the present theory. Development of improved analytical formula to address these subtleties is the subject of ongoing work.

## 4.13 Conclusions

For the first time, the effects of compliance are considered in general for processes involving moving heat sources such additive manufacturing, welding, and laser processing. The predictions require no calibrations or fitting to previous experiments and are based only on the component geometry and tabulated material properties.

- Simple and accurate closed-form expressions are provided for the first yield temperature ( $\Delta T_{Y1}$ , Equations (4.47) and (4.48)), the second yield tempera-

ture ( $\Delta T_{Y2}$ , Equations (4.56) and (4.57)), and the tendon force ( $F_{\text{TEN}}$ , Equations (4.63) and (4.64)). These expressions are valid for general geometries and materials beyond steels or flat plates.

- Rigorous mathematical treatment of the thermal-mechanical theory of residual stress using dimensional analysis, asymptotics, and blending demonstrates that for fast moving heat sources (as is the near universal case) the effect of compliance depends on a single dimensionless group, the Okerblom number (Equation (4.43)), which captures all effects of material and geometry.
- The proposed expressions are validated by comparison to published literature data for the plastic zone width (Figure 4.6) and tendon force (Figure 4.7) in butt welded flat plates, T-sections, and circumferential joints. The results reduce to particular cases to reproduce previous empirical expressions developed for specific materials, such as structural steel.
- This fundamental work provides a foundation for future consideration of the effects of consecutive thermal cycles, phase transformations, and pre-existing residual stresses. Because of their closed form, these expressions are ideally suited for use in metamodels, practical engineering calculations, as well as codes and standards.

## 4.14 Acknowledgements

Valuable discussions and feedback from Y. Lu and E. Alvarez Rocha are gratefully acknowledged. The implementation of the blending optimization algorithm was coded in MATLAB by Y. Lu. Special thanks to R. Ramgopal for assistance with digitizing literature data.

## 4.15 Appendix: Calculation of Compliance

### Centre heating of a thin flat section

The compliance for heating at the centreline of a thin flat section with thickness ( $d$ ), width ( $w$ ), and cross-sectional area ( $A_c$ ) is associated with the uniform axial strain given by:

$$\epsilon_{\text{ax}} = \frac{F}{EA_c} \quad (4.74)$$

where  $F$  is a unit load at the line of heating.

The compliance ( $S$ ) is therefore:

$$S = \frac{\epsilon_{\text{ax}}}{F} = \frac{1}{E} \frac{1}{wd} \quad (4.75)$$

### Longitudinal heating of a general thin section geometry

The total strain for longitudinal heating of a general thin section can be written as the sum of the axial strain and bending strain.

The axial strain is given by Equation (4.74). The bending strain is obtained as [73]:

$$\epsilon_{\text{bend}}|_{y_0} = \frac{Mz}{EI_{yy}} = \frac{Fz^2}{I_{yy}} \quad (4.76)$$

where  $M = Fz$  is the bending moment produced by the unit load,  $z$  is the eccentric distance between the heat source trajectory and the centre of gravity, and  $I_{yy}$  is the area moment of inertia of the section.

The compliance ( $S$ ) is therefore:

$$S = \frac{\epsilon_{\text{ax}} + \epsilon_{\text{bend}}|_{y_0}}{F} = \frac{1}{E} \left( \frac{1}{A_c} + \frac{z^2}{I_{yy}} \right) \quad (4.77)$$

This expression may be used for a variety of open or closed sections, provided

that the geometry is sufficiently thin that the 2-D Rosenthal heat source model is appropriate.

### Edge heating of a thin flat section

The compliance for edge heating of a thin flat section with thickness ( $d$ ) and width ( $w$ ) may be considered as a special case of the general thin section above, where the moment of inertia is  $I_{yy} = w^3d/12$  and the eccentric distance between the load and centre of gravity is  $z = w/2$ .

The compliance ( $S$ ) is therefore:

$$S = \frac{1}{E} \left( \frac{1}{A_c} + \frac{z^2}{I_{yy}} \right) = \frac{1}{E} \left( \frac{1}{wd} + \frac{3w^2}{w^3d} \right) = \frac{1}{E} \frac{4}{wd} \quad (4.78)$$

### Edge heating of a thin cylinder

The compliance for edge (i.e., circumferential) heating of a thin cylinder with length ( $L$ ), radius ( $r$ ), and thickness ( $d$ ) is related to the cylinder stiffness parameter ( $\beta$ ) defined as:

$$\beta = \left[ \frac{2(1 - \nu^2)}{r^2d^2} \right]^{0.25} \quad (4.79)$$

A unit hoop load ( $F$ ) at the cylinder end produces an equivalent stress state to a unit radial load ( $F/r$ ). The resulting hoop strain at the end of the cylinder is thus given by [88]:

$$\epsilon_{\text{hoop}}|_{y_0} = \frac{2F\beta}{Ed} \quad (4.80)$$

The compliance ( $S$ ) is therefore:

$$S = \frac{\epsilon_{\text{hoop}}|_{y_0}}{F} = \frac{1}{E} \frac{2\beta}{d} \quad (4.81)$$

A similar expression may also be used to consider a circumferential joint between two cylinders (or pipes) although the compliance will be exactly half of the value shown above since the unit load is distributed between the two pipe halves.

Additional considerations for bending stresses developed at the location of the joint may also be necessary, and will depend on whether it is a partial penetration (i.e., root weld) or single pass, full penetration joint.

## 4.16 Appendix: Higher Order Correction

Consideration of the tendon force as a distributed load necessitates a higher order correction factor ( $f_S$ ) which is applied to the compliance itself. Analytical estimates of this factor are obtained for two example geometries below which are particularly relevant in welding and additive manufacturing applications.

A reasonable improvement over the concentrated force assumption is obtained by considering a uniform distribution of the net residual plastic strain (i.e., the tendon force) throughout the plastic zone size. In practice, the distribution of residual plastic strain within the plastic zone is expected to be non-uniform with a higher value in the region immediately adjacent to the line of heating as shown in Ref. [84]. The analytical correction factors below may thus be expected to somewhat over compensate for the distribution effect with the true compliance value somewhere between this estimate and the value predicted for a concentrated load (i.e.,  $f_S = 1$ ).

### Edge heating of a thin flat section

Distribution of a unit load ( $F$ ) over the region  $0 \leq y \leq y_{pl}$  from the edge of a plate with width ( $w$ ) gives rise to a bending moment:

$$M = (w/2 - y_{pl}/2)F \tag{4.82}$$

The total strain at the edge of the plastic zone ( $z = w/2 - y_{\text{pl}}$ ) is thus given by:

$$\epsilon_{\text{bend}}|_{y_{\text{pl}}} = \frac{Mz}{EI_{yy}} = \frac{12(w/2 - y_{\text{pl}}/2)(w/2 - y_{\text{pl}})F}{Ew^3d} \quad (4.83)$$

The axial strain ( $\epsilon_{\text{ax}}$ ) is unchanged by the distribution, so the compliance ( $S$ ) is then obtained as:

$$S = \frac{1}{Ewd} [1 + 3(1 - y_{\text{pl}}/w)(1 - 2y_{\text{pl}}/w)] \quad (4.84)$$

The correction factor ( $f_S$ ) is obtained from dividing Equation (4.84) by Equation (4.78) to give:

$$f_S(y_{\text{pl}}^*) = 1 + (3/2 y_{\text{pl}}^*)(y_{\text{pl}}^* - 3/2) \quad (4.85)$$

$$y_{\text{pl}}^* = \frac{y_{\text{pl}}}{w} \quad (4.86)$$

## Edge heating of a thin cylinder

The hoop strain due to a load ( $P$ ) acting at a distance ( $\varepsilon$ ) from the end of a thin cylinder of thickness ( $d$ ) and radius ( $r$ ) is given by [89]:

$$\epsilon_{\text{hoop}} = \frac{P\beta r}{2Ed} [\theta(\beta y - \beta\varepsilon) + \zeta(\beta y - \beta\varepsilon) + 2\theta(\beta y)\theta(\beta\varepsilon) + \psi(\beta y)\psi(\beta\varepsilon)] \quad (4.87)$$

where for convenience the following notation is used:

$$\theta(x) = \exp(-x) \cos(x) \quad (4.88)$$

$$\zeta(x) = \exp(-x) \sin(x) \quad (4.89)$$

$$\psi(x) = \exp(-x) [\cos(x) - \sin(x)] \quad (4.90)$$

An expression for the hoop strain due to the distributed unit hoop load ( $F$ ) is obtained by substituting  $Pr = (F/y_{pl})d\epsilon$  into Equation (4.87) and integrating across  $0 \leq \epsilon \leq y_{pl}$ . The resulting hoop strain at the edge of the plastic zone ( $y = y_{pl}$ ) is given by:

$$\epsilon_{\text{hoop}}|_{y_{pl}} = \frac{1}{E} \frac{F}{2y_{pl}d} [1 + 2\theta(\beta y_{pl})\zeta(\beta y_{pl}) - \exp(-2\beta y_{pl})] \quad (4.91)$$

The compliance is therefore:

$$S = \frac{1}{E} \frac{2\beta}{d} \frac{1 + \exp(-2\beta y_{pl}) [2 \cos(\beta y_{pl}) \sin(\beta y_{pl}) - 1]}{4\beta y_{pl}} \quad (4.92)$$

The correction factor ( $f_S$ ) is obtained from dividing Equation (4.92) by Equation (4.81) to give:

$$f_S(y_{pl}^*) = \frac{1 + \exp(-2y_{pl}^*) [2 \sin(y_{pl}^*) \cos(y_{pl}^*) - 1]}{4y_{pl}^*} \quad (4.93)$$

$$y_{pl}^* = \beta y_{pl} \quad (4.94)$$

## References

- [11] N. S. Boulton and H. E. Lance Martin, “Residual stresses in arc-welded plates,” *Proc. Inst. Mech. Eng.*, vol. 133, no. 1, pp. 295–347, June 1936. DOI: 10.1243/pime\_proc\_1936\_133\_017\_02.
- [14] L. Tall, “Residual stresses in welded plates - a theoretical study,” *Welding J.*, vol. 43, no. 1, pp. 10s–23s, Jan. 1964.
- [16] Y. Ueda, K. Fukuda, K. Nakacho, and S. Endo, “A new measuring method of residual stresses with the aid of finite element method and reliability of estimated values,” *Trans. JWRI*, vol. 4, no. 2, pp. 123–131, Oct. 1975. DOI: 11094/11113.
- [20] Y. Ueda and M. G. Yuan, “Prediction of residual stresses in butt welded plates using inherent strains,” *ASME J. Eng. Mater. Technol.*, vol. 115, no. 4, pp. 417–423, Oct. 1993. DOI: 10.1115/1.2904240.
- [21] M. G. Yuan and Y. Ueda, “Prediction of residual stresses in welded T- and I-joints using inherent strains,” *ASME J. Eng. Mater. Technol.*, vol. 118, no. 2, pp. 229–234, Apr. 1996. DOI: 10.1115/1.2804892.
- [26] J. B. Dwight and K. E. Moxham, “Welded steel plates in compression,” *Struct. Eng.*, vol. 47, no. 2, pp. 49–66, Feb. 1969.
- [33] Y. Lu, Y. Wang, and P. F. Mendez, “Width of thermal features induced by a 2-D moving heat source,” *Int. J. Heat Mass Transfer*, vol. 156, pp. 119793, Aug. 2020. DOI: 10.1016/j.ijheatmasstransfer.2020.119793.
- [34] Y. Lu and P. F. Mendez, “Characteristic values of the temperature field induced by a moving line heat source,” *Int. J. Heat Mass Transfer*, vol. 166, pp. 120671, Feb. 2021. DOI: 10.1016/j.ijheatmasstransfer.2020.120671.
- [35] K. Satoh, “Transient thermal stresses of weld heat-affected zone by both-ends-fixed bar analogy,” *Trans. JWS*, vol. 3, no. 1, pp. 125–134, Apr. 1972.
- [36] M. Watanabe, “Thermal stress and its residual stress of rectangular plate under one-dimensionally distributed temperature,” *J. Zosen Kiokai* [in Japanese], vol. 86, pp. 173–184, 1954. DOI: 10.2534/jjasnaoe1952.1954.86.173.
- [40] D. Rosenthal, “The theory of moving sources of heat and its application to metal treatments,” *Trans. ASME*, vol. 68, no. 11, pp. 849–866, Nov. 1946.
- [43] N. O. Okerblom, *Raschet Deformatsii Metallokonstruktsii pri Svarke* [The Calculations of Deformations of Welded Metal Structures]. Moscow: Mashgiz, 1955 (Transl. by London: HMSO, 1958).
- [44] J. White, “Longitudinal shrinkage of a single pass weld,” *Univ. Cambridge Tech. Rep.*, CUED/C–Struct/TR.57, 1977.
- [50] S. Okano and M. Mochizuki, “Dominant factors and quantification of tendon force in welded structural materials,” *Trans. JSME* [in Japanese], vol. 81, no. 830, pp. 15–00277, Sept. 2015. DOI: 10.1299/transjsme.15-00277.

- [51] P. F. Mendez, “Reduced order models for welding and solidification processes,” *IOP Conf. Ser.: Mater. Sci. Eng.*, vol. 861, pp. 012003, June 2020. DOI: 10.1088/1757-899X/861/1/012003.
- [56] M. R. Grams, L. Ludwig, and P. F. Mendez, “A quantitative index to assess the influence of joint fit-up on pipeline weld root discontinuities,” in *Proc. ASME 13th Int. Pipeline Conf.*, Calgary, Canada, Sep. 28-30, 2020, (IPC2020-9706), pp. V003T05A032. DOI: 10.1115/IPC2020-9706.
- [60] O. W. Blodgett, “Joint design and production: Control of shrinkage and distortion,” in *Design of Welded Structures*, Cleveland, OH: The James F. Lincoln Arc Welding Foundation, 1966, ch. 7.7.
- [62] P. F. Mendez, Y. Lu, and Y. Wang, “Scaling analysis of a moving point heat source in steady-state on a semi-infinite solid,” *ASME J. Heat Transfer*, vol. 140, no. 8, pp. 081301, Apr. 2018. DOI: 10.1115/1.4039353.
- [63] Y. Wang, Y. Lu, and P. F. Mendez, “Scaling expressions of characteristic values for a moving point heat source in steady state on a semi-infinite solid,” *Int. J. Heat Mass Transfer*, vol. 135, pp. 1118–1129, June 2019. DOI: 10.1016/j.ijheatmasstransfer.2019.02.042.
- [65] T. Sasayama, K. Masubuchi, and S. Moriguchi, “Longitudinal deformation of long beam due to fillet welding,” *Welding J.*, vol. 34, no. 12, pp. 581s–582s, Dec. 1955.
- [66] M. R. Grams and P. F. Mendez, “Scaling analysis of the thermal stress field produced by a moving point heat source in a thin plate,” *ASME J. Appl. Mech.*, vol. 88, no. 1, pp. 011001, Jan. 2021. DOI: 10.1115/1.4048318.
- [73] S. Timoshenko, “Combined bending and tension,” in *Strength of Materials, Part I: Elementary Theory and Problems*, 2nd, New York: D. Van Nostrand Company, Inc., 1940, ch. 8, pp. 226–260.
- [75] E. R. Denlinger, J. C. Heigel, P. Michaleris, and T. A. Palmer, “Effect of inter-layer dwell time on distortion and residual stress in additive manufacturing of titanium and nickel alloys,” *J. Mater. Process. Technol.*, vol. 215, pp. 123–131, Jan. 2015. DOI: 10.1016/j.jmatprotec.2014.07.030.
- [76] L. Bass, J. Milner, T. Gnäupel-Herold, and S. Moylan, “Residual stress in additive manufactured nickel alloy 625 parts,” *J. Manuf. Sci. Eng.*, vol. 140, no. 6, pp. 061004, Mar. 2018. DOI: 10.1115/1.4039063.
- [77] J. D. White, “Longitudinal Stresses in a Member Containing Non-Interacting Welds,” *Univ. Cambridge Tech. Rep.*, CUED/C-Struct/TR.58, 1977.
- [78] T. Terasaki, M. Nakatani, and T. Ishimura, “Study of tendon force generating in welded joint,” *Q. J. Jpn. Weld. Soc.* [in Japanese], vol. 18, no. 3, pp. 479–486, Aug. 2000. DOI: 10.2207/qjjws.18.479.
- [79] T. Terasaki, T. Ishimura, K. Matsuishi, and T. Akiyama, “Study on longitudinal shrinkage of bead on plate,” *Q. J. Jpn. Weld. Soc.* [in Japanese], vol. 20, no. 1, pp. 136–142, Feb. 2002. DOI: 10.2207/qjjws.20.136.

- [80] T. Terasaki, T. Kitamura, I. Kidota, T. Ishimura, and S. Hamashima, “Study on longitudinal shrinkage and bending distortion of fillet T joint,” *Q. J. Jpn. Weld. Soc.* [in Japanese], vol. 21, no. 1, pp. 81–86, Feb. 2003. DOI: 10.2207/qjjws.21.81.
- [81] Y. Wang, Y. Lu, M. R. Grams, A. Hintze Cesaro, and P. F. Mendez, “Asymptotics and blending in the modeling of welding,” *Mathematical Modelling of Weld Phenomena 12*, pp. 907–932, July 2019.
- [82] S. W. Churchill and R. Usagi, “A general expression for the correlation of rates of transfer and other phenomena,” *AIChE Journal*, vol. 18, no. 6, pp. 1121–1128, Nov. 1972. DOI: 10.1002/aic.690180606.
- [83] S. W. Churchill and R. Usagi, “A standardized procedure for the production of correlations in the form of a common empirical equation,” *Ind. Eng. Chem. Fundamen.*, vol. 13, no. 1, pp. 39–44, Feb. 1974. DOI: 10.1021/i160049a008.
- [84] M. R. Grams and P. F. Mendez, “A general expression for the welding tendon force,” *ASME J. Manuf. Sci. Eng.* (under review), 2021.
- [85] Y. Luo, H. Murakawa, and Y. Ueda, “Prediction of welding deformation and residual stress by elastic FEM based on inherent strain (1st Report): Mechanism of inherent strain production,” *Trans. JWRI*, vol. 26, no. 2, pp. 49–57, Dec. 1997. DOI: 11094/7958.
- [86] D. Rosenthal, “Mathematical theory of heat distribution during welding and cutting,” *Welding J.*, vol. 20, no. 5, pp. 220s–234s, May 1941.
- [87] K. Satoh, M. Toyoda, Y. Suita, M. Tanaka, and T. Hirano, “Controlling parameters of residual stresses and deformations in welded thin cylindrical shells,” *Trans. JWS*, vol. 17, no. 1, pp. 3–9, Apr. 1986.
- [88] S. Timoshenko and S. Woinowsky-Krieger, “General theory of cylindrical shells,” in *Theory of Plates and Shells*, 2nd, McGraw-Hill Book Company, 1959, ch. 15, pp. 466–532.
- [89] S. Timoshenko, “Special problems in bending of beams,” in *Strength of Materials, Part II: Advanced Theory and Problems*, 2nd, New York: D. Van Nostrand Company, Inc., 1940, ch. 1, pp. 1–64.

# Chapter 5

## A Quantitative Index to Assess the Influence of Joint Fit-Up on Pipeline Weld Root Discontinuities

### 5.1 Introduction

Manual shielded metal arc welding (SMAW) remains one of the most common processes used to weld field tie-in circumferential joints on oil and gas pipelines in North America. During the deposition of the root weld pass, significant plastic strains are produced in the hoop direction of the pipe as a result of the constrained thermal expansion and shrinkage in the weld fusion zone and surrounding material. After the material has cooled to a uniform temperature, this plastic strain results in a residual tensile hoop stress which will tend to produce local bending across the weld joint. In production welds, the presence of non-ideal joint geometry at the weld root has the potential to produce more severe conditions for latent discontinuity formation than those present during qualification.

In reference to high-low offset, both American (API 1104) [90] and Canadian (CSA Z662) [6] pipeline welding and construction codes provide only a single recommended tolerance regardless of values experienced during procedure qualification. These nominal permissible values of high-low offset vary between the two codes, but both have caveats that larger values are acceptable if the deviation is the result of manufactur-

ing tolerances on pipe end dimensions. These tolerances present a significant concern since allowable deviations on pipe radius or ovality ( $\Delta a$ ) and wall thickness ( $\Delta d$ ) can combine to produce significant levels of high-low offset as shown in Figure 5.1.

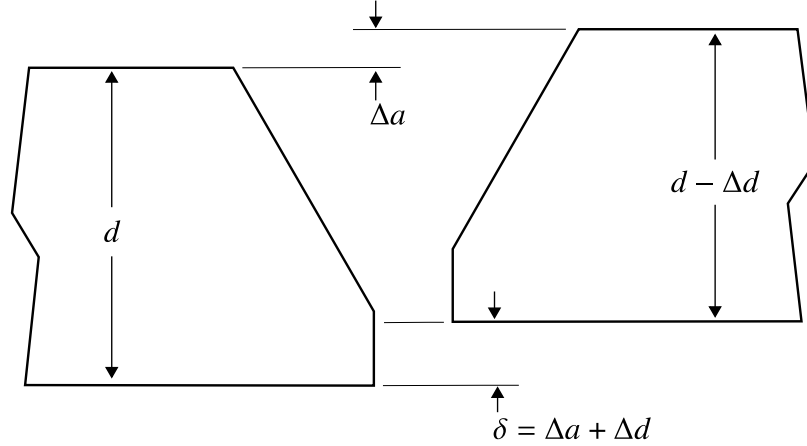


Figure 5.1: High-low offset at weld root ( $\delta$ ) due to local pipe radius mismatch or ovality ( $\Delta a$ ) combined with local wall thickness mismatch ( $\Delta d$ ).

There is limited fundamental work addressing the role of non-ideal joint geometry in the susceptibility of girth welds to root pass discontinuities. Ref. [91] conducted several numerical and experimental studies in the 1970s considering the effect of residual stresses and high-low offset on root pass integrity. This work was primarily focused on understanding the interaction between these factors and the large lifting stresses imposed by historical construction practices. In addition, the use of relatively early numerical techniques for validation poses limitations on any attempt to generalize the results obtained to modern pipeline materials, joint configurations, pipe dimensions, and welding procedures. More recent work considering the influence of non-ideal geometry on the integrity of circumferential welds is heavily focused on the assessment of completed welds under in-service loading conditions [92–94].

The goal of this study is to provide a general model applicable to the wide range of different welding conditions present in North American pipeline construction. The parameters considered include: pipe wall thickness, pipe diameter, weld bead width, weld bead thickness, welding heat input, and high-low offset. This study focuses on

the susceptibility to latent root discontinuities directly following the completion of the root pass weld. The root pass typically combines a relatively low heat input (i.e., high cooling rate), with a small weld pass and a cellulosic (i.e., high hydrogen) welding consumable. These factors combine to produce the highest susceptibility to formation of latent discontinuities, such as cracks, in this time period.

Fundamental concepts of heat transfer and solid mechanics are used to derive an analytical expression for the angular distortion of a pipe end due to the plastic strains produced by welding. Both the theoretical analysis and numerical validation presented in this work assume that the processes of local plastic strain development and the resulting overall structural distortion may be treated separately. In reality, these processes occur simultaneously and there is the potential for the structural distortion to influence the size of the plastic strain region. This effect is expected to be small for pipes due to the relatively rigid geometry. The angular distortion is applied to the weld root to obtain an estimate of the tensile strain on the inner surface under ideal fit-up conditions. A stress concentration factor is introduced to account for the presence of a high-low offset. This strain is treated as a numerical index which can be computed prior to welding and requires input of only a small number of welding parameters and fit-up dimensions which are readily attainable by industrial practitioners under field conditions.

## 5.2 List of Symbols

Symbol	SI Unit	Description
<b>Roman Letters</b>		
$a$	m	Pipe radius
$2c$	m	Weld bead thickness
$D$	N m	Pipe flexural rigidity
$d$	m	Pipe wall thickness
$E$	$\text{N m}^{-2}$	Elastic modulus
$F_{\text{Ten}}$	N	Tendon force
$f_D$	1	Correction factor for load distribution
$f_G$	1	Correction factor for non-ideal fit-up
$f_M$	1	Correction factor for weld bead moment
$g$	m	Weld bead width
$\mathbf{I}_{\text{root}}$	1	Root susceptibility index
$Q'$	$\text{J m}^{-1}$	Linear energy input (i.e., heat input)
$r$	m	Weld bead radius of curvature
$T_0$	K	Preheat temperature
$T_{Y1}$	K	First yield temperature
$T_{Y2}$	K	Second yield temperature
$w'$	rad	Angular rotation at pipe end
$y_{\text{pl}}$	m	Plastic zone size (i.e., half-width)
<b>Greek Letters</b>		
$\alpha$	$\text{K}^{-1}$	Coefficient of thermal expansion
$\beta$	$\text{m}^{-1}$	Geometric stiffness parameter
$\delta$	m	High-low offset (i.e., non-ideal fit-up)
$\eta$	1	Heat transfer efficiency
$\Pi_1$	1	Normalized plastic zone width
$\Pi_2$	1	Normalized weld bead resistance parameter
$\Pi_3$	1	Dimensionless fit-up parameter
$\rho c$	$\text{J m}^{-3} \text{K}^{-1}$	Volumetric specific heat capacity
$\theta$	rad	Total angular distortion of weld bead
$\sigma_Y$	$\text{N m}^{-2}$	Material yield strength

## 5.3 Ideal Model

### 5.3.1 Tendon Force

Ref. [44] first proposed that the plastic strains produced during welding might be substituted for an equivalent external load for the purposes of predicting the resulting distortion. This equivalent external load is termed the “tendon force”. Building on the work of Ref. [43], the authors have previously proposed the following general expression for the welding tendon force [95]:

$$F_{\text{Ten}} = \sqrt{\frac{2}{\pi e}} \ln \left( \frac{\Delta T_{Y2}}{\Delta T_{Y1}} \right) \frac{E \alpha_{\text{eff}}}{\rho c} Q' \quad (5.1)$$

where  $\Delta T_{Y1}$  and  $\Delta T_{Y2}$  are the first and second yield temperatures for the material,  $E$  is the elastic modulus,  $\alpha_{\text{eff}}$  is the effective coefficient of thermal expansion (CTE),  $\rho c$  is the volumetric specific heat capacity, and  $Q'$  is the welding heat input.

The first and second yield temperatures correspond to the temperature changes necessary to produce plastic strain during heating and cooling respectively, under conditions of uniaxial constraint. Exact values for these temperatures may be obtained through experimental or numerical methods, but the simple analytical expressions shown below provide reasonable accuracy for the purposes of estimation:

$$\Delta T_{Y1} = \frac{\sigma_Y}{E \bar{\alpha}} \Big|_{\Delta T_{Y1} + T_0} \quad (5.2)$$

$$\Delta T_{Y2} = \frac{1}{\bar{\alpha}} \Big|_{\Delta T_{Y2} + T_0} \left( \frac{\sigma_Y}{E} \Big|_{T_0} + \frac{\sigma_Y}{E} \Big|_{\Delta T_{Y2} + T_0} \right) \quad (5.3)$$

where  $\bar{\alpha}|_T$  denotes the mean CTE between  $T_0$  and  $T$ . For a material with a constant CTE as well as a yield stress and elastic modulus which are either constant or linear functions of temperature, the ratio of the two yield temperatures is equal to 2.

A key advantage of the tendon force approach over alternative concepts, such as

the shrinkage force [64], is that it depends solely on material properties and welding parameters and is approximately independent of the structural geometry. This approximation is known to be only exact for infinitely rigid geometries [43, 50] and a generalized extension of the tendon force model to account for these so-called compliance effects is under development.

The effective CTE is introduced to account for the temperature dependence of relevant material properties. Considering a material with a temperature dependent uniaxial yield strain ( $\sigma_Y/E$ ), the effective CTE may be calculated as:

$$\alpha_{\text{eff}} = \frac{\sigma_Y}{E} \Big|_{T_0} \frac{1}{\Delta T_{Y2} - \Delta T_{Y1}} \quad (5.4)$$

With the exception of the welding heat input, all other variables in Equation (5.1) are material properties. For application to a particular class of material, such as line pipe, it is convenient to combine these material properties in a single non-dimensional material parameter:

$$H = \sqrt{\frac{2}{\pi e}} \ln \left( \frac{\Delta T_{Y2}}{\Delta T_{Y1}} \right) \frac{E\alpha_{\text{eff}}}{\rho c} \quad (5.5)$$

The non-dimensional grouping  $3E\alpha/\rho c$  arises in the field of solid state physics and is termed the Grüneisen parameter [69]. This parameter is known to be only a weak function of temperature and typically has a value of  $\approx 2$  for metals [68]. Considering a material with both a CTE and yield strain that are independent of temperature (i.e.,  $\alpha_{\text{eff}} = \alpha$  and  $\Delta T_{Y2}/\Delta T_{Y1} = 2$ ) the parameter  $H$  has a theoretical value of  $\approx 0.22$ .

To obtain a more precise value for  $H$ , specific to line pipe materials, the materials software JMatPro [46] was used to determine the temperature dependence of all relevant mechanical and thermal properties. The results are shown in Figure 5.2.

Ref. [96] provides experimental data for the high temperature strength of 4 different acceptable compositions of CSA Gr.483 (X70) line pipe steel. An approximate

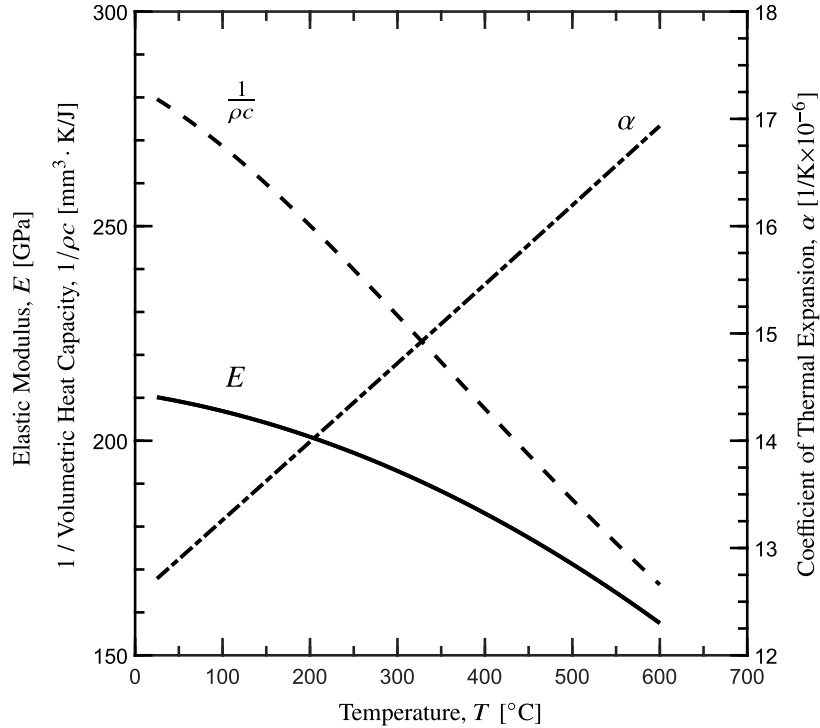


Figure 5.2: Calculated properties for CSA Gr.483 (X70) pipe material from JMatPro.

curve for the temperature dependence of the yield stress was obtained for each composition by linear interpolation between the data points at test temperatures of 25°C, 200°C, and 350°C. The four samples of pipe exhibit significant variation in the room temperature yield strength (505-575 MPa) as well as the change in strength from 25–200°C (−0.17 to +0.03 MPa/°C) and from 200–350°C (−0.63 to −0.13 MPa/°C). This observed change in strength is in approximate agreement with the limiting values proposed in other literature; the DNV offshore submarine pipe design standard [97] specifies a factor equivalent to −0.46 MPa/°C for C-Mn steels within a temperature range of 50–200°C.

Table 5.1 contains estimates for the yield temperatures, effective CTE, and factor  $H$  using the combined data from Ref. [96] and Figure 5.2. The calculation of  $H$  uses a value for the elastic modulus at the preheat temperature ( $T_0$ ) and for the volumetric specific heat capacity ( $\rho c$ ) at the first yield temperature ( $\Delta T_{Y1} + T_0$ ). Values were obtained for preheat temperatures ranging from ambient to 150°C. A

value of  $H = 0.23$  was found to result in an error of  $<10\%$  throughout this range. This value is in close agreement with the theoretical estimate as well as the approximate value of  $H = 0.2$  proposed in existing theoretical and experimental work on C-Mn structural steels [44].

Table 5.1: Calculated values of the first yield temperature change  $\Delta T_{Y1}$  (Equation (5.2)) and non-dimensional coefficient  $H$  (Equation (5.5)) for CSA Gr.483 (X70) pipe with a preheat of  $T_0 = 25 - 150^\circ\text{C}$ .

ID	$T_0$ [ $^\circ\text{C}$ ]	$\Delta T_{Y1}$ [ $^\circ\text{C}$ ]	$\Delta T_{Y2}/\Delta T_{Y1}$	$E\alpha_{\text{eff}}/\rho c$	$H$
483A	25	190	1.77	0.874	0.242
	50	185	1.79	0.863	0.244
	100	174	1.84	0.838	0.246
	150	164	1.88	0.810	0.248
483B	25	193	1.91	0.756	0.236
	50	190	1.91	0.743	0.233
	100	186	1.92	0.715	0.227
	150	182	1.94	0.684	0.219
483C	25	211	1.82	0.807	0.234
	50	207	1.84	0.794	0.233
	100	199	1.87	0.767	0.232
	150	191	1.90	0.737	0.229
483D	25	177	1.95	0.748	0.242
	50	175	1.95	0.735	0.238
	100	172	1.95	0.708	0.229
	150	169	1.95	0.677	0.220

It should be noted that the higher preheats result in values for  $T_{Y1}$  and  $T_{Y2}$  that exceed the range of experimental data from Ref. [96]. Approximate values for the yield stress at temperatures in excess of  $350^{\circ}\text{C}$  were obtained from linear extrapolation using the same rate of decrease as from  $200\text{--}350^{\circ}\text{C}$ . If rather than remaining constant, this rate is assumed to increase at higher temperatures, the resulting values of  $H$  are closer to the room temperature values. If this rate were instead to decrease, the effect of preheat on the value of  $H$  would be slightly magnified. Data on high temperature derating factors for in-service pipelines provides some evidence to suggest that the latter case is more likely [98]. The potential error due to extrapolation was bounded by recalculating values for  $H$  at the highest preheat ( $T_0 = 150^{\circ}\text{C}$ ) and the limiting case of a constant yield strength above  $350^{\circ}$ . The average value of the first yield temperature was unaffected ( $\Delta T_{Y1} = 176^{\circ}\text{C}$ ) while the average value of the second yield temperature increased by  $19^{\circ}\text{C}$  (from  $\Delta T_{Y2} = 339^{\circ}\text{C}$  to  $358^{\circ}\text{C}$ ). This resulted in an increase to the average value of the yield temperature ratio (from 1.92 to 2.03) and a decrease in the average value of  $E\alpha_{\text{eff}}/\rho c$  (from 0.727 to 0.649). The resulting effect on the mean value of  $H$  was found to be minimal ( $\approx 3\%$  decrease) therefore verifying that the extrapolated values are acceptable. Ref. [44] also proposes a modifier for preheat which is equivalent to a reduction factor of 0.95 for a preheat temperature of  $T_0 = 150^{\circ}\text{C}$ . Although there is some lack of clarity on the methodology used to validate this modifier, the values of  $H$  at  $150^{\circ}\text{C}$  in Table 5.1 are on average  $\approx 95\%$  of the values at  $25^{\circ}\text{C}$ . The similarity with the literature value further supports the viability of the results obtained here.

In industrial practice, the welding heat input is typically calculated based on the linear rate of electrical energy input according to the formula  $Q' = VI/U$  where  $V$  is the welding voltage,  $I$  is the welding current, and  $U$  is the welding travel speed. Substituting this heat input directly into Equation (5.1) would produce erroneous results as it does not account for the losses incurred during transfer of the electrical energy in the arc to thermal energy in the plate. The standard method to account for

these losses is to include an arc efficiency factor ( $\eta$ ) which can range anywhere from 0.2–0.99 depending on the welding process. For the SMAW process, the arc efficiency factor on steel varies from 0.75–0.85 with a mean value of 0.8 [99]. This results in a final practical formula for pipeline welding of  $F_{\text{Ten}} = H\eta Q' \approx 0.18Q'$ .

### 5.3.2 Angular Distortion

Application of the tendon force concept to pipe geometry results in a circumferential load that tends to produce radial displacement and angular rotation as shown in Figure 5.3. The reactionary bending stresses accompanying this distortion have been previously studied for full penetration, single pass welds on tubular joints [37, 55], as well as for a multi-pass, partial penetration joint with dissimilar filler material [100]. In the former case, it is appropriate to treat the joint as a continuous cylinder with a load applied at the midpoint, and in the latter, each half of the joint is considered separately with the weld treated as a plastic hinge.

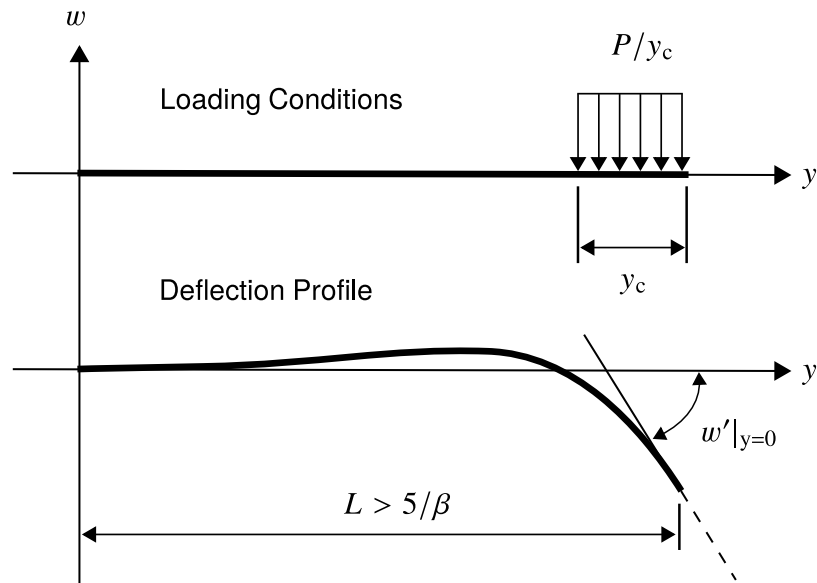


Figure 5.3: Deflection profile due to distributed radial load ( $P$ ) over a distance ( $y_c$ ) from the pipe end.

Consideration of a partially complete (i.e., root pass only) pipeline girth weld requires a modified mathematical formulation since this geometry lies between the

two cases studied formerly. The angular rotation of a semi-infinite thin cylindrical shell with a concentrated radial load ( $P$ ) at one end ( $y = 0$ ) is given by the following expression [88]:

$$w'(y) = \frac{P}{2\beta^2 D} \exp(-\beta y) (\cos \beta y + \sin \beta y) \quad (5.6)$$

The parameter  $D$  is the flexural rigidity of the pipe and has units of force  $\times$  length. The geometric parameter  $\beta$  has units of inverse length. These parameters are defined as:

$$\beta^4 = \frac{3(1 - \nu^2)}{a^2 d^2} \quad \text{and} \quad D = \frac{E d^3}{12(1 - \nu^2)}$$

where  $\nu$  is Poisson's ratio,  $a$  is the pipe radius,  $d$  is the pipe wall thickness, and  $E$  is the elastic modulus.

The tendon force given in Equation (5.1) is transformed into an equivalent radial load by dividing by the pipe diameter such that  $P = F_{\text{Ten}}/2a$ . Applying this load independently to each end of the two joining pipe segments results in a symmetric angular distortion of:

$$w'|_{y=0} = \frac{\sqrt{3(1 - \nu^2)} H \eta Q'}{E d^2} \quad (5.7)$$

The above formulae are valid if two conditions are met: (1) the pipe must have a sufficient length to be treated as semi-infinite ( $L > 5/\beta$  [88]); and (2) the ratio of pipe radius/wall thickness must be sufficient to treat it as a thin shell ( $a/d > 20$  [101]).

### 5.3.3 Correction Factor for Tendon Force Distribution

Consideration of the tendon force as a concentrated line load is only suitable if the plastic strain zone from welding is relatively small compared to the characteristic length  $1/\beta$ , which may not always be true for pipeline welding. It is necessary there-

fore to apply a correction to Equation (5.7) which accounts for the distribution of the tendon force over a critical length ( $y_c$ ) as shown in Figure 5.3. An expression for this correction factor is obtained as [88]:

$$f_D(\Pi_1) = \frac{\exp(-\Pi_1) \sin \Pi_1}{\Pi_1} \quad (5.8)$$

$$\Pi_1 = \beta y_c \quad (5.9)$$

The plastic strain distribution used to derive the tendon force in Equation (5.1) yields  $y_c \approx \ln(2)y_{pl}$  where the size of the plastic region ( $y_{pl}$ ) corresponds to the maximum half-width of the first yield temperature isotherm ( $\Delta T_{Y1}$ ). This dimension may be approximated for a 2-D temperature field using the asymptotic Rosenthal equation [40]:

$$y_{pl} = \frac{1}{\sqrt{2\pi e}} \frac{\eta Q'}{d} \frac{1}{\rho c} \frac{1}{\Delta T_{Y1}} \quad (5.10)$$

Note that for CSA Gr.483 (X70) line pipe it is reasonable to use  $\sqrt{2\pi e} \rho c \Delta T_{Y1} \approx 1/330 \text{ kJ/mm}^3$ .

The non-dimensional parameter  $\Pi_1$  may be interpreted as the normalized width of the effective plastic zone. The 2-D Rosenthal model captures the primary factors which control the size and shape of the thermal field produced under typical pipeline welding conditions. Secondary effects, such as heat dissipation and the possibility for an uneven distribution of heat between the pipe segments are not considered here, but may be compensated with additional correction factors if necessary.

### 5.3.4 Correction Factor for Resistance of Weld Bead

Equation (5.7) assumes each of the two pipe segments are free to deform independently. In reality, the presence of the weld metal joining these two components will influence the distortion at the pipe end due to reactionary bending stresses and strains

which develop in the weld metal.

Figure 5.4 illustrates the relevant geometry and resulting strain distribution from treatment of the root pass as a 1-D beam. This simplified representation is well suited to identification of the parametric dependence for stress and strain developed in the weld metal. The bending stress is proportional to the ratio of weld bead thickness/width ( $c/g$ ) and the total angular distortion of the weld bead ( $\theta = 2w'|_{y=0}$ ).

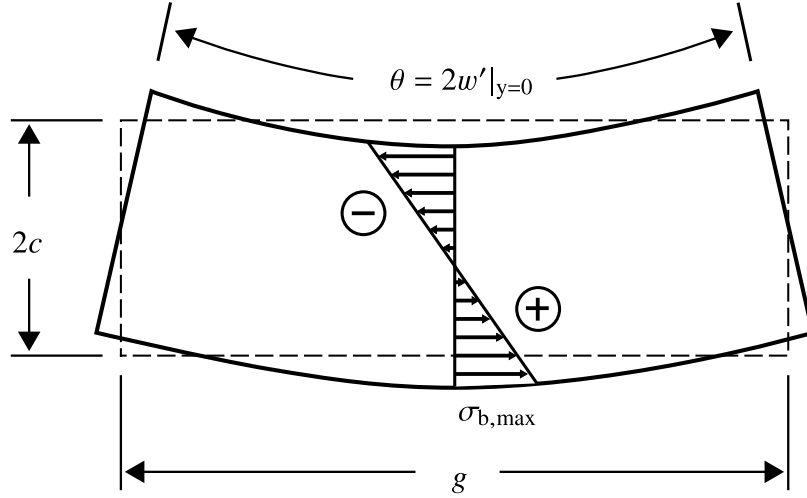


Figure 5.4: Geometry and bending stress distribution resulting from 1-D beam approximation of weld root pass.

The maximum tensile bending strain is expected to occur at the inside surface of the weld root with a magnitude of  $\sigma_{b,max}/E = (\theta/2)(c/g)$ . This estimate requires correction for the 2-D weld bead geometry as well as the presence of a bevel at the pipe end. This is done by introducing the empirical fitting parameters  $m$  and  $n$  so that the relationship between the root strain and deflection may be fit to a general power law of the form:

$$\frac{\sigma_{b,max}}{E} = \frac{\theta}{2} m \left( \frac{c}{g} \right)^n \quad (5.11)$$

Assuming bending stress is linearly distributed over the thickness, the bending

moment associated with this maximum stress level is given by:

$$M = \frac{\theta E c^2}{3} m \left( \frac{c}{g} \right)^n \quad (5.12)$$

Equation (5.12) is substituted into the expression given by Ref. [88] for a moment applied to the end of a semi-infinite cylinder to obtain a correction factor for the effect of the weld moment:

$$f_M(\Pi_2) = \frac{1}{1 + \Pi_2} \quad (5.13)$$

$$\Pi_2 = \frac{8(1 - \nu^2)}{\beta d} \left( \frac{c}{d} \right)^2 m \left( \frac{c}{g} \right)^n \quad (5.14)$$

Values of  $m = 0.625$  and  $n = 0.5$  were selected based on the results of the numerical validation performed in the following section. The non-dimensional parameter  $\Pi_2$  may be interpreted as the ratio of the rotational bending stiffness of the weld bead to the rotational bending stiffness of the pipe wall.

Under certain conditions, the stresses predicted by Equation (5.11) may produce yielding in the weld material. In this case, the bending stress will not follow a linear distribution through the thickness, but will be truncated at the maximum allowable value limited by yield. Significant hoop stresses may also be present and the resulting biaxial stress state must be considered to identify the yield criterion. The “true” correction factor could therefore be somewhat higher than the value predicted by Equation (5.13). The limiting case of  $f_M = 1$  corresponds to a condition in which yielding limits the reaction moment to a value that is negligible compared to the tendon force. This is the case for the low melting point dissimilar weld metal studied by Ref. [100] in which the weld was assumed to behave as a plastic hinge.

### 5.3.5 Susceptibility Index

Including the effects of the above correction factors, the total angular distortion of the weld bead ( $\theta = 2w'|_{y=0}$ ) is:

$$\theta = \frac{2\sqrt{3(1-\nu^2)} H\eta Q'}{E d^2} f_D f_M \quad (5.15)$$

It is expected that the propensity for latent discontinuity formation is related to the magnitude of the strain at the weld root (Equation (5.11)). Substituting in Equation (5.15) the weld root strain is therefore expressed as the susceptibility index:

$$\mathbf{I}_{\text{root}} = \frac{H\eta Q' c^{0.5}}{E d^2 g^{0.5}} f_D f_M \quad (5.16)$$

Note that the coefficient from Equation (5.15) has been eliminated by substituting in the Poisson's ratio for steel ( $\nu = 0.3$ ) which gives  $2\sqrt{3(1-\nu^2)} (0.625/2) \approx 1$ . A higher index value corresponds to greater strain and indicates a weld that is more susceptible to latent discontinuities.

### 5.3.6 Numerical Validation

Validation of the susceptibility index (Equation (5.16)) and related correction factors (Equation (5.8) and Equation (5.13)) is performed using an axisymmetric numerical simulation in COMSOL Multiphysics [102]. Validation of the model relating the tendon force (Equation (5.1)) to the welding parameters is presented elsewhere [44, 50] and is beyond the scope of this work. All simulations in this study employ a static structural analysis with constant material properties. The pipe is assumed to be a homogeneous, isotropic, linear elastic material with an elastic modulus of  $E = 2 \times 10^5$  MPa and Poisson's ratio of  $\nu = 0.3$ . The tendon force is applied as a distributed radial load to the pipe body with a magnitude according to Equation (5.1). These simulations use the theoretical distribution of plastic strain proposed in Ref. [43],

which is constant from  $y = 0$  to  $y_{\text{pl}}/2$  and varies inversely with distance between  $y_{\text{pl}}/2$  and  $y_{\text{pl}}$ , where the plastic zone width ( $y_{\text{pl}}$ ) is computed using Equation (5.10).

Appropriate ranges for each of the relevant welding parameters and geometric variables were selected based on typical modern North American construction practices as shown in Table 5.2. The simulations were performed for selected combinations of wall thickness ( $d = \{6.35, 12.7, 15.9\}$  mm), pipe diameter ( $2a = \{0.51, 0.91, 1.2\}$  m), heat input ( $Q' = \{0.60, 1.2, 1.8\}$  kJ/mm), weld thickness ( $2c = \{1.2, 3.2\}$  mm), and weld width/thickness ratios of ( $g/c = \{2, 4\}$ ). The weld width/thickness ratio is parametrized rather than varying  $g$  directly to ensure all tests used realistic weld shapes. A pipe wall thickness in excess of 15.9 mm is possible for larger diameter pipes. This analysis is applicable to wall thickness beyond the range used for validation provided the thin shell condition ( $a/d > 20$ ) is satisfied.

The correction factor for the distribution of the tendon force is validated by plotting the results of the numerical simulations against the normalized plastic zone width  $\Pi_1$  in Figure 5.5. The independent parameter  $\Pi_1$  has a functional dependence on  $Q' a^{-0.5} d^{-1.5}$ . For the parameter range tested, the lowest value for this correction factor was  $\approx 0.14$ . The two strongest dependencies (heat input, wall thickness) also correspond to variables which have significant allowable variation per the typical industrial practice for development of weld procedures.

The correction factor for the weld moment is validated by plotting the results of the numerical simulations against the normalized weld bead resistance  $\Pi_2$  in Figure 5.6. The best fit was obtained for a value of the empirical factor of  $n = 0.5$  and therefore the independent parameter  $\Pi_2$  has a functional dependence on  $d^{-2.5} g^{-0.5} c^{2.5} a^{0.5}$ .

The lowest value for this correction factor ( $\approx 0.4$ ) is greater than for the distribution correction factor but overall the significance of  $f_D$  and  $f_M$  are comparable. The pipe wall thickness ( $d$ ) and pipe radius ( $a$ ) appear in both parameters  $\Pi_1$  and  $\Pi_2$ . Considering together the correction factors  $f_D$  and  $f_M$ , the influence of pipe wall thickness is magnified while the effect of pipe radius is lessened.

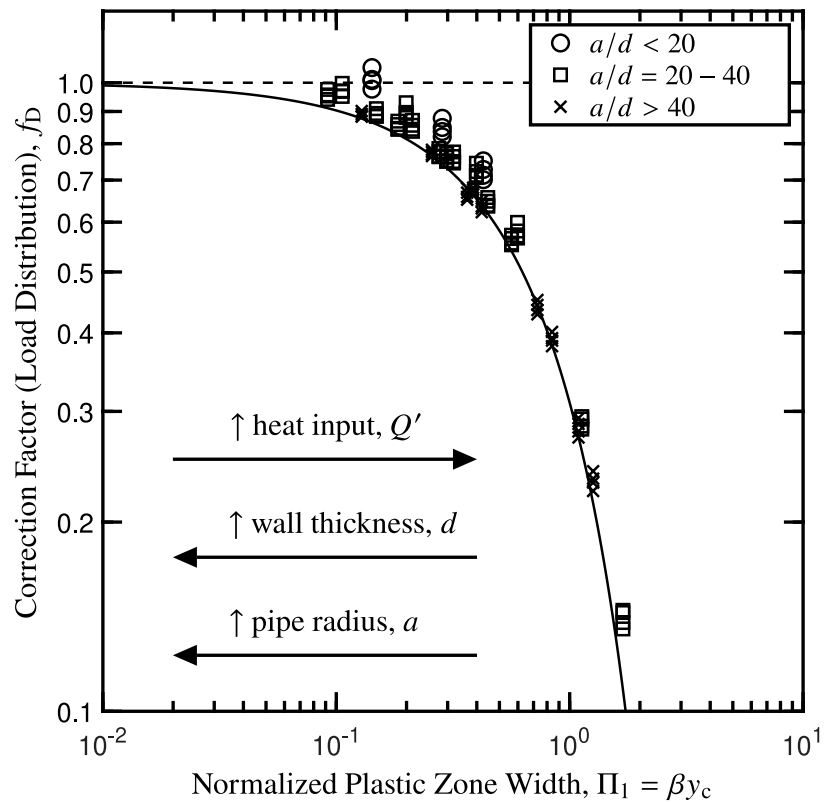


Figure 5.5: Numerical validation of the correction factor on the susceptibility index to account for distribution of the tendon force over a length ( $y_c$ ) from the pipe end.

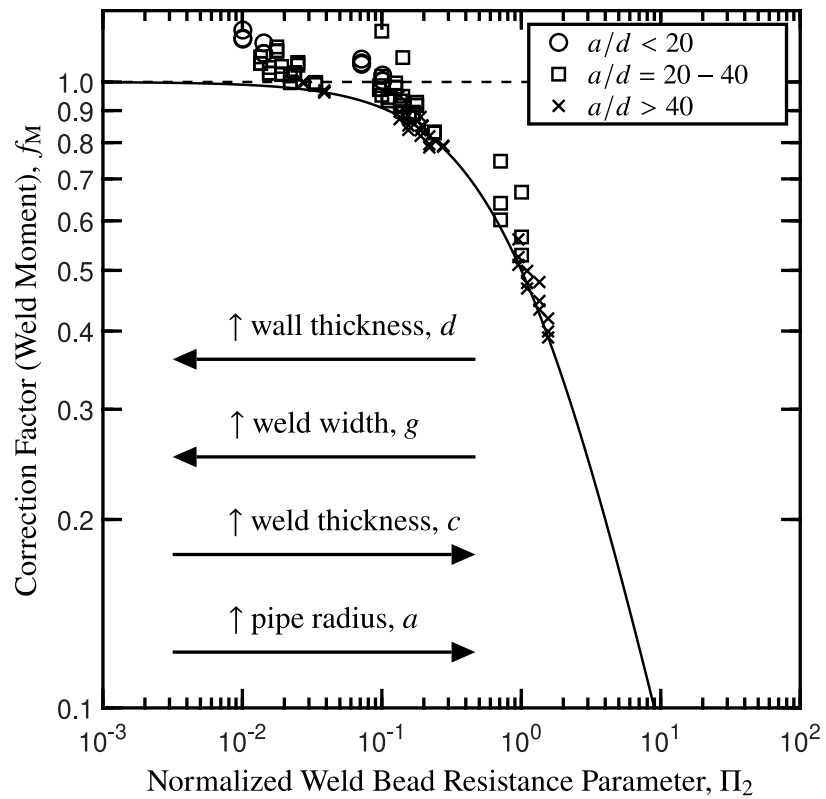


Figure 5.6: Numerical validation of the correction factor on the susceptibility index to account for the effect of a reactionary moment in the weld bead.

Table 5.2: Parameter ranges for root pass welding with SMAW on CSA Gr.483 (X70) pipe material.

Parameter	Typical	Minimum	Maximum
Pipe Diameter, $2a$	0.91 m (36 in.)	0.51 m (20 in.)	1.2 m (48 in.)
Wall Thickness, $d$	12.7 mm (0.500 in.)	6.35 mm (0.250 in.)	15.9 mm (0.625 in.)
Heat Input, $Q'$	1.2 kJ/mm (30 kJ/in.)	0.60 kJ/mm (15 kJ/in.)	1.8 kJ/mm (45 kJ/in.)
Weld Thickness, $2c$	2.4 mm (3/32 in.)	1.2 mm (3/64 in.)	3.2 mm (1/8 in.)
Weld Width, $g$	3.2 mm (1/8 in.)	1.2 mm (3/64 in.)	6.4 mm (1/4 in.)

The maximum deviation from the predicted correction factors is observed to be on the order of  $\approx 10\%$  with a significant negative bias (i.e., overcorrection). These deviations are primarily associated with values for the ratio of pipe radius to wall thickness which fail to satisfy the thin shell criterion ( $a/d > 20$ ). Under such conditions the pipe will be more resistant to deformation than expected resulting in less angular distortion and higher apparent correction factors.



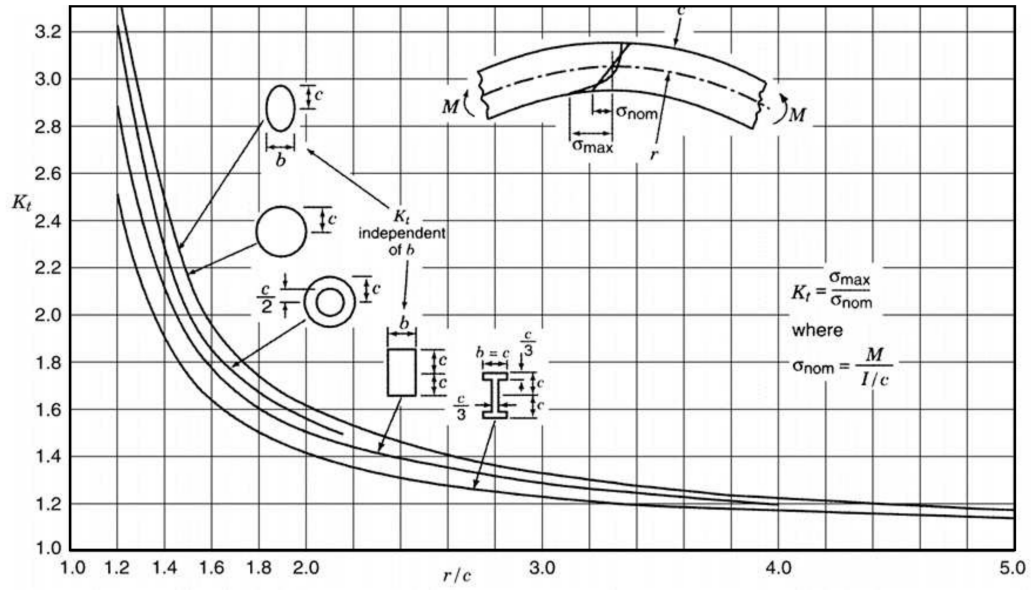


Figure 5.8: Stress concentration factor for a curved beam in bending. Source: Pilkey 1997, chart 5.14, p. 425 [103]. Reproduced with permission of John Wiley & Sons Inc.

with the mid-line of the weld bead. The relationship between this radius and the weld bead geometry is given by:

$$r = c + \delta \frac{\sqrt{1 + (g/\delta)^2}}{2 \sin(\phi/2)} \quad g/\delta \geq 1 \quad (5.17)$$

$$\phi = \pi - 2 \tan^{-1}(g/\delta)$$

Note that if Equation (5.17) is normalized by the weld thickness, the ratio  $r/c$  may be expressed as a function of only the two parameters  $g/\delta$  and  $c/\delta$ . These parameters are the ratios of the weld bead width and thickness to high-low offset. Equation (5.17) is valid within the restricted domain  $g/\delta \geq 1$ . This should not be interpreted as a limit on high-low offset, but rather a limit on the bead width so it is not less than the offset. This condition is appropriate as a larger high-low offset will typically necessitate a larger root gap and consequently a larger weld width to achieve adequate penetration.

An analytical expression for the stress concentration factor is obtained by fitting a power law of the form  $1 + ax^{-b}$  to the data reported by Ref. [103] for values of  $r/c > 2$ . The best fit coefficients are obtained as  $a = 1.296$  and  $b = 1.362$ . The limited domain for fitting was selected to provide the optimal fit within the range of interest. Referring to Equation (5.17), values of  $r/c < 2$  correspond to relatively small values of the ratio  $g/\delta$  coupled with relatively large values of the ratio  $c/\delta$ . Given that the weld thickness and weld width are typically similar in magnitude, the range  $r/c > 2$  then encompasses most conditions of practical relevance.

The stress concentration factor ( $K_t \geq 1$ ) can be converted into an equivalent correction factor ( $0 < f_G < 1$ ) by inverting the expression such that  $f_G = 1/K_t$ . The correction factor for non-ideal geometry is therefore:

$$f_G(\Pi_3) = \frac{1}{1 + 1.296 \Pi_3^{1.362}} \quad (5.18)$$

$$\Pi_3 = c/r \quad (5.19)$$

The independent parameter  $\Pi_3$  is the ratio of the weld bead thickness to the effective radius of curvature (Equation (5.17)).

### 5.4.3 Modified Susceptibility Index

The susceptibility index proposed for ideal geometry (Equation (5.16)) is adapted to consider high-low offset by introducing the non-ideal geometry correction factor ( $f_G$ ):

$$\mathbf{I}_{\text{root}} = \frac{H\eta Q' c^{0.5} f_D f_M}{E d^2 g^{0.5} f_G} \quad (5.20)$$

where for CSA Gr.483 (X70) line pipe material  $H\eta \approx 0.18$  and  $E \approx 2 \times 10^5$  MPa (based on Figure 5.2 at typical preheat temperature).

Note that the non-ideal geometry correction factor (Equation (5.18)) depends on only the parameter  $\Pi_3 = c/r$ . Since this parameter is a unique function of the

normalized weld bead width ( $g/\delta$ ) and thickness ( $c/\delta$ ), the influence of the high-low offset may not be separated from the bead geometry. A single acceptable tolerance for  $\delta$  will result in dramatically different stress concentration factors depending on the size of the weld bead. This is a key distinction from the existing methodologies for assessing high-low offset which specify a limiting value irrespective of the welding procedure and fit-up.

#### 5.4.4 Numerical Validation

Validation of the proposed non-ideal geometry correction factor was performed using a 2-D plane stress analysis with COMSOL Multiphysics. To isolate the effect of non-ideal geometry, these simulations only considered a reduced portion of the weld cross-section in the immediate vicinity of the weld joint. A specified angular distortion ( $\theta$ ) was applied to the cross-section and the resulting maximum strain on the bottom surface of the weld root was recorded. Preliminary testing verified that the results were independent of pipe wall thickness and angular distortion so constant values of  $d = 12.7$  mm and  $\theta = 0.01$  rad were used.

The geometry was varied parametrically to consider the same combinations of weld bead thickness ( $2c$ ) and width/thickness ratios ( $g/c$ ) that were used for the previous numerical validation. Each combination of parameters was tested with values of high-low offset which resulted in the ratios  $\delta/c = \{0.1, 0.25, 0.5, 0.75, 1, 2\}$ . The correction factor was computed for each case as the magnitude of the maximum strain divided by the maximum strain with the same geometry and a negligible level of high-low offset (i.e.,  $\delta/c = 0.01$ ).

The high-low offset was parametrized relative to the weld thickness to test the widest range of possible values for  $\delta$  while maintaining a weld geometry which is representative of reality. These ranges also ensured that for all tests the ratio  $\delta/g$  was within the allowable domain of Equation (5.18) (i.e.,  $\delta/g \leq 1$ ). The results of the parametric study are shown in Figure 5.9.

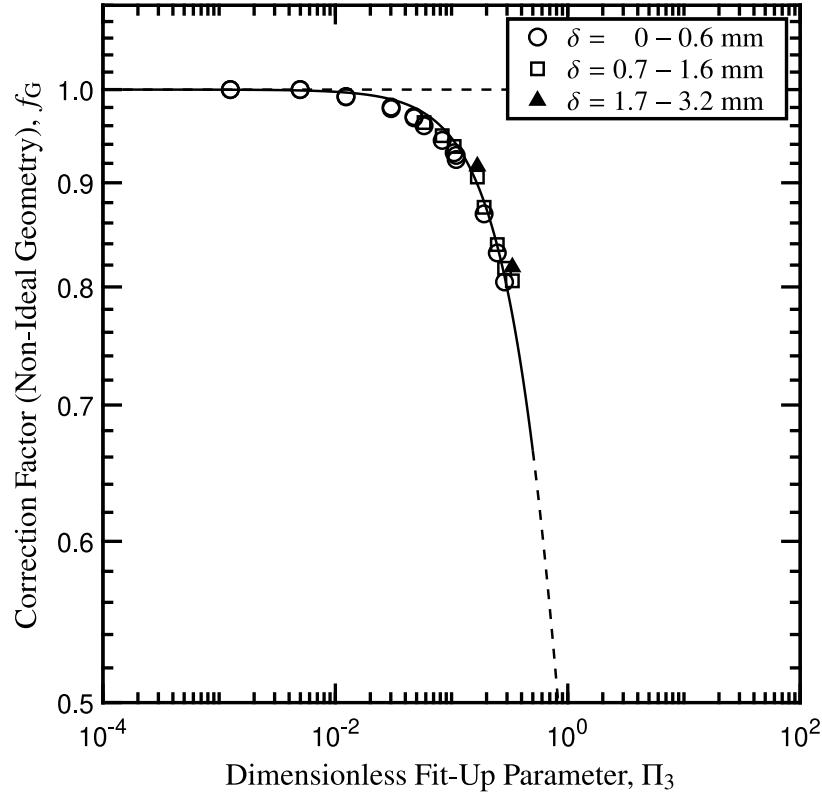


Figure 5.9: Numerical validation of the proposed correction factor on the susceptibility index to account for the effect of high-low offset.

In all cases, good agreement was obtained between the numerical simulations and the theoretical curve given by Equation (5.18). As may be expected, the highest values for the correction factor (i.e.,  $f_G \approx 1$ ) were associated with decreased high-low offset. Note that some values of the high-low offset above the recommended limit in CSA Z662 of 1.6 mm (indicated in Figure 5.9 with solid markers) resulted in a larger correction factor (i.e., less susceptible weld) than tests with a high-low offset below the recommended limit. Equation (5.17) shows that the effect of the non-ideal geometry depends on the ratio of high-low offset to the weld bead width and height rather than the value of the high-low offset itself. The results of these simulations highlight the utility of the proposed susceptibility index compared to a single permissible limit for the high-low offset.

## 5.5 Case Study

The root susceptibility index (Equation (5.20)) provides a quantitative measure of the propensity for latent discontinuities in a given welding procedure and joint geometry. Comparison of this index to a threshold value may be used as a go/no-go assessment prior to welding, or as a tool for practitioners to rank and compare different welding practices.

Figure 5.10 presents two procedures on a pipe with a diameter of 0.91 m and a wall thickness of 12.7 mm. Table 5.3 contains values of the susceptibility index for these procedures with varying amounts of high-low offset.

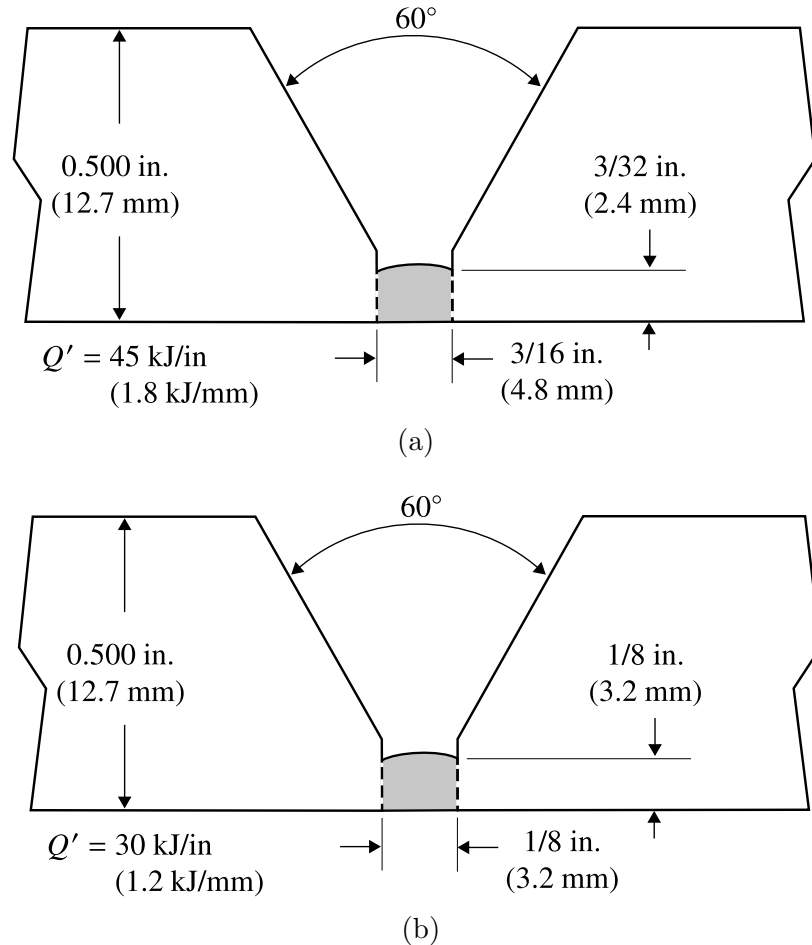


Figure 5.10: Welding variables and geometry for (a) a procedure with a higher heat input and a thinner, wider weld bead; and (b) a procedure with a lower heat input and a thicker, narrower weld bead.

Table 5.3: Comparison of latent discontinuity susceptibility for two different SMAW root pass weld procedures on 36 in. (0.91 m) diameter, CSA Gr.483 (X70) pipe material with varying levels of high-low offset.

	Procedure A			Procedure B		
$\Pi_1$ / $f_D$	0.44	0.63		0.29	0.74	
$\Pi_2$ / $f_M$	0.09	0.91		0.24	0.81	
$\delta$ [mm]	0	1.6	3.2	0	1.6	3.2
$\Pi_3$	–	0.13	0.19	–	0.29	0.33
$f_G$	1	0.93	0.88	1	0.81	0.78
$I_{\text{root}}$ [mm/m]	2.9	3.1	3.3	2.8	3.5	3.6

With negligible high-low offset ( $\delta = 0$  mm), the value of the index is larger for procedure A than procedure B indicating that procedure A has a higher probability of latent discontinuity formation. However, with moderate ( $\delta = 1.6$  mm) or severe ( $\delta = 3.2$  mm) amounts of high-low offset, the index for procedure A is observed to be smaller than procedure B. Without an experimentally established threshold value, neither of these indices should be considered unacceptable. It is however demonstrated that procedure B is more sensitive to high-low offset than procedure A. In addition, the qualification weld for procedure B, if made with ideal fit-up, may not give a good indication of the latent discontinuity susceptibility of field welds that experience significant high-low offset.

Incorporation of this index in a simple app or software tool could be used to help facilitate rapid computation in the field. Acceptable ranges for the necessary input data (i.e., heat input, ideal joint fit-up, and bead geometry) could be pre-loaded for a given joint. In addition to a maximum allowable high-low offset, this would provide field engineers and quality inspectors with recommended limits on the procedural ranges to compensate for any larger high-low offset measured in the field.

Consider a hypothetical situation where it has been verified that an index of  $I_{\text{root}} \leq 3.1$  will lead to an acceptably low occurrence of latent discontinuities. For procedure B, it may be readily calculated that the high-low offset should be kept to a maximum of 0.6 mm. Alternatively, limiting the heat input of procedure B to 0.96 kJ/mm will result in acceptable values of the susceptibility index with a high-low offset up to 3.2 mm. The susceptibility index provides practitioners with the flexibility to compute adjustments to their procedures or set limits on fit-up geometry depending on the requirements of a specific job.

## 5.6 Discussion

To arrive at a practical index, a number of simplifying assumptions were necessary. The mechanical restraint of the root pass was considered as a 1-D beam; however, for the typical width/thickness ratio of root passes, a 2-D formulation might be more appropriate. Equation (5.11) aims to capture empirically (based on computer simulations) 2-D implications of actual roots. This correction has so far been tested on root passes with a width/thickness ( $g/c$ ) ratio between 2 and 4.

The joint preparation bevel has mechanical and thermal implications. In formulation of the index, the pipe wall thickness was considered constant, allowing the use of existing solutions for the thermal and solid mechanics problems. The computer simulations considered a bevel of 60 deg, as is typical in practice. The thermal effect of the bevel is expected to be secondary, as the width of the plastic zone is typically larger than the size of the bevel. Welds done at relatively small heat input for a given wall thickness may show larger effects, with Equation (5.10) under predicting the size of the plastic zone. Less material at the bevel would create a smaller tendon force, causing a systematic error in the opposite (compensating) direction of the thermal error.

The index is based on stress concentration at the root of the weld due to high-low offset assuming linear elastic behaviour. Deviation from the simplified geometry

shown in Figure 5.7 may introduce additional local notching effects due to undercut at the weld root. These effects may be present in all welds, including those with minimal high-low offset. The presence of local stress concentrators may be considered using superposition but is complicated by the likelihood of plasticity at the weld root. Ongoing research aims to extend the proposed criterion to include strain concentration in elastic-plastic behaviour. This extension will allow the proper treatment of the weld toe profile at the root, which cannot be incorporated within the current framework.

The proposed index provides a way to rank susceptibility to latent discontinuities, but the determination of a concrete threshold for rejection of a weld requires a large effort of controlled full-scale experiments and data from field welding. As cold cracking and rejection are uncommon, a large number of tests are necessary to propose a statistically significant threshold. Validation of the susceptibility index for a given joint necessitates knowledge of both the weld procedure and fit-up. Application of the index retrospectively has not been possible because rejected field welds are discarded and not all necessary parameters are recorded. Modern integrity and data retention practices should enable the use of future field data to help determine a threshold.

## 5.7 Conclusions

A study of root pass susceptibility to latent discontinuity formation during tie-in welding of pipelines was carried out based on the fundamental theories of heat transfer and solid mechanics. The conclusions are as follows:

- An index is proposed to quantify the susceptibility to latent root discontinuities under conditions of high-low offset. This index is displayed in Equation (5.20) and includes the effect of interactions between bending stresses due to welding plastic strains and a stress concentration at the root. Higher values of this index correspond to a more severe risk of latent discontinuity formation.

- The key variables needed to evaluate the index are the welding heat input, the thickness and width of the root pass, and the pipe wall thickness. In general, the severity of the index is reduced for procedures with decreased heat input, increased wall thickness, and a higher ratio of weld width/thickness.
- The effect of high-low offset is considered with a correction factor shown in Equation (5.18) that depends on the ratio of high-low offset to both the weld bead width and thickness. Correction factors are also presented in Equation (5.8) and Equation (5.13) to account for the secondary effects of the tendon force distribution and the weld bead stiffness.
- Manual welding processes contain an element of operator dependence which should not be ignored. Changes in welding technique in response to non-ideal geometry may result in variation in the weld bead profile and heat input. The effects of these changes may be readily anticipated using the theory presented here.
- The index proposed has been validated against numerical simulations, and is ready to be tested against field data for further validation under industrial conditions, and to determine a practical threshold of acceptance.

## References

- [6] CSA Group, *Oil and Gas Pipeline Systems*. CAN/CSA-Z662, 2019.
- [37] S. Vaidyanathan, A. F. Todaro, and I. Finnie, “Residual stresses due to circumferential welds,” *ASME J. Eng. Mater. Technol.*, vol. 95, no. 4, pp. 233–237, Oct. 1973. DOI: 10.1115/1.3443159.
- [40] D. Rosenthal, “The theory of moving sources of heat and its application to metal treatments,” *Trans. ASME*, vol. 68, no. 11, pp. 849–866, Nov. 1946.
- [43] N. O. Okerblom, *Raschet Deformatsii Metallokonstruktsii pri Svarke [The Calculations of Deformations of Welded Metal Structures]*. Moscow: Mashgiz, 1955 (Transl. by London: HMSO, 1958).
- [44] J. White, “Longitudinal shrinkage of a single pass weld,” *Univ. Cambridge Tech. Rep.*, CUED/C-Struct/TR.57, 1977.
- [46] Sente Software Ltd., *JMatPro* (ver. 11.0), Computer Software, Guildford, UK, 2019. [Online]. Available: [www.sentesoftware.co.uk/jmatpro](http://www.sentesoftware.co.uk/jmatpro).
- [50] S. Okano and M. Mochizuki, “Dominant factors and quantification of tendon force in welded structural materials,” *Trans. JSME* [in Japanese], vol. 81, no. 830, pp. 15–00277, Sept. 2015. DOI: 10.1299/transjsme.15-00277.
- [55] R. H. Legatt, “Residual stresses at girth welds in pipes,” in *Welding in Energy-Related Projects*, 1984, pp. 429–440.
- [64] A. G. Kamtekar, K. D. White, and J. B. Dwight, “Shrinkage stresses in a thin plate with a central weld,” *J. Strain Anal. Eng. Des.*, vol. 12, no. 2, pp. 140–147, Apr. 1977. DOI: 10.1243/03093247V122140.
- [68] F. D. Stacey and J. H. Hodgkinson, “Thermodynamics with the Grüneisen parameter: Fundamentals and applications to high pressure physics and geophysics,” *Phys. Earth Planet. Inter.*, vol. 286, no. 1, pp. 42–68, Jan. 2019. DOI: 10.1016/j.pepi.2018.10.006.
- [69] E. Grüneisen, “Zustand des festen körpers [the state of a solid body],” in *Handbuch der Physik, Bd. 10*, Berlin: Julius Springer, 1926 (Transl. by NASA, 1959), pp. 1–52.
- [88] S. Timoshenko and S. Woinowsky-Krieger, “General theory of cylindrical shells,” in *Theory of Plates and Shells*, 2nd, McGraw-Hill Book Company, 1959, ch. 15, pp. 466–532.
- [90] American Petroleum Institute, *Welding of Pipelines and Related Facilities*. API-1104, 2013.
- [91] H. I. Higdon, C. A. Weickert, R. J. Pick, and D. J. Burns, “Root pass stresses in pipeline girth welds due to lifting,” in *Proc. WIC Pipeline Energy Plant Pip. Conf.* Toronto, Canada: Pergamon Press, 1980, pp. 263–272. DOI: 10.1016/B978-0-08-025368-8.50032-4.

- [92] I. Lotsberg, “Stress concentrations due to misalignment at butt welds in plated structures and at girth welds in tubulars,” *Int. J. Fatigue*, vol. 31, no. 8, pp. 1337–1345, Aug. 2009. DOI: 10.1016/j.ijfatigue.2009.03.005.
- [93] L. Wei, “The effects of classification of misalignment-induced stresses in engineering critical assessments of welded joints with some misalignment,” in *Proc. ASME 2010 Pressure Vessels Pip. Conf.* Bellevue, WA, July 18-22, 2010, (PVP2010-25335), pp. 771–781. DOI: 10.1115/PVP2010-25335.
- [94] O. ÖRJASAETER, “Fatigue of high quality girth welds,” in *Proc. ASME 30th Int. Conf. Ocean Offshore Arct. Eng.* Rotterdam, The Netherlands, June 19-24, 2011, (OMAE2011-50306), pp. 619–627. DOI: 10.1115/OMAE2011-50306.
- [95] M. R. Grams and P. F. Mendez, “Practical considerations for analytical modelling of residual stress,” in *Fabtech/AWS Prof. Program*, Chicago, IL, Nov. 11-14, 2019.
- [96] T. R. Jacobs, D. K. Matlock, K. O. Findley, and L. Collins, “The short and long term effects of elevated temperature on the mechanical properties of line pipe steels,” in *Proc. ASME 11th Int. Pipeline Conf.* Calgary, Canada, Sept. 26-30, 2016, (IPC2016-64568), pp. V003T05A035. DOI: 10.1115/IPC2016-64568.
- [97] Det Norske Veritas AS, *Submarine Pipeline Systems*. DNV-OS-F101, 2013.
- [98] ASME Standards Technology, *Investigation of Temperature Derating Factors for High-Strength Line Pipe*. New York, 2012, ASME STP-PT-049.
- [99] S. Kou, *Welding Metallurgy*, 2nd. Hoboken, NJ: John Wiley & Sons, Inc., 2007.
- [100] S. Vaidyanathan, H. Weiss, and I. Finnie, “A further study of residual stresses in circumferential welds,” *ASME J. Eng. Mater. Technol.*, vol. 95, no. 10, pp. 238–242, Oct. 1973. DOI: 10.1115/1.3443160.
- [101] V. V. Novozhilov, *Thin Shell Theory*, 2nd. Groningen, The Netherlands: P. Noordhoff Ltd., 1964.
- [102] COMSOL, Inc., *COMSOL Multiphysics* (ver. 5.4a), Computer Software, Stockholm, Sweden. [Online]. Available: [www.comsol.com](http://www.comsol.com).
- [103] W. D. Pilkey, *Peterson’s Stress Concentration Factors*, 2nd. New York: John Wiley & Sons, Inc., 1997.

# Chapter 6

## Conclusions and Future Work

### 6.1 Conclusions

A general analytical model is presented for prediction of residual stress and distortion produced due to thermal manufacturing processes. The complex interactions between various thermal-mechanical phenomena are distilled into simple engineering equations suitable for use in procedure development and process design.

The OMS (Order of Magnitude Scaling) technique was used to produce a dimensionless formulation of the thermal stress and strain fields around a moving point heat source. The 2-D Rosenthal model provides analytical expressions for characteristic values of the temperature field. Typical heat source parameters produce a dominant balance that corresponds to uniaxial constraint in the direction of heat source movement. Plasticity effects are incorporated into the linear elastic theory by consideration of plastic strain development when the instantaneous thermal strain exceeds the elastic yield point.

For the first time, a simple, accurate, and general methodology is presented for computing the residual net plastic strain and the associated residual stress distribution. This analytical theory has two key advantages over competing experimental and numerical approaches: (1) there is a clear understanding of the relationship and dependency between input parameters and output characteristic values; and (2) it may be readily adapted to consider the effect of changing heat source properties, new

materials, or variations of any other essential input parameters.

Formal definitions are provided and general formulae are derived for three key attributes of the residual plastic strain distribution: the first yield temperature, the second yield temperature, and the tendon force. The yield temperatures are material properties which describe the respective boundaries of the plastic strain zone during heating and cooling. The aspect ratio of the first yield isotherm is proposed as a novel criterion to confirm the suitability of the uniaxial stress model. The tendon force is proportional to the integral of the residual plastic strain and characterizes the driving force for reaction stresses and geometric distortion. This value is a function of the linear energy input (i.e., heat input), the dimensionless Grüneisen material parameter, and the ratio of the two yield temperatures. In the asymptotic case, a universal factor of  $\hat{H} \approx 0.23$  is found to approximate the relationship between the heat input and tendon force for all metals.

General engineering equations for each characteristic value are presented as the combination of a simple closed-form expression, based on idealized treatment, and correction factors to account for additional complexity. The asymptotic ideal case corresponds to instantaneous line heating of an infinite thin section with constant (i.e., temperature independent) material properties. Secondary phenomena considered expressly in this work include: incomplete thermal constraint, temperature dependent thermal and mechanical properties, and limited rigidity of finite section geometry.

Slower moving, lower power heat sources produce shallower thermal gradients which are not sufficient to establish the complete uniaxial constraint considered for the asymptotic case. An approximate fit is provided to correct for this effect as a function of the aspect ratio of the first yield isotherm. Explicit, exact correction factors for temperature dependent material behaviour are derived based on rigorous mathematical treatment without the need for empirical correlations. The variation of all relevant thermal and mechanical properties is captured accurately using effective values which relate to four independent dimensionless groups. The concept of

compliance is introduced as a measure of the tendency for less rigid sections to considerably deform in reaction to an applied force. Correction factors for the compliance effect are found to be fundamentally dependent on a novel dimensionless parameter, the Okerblom number ( $Ok$ ). For symmetric flat plate geometry, this parameter has a physical interpretation as the normalized equilibrium temperature rise. For all other geometries, this parameter may be calculated as the product of the equilibrium temperature rise and the normalized compliance.

Verification of the theory and assumptions in this work, as well as validation of the results, were carried out at each stage. Comparisons were made with industrial data, experimental results from literature, and simulations performed with state-of-the-art computational weld mechanics software tools. In almost all cases, the deviation between the results and model predictions did not exceed the typical limits for measurement precision ( $\pm 10\%$ ) in industrial practice. To demonstrate their practical utility, the new engineering formulae were applied to several case studies including estimation of the plastic zone size, prediction of distortion during welded fabrication, and design of procedures to achieve specified manufacturing tolerances.

A detailed investigation was also undertaken which applies the proposed methodology to the concrete and immediate industrial concern of non-ideal fit-up in circumferential pipeline joints. A novel index is proposed as a quantitative criterion for acceptance of high-low offset, ranking the susceptibility to latent discontinuities as a function of variables available to practitioners during field welding. The estimations of this index both broadly agree with institutional knowledge and also bring a generality that addresses the uncertainty and limitations of existing guidance.

The analytical procedure, equations, and results presented here represent a powerful and much needed tool to address critical issues in a wide range of industries, including the rapidly developing field of additive manufacturing. The fundamental nature of this work produces a depth of understanding that is unmatched by conventional empirical based approaches. This understanding is embodied in simple,

general, and accurate engineering equations that are ideally suited for incorporation into engineering design guidelines, or codes and standards.

## 6.2 Future Work

The theory presented here provides a fundamental framework for consideration of additional applications and complexity in the future. In particular, the following potential opportunities for expansion upon this work are identified:

- Incorporate the general expressions for tendon force and compliance correction into a linear FEA package; apply this methodology to problems of weld sequence optimization and distortion mitigation.
- Explore the distribution of thermal stress around slow moving heat sources; replace empirical fit for low aspect ratios with blended asymptotic expression.
- Apply the tendon force model to 3-D temperature fields relevant for cladding or deposition of initial passes in additive manufacturing on a thick substrate.
- Develop an explicit criterion for consideration of phase transformations in high strength alloys; derive additional correction factors to compensate for these effects when necessary.
- Extend the compliance concept to include the influence of pre-existing strain relevant for additive manufacturing and multi-pass weld procedures.
- Perform full-scale experimental trials to validate the proposed pipeline root discontinuity susceptibility index.

# Bibliography

- [1] M. Asadi, J. A. Goldak, J. Nielsen, J. Zhou, S. Tchernov, and D. Downey, “Analysis of predicted residual stress in a weld and comparison with experimental data using regression model,” *Int. J. Mech. Mater. Des.*, vol. 5, no. 4, pp. 353–364, Nov. 2009. DOI: 10.1007/s10999-009-9107-5.
- [2] D. Deng, C. Zhang, X. Pu, and W. Liang, “Influence of material model on prediction accuracy of welding residual stress in an austenitic stainless steel multi-pass butt-welded joint,” *J. Mater. Eng. Perform.*, vol. 26, pp. 1494–1505, Mar. 2017. DOI: 10.1007/s11665-017-2626-6.
- [3] T. Mukherjee, W. Zhang, and T. DebRoy, “An improved prediction of residual stresses and distortion in additive manufacturing,” *Comput. Mater. Sci.*, vol. 126, pp. 360–372, Jan. 2017. DOI: 10.1016/j.commatsci.2016.10.003.
- [4] CSA Group, *Certification of companies for fusion welding of steel*. CSA W47.1, 2019.
- [5] ASME, *Welding, brazing, and fusing qualifications*. BPVC-IX, 2019.
- [6] CSA Group, *Oil and Gas Pipeline Systems*. CAN/CSA-Z662, 2019.
- [7] V. Papazoglou and K. Masubuchi, “Integration of M.I.T. studies on prediction and control of distortion in welded aluminum structures,” *M.I.T. Tech. Rep.* (submitted to Office Nav. Res.), Contract No. N00014-75-C-0469, NR 031-773, Sept. 1976.
- [8] S. Kou, “Weld metal solidification cracking,” in *Welding Metallurgy*, 2nd, Hoboken, NJ: John Wiley & Sons, Inc., 2003, ch. 11, pp. 263–300.
- [9] Z. Barsoum and I. Barsoum, “Residual stress effects on fatigue life of welded structures using LEFM,” *Eng. Fail. Anal.*, vol. 16, no. 1, pp. 449–467, Jan. 2009. DOI: 10.1016/j.engfailanal.2008.06.017.
- [10] K. Satoh, “Preheat and restraint versus weld cracking in steel constructions,” *Trans. JWS*, vol. 1, no. 1, pp. 43–50, Apr. 1970.
- [11] N. S. Boulton and H. E. Lance Martin, “Residual stresses in arc-welded plates,” *Proc. Inst. Mech. Eng.*, vol. 133, no. 1, pp. 295–347, June 1936. DOI: 10.1243/pime\_proc\_1936\_133\_017\_02.
- [12] O. E. Rodgers and J. R. Fetcher, “Determination of internal stress from the temperature history to a butt-welded plate,” *Welding J.*, vol. 17, no. 11, pp. 4s–7s, Nov. 1938.

- [13] A. A. Wells, "The mechanics of notch brittle fracture," *Weld. Res.*, vol. 7, no. 2, pp. 34r–56r, Feb. 1953.
- [14] L. Tall, "Residual stresses in welded plates - a theoretical study," *Welding J.*, vol. 43, no. 1, pp. 10s–23s, Jan. 1964.
- [15] K. Masubuchi, F. B. Simmons, and R. E. Monroe, "Analysis of thermal stresses and metal movement during welding," in *Batelle Memorial Institute Tech. Rep.* Restone Arsenal, AL: Redstone Scientific Information Centre, Jul. 1968, RSIC–820.
- [16] Y. Ueda, K. Fukuda, K. Nakacho, and S. Endo, "A new measuring method of residual stresses with the aid of finite element method and reliability of estimated values," *Trans. JWRI*, vol. 4, no. 2, pp. 123–131, Oct. 1975. DOI: 11094/11113.
- [17] P. Michaleris and A. Debiccari, "Prediction of welding distortion," *Welding J.*, vol. 76, no. 4, pp. 172s–181s, Apr. 1997.
- [18] G. H. Jung and C. L. Tsai, "Plasticity-based distortion analysis for fillet welded thin-plate T-joints," *Welding J.*, vol. 83, no. 6, pp. 177s–187s, June 2004.
- [19] L. Zhang, P. Michaleris, and P. Marugabandhu, "Evaluation of applied plastic strain methods for welding distortion prediction," *ASME J. Manuf. Sci. Eng.*, vol. 129, no. 6, pp. 1000–1010, Dec. 2007. DOI: 10.1115/1.2716740.
- [20] Y. Ueda and M. G. Yuan, "Prediction of residual stresses in butt welded plates using inherent strains," *ASME J. Eng. Mater. Technol.*, vol. 115, no. 4, pp. 417–423, Oct. 1993. DOI: 10.1115/1.2904240.
- [21] M. G. Yuan and Y. Ueda, "Prediction of residual stresses in welded T- and I-joints using inherent strains," *ASME J. Eng. Mater. Technol.*, vol. 118, no. 2, pp. 229–234, Apr. 1996. DOI: 10.1115/1.2804892.
- [22] D. Deng and H. Murakawa, "Prediction of welding distortion and residual stress in a thin plate butt-welded joint," *Comput. Mater. Sci.*, vol. 43, no. 2, pp. 353–365, Aug. 2008. DOI: 10.1016/j.commatsci.2007.12.006.
- [23] D. Deng and H. Murakawa, "FEM prediction of buckling distortion induced by welding in thin plate panel structures," *Comput. Mater. Sci.*, vol. 43, no. 4, pp. 591–607, Oct. 2008. DOI: 10.1016/j.commatsci.2008.01.003.
- [24] H. Murakawa, D. Deng, N. Ma, and J. Wang, "Applications of inherent strain and interface element to simulation of welding deformation in thin plate structures," *Comput. Mater. Sci.*, vol. 51, pp. 43–52, Jan. 2012. DOI: 10.1016/j.commatsci.2011.06.040.
- [25] O. W. Blodgett, "Joint design and production: Determining weld size," in *Design of Welded Structures*, Cleveland, OH: The James F. Lincoln Arc Welding Foundation, 1966, ch. 7.4.
- [26] J. B. Dwight and K. E. Moxham, "Welded steel plates in compression," *Struct. Eng.*, vol. 47, no. 2, pp. 49–66, Feb. 1969.

- [27] K. Masubuchi, “Distortion in weldments,” in *Analysis of Welded Structures*, 1st, Oxford, UK: Pergamon Press Ltd., 1980, pp. 235–327.
- [28] O. W. Blodgett and D. K. Miller, “Welded connections,” in *Structural Engineering Handbook*, Boca Raton, FL: CRC Press LLC, 1999, ch. 22.
- [29] N. Hempel, J. R. Bunn, T. Nitschke-Pagel, E. A. Payzant, and K. Dilger, “Study on the residual stress relaxation in girth-welded steel pipes under bending load using diffraction methods,” *Mater. Sci. Eng., A*, vol. 688, pp. 289–300, Mar. 2017. DOI: 10.1016/j.msea.2017.02.005.
- [30] H. Suzuki, J. Katsuyama, and Y. Morii, “Comparison of residual stress distributions of similar and dissimilar thick butt-weld plates,” *J. Solid Mech. Mater. Eng.*, vol. 6, no. 6, pp. 574–583, June 2012. DOI: 10.1299/jmmp.6.574.
- [31] D. Qiao, Z. Feng, W. Zhang, Y. Wang, and P. Crooker, “Modeling of weld residual plastic strain and stress in dissimilar metal butt weld in nuclear reactors,” in *Proc. ASME 2013 Pressure Vessels Pip. Conf.*, Paris, July 14–18, 2013, (PVP2013–9801), pp. V06BT06A091. DOI: 10.1115/pvp2013-98081.
- [32] H. Eisazadeh, A. Achuthan, J. A. Goldak, and D. K. Aidun, “Effect of material properties and mechanical tensioning load on residual stress formation in GTA 304-A36 dissimilar weld,” *J. Mater. Process. Technol.*, vol. 222, pp. 344–355, Aug. 2015. DOI: 10.1016/j.jmatprotec.2015.03.021.
- [33] Y. Lu, Y. Wang, and P. F. Mendez, “Width of thermal features induced by a 2-D moving heat source,” *Int. J. Heat Mass Transfer*, vol. 156, pp. 119793, Aug. 2020. DOI: 10.1016/j.ijheatmasstransfer.2020.119793.
- [34] Y. Lu and P. F. Mendez, “Characteristic values of the temperature field induced by a moving line heat source,” *Int. J. Heat Mass Transfer*, vol. 166, pp. 120671, Feb. 2021. DOI: 10.1016/j.ijheatmasstransfer.2020.120671.
- [35] K. Satoh, “Transient thermal stresses of weld heat-affected zone by both-ends-fixed bar analogy,” *Trans. JWS*, vol. 3, no. 1, pp. 125–134, Apr. 1972.
- [36] M. Watanabe, “Thermal stress and its residual stress of rectangular plate under one-dimensionally distributed temperature,” *J. Zosen Kiokai* [in Japanese], vol. 86, pp. 173–184, 1954. DOI: 10.2534/jjasnaoe1952.1954.86.173.
- [37] S. Vaidyanathan, A. F. Todaro, and I. Finnie, “Residual stresses due to circumferential welds,” *ASME J. Eng. Mater. Technol.*, vol. 95, no. 4, pp. 233–237, Oct. 1973. DOI: 10.1115/1.3443159.
- [38] P. F. Mendez and N. Stier, “OMS: a computer algorithm to develop closed-form solutions to multicoupled multiphysics problems,” Graz-Seggau, Austria: TU Graz, 2012, pp. 219–254.
- [39] P. F. Mendez and T. W. Eagar, “Order of Magnitude Scaling: a systematic approach to approximation and asymptotic scaling of equations in engineering,” *ASME J. Appl. Mech.*, vol. 80, no. 1, pp. 011009, Oct. 2013. DOI: 10.1115/1.4006839.

- [40] D. Rosenthal, “The theory of moving sources of heat and its application to metal treatments,” *Trans. ASME*, vol. 68, no. 11, pp. 849–866, Nov. 1946.
- [41] S. Timoshenko and J. Goodier, *Theory of Elasticity*, 2nd. McGraw-Hill, 1951.
- [42] O. R. Myhr and Ø. Grong, “Dimensionless maps for heat flow analyses in fusion welding,” *Acta Metall. Mater.*, vol. 38, no. 3, pp. 449–460, Mar. 1990. DOI: 10.1016/0956-7151(90)90151-6.
- [43] N. O. Okerblom, *Raschet Deformatsii Metallokonstruktsii pri Svarke [The Calculations of Deformations of Welded Metal Structures]*. Moscow: Mashgiz, 1955 (Transl. by London: HMSO, 1958).
- [44] J. White, “Longitudinal shrinkage of a single pass weld,” *Univ. Cambridge Tech. Rep.*, CUED/C–Struct/TR.57, 1977.
- [45] *The Procedural Handbook of Arc Welding*, 14th. Cleveland, OH: The James F. Lincoln Arc Welding Foundation, 2000.
- [46] Sente Software Ltd., *JMatPro* (ver. 11.0), Computer Software, Guildford, UK, 2019. [Online]. Available: [www.sentesoftware.co.uk/jmatpro](http://www.sentesoftware.co.uk/jmatpro).
- [47] P. F. Mendez, “Characteristic values in the scaling of differential equations in engineering,” *ASME J. Appl. Mech.*, vol. 77, no. 6, pp. 061017, Sept. 2010. DOI: 10.1115/1.4001357.
- [48] G. N. Greaves, A. L. Greer, R. S. Lakes, and T. Rouxel, “Poisson’s ratio and modern materials,” *Nat. Mater.*, vol. 10, no. 11, pp. 823–837, Oct. 2011. DOI: 10.1038/nmat3134.
- [49] S. Li, S. Ren, Y. Zhang, D. Deng, and H. Murakawa, “Numerical investigation of formation mechanism of welding residual stress in P92 steel multi-pass joints,” *J. Mater. Process. Technol.*, vol. 244, pp. 240–252, June 2017. DOI: 10.1016/j.jmatprotec.2017.01.033.
- [50] S. Okano and M. Mochizuki, “Dominant factors and quantification of tendon force in welded structural materials,” *Trans. JSME* [in Japanese], vol. 81, no. 830, pp. 15–00277, Sept. 2015. DOI: 10.1299/transjsme.15-00277.
- [51] P. F. Mendez, “Reduced order models for welding and solidification processes,” *IOP Conf. Ser.: Mater. Sci. Eng.*, vol. 861, pp. 012003, June 2020. DOI: 10.1088/1757-899X/861/1/012003.
- [52] P. F. Mendez, K. E. Tello, and T. J. Lienert, “Scaling of coupled heat transfer and plastic deformation around the pin in friction stir welding,” *Acta Mater.*, vol. 58, no. 18, pp. 6012–6026, Oct. 2010. DOI: 10.1016/j.actamat.2010.07.019.
- [53] American Welding Society, *Standard Welding Terms and Definitions*. AWS A3.0M/A3.0:2020, 2020.
- [54] Y. Lu and P. F. Mendez, “Analytical modelling of moving heat source based on a 3-D conduction model,” in *Proc. CanWeld Conf.*, Montreal, Canada, Sept. 12-13, 2018.

- [55] R. H. Legatt, “Residual stresses at girth welds in pipes,” in *Welding in Energy-Related Projects*, 1984, pp. 429–440.
- [56] M. R. Grams, L. Ludwig, and P. F. Mendez, “A quantitative index to assess the influence of joint fit-up on pipeline weld root discontinuities,” in *Proc. ASME 13th Int. Pipeline Conf.*, Calgary, Canada, Sep. 28–30, 2020, (IPC2020–9706), pp. V003T05A032. DOI: 10.1115/IPC2020-9706.
- [57] D. Camilleri, T. Comlekci, and T. G. F. Gray, “Design support tool for prediction of welding distortion in multiply-stiffened plate structures experimental and computational investigation,” *J. Ship. Prod.*, vol. 21, no. 4, pp. 219–234, Nov. 2005. DOI: 10.5957/jsp.2005.21.4.219.
- [58] C. R. Fisher, L. L. Denault, S. Rhodes, J. Finley, and Y. Gooroochurn, “Computational tool development for weld sequence planning in major assemblies,” *J. Ship. Prod.*, vol. 35, no. 3, pp. 281–288, Aug. 2019. DOI: 10.5957/JSPD.11170054.
- [59] E. R. Denlinger, J. Irwin, and P. Michaleris, “Thermomechanical modeling of additive manufacturing large parts,” *ASME J. of Manuf. Sci. Eng.*, vol. 136, no. 6, pp. 061007, Dec. 2014. DOI: 10.1115/1.4028669.
- [60] O. W. Blodgett, “Joint design and production: Control of shrinkage and distortion,” in *Design of Welded Structures*, Cleveland, OH: The James F. Lincoln Arc Welding Foundation, 1966, ch. 7.7.
- [61] H. Murakawa, D. Deng, N. Ma, and J. Wang, “Applications of inherent strain and interface element to simulation of welding deformation in thin plate structures,” *Comput. Mater. Sci.*, vol. 51, no. 1, pp. 43–52, Jan. 2012. DOI: 10.1016/j.commatsci.2011.06.040.
- [62] P. F. Mendez, Y. Lu, and Y. Wang, “Scaling analysis of a moving point heat source in steady-state on a semi-infinite solid,” *ASME J. Heat Transfer*, vol. 140, no. 8, pp. 081301, Apr. 2018. DOI: 10.1115/1.4039353.
- [63] Y. Wang, Y. Lu, and P. F. Mendez, “Scaling expressions of characteristic values for a moving point heat source in steady state on a semi-infinite solid,” *Int. J. Heat Mass Transfer*, vol. 135, pp. 1118–1129, June 2019. DOI: 10.1016/j.ijheatmasstransfer.2019.02.042.
- [64] A. G. Kamtekar, K. D. White, and J. B. Dwight, “Shrinkage stresses in a thin plate with a central weld,” *J. Strain Anal. Eng. Des.*, vol. 12, no. 2, pp. 140–147, Apr. 1977. DOI: 10.1243/03093247V122140.
- [65] T. Sasayama, K. Masubuchi, and S. Moriguchi, “Longitudinal deformation of long beam due to fillet welding,” *Welding J.*, vol. 34, no. 12, pp. 581s–582s, Dec. 1955.
- [66] M. R. Grams and P. F. Mendez, “Scaling analysis of the thermal stress field produced by a moving point heat source in a thin plate,” *ASME J. Appl. Mech.*, vol. 88, no. 1, pp. 011001, Jan. 2021. DOI: 10.1115/1.4048318.

- [67] A. M. Freudenthal, “Effect of rheological behavior on thermal stresses,” *J. Appl. Phys.*, vol. 25, no. 9, pp. 1110–1117, Sept. 1954. DOI: 10.1063/1.1721824.
- [68] F. D. Stacey and J. H. Hodgkinson, “Thermodynamics with the Grüneisen parameter: Fundamentals and applications to high pressure physics and geophysics,” *Phys. Earth Planet. Inter.*, vol. 286, no. 1, pp. 42–68, Jan. 2019. DOI: 10.1016/j.pepi.2018.10.006.
- [69] E. Grüneisen, “Zustand des festen körpers [the state of a solid body],” in *Handbuch der Physik, Bd. 10*, Berlin: Julius Springer, 1926 (Transl. by NASA, 1959), pp. 1–52.
- [70] V. N. Belomestnykh and E. P. Tesleva, “Interrelation between anharmonicity and lateral strain in quasi-isotropic polycrystalline solids,” *Tech. Phys.*, vol. 49, no. 8, pp. 1098–1100, Aug. 2004. DOI: 10.1134/1.1787679.
- [71] Simufact Engineering GmbH, *Simufact Welding* (ver. 8.0, 2019), Computer Software, Hamburg, Germany. [Online]. Available: [www.simufact.com](http://www.simufact.com).
- [72] The Mathworks, Inc., “Trapezoidal numerical integration (trapz),” in *MATLAB Function Reference(R2020b)*, Natick, MA, 2020, 1–13245–13250. [Online]. Available: [www.mathworks.com/help/pdf\\_doc/matlab/matlab\\_ref.pdf](http://www.mathworks.com/help/pdf_doc/matlab/matlab_ref.pdf).
- [73] S. Timoshenko, “Combined bending and tension,” in *Strength of Materials, Part I: Elementary Theory and Problems*, 2nd, New York: D. Van Nostrand Company, Inc., 1940, ch. 8, pp. 226–260.
- [74] J. J. Vagi, R. E. Monroe, R. M. Evans, and D. C. Martin, “Welding processes: MIG welding,” in *Welding Procedures for Titanium and Titanium Alloys*, NASA, 1965, TM X–53432, pp. 84–102.
- [75] E. R. Denlinger, J. C. Heigel, P. Michaleris, and T. A. Palmer, “Effect of interlayer dwell time on distortion and residual stress in additive manufacturing of titanium and nickel alloys,” *J. Mater. Process. Technol.*, vol. 215, pp. 123–131, Jan. 2015. DOI: 10.1016/j.jmatprotec.2014.07.030.
- [76] L. Bass, J. Milner, T. Gnäupel-Herold, and S. Moylan, “Residual stress in additive manufactured nickel alloy 625 parts,” *J. Manuf. Sci. Eng.*, vol. 140, no. 6, pp. 061004, Mar. 2018. DOI: 10.1115/1.4039063.
- [77] J. D. White, “Longitudinal Stresses in a Member Containing Non-Interacting Welds,” *Univ. Cambridge Tech. Rep.*, CUED/C–Struct/TR.58, 1977.
- [78] T. Terasaki, M. Nakatani, and T. Ishimura, “Study of tendon force generating in welded joint,” *Q. J. Jpn. Weld. Soc.* [in Japanese], vol. 18, no. 3, pp. 479–486, Aug. 2000. DOI: 10.2207/qjjws.18.479.
- [79] T. Terasaki, T. Ishimura, K. Matsuishi, and T. Akiyama, “Study on longitudinal shrinkage of bead on plate,” *Q. J. Jpn. Weld. Soc.* [in Japanese], vol. 20, no. 1, pp. 136–142, Feb. 2002. DOI: 10.2207/qjjws.20.136.

- [80] T. Terasaki, T. Kitamura, I. Kidota, T. Ishimura, and S. Hamashima, “Study on longitudinal shrinkage and bending distortion of fillet T joint,” *Q. J. Jpn. Weld. Soc.* [in Japanese], vol. 21, no. 1, pp. 81–86, Feb. 2003. DOI: 10.2207/qjjws.21.81.
- [81] Y. Wang, Y. Lu, M. R. Grams, A. Hintze Cesaro, and P. F. Mendez, “Asymptotics and blending in the modeling of welding,” *Mathematical Modelling of Weld Phenomena 12*, pp. 907–932, July 2019.
- [82] S. W. Churchill and R. Usagi, “A general expression for the correlation of rates of transfer and other phenomena,” *AIChE Journal*, vol. 18, no. 6, pp. 1121–1128, Nov. 1972. DOI: 10.1002/aic.690180606.
- [83] S. W. Churchill and R. Usagi, “A standardized procedure for the production of correlations in the form of a common empirical equation,” *Ind. Eng. Chem. Fundamen.*, vol. 13, no. 1, pp. 39–44, Feb. 1974. DOI: 10.1021/i160049a008.
- [84] M. R. Grams and P. F. Mendez, “A general expression for the welding tendon force,” *ASME J. Manuf. Sci. Eng.* (under review), 2021.
- [85] Y. Luo, H. Murakawa, and Y. Ueda, “Prediction of welding deformation and residual stress by elastic FEM based on inherent strain (1st Report): Mechanism of inherent strain production,” *Trans. JWRI*, vol. 26, no. 2, pp. 49–57, Dec. 1997. DOI: 11094/7958.
- [86] D. Rosenthal, “Mathematical theory of heat distribution during welding and cutting,” *Welding J.*, vol. 20, no. 5, pp. 220s–234s, May 1941.
- [87] K. Satoh, M. Toyoda, Y. Suita, M. Tanaka, and T. Hirano, “Controlling parameters of residual stresses and deformations in welded thin cylindrical shells,” *Trans. JWS*, vol. 17, no. 1, pp. 3–9, Apr. 1986.
- [88] S. Timoshenko and S. Woinowsky-Krieger, “General theory of cylindrical shells,” in *Theory of Plates and Shells*, 2nd, McGraw-Hill Book Company, 1959, ch. 15, pp. 466–532.
- [89] S. Timoshenko, “Special problems in bending of beams,” in *Strength of Materials, Part II: Advanced Theory and Problems*, 2nd, New York: D. Van Nostrand Company, Inc., 1940, ch. 1, pp. 1–64.
- [90] American Petroleum Institute, *Welding of Pipelines and Related Facilities*. API-1104, 2013.
- [91] H. I. Higdon, C. A. Weickert, R. J. Pick, and D. J. Burns, “Root pass stresses in pipeline girth welds due to lifting,” in *Proc. WIC Pipeline Energy Plant Pip. Conf.* Toronto, Canada: Pergamon Press, 1980, pp. 263–272. DOI: 10.1016/B978-0-08-025368-8.50032-4.
- [92] I. Lotsberg, “Stress concentrations due to misalignment at butt welds in plated structures and at girth welds in tubulars,” *Int. J. Fatigue*, vol. 31, no. 8, pp. 1337–1345, Aug. 2009. DOI: 10.1016/j.ijfatigue.2009.03.005.

- [93] L. Wei, “The effects of classification of misalignment-induced stresses in engineering critical assessments of welded joints with some misalignment,” in *Proc. ASME 2010 Pressure Vessels Pip. Conf.* Bellevue, WA, July 18-22, 2010, (PVP2010-25335), pp. 771–781. DOI: 10.1115/PVP2010-25335.
- [94] O. Örjasaeter, “Fatigue of high quality girth welds,” in *Proc. ASME 30th Int. Conf. Ocean Offshore Arct. Eng.* Rotterdam, The Netherlands, June 19-24, 2011, (OMAE2011-50306), pp. 619–627. DOI: 10.1115/OMAE2011-50306.
- [95] M. R. Grams and P. F. Mendez, “Practical considerations for analytical modelling of residual stress,” in *Fabtech/AWS Prof. Program*, Chicago, IL, Nov. 11-14, 2019.
- [96] T. R. Jacobs, D. K. Matlock, K. O. Findley, and L. Collins, “The short and long term effects of elevated temperature on the mechanical properties of line pipe steels,” in *Proc. ASME 11th Int. Pipeline Conf.* Calgary, Canada, Sept. 26-30, 2016, (IPC2016-64568), pp. V003T05A035. DOI: 10.1115/IPC2016-64568.
- [97] Det Norske Veritas AS, *Submarine Pipeline Systems*. DNV-OS-F101, 2013.
- [98] ASME Standards Technology, *Investigation of Temperature Derating Factors for High-Strength Line Pipe*. New York, 2012, ASME STP-PT-049.
- [99] S. Kou, *Welding Metallurgy*, 2nd. Hoboken, NJ: John Wiley & Sons, Inc., 2007.
- [100] S. Vaidyanathan, H. Weiss, and I. Finnie, “A further study of residual stresses in circumferential welds,” *ASME J. Eng. Mater. Technol.*, vol. 95, no. 10, pp. 238–242, Oct. 1973. DOI: 10.1115/1.3443160.
- [101] V. V. Novozhilov, *Thin Shell Theory*, 2nd. Groningen, The Netherlands: P. Noordhoff Ltd., 1964.
- [102] COMSOL, Inc., *COMSOL Multiphysics* (ver. 5.4a), Computer Software, Stockholm, Sweden. [Online]. Available: [www.comsol.com](http://www.comsol.com).
- [103] W. D. Pilkey, *Peterson’s Stress Concentration Factors*, 2nd. New York: John Wiley & Sons, Inc., 1997.

# Appendix A: Experimental Data

## A.1 Plastic Zone and Tendon Force in Flat Plates

Table A.1: Correction factors for plastic zone and tendon force for centre weld on flat plate; data after Ref. [20], given  $\alpha = 1.2 \times 10^{-5} \text{ K}^{-1}$ ,  $\epsilon_{Y,0} = 1.57 \times 10^{-3}$ ,  $\sigma_{Y,w} = 460 \text{ MPa}$ ,  $\sigma_{Y,b} = 330 \text{ MPa}$ ,  $\hat{y}_{pl} \approx 50 \text{ mm}$ ,  $\hat{F}_{Ten} \approx 158 \text{ kN}$ ,  $S^* = 1$ .

ID	$T_{eq} [^{\circ}\text{C}]$	$Ok = T_{eq}^*$	$y_{pl} [\text{mm}]$	$f_{Y1}$	$F_{Ten} [\text{kN}]$	$f_{Ten}$
01	30	0.229	47.3	0.946	164	1.04
02	50	0.382	45.0	0.900	167	1.06
03	100	0.764	39.1	0.781	156	0.984
04	150	1.145	33.4	0.668	146	0.919
05	200	1.527	28.8	0.577	139	0.878

Table A.2: Correction factor for tendon force in aluminum for centre weld on flat plate ( $d = 10 \text{ mm}$ ,  $l = 1500 \text{ mm}$ ,  $w = 200 - 1500 \text{ mm}$ ); data after Ref. [50], given  $\alpha = 2.4 \times 10^{-5} \text{ K}^{-1}$ ,  $\epsilon_{Y,0} = 2.0 \times 10^{-3}$ ,  $E \approx 75 \text{ GPa}$ ,  $\rho c = 0.0022 \text{ J mm}^{-3} \text{ K}^{-1}$ .

ID	$Q' = 0.60 [\text{kJ/mm}]$		$Q' = 1.2 [\text{kJ/mm}]$	
	$T_{eq}^*$	$f_{Ten}$	$T_{eq}^*$	$f_{Ten}$
01	0.20	0.99	0.41	1.00
02	0.25	0.99	0.50	0.99
03	0.34	0.99	0.67	1.00
04	0.50	1.00	1.01	1.00
05	0.67	0.99	1.35	0.94
06	1.01	0.95	2.02	0.84
07	1.51	0.91	3.03	0.45

Table A.3: Correction factor for tendon force in lower strength structural steel for centre weld on flat plate ( $d = 10$  mm,  $l = 1500$  mm,  $w = 200 - 1500$  mm); data after Ref. [50], given  $\alpha = 1.2 \times 10^{-5}$  K $^{-1}$ ,  $\epsilon_{Y,0} = 2.0 \times 10^{-3}$ ,  $E \approx 200$  GPa,  $\rho c = 0.0040$  J mm $^{-3}$  K $^{-1}$ .

ID	$Q' = 0.60$ [kJ/mm]		$Q' = 1.2$ [kJ/mm]	
	$T_{\text{eq}}^*$	$f_{\text{Ten}}$	$T_{\text{eq}}^*$	$f_{\text{Ten}}$
01	0.06	0.99	0.12	1.01
02	0.07	0.99	0.15	1.01
03	0.10	0.99	0.20	1.01
04	0.15	0.98	0.30	1.01
05	0.20	0.98	0.40	1.01
06	0.30	0.99	0.60	1.01
07	0.45	1.00	0.90	1.00

Table A.4: Correction factor for tendon force in higher strength structural steel for centre weld on flat plate ( $d = 10$  mm,  $l = 1500$  mm, width  $w = 200 - 1500$  mm); data after Ref. [50], given  $\alpha = 1.2 \times 10^{-5}$  K $^{-1}$ ,  $\epsilon_{Y,0} = 4.0 \times 10^{-3}$ ,  $E \approx 200$  GPa,  $\rho c = 0.0040$  J mm $^{-3}$  K $^{-1}$ .

ID	$Q' = 0.60$ [kJ/mm]		$Q' = 1.2$ [kJ/mm]	
	$T_{\text{eq}}^*$	$f_{\text{Ten}}$	$T_{\text{eq}}^*$	$f_{\text{Ten}}$
01	0.03	1.01	0.07	1.01
02	0.04	1.01	0.08	1.01
03	0.05	1.00	0.10	1.01
04	0.07	1.00	0.15	1.00
05	0.10	0.99	0.20	1.00
06	0.15	1.00	0.30	1.00
07	0.22	1.01	0.45	1.00

Table A.5: Correction factor for tendon force in austenitic stainless steel for centre weld on flat plate ( $d = 10$  mm,  $l = 1500$  mm, width  $w = 200 - 1500$  mm); data after Ref. [50], given  $\alpha = 1.8 \times 10^{-5}$  K $^{-1}$ ,  $\epsilon_{Y,0} = 1.4 \times 10^{-3}$ ,  $E \approx 200$  GPa,  $\rho c = 0.0040$  J mm $^{-3}$  K $^{-1}$ .

ID	$Q' = 0.60$ [kJ/mm]		$Q' = 1.2$ [kJ/mm]	
	$T_{\text{eq}}^*$	$f_{\text{Ten}}$	$T_{\text{eq}}^*$	$f_{\text{Ten}}$
01	0.13	0.99	0.26	0.99
02	0.16	0.99	0.32	1.00
03	0.21	1.00	0.43	1.00
04	0.32	0.99	0.64	0.99
05	0.43	1.00	0.86	0.98
06	0.64	0.99	1.28	0.94
07	0.96	0.97	1.93	0.86

## A.2 Plastic Zone and Tendon Force in T-Sections

Table A.6: Geometry of T-sections fabricated from two plates with thickness ( $d$ ), vertical plate height ( $h$ ), horizontal plate width ( $w$ ), and distance ( $z$ ) between mid-thickness of horizontal plate and section centre of gravity; data after Ref. [21].

ID	$d$ [mm]	$h$ [mm]	$w$ [mm]	$z$ [mm]	$A_c$ [mm <sup>2</sup> ]	$I_{yy}$ [mm <sup>4</sup> ]	$S^*$
01	12	800	600	232	$1.68 \times 10^4$	$1.19 \times 10^9$	1.76
02	12	1000	400	361	$1.68 \times 10^4$	$1.88 \times 10^9$	2.17
03	12	500	300	160	$9.60 \times 10^3$	$2.73 \times 10^8$	1.90
04	12	220	200	61	$5.04 \times 10^3$	$2.76 \times 10^7$	1.67
05	12	300	120	111	$5.04 \times 10^3$	$5.21 \times 10^7$	2.20
06	12	190	100	66	$3.48 \times 10^3$	$1.49 \times 10^7$	2.02
07	12	90	120	22	$2.52 \times 10^3$	$2.35 \times 10^6$	1.51
08	12	130	80	44	$2.52 \times 10^3$	$5.20 \times 10^6$	1.94
09	12	100	70	33	$2.04 \times 10^3$	$2.56 \times 10^6$	1.86
10	12	250	200	73	$5.40 \times 10^3$	$3.85 \times 10^7$	1.74
11	12	300	150	104	$5.40 \times 10^3$	$5.62 \times 10^7$	2.04

Table A.7: Correction factors for plastic zone size and tendon force; data after Ref. [21], given  $\alpha = 1.2 \times 10^{-5} \text{ K}^{-1}$ ,  $E = 210 \text{ GPa}$ ,  $\sigma_{Y,w} = 520 \text{ MPa}$ ,  $\sigma_{Y,b} = 330 \text{ MPa}$ ,  $\hat{y}_{pl} = 50 \text{ mm}$ ,  $\hat{F}_{T\text{en}} = 499 \text{ kN}$ .

ID	$T_{\text{eq}}$ [°C]	$T_{\text{eq}}^*$	$S^*$	Ok	$y_{pl}$ [mm]	$f_{Y1}$	$F_{T\text{en}}$ [kN]	$f_{T\text{en}}$
01	30	0.229	1.76	0.403	46.6	0.932	–	–
02	30	0.229	2.17	0.497	46.3	0.926	–	–
03	50	0.382	1.90	0.726	40.2	0.804	–	–
04	100	0.764	1.67	1.28	34.1	0.682	–	–
05	100	0.764	2.20	1.68	28.7	0.574	–	–
06	150	1.145	2.02	2.32	23.0	0.460	412	0.824
07	200	1.527	1.51	2.31	24.2	0.484	–	–
08	200	1.527	1.94	2.96	19.0	0.380	378	0.756
09	250	1.909	1.86	3.56	20.0	0.400	–	–
10	90	0.687	1.74	1.20	35.0	0.700	–	–
11	90	0.687	2.04	1.40	33.0	0.660	–	–

### A.3 Plastic Zone in Circumferential Joints

Table A.8: Geometry and compliance for circumferential joint between two thin cylinders; data after Ref. [87], given  $\nu = 0.3$ .

ID	$d$ [mm]	$r$ [mm]	$L$ [mm]	$\beta$	$S^*$
01	6.0	487	1524	0.024	36
02	8.2	104	292	0.044	13
03	4.5	68	349	0.074	26
04	4.5	106	218	0.059	13
05	4.5	106	328	0.059	19
06	4.5	106	371	0.059	22
07	8.2	104	292	0.044	13
08	8.2	104	292	0.044	13
09	8.2	104	584	0.044	26
10	4.5	80	380	0.068	26
11	4.5	80	190	0.068	13
12	8.2	104	292	0.044	13

Table A.9: Correction factor for plastic zone size; data after Ref. [87], given  $\alpha = 1.2 \times 10^{-5}$ ,  $\epsilon_Y \approx 1.81 \times 10^{-3}$  ( $\sigma_Y = 380$  MPa,  $E = 210$  GPa),  $\Delta T_{Y1} \approx \epsilon_Y/\alpha = 151$  °C.

ID	$T_{eq}$ [°C]	$T_{eq}^*$	$f_S$	Ok	$\hat{y}_{pl}$ [mm]	$y_{pl}$ [mm]	$f_{Y1}$
01	14	0.093	0.52	1.8	34.2	18.1	0.53
02	50	0.332	0.43	1.8	23.4	12.7	0.54
03	50	0.332	0.19	1.6	28.0	17.3	0.62
04	77	0.511	0.31	2.0	26.9	13.7	0.51
05	87	0.577	0.19	2.1	45.8	21.5	0.47
06	94	0.623	0.14	1.9	56.0	29.3	0.52
07	100	0.663	0.23	2.0	46.9	23.9	0.51
08	100	0.663	0.22	1.9	46.9	25.0	0.53
09	100	0.663	–	–	93.7	–	–
10	100	0.663	–	–	61.0	–	–
11	150	0.995	0.17	2.2	45.7	20.7	0.45
12	200	1.326	0.18	3.0	93.7	30.7	0.33

# Appendix B: Simulation Data

## B.1 Effect of Aspect Ratio on Plastic Zone Size

Table B.1: Welding parameters used for numerical studies of plastic zone size for centre weld on flat plate ( $d = 3$  mm,  $l = 2400$  mm,  $w = 2000$  mm).

ID	$q$ [W]	$U$ [mm/s] for $Q'$ [kJ/mm]=		
		0.12	0.24	0.48
01	60	0.50	0.25	0.125
02	120	1.0	0.50	0.25
03	240	2.0	1.0	0.50
04	480	4.0	2.0	1.0
05	960	8.0	4.0	2.0
06	$1.92 \times 10^3$	16	8.0	4.0
07	$3.84 \times 10^3$	32	16	8.0
08	$7.68 \times 10^3$	64	32	16
09	$1.536 \times 10^4$	128	64	32
10	$3.072 \times 10^4$	256	128	64

Table B.2: Numerical results for first yield aspect ratio, plastic zone size, and correction factor for ASTM A36 structural steel ( $\rho c = 0.0037 \text{ J mm}^{-3} \text{ K}^{-1}$ ,  $\Delta T_{Y1} = 80 \text{ }^\circ\text{C}$ ,  $\hat{y}_{\text{pl}} \approx 33 \text{ mm}$ ), and  $Q' = 0.12 \text{ kJ/mm}$ .

ID	$\mathcal{R}$	$y_{\text{max}} _{T_{Y1}} \text{ [mm]}$	$y_{\text{pl}} \text{ [mm]}$	$f_{\mathcal{R}}$
02	1.41	19.7	6.25	0.32
03	2.04	27.8	16.3	0.59
04	3.59	31.1	27.5	0.88
05	6.82	32.5	32.5	1.0
06	13.4	33.1	32.5	0.98
07	26.7	33.1	32.5	0.98
08	53.5	32.8	32.5	0.99
09	108	32.3	32.5	1.0
10	218	32.0	32.5	1.0

Table B.3: Numerical results for first yield aspect ratio, plastic zone size, and correction factor for ASTM A36 structural steel ( $\rho c = 0.0037 \text{ J mm}^{-3} \text{ K}^{-1}$ ,  $\Delta T_{Y1} = 80 \text{ }^\circ\text{C}$ ,  $\hat{y}_{\text{pl}} \approx 65 \text{ mm}$ ), and  $Q' = 0.24 \text{ kJ/mm}$ .

ID	$\mathcal{R}$	$y_{\text{max}} _{T_{Y1}} \text{ [mm]}$	$y_{\text{pl}} \text{ [mm]}$	$f_{\mathcal{R}}$
01	1.32	41.0	13.8	0.34
02	1.99	56.2	32.5	0.58
03	3.53	62.7	47.5	0.76
04	6.76	65.0	57.5	0.88
05	13.4	66.2	62.5	0.94
06	27.2	67.4	62.5	0.93
07	54.9	67.7	62.5	0.92
08	109	67.2	62.5	0.93
09	217	66.7	62.5	0.94
10	430	66.0	62.5	0.95

Table B.4: Numerical results for first yield aspect ratio, plastic zone size, and correction factor for ASTM A36 structural steel ( $\rho c = 0.0037 \text{ J mm}^{-3} \text{ K}^{-1}$ ,  $\Delta T_{Y1} = 80 \text{ }^\circ\text{C}$ ,  $\hat{y}_{\text{pl}} \approx 130 \text{ mm}$ ), and  $Q' = 0.48 \text{ kJ/mm}$ .

ID	$\mathcal{R}$	$y_{\text{max}} _{T_{Y1}} \text{ [mm]}$	$y_{\text{pl}} \text{ [mm]}$	$f_{\mathcal{R}}$
01	1.97	113	52.5	0.47
02	3.50	126	87.5	0.70
03	6.74	131	103	0.78
04	13.4	133	113	0.85
05	26.9	134	113	0.84
06	54.0	135	118	0.87
07	108	135	118	0.87
08	217	135	113	0.83
09	432	134	113	0.84
10	863	135	113	0.84

Table B.5: Numerical results for first yield aspect ratio, plastic zone size, and correction factor for aluminum alloy 6082-T6 ( $\rho c = 0.0025 \text{ J mm}^{-3} \text{ K}^{-1}$ ,  $\Delta T_{Y1} = 59 \text{ }^\circ\text{C}$ ,  $\hat{y}_{\text{pl}} \approx 133 \text{ mm}$ ), and  $Q' = 0.24 \text{ kJ/mm}$ .

ID	$\mathcal{R}$	$y_{\text{max}} _{T_{Y1}} \text{ [mm]}$	$y_{\text{pl}} \text{ [mm]}$	$f_{\mathcal{R}}$
02	1.12	57.0	6.25	0.11
03	1.51	99.6	32.5	0.33
04	2.45	122	62.5	0.51
05	4.51	131	92.5	0.70
06	8.76	134	108	0.80
07	17.5	134	113	0.84
08	35.4	135	113	0.83
09	70.3	134	113	0.84
10	123	132	97.5	0.74

Table B.6: Numerical results for first yield aspect ratio, plastic zone size, and correction factor for 316L stainless steel ( $\rho c = 0.0040 \text{ J mm}^{-3} \text{ K}^{-1}$ ,  $\Delta T_{Y1} = 66 \text{ }^\circ\text{C}$ ,  $\hat{y}_{\text{pl}} \approx 73 \text{ mm}$ ), and  $Q' = 0.24 \text{ kJ/mm}$ .

ID	$\mathcal{R}$	$y_{\text{max}} _{T_{Y1}} \text{ [mm]}$	$y_{\text{pl}} \text{ [mm]}$	$f_{\mathcal{R}}$
01	3.62	71.5	52.5	0.73
02	6.87	73.9	62.5	0.85
03	13.5	74.8	67.5	0.90
04	27.0	75.5	72.5	0.96
05	55.0	77.0	72.5	0.94
06	109	75.9	72.5	0.95
07	215	75.0	72.5	0.97
08	425	74.4	72.5	0.98
09	844	73.9	67.5	0.91
10	1689	74.0	67.5	0.91

Table B.7: Numerical results for first yield aspect ratio, plastic zone size, and correction factor for P91 alloy steel ( $\rho c = 0.0039 \text{ J mm}^{-3} \text{ K}^{-1}$ ,  $\Delta T_{Y1} = 191 \text{ }^\circ\text{C}$ ,  $\hat{y}_{\text{pl}} \approx 26 \text{ mm}$ ), and  $Q' = 0.24 \text{ kJ/mm}$ .

ID	$\mathcal{R}$	$y_{\text{max}} _{T_{Y1}} \text{ [mm]}$	$y_{\text{pl}} \text{ [mm]}$	$f_{\mathcal{R}}$
02	1.84	21.6	8.75	0.41
03	3.09	25.4	16.3	0.64
04	5.71	26.9	21.3	0.79
05	11.1	27.4	23.8	0.87
06	22.2	28.0	27.5	0.98
07	44.4	27.9	27.5	0.98
08	88.9	27.6	27.5	1.0
09	178	27.2	27.5	1.0
10	357	27.0	27.5	1.0

## B.2 Tendon Force

Table B.8: Summary of results from Simufact numerical studies of tendon force for centre weld on flat plate ( $d = 3$  mm,  $l = 2400$  mm,  $w = 1200$  mm).

Material	$Q'$ [kJ/mm]	$y_{pl}$ [mm]	$\sigma_{rxn}$ [MPa]	$F_{Ten}$ [kN]	$H$
ASTM A36	0.12	32.5	-8.58	30.5	0.25
	0.24	62.5	-17.5	62.2	
	0.36	87.5	-25.3	89.9	
P91	0.12	11.3	-6.48	22.4	0.20
	0.24	27.5	-13.7	48.9	
	0.36	37.5	-20.3	72.2	
SS 304	0.12	37.5	-10.5	37.8	0.30
	0.24	67.5	-20.8	74.3	
	0.36	92.5	-30.0	107	
Al 6082-T6	0.12	57.5	-7.40	26.4	0.21
	0.24	108.	-14.3	51.1	
	0.36	143.	-20.2	72.2	
TiAl6V4	0.12	6.25	-7.41	27.5	0.22
	0.24	11.3	-15.7	53.4	
	0.36	16.3	-22.9	80.9	

## B.3 Pipe Root Strain

Table B.9: Input geometry and plastic zone size used for numerical simulations of circumferential pipe joint, given  $\eta = 0.8$ ,  $1/\rho c = 250 \text{ J}^{-1} \text{ mm}^3 \text{ K}$  and  $\Delta T_{Y1} = 180 \text{ }^\circ\text{C}$ .

ID	$2a$ [m]	$d$ [mm]	$a/d$	$2c$ [mm]	$g$ [mm]	$\beta$	$y_{\text{pl}}$ [mm] for $Q'$ [kJ/mm] =		
							0.60	1.2	1.8
01	0.508	6.35	40.0	1.2	1.2	0.032	25.4	50.8	76.2
02	0.508	6.35	40.0	3.2	3.2	0.032	25.4	50.8	76.2
03	0.508	12.7	20.0	1.2	1.2	0.023	12.7	25.4	38.1
04	0.508	12.7	20.0	3.2	3.2	0.023	12.7	25.4	38.1
05	0.508	15.9	16.0	1.2	1.2	0.020	10.1	20.3	30.4
06	0.508	15.9	16.0	3.2	3.2	0.020	10.1	20.3	30.4
07	0.508	6.35	40.0	1.2	2.4	0.032	25.4	50.8	76.2
08	0.508	6.35	40.0	3.2	6.4	0.032	25.4	50.8	76.2
09	0.508	12.7	20.0	1.2	2.4	0.023	12.7	25.4	38.1
10	0.508	12.7	20.0	3.2	6.4	0.023	12.7	25.4	38.1
11	0.508	15.9	16.0	1.2	2.4	0.020	10.1	20.3	30.4
12	0.508	15.9	16.0	3.2	6.4	0.020	10.1	20.3	30.4
13	0.914	6.35	72.0	1.2	1.2	0.024	25.4	50.8	76.2
14	0.914	6.35	72.0	3.2	3.2	0.024	25.4	50.8	76.2
15	0.914	12.7	36.0	1.2	1.2	0.017	12.7	25.4	38.1
16	0.914	12.7	36.0	3.2	3.2	0.017	12.7	25.4	38.1
17	0.914	15.9	28.7	1.2	1.2	0.015	10.1	20.3	30.4
18	0.914	15.9	28.7	3.2	3.2	0.015	10.1	20.3	30.4
19	0.914	6.35	72.0	1.2	2.4	0.024	25.4	50.8	76.2
20	0.914	6.35	72.0	3.2	6.4	0.024	25.4	50.8	76.2
21	0.914	12.7	36.0	1.2	2.4	0.017	12.7	25.4	38.1
22	0.914	12.7	36.0	3.2	6.4	0.017	12.7	25.4	38.1
23	0.914	15.9	28.7	1.2	2.4	0.015	10.1	20.3	30.4
24	0.914	15.9	28.7	3.2	6.4	0.015	10.1	20.3	30.4
25	1.22	6.35	96.1	1.2	1.2	0.021	25.4	50.8	76.2
26	1.22	6.35	96.1	3.2	3.2	0.021	25.4	50.8	76.2
27	1.22	12.7	48.0	1.2	1.2	0.015	12.7	25.4	38.1
28	1.22	12.7	48.0	3.2	3.2	0.015	12.7	25.4	38.1
29	1.22	15.9	38.4	1.2	1.2	0.013	10.1	20.3	30.4
30	1.22	15.9	38.4	3.2	3.2	0.013	10.1	20.3	30.4
31	1.22	6.35	96.1	1.2	2.4	0.021	25.4	50.8	76.2
32	1.22	6.35	96.1	3.2	6.4	0.021	25.4	50.8	76.2
33	1.22	12.7	48.0	1.2	2.4	0.015	12.7	25.4	38.1
34	1.22	12.7	48.0	3.2	6.4	0.015	12.7	25.4	38.1
35	1.22	15.9	38.4	1.2	2.4	0.013	10.1	20.3	30.4
36	1.22	15.9	38.4	3.2	6.4	0.013	10.1	20.3	30.4

Table B.10: Comparison of model predictions with numerical results of pipe root strain, for tests with  $Q' = 0.6$  kJ/mm, given  $H\eta = 0.18$  and  $E = 200$  GPa. Values for  $f_D$  (Sim.) are estimated using the theoretical moment correction factor  $f_M(\Pi_2)$ ; values for  $f_M$  (Sim.) assume the theoretical distribution correction factor  $f_D(\Pi_1)$ .

ID	$\hat{\theta}$ [mrad]	$\hat{\sigma}_{b,\max}$ [MPa]	$\Pi_1$	$f_D$ Sim.	$\Pi_2$	$f_M$ Sim.	$\mathbf{I}_{\text{root}} = \sigma_{b,\max}/E$ [mm/m]		
							Sim.	Eq.	Rel. Err.
01	44.3	1956	0.56	0.55	0.14	0.90	4.7	4.6	-2%
02	44.3	1956	0.56	0.57	1.0	0.53	2.8	2.6	-6%
03	11.1	489	0.20	0.89	0.025	1.1	2.1	1.9	-9%
04	11.1	489	0.20	0.88	0.18	0.92	1.8	1.7	-8%
05	7.06	312	0.14	1.0	0.014	1.2	1.6	1.3	-16%
06	7.06	312	0.14	0.98	0.10	1.0	1.4	1.2	-12%
07	44.3	1383	0.56	0.57	0.10	0.95	3.6	3.4	-5%
08	44.3	1383	0.56	0.56	0.71	0.60	2.2	2.2	-
09	11.1	346	0.20	0.93	0.018	1.1	1.6	1.4	-13%
10	11.1	346	0.20	0.90	0.13	0.98	1.4	1.3	-10%
11	7.06	221	0.14	1.1	0.010	1.2	1.2	0.94	-20%
12	7.06	221	0.14	1.0	0.072	1.1	1.0	0.89	-15%
13	44.3	1956	0.42	0.62	0.19	0.82	5.1	5.2	+3%
14	44.3	1956	0.42	0.65	1.3	0.43	2.7	2.7	-
15	11.1	489	0.15	0.89	0.034	1.0	2.1	2.0	-3%
16	11.1	489	0.15	0.88	0.24	0.83	1.7	1.7	-
17	7.06	312	0.11	0.97	0.019	1.1	1.5	1.4	-8%
18	7.06	312	0.11	0.95	0.14	0.93	1.3	1.2	-6%
19	44.3	1383	0.42	0.63	0.13	0.87	3.8	3.9	+1%
20	44.3	1383	0.42	0.64	0.95	0.51	2.3	2.3	-
21	11.1	346	0.15	0.91	0.024	1.0	1.5	1.5	-
22	11.1	346	0.15	0.89	0.17	0.89	1.3	1.3	-
23	7.06	221	0.11	1.0	0.014	1.1	1.1	0.98	-11%
24	7.06	221	0.11	0.97	0.096	0.99	0.98	0.90	-8%
25	44.3	1956	0.36	0.65	0.22	0.79	5.2	5.5	+4%
26	44.3	1956	0.36	0.68	1.6	0.39	2.6	2.6	-
27	11.1	489	0.13	0.88	0.039	0.97	2.1	2.1	-
28	11.1	489	0.13	0.88	0.28	0.79	1.7	1.7	-
29	7.06	312	0.092	0.95	0.022	1.0	1.5	1.4	-4%
30	7.06	312	0.092	0.94	0.16	0.89	1.3	1.2	-3%
31	44.3	1383	0.36	0.66	0.15	0.84	3.9	4.1	+3%
32	44.3	1383	0.36	0.67	1.1	0.47	2.2	2.2	-
33	11.1	346	0.13	0.90	0.027	1.0	1.5	1.5	-
34	11.1	346	0.13	0.89	0.19	0.85	1.3	1.3	-
35	7.06	221	0.092	0.98	0.016	1.1	1.1	0.99	-7%
36	7.06	221	0.092	0.96	0.11	0.94	0.95	0.90	-5%

Table B.11: Comparison of model predictions with numerical results of pipe root strain, for tests with  $Q' = 1.2$  kJ/mm, given  $H\eta = 0.18$  and  $E = 200$  GPa. Values for  $f_D$  (Sim.) are estimated using the theoretical moment correction factor  $f_M(\Pi_2)$ ; values for  $f_M$  (Sim.) assume the theoretical distribution correction factor  $f_D(\Pi_1)$ .

ID	$\hat{\theta}$ [mrad]	$\hat{\sigma}_{b,\max}$ [MPa]	$\Pi_1$	$f_D$ Sim.	$\Pi_2$	$f_M$ Sim.	$\mathbf{I}_{\text{root}} = \sigma_{b,\max}/E$ [mm/m]		
							Sim.	Eq.	Rel. Err.
01	88.5	3912	1.1	0.28	0.14	0.95	4.8	4.4	-8%
02	88.5	3912	1.1	0.29	1.0	0.57	2.9	2.5	-13%
03	22.1	978	0.40	0.71	0.025	1.1	3.4	3.1	-9%
04	22.1	978	0.40	0.71	0.18	0.92	2.9	2.7	-8%
05	14.1	624	0.28	0.84	0.014	1.1	2.6	2.3	-12%
06	14.1	624	0.28	0.82	0.10	1.0	2.3	2.1	-10%
07	88.5	2766	1.1	0.29	0.10	1.0	3.7	3.3	-12%
08	88.5	2766	1.1	0.28	0.71	0.64	2.3	2.1	-9%
09	22.1	691	0.40	0.74	0.018	1.1	2.5	2.2	-13%
10	22.1	691	0.40	0.72	0.13	0.98	2.2	2.0	-10%
11	14.1	441	0.28	0.88	0.010	1.2	1.9	1.6	-17%
12	14.1	441	0.28	0.85	0.072	1.1	1.7	1.5	-13%
13	88.5	3912	0.84	0.38	0.19	0.84	6.3	6.3	-
14	88.5	3912	0.84	0.40	1.3	0.45	3.3	3.2	-5%
15	22.1	978	0.30	0.75	0.034	0.99	3.5	3.5	-
16	22.1	978	0.30	0.75	0.24	0.83	3.0	2.9	-3%
17	14.1	624	0.21	0.84	0.019	1.0	2.6	2.5	-5%
18	14.1	624	0.21	0.84	0.14	0.92	2.3	2.2	-4%
19	88.5	2766	0.84	0.39	0.13	0.90	4.7	4.7	-
20	88.5	2766	0.84	0.39	0.95	0.52	2.8	2.7	-3%
21	22.1	691	0.30	0.77	0.024	1.0	2.6	2.5	-5%
22	22.1	691	0.30	0.76	0.17	0.89	2.3	2.2	-4%
23	14.1	441	0.21	0.87	0.014	1.1	1.9	1.7	-8%
24	14.1	441	0.21	0.86	0.096	0.97	1.7	1.6	-6%
25	88.5	3912	0.73	0.43	0.22	0.80	6.9	7.1	+3%
26	88.5	3912	0.73	0.45	1.6	0.40	3.5	3.4	-2%
27	22.1	978	0.26	0.76	0.039	0.96	3.6	3.6	-
28	22.1	978	0.26	0.77	0.28	0.79	2.9	2.9	-
29	14.1	624	0.18	0.85	0.022	1.0	2.6	2.5	-2%
30	14.1	624	0.18	0.84	0.16	0.88	2.3	2.2	-2%
31	88.5	2766	0.73	0.43	0.15	0.85	5.2	5.3	+2%
32	88.5	2766	0.73	0.44	1.1	0.48	2.9	2.9	-
33	22.1	691	0.26	0.78	0.027	1.0	2.6	2.6	-
34	22.1	691	0.26	0.78	0.19	0.85	2.2	2.2	-
35	14.1	441	0.18	0.87	0.016	1.0	1.9	1.8	-5%
36	14.1	441	0.18	0.86	0.11	0.93	1.7	1.6	-4%

Table B.12: Comparison of model predictions with numerical results of pipe root strain, for tests with  $Q' = 1.8$  kJ/mm, given  $H\eta = 0.18$  and  $E = 200$  GPa. Values for  $f_D$  (Sim.) are estimated using the theoretical moment correction factor  $f_M(\Pi_2)$ ; values for  $f_M$  (Sim.) assume the theoretical distribution correction factor  $f_D(\Pi_1)$ .

ID	$\hat{\theta}$ [mrad]	$\hat{\sigma}_{b,\max}$ [MPa]	$\Pi_1$	$f_D$ Sim.	$\Pi_2$	$f_M$ Sim.	$\mathbf{I}_{\text{root}} = \sigma_{b,\max}/E$ [mm/m]		
							Sim.	Eq.	Rel. Err.
01	133	5867	1.7	0.14	0.14	1.1	3.5	2.8	-22%
02	133	5867	1.7	0.14	1.0	0.67	2.1	1.6	-29%
03	33.2	1467	0.60	0.57	0.025	1.1	4.1	3.7	-10%
04	33.2	1467	0.60	0.57	0.18	0.93	3.5	3.2	-9%
05	21.2	936	0.43	0.71	0.014	1.1	3.3	2.9	-12%
06	21.2	936	0.43	0.70	0.10	1.0	3.0	2.7	-10%
07	133	4149	1.7	0.14	0.10	1.2	2.7	2.0	-28%
08	133	4149	1.7	0.14	0.71	0.75	1.7	1.3	-25%
09	33.2	1037	0.60	0.60	0.018	1.1	3.1	2.6	-15%
10	33.2	1037	0.60	0.58	0.13	1.0	2.7	2.4	-12%
11	21.2	662	0.43	0.75	0.010	1.2	2.5	2.1	-17%
12	21.2	662	0.43	0.73	0.072	1.1	2.2	2.0	-14%
13	133	5867	1.3	0.22	0.19	0.88	5.5	5.3	-5%
14	133	5867	1.3	0.24	1.3	0.48	3.0	2.7	-12%
15	33.2	1467	0.45	0.64	0.034	0.99	4.5	4.4	-3%
16	33.2	1467	0.45	0.64	0.24	0.83	3.8	3.7	-3%
17	21.2	936	0.32	0.75	0.019	1.0	3.4	3.3	-5%
18	21.2	936	0.32	0.75	0.14	0.92	3.1	2.9	-4%
19	133	4149	1.3	0.23	0.13	0.95	4.2	3.9	-8%
20	133	4149	1.3	0.23	0.95	0.56	2.5	2.3	-9%
21	33.2	1037	0.45	0.66	0.024	1.0	3.3	3.1	-6%
22	33.2	1037	0.45	0.65	0.17	0.89	2.9	2.7	-5%
23	21.2	662	0.32	0.78	0.014	1.1	2.5	2.3	-8%
24	21.2	662	0.32	0.76	0.096	0.97	2.3	2.2	-7%
25	133	5867	1.1	0.27	0.22	0.82	6.6	6.6	-
26	133	5867	1.1	0.29	1.6	0.42	3.4	3.1	-7%
27	33.2	1467	0.39	0.66	0.039	0.96	4.7	4.7	-
28	33.2	1467	0.39	0.67	0.28	0.79	3.8	3.8	-
29	21.2	936	0.28	0.76	0.022	1.0	3.5	3.4	-2%
30	21.2	936	0.28	0.76	0.16	0.88	3.1	3.0	-2%
31	133	4149	1.1	0.28	0.15	0.88	5.0	4.9	-2%
32	133	4149	1.1	0.29	1.1	0.50	2.8	2.7	-5%
33	33.2	1037	0.39	0.68	0.027	1.0	3.4	3.3	-3%
34	33.2	1037	0.39	0.68	0.19	0.85	2.9	2.9	-
35	21.2	662	0.28	0.79	0.016	1.0	2.6	2.4	-5%
36	21.2	662	0.28	0.78	0.11	0.93	2.3	2.2	-4%

## B.4 Non-Ideal Stress Concentration

Table B.13: Numerical results for non-ideal susceptibility index and geometry stress concentration factor, given  $a = 0.914$  m,  $d = 12.7$  mm, and  $\theta = 0.01$  rad.

ID	$c$ [mm]	$g$ [mm]	$\delta$ [mm]	$\delta/c$	$\phi$ [rad]	$\Pi_3 = c/r$	$\mathbf{I}_{\text{root}}$ [mm/m]	$f_G$
01	0.60	1.2	0.006	0.01	0.01	0.005	2.15	1
02	0.60	2.4	0.006	0.01	0.005	0.001	1.50	1
03	1.6	3.2	0.016	0.01	0.01	0.005	2.17	1
04	1.6	6.4	0.016	0.01	0.005	0.001	1.51	1
05	0.60	1.2	0.060	0.10	0.10	0.048	2.22	0.97
06	0.60	2.4	0.060	0.10	0.050	0.012	1.52	0.99
07	1.6	3.2	0.16	0.10	0.10	0.048	2.24	0.97
08	1.6	6.4	0.16	0.10	0.050	0.012	1.52	0.99
09	0.60	1.2	0.15	0.25	0.25	0.110	2.33	0.92
10	0.60	2.4	0.15	0.25	0.12	0.030	1.54	0.98
11	1.6	3.2	0.40	0.25	0.25	0.110	2.34	0.93
12	1.6	6.4	0.40	0.25	0.12	0.030	1.54	0.98
13	0.60	1.2	0.30	0.50	0.49	0.190	2.48	0.87
14	0.60	2.4	0.30	0.50	0.25	0.058	1.57	0.96
15	1.6	3.2	0.80	0.50	0.49	0.190	2.48	0.88
16	1.6	6.4	0.80	0.50	0.25	0.058	1.57	0.96
17	0.60	1.2	0.45	0.75	0.72	0.247	2.59	0.83
18	0.60	2.4	0.45	0.75	0.37	0.083	1.59	0.94
19	1.6	3.2	1.2	0.75	0.72	0.247	2.59	0.84
20	1.6	6.4	1.2	0.75	0.37	0.083	1.59	0.95
21	0.60	1.2	0.60	1.0	0.93	0.286	2.68	0.80
22	0.60	2.4	0.60	1.0	0.49	0.105	1.62	0.93
23	1.6	3.2	1.6	1.0	0.93	0.286	2.66	0.82
24	1.6	6.4	1.6	1.0	0.49	0.105	1.61	0.94
25	0.60	1.2	1.2	2.0	1.6	0.333	2.67	0.81
26	0.60	2.4	1.2	2.0	0.93	0.167	1.66	0.91
27	1.6	3.2	3.2	2.0	1.6	0.333	2.66	0.82
28	1.6	6.4	3.2	2.0	0.93	0.167	1.65	0.92

# Appendix C: Material Properties

## C.1 ASTM A36 Structural Steel

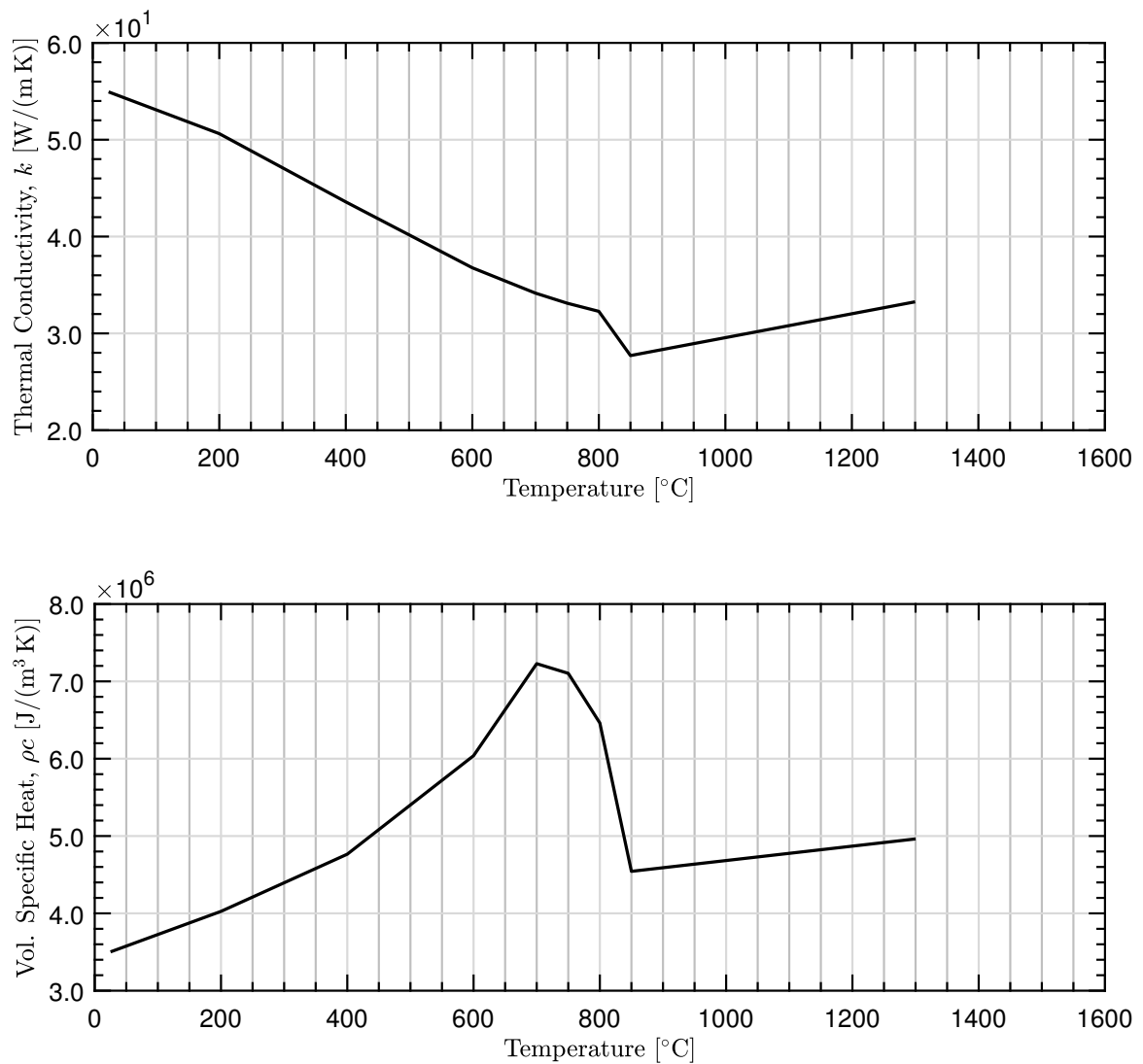


Figure C.1: Thermal property data for ASTM A36 structural steel.

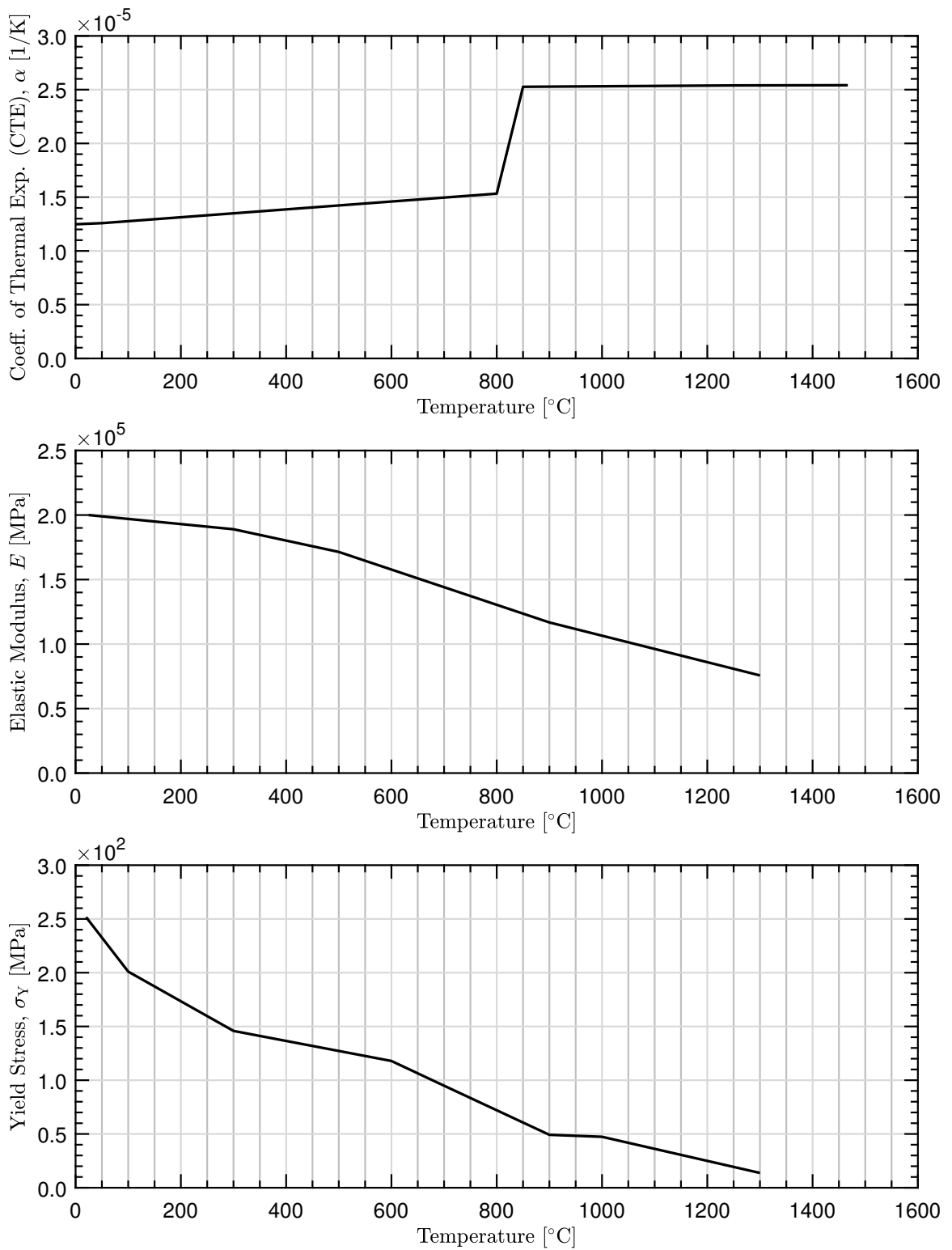


Figure C.2: Mechanical property data for ASTM A36 structural steel.

## C.2 Aluminum Alloy 6082-T6

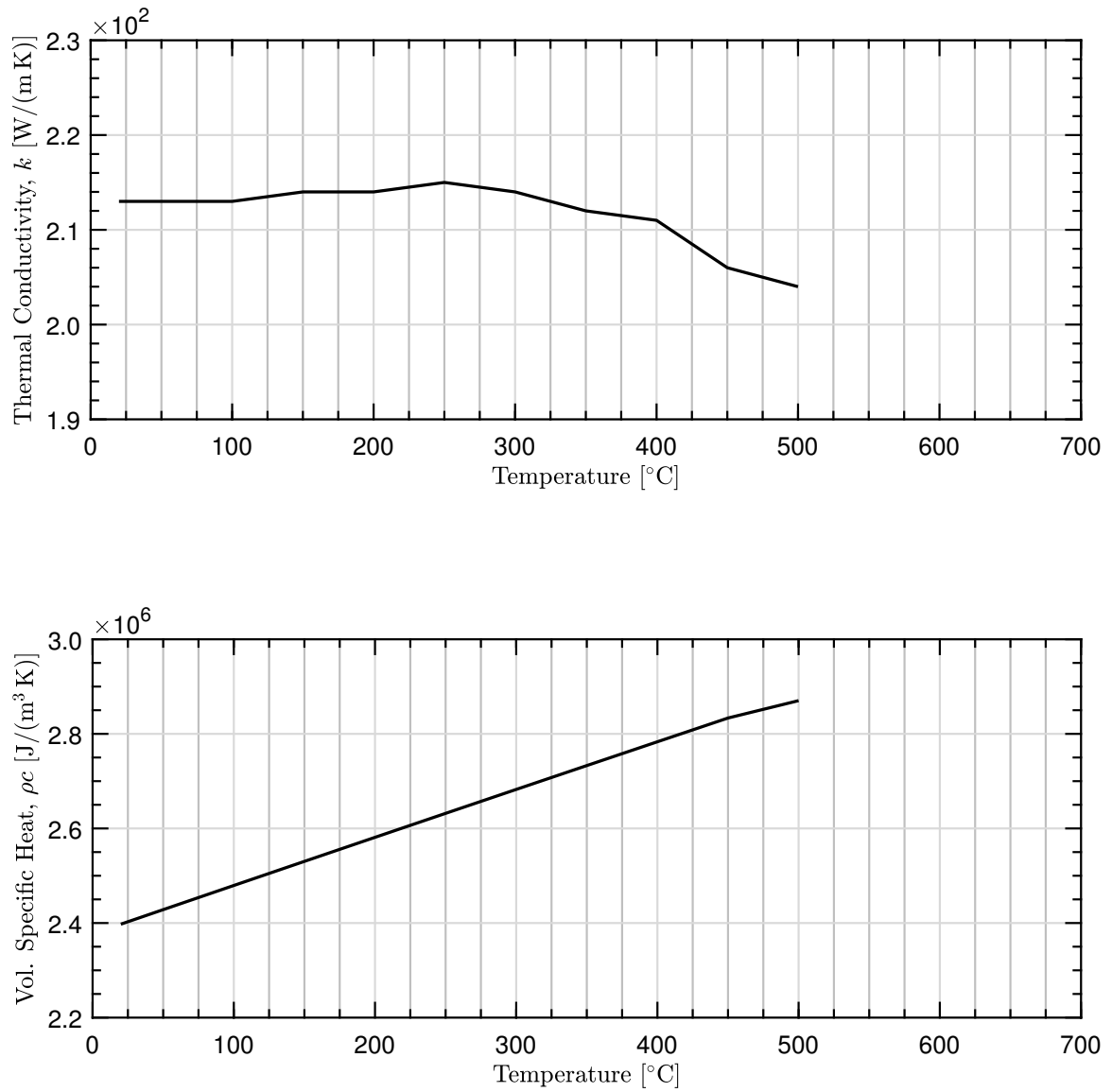


Figure C.3: Thermal property data for aluminum alloy 6082-T6.

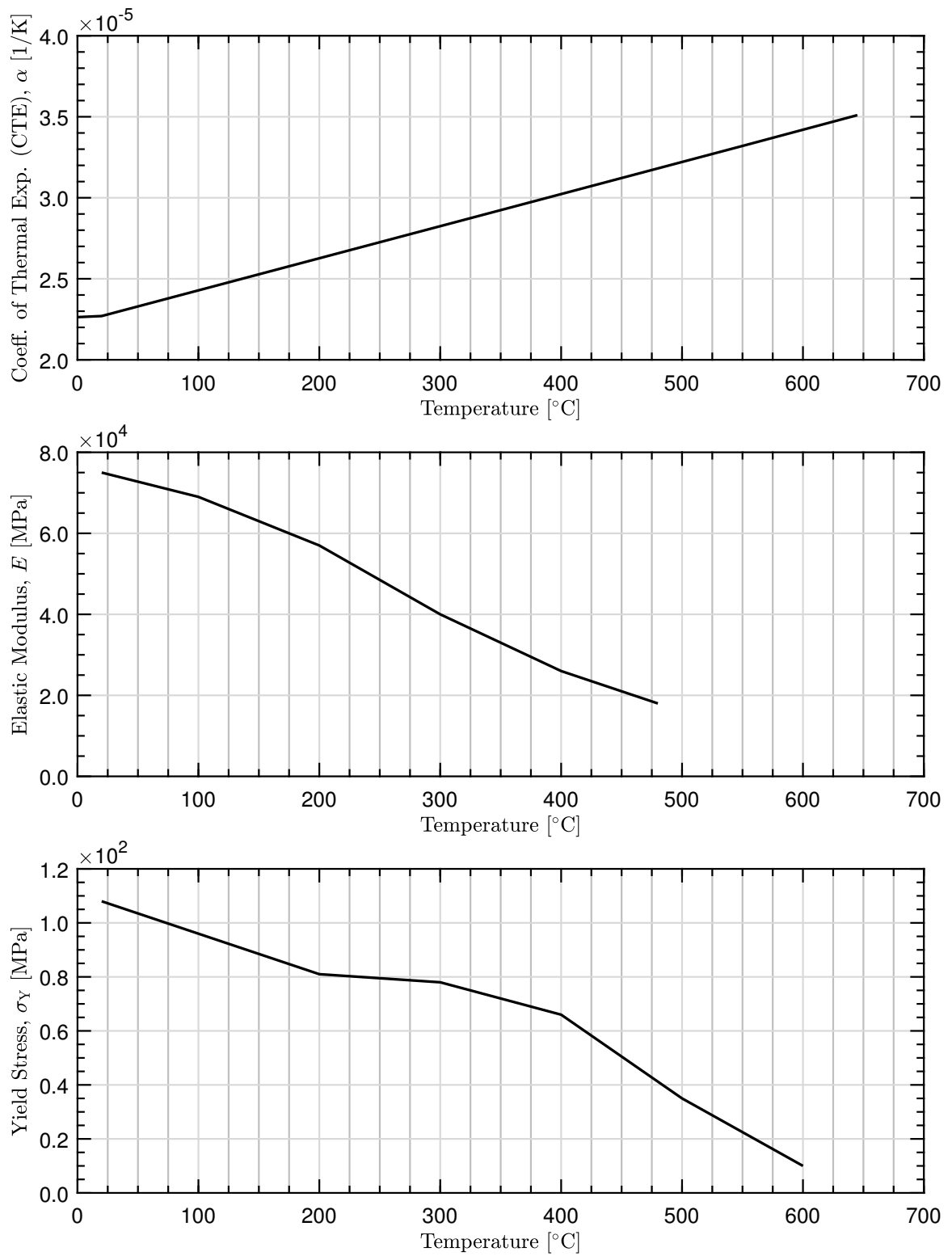


Figure C.4: Mechanical property data for aluminum alloy 6082-T6.

### C.3 304 Stainless Steel

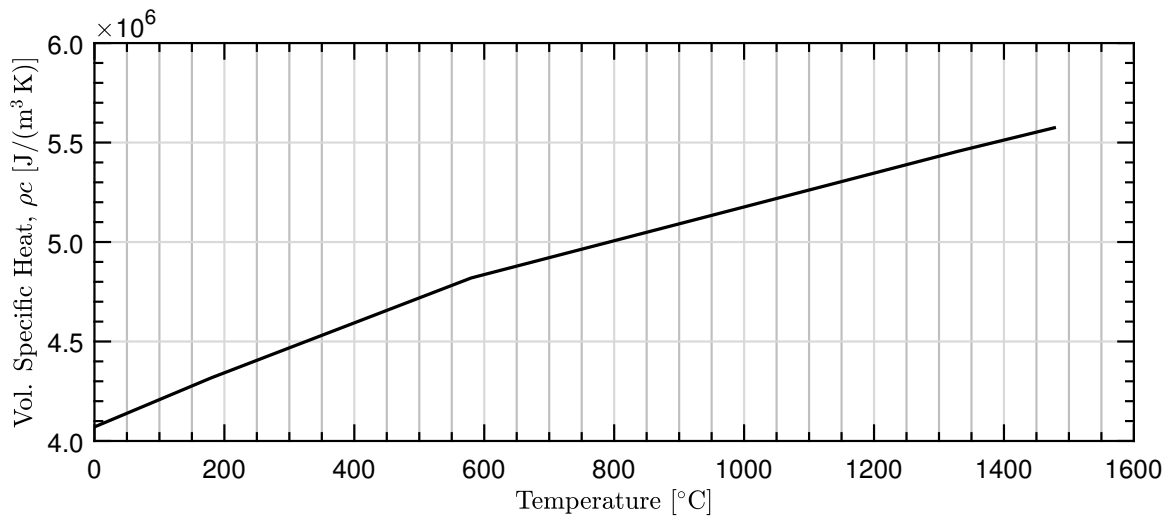
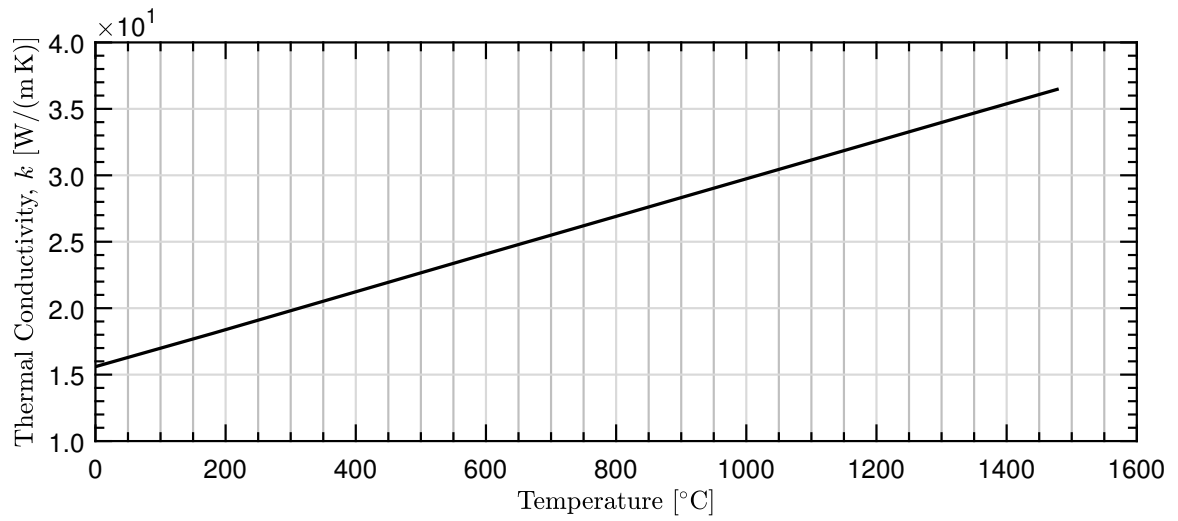


Figure C.5: Thermal property data for 304 stainless steel.

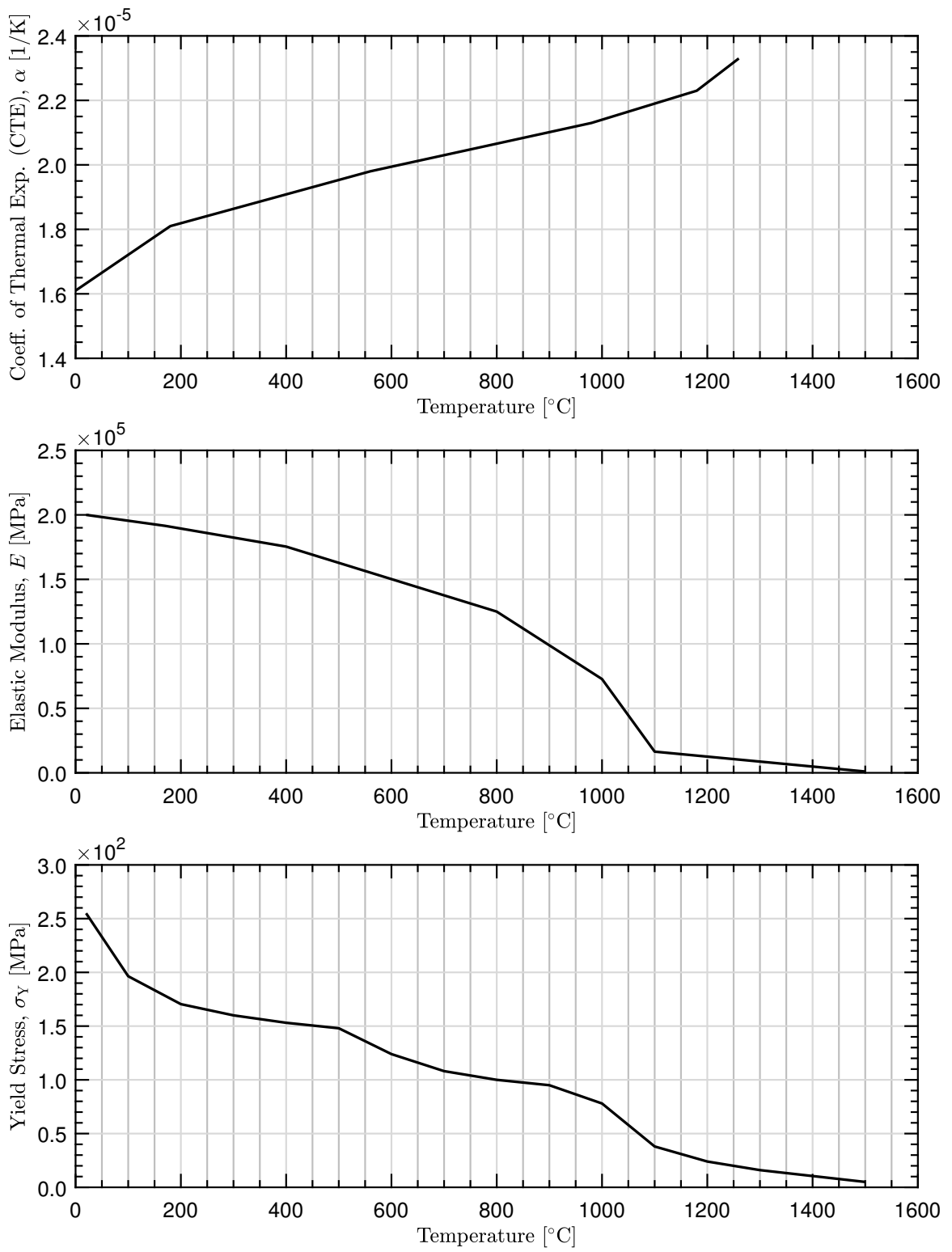


Figure C.6: Mechanical property data for 304 stainless steel.

## C.4 316L Stainless Steel

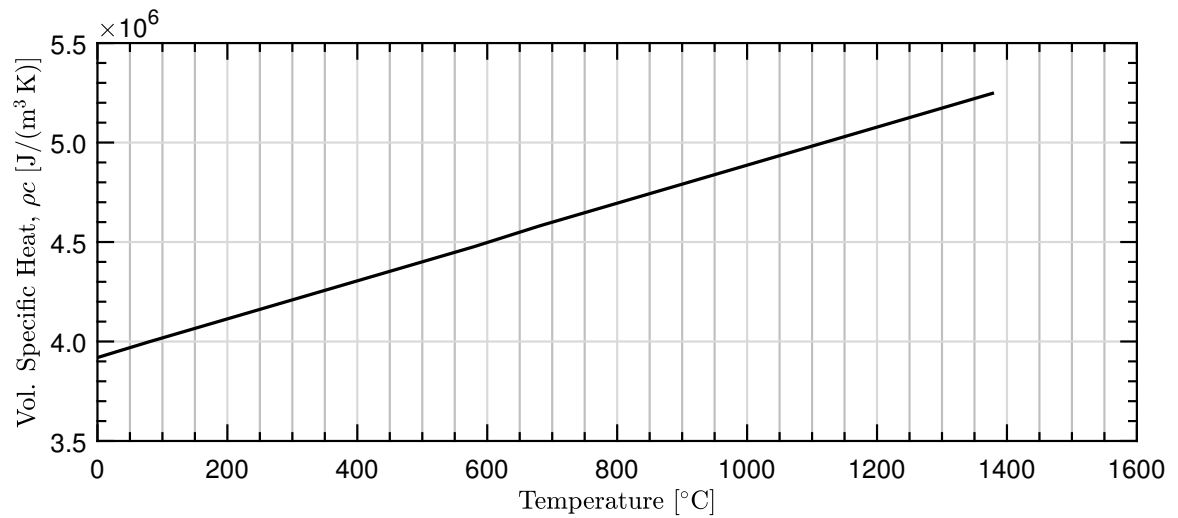
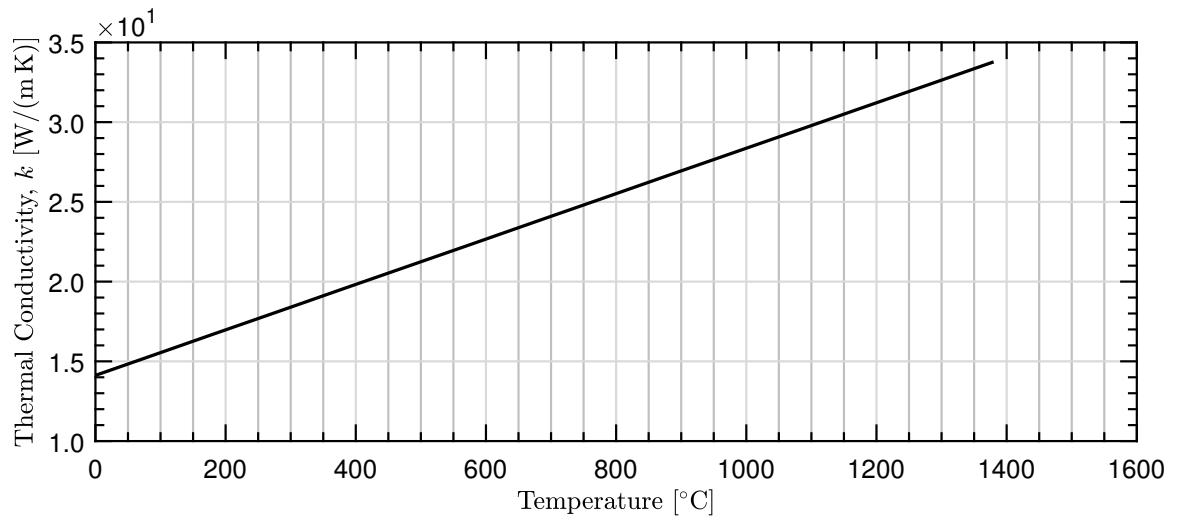


Figure C.7: Thermal property data for 316L stainless steel.

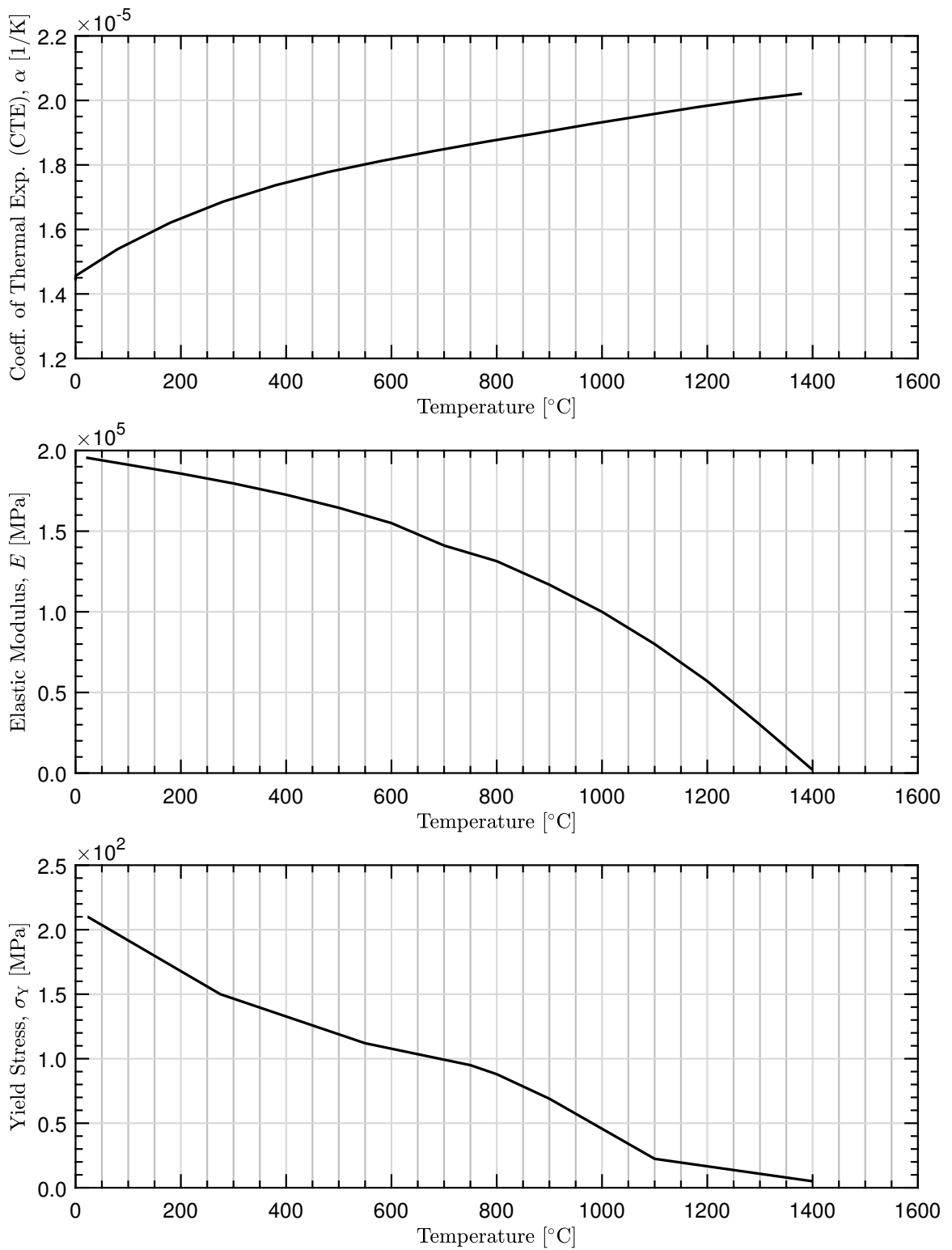


Figure C.8: Mechanical property data for 316L stainless steel.

## C.5 P91 Alloy Steel

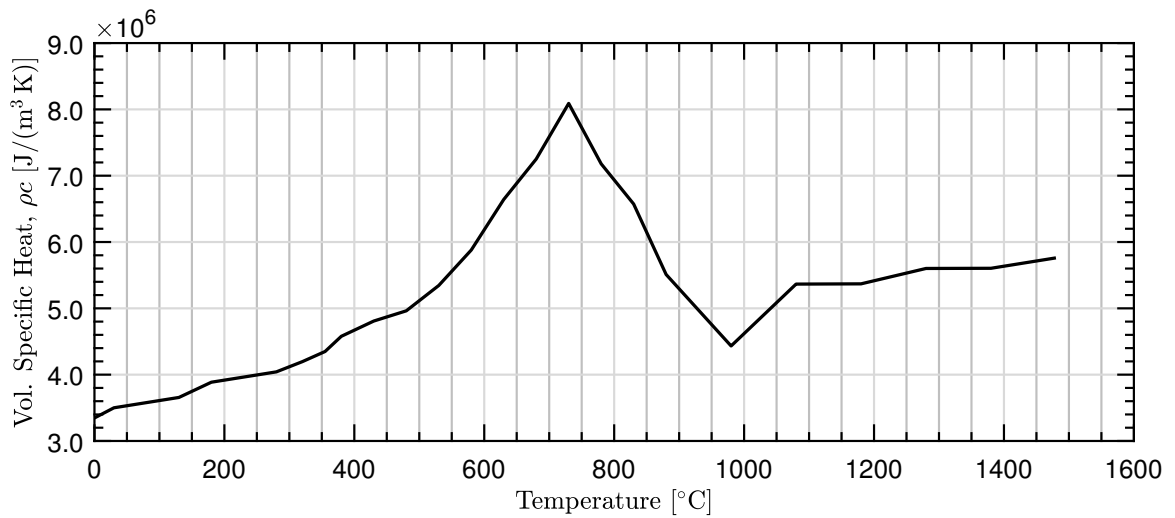
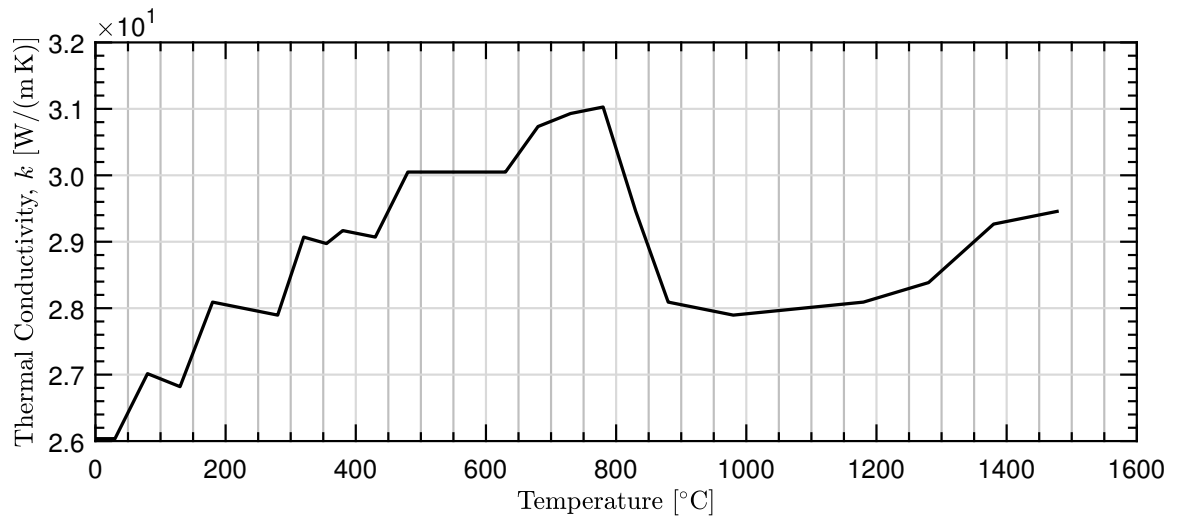


Figure C.9: Thermal property data for P91 alloy steel.

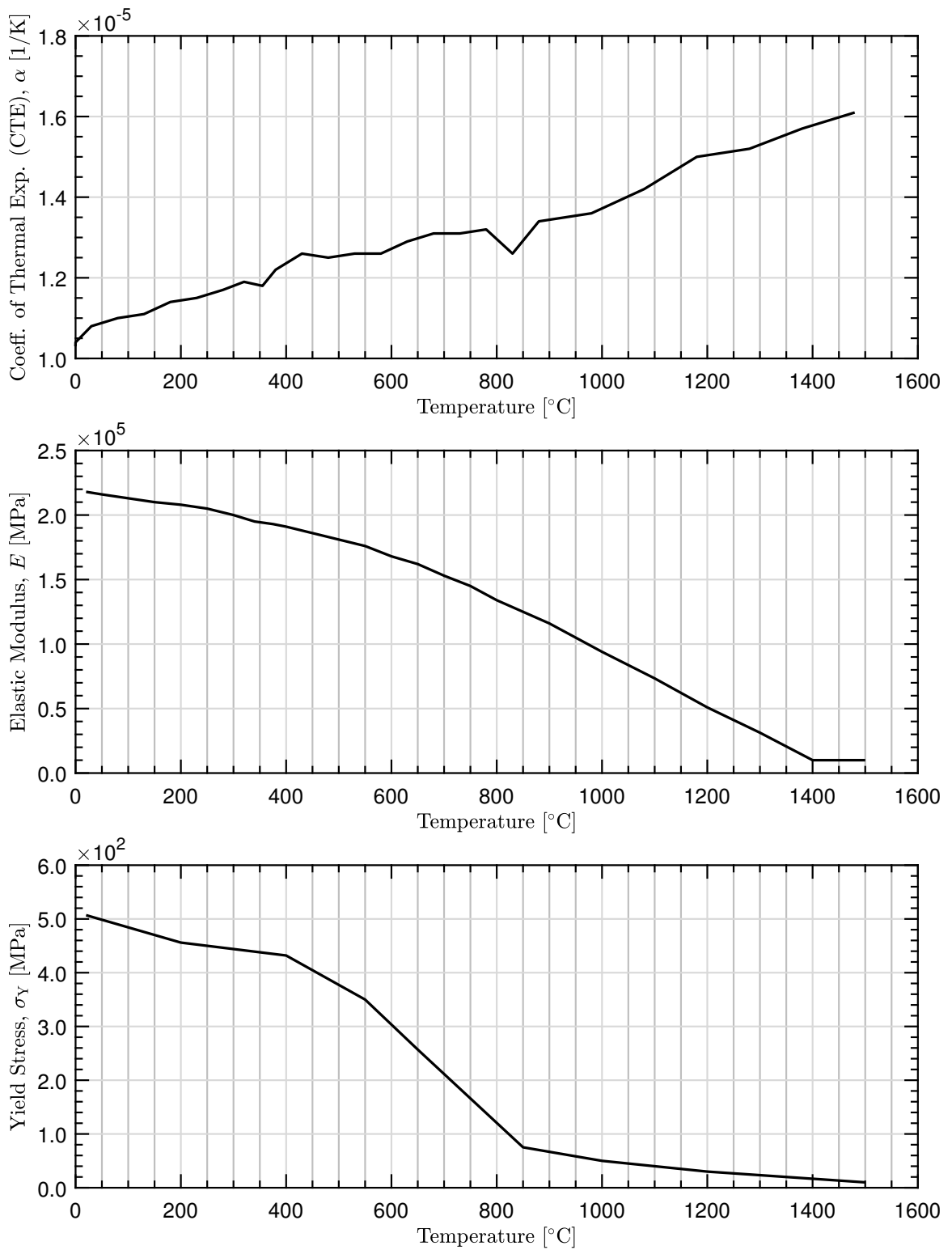


Figure C.10: Mechanical property data for P91 alloy steel.

## C.6 Titanium Alloy TiAl6V4

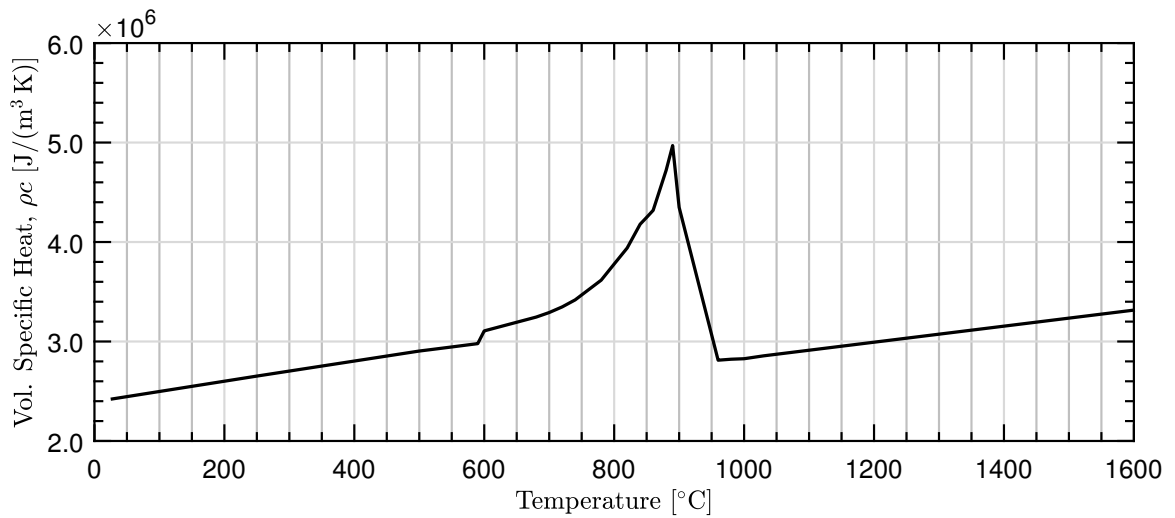
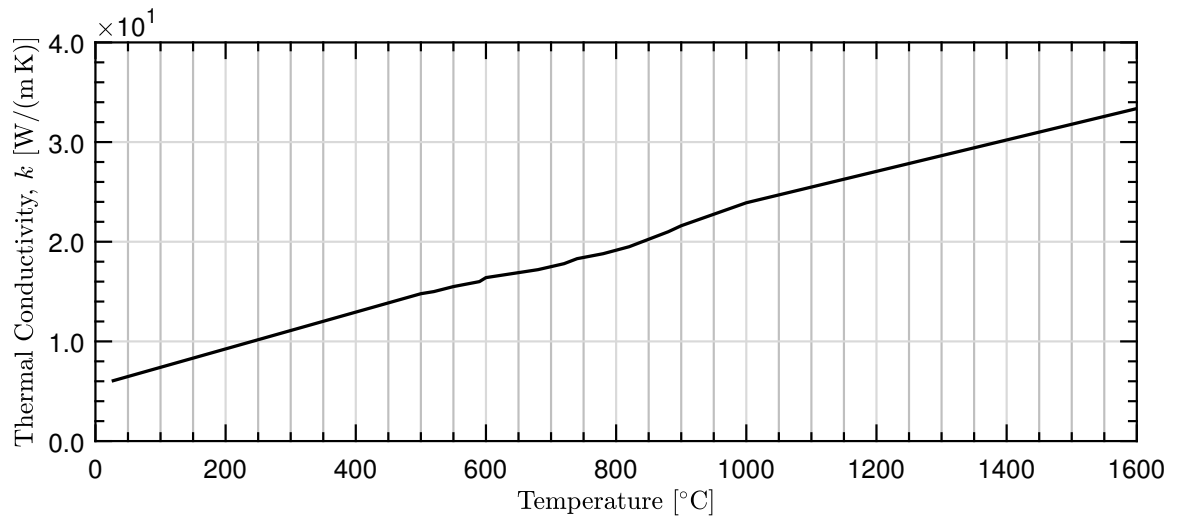


Figure C.11: Thermal property data for titanium alloy TiAl6V4.

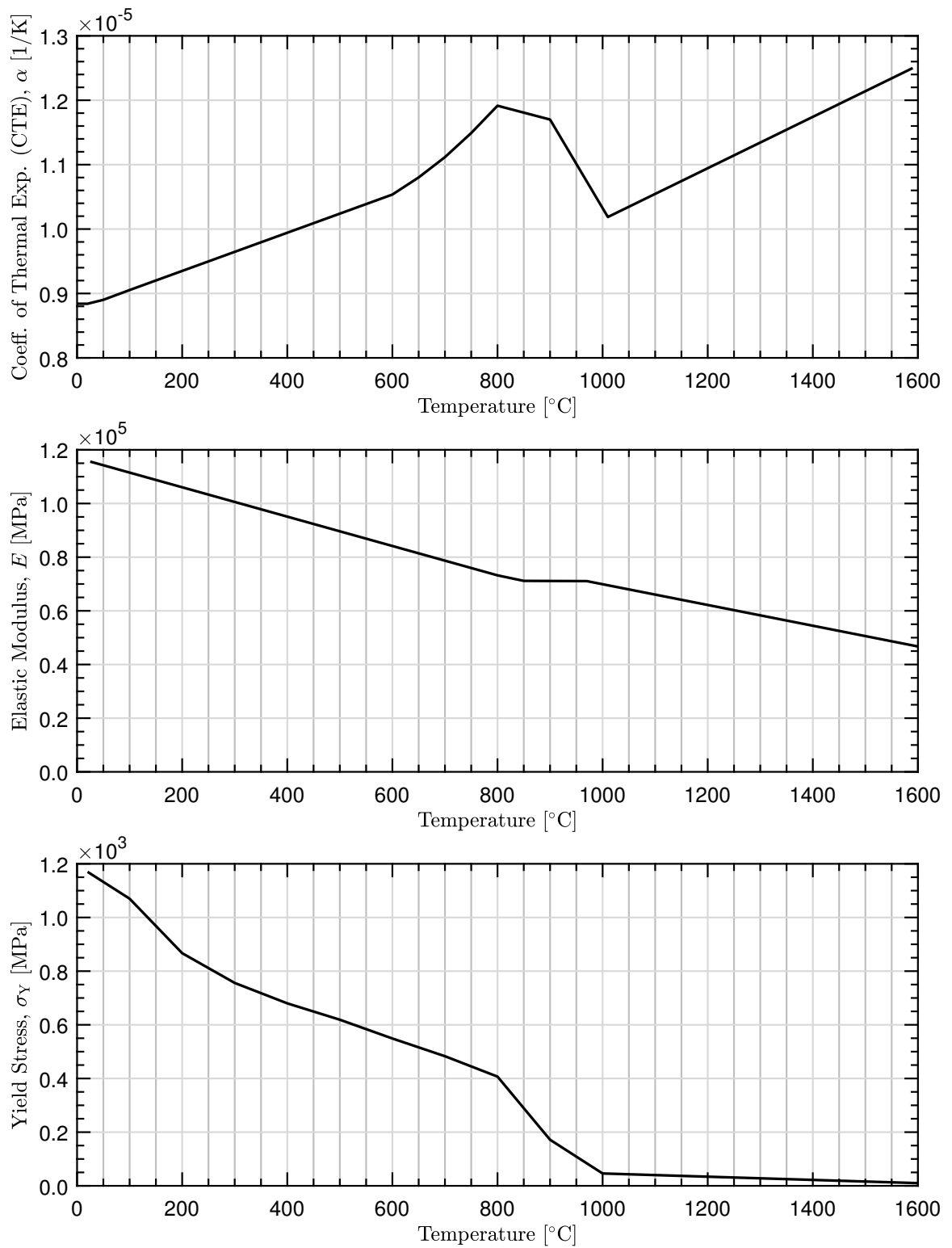


Figure C.12: Mechanical property data for titanium alloy TiAl6V4.